UNIVERSITÉ de Liège

Département MSM
1, chemin des Chevreuils
B 4000 Liège
Belgium

Anne.Habraken@ulg.ac.be

CONTRIBUTIONS TO CONSTITUTIVE LAWS OF METALS:

MICRO-MACRO AND DAMAGE MODELS

Parts C and D

Thèse présentée en vue de l'obtention du grade d'Agrégé de l'Enseignement Supérieur
par Anne-Marie HABRAKEN

Année académique 2000-2001

PART C

DAMAGE MODELS APPLIED TO METALS

Thèse présentée en vue de l'obtention du grade d'Agrégé de l'Enseignement Supérieur

par Anne Marie HABRAKEN

Année académique 2000-2001

Part C- Introduction

MSM research on damage began with Yongui Zhu's thesis, completed in December 1992. Supervised by Professor Serge Cescotto, this Ph.D. thesis proposes an isotropic elasto-plastic damage model, identified and validated on an aluminum alloy, and the theory of an anisotropic elasto-plastic damage model. As a member of the jury and a permanent member of the LAGAMINE team, I devoted much attention to this thesis and its programming work in order to be able to pursue research on this topic. By means of numerous research projects and with the help of several coworkers, Zhu's models have found new applications and new approaches have been developed. Here below are listed all the projects that I have supervised; their results are partially presented in part C of the thesis:

- *Numerical and Physical Study of Material Forming Processes, 1994-1996.* This scientific network groups 14 laboratories thanks to the Human Capital and Mobility Program of European Community. It enabled me to attend numerous meetings and to know other European teams working on Metal Forming Processes. This program supported Raphaël Estevez's 6-months post-doctoral stay with MSM.
- *Dynamic Forging Modeling, second phase, 1993-1996.* This project, which was financed by the Région Wallonne, concerned the improvement of our nonlinear finite element code (LAGAMINE) in order to model dynamic forging processes. I conducted this research with the help of Wang Xiao Chuan.
- *Integration of Micro-Macro Interactions in Metal Forming Finite Element Modeling, 1996-1998.* This Région Wallonne project involved a small part on damage, performed by Jean-François Charles.
- *Rupture Prediction, 1996-1997.* I supervised this graduation work by Anne-France Cambron for her degree in Physics Engineering.
- *Application of an Isotropic Elasto-Plastic Model coupled with Damage Theory to an Aluminum, 1997-1998.* This research comprised another student graduation work by Sylvie Castagne to obtain the degree in Physics Engineering.
- *Experimental and Numerical Approach of Metal Rupture thanks to Damage Theory, 1997-2001.* This research consists in Michaël Wauters's Ph.D. thesis, financed by FRIA (the Industry and Agriculture Research Training Fund of the Belgian French Community). I directed this thesis focused on metal sheet behavior.
- *Bodner's Model Coupled with Damage Theory, 1996-1999.* This research was performed by Zhang Li Hong thanks to the support of the University Research Council of Liège.

Chapters 1 to 5 summarize what is important to know before entering the ductile damage field; this review attempts to summarize the important concepts. Then Chapters 6 and 7 describe the models developed with my guidance. Chapter 8 concludes.

CONTENTS

Notations

Second order tensors are underlined once or noted with their 2 subscripts and fourth order tensor are identified by four subscripts or underlined twice. Capital Latin letters or Greek letters are used for these tensors. Einstein's summation on identical indices is always assumed unless otherwise specified.

The simple contracted tensor product is identified by ".".

$$\underline{C} = \underline{A}.\underline{B} \Leftrightarrow C_{ij} = A_{ik} B_{kj}$$

The tensorial product is :

$$\underline{\underline{C}} = \underline{A} \otimes \underline{B} \Leftrightarrow C_{ijkl} = A_{ij} B_{kl}$$

The double contracted tensor product is noted by ":"

$$s = \underline{A} : \underline{B} \Leftrightarrow s = A_{ij} B_{ij} \quad \underline{C} = \underline{\underline{S}} : \underline{B} \Leftrightarrow S_{ijkl} B_{kl}$$
$$s = \underline{A} : \underline{\underline{S}} : \underline{B} \Leftrightarrow s = A_{ij} S_{ijkl} B_{kl}$$

The tensorial norm is defined by :

$$|\underline{A}| = \sqrt{\underline{A} : \underline{A}}$$
$$|\underline{\underline{S}}| = \sqrt{S_{ijkl} S_{ijkl}}$$

The inverse operator is defined by the superscript -1 :

$$\underline{A}^{-1} \underline{A} = \underline{I} \Leftrightarrow A^{-1}_{ik} A_{kj} = \delta_{ij}$$

with $\underline{I}$ the unit second order tensor, δ_{ik} Kronecker symbol.

The transverse operator is defined by the subscript T :

$$(A^T)_{ij} = A_{ji}$$

Vectors are also underlined once, but small Latin letters are used. They can also be noted with one subscript. The vector operations are :

$$\underline{s} = \underline{v}.\underline{u} \Leftrightarrow s = v_i u_i$$

$$\underline{C} = \underline{v} \otimes \underline{u} \Leftrightarrow C_{ij} = v_i u_j$$

$$|\underline{v}| = \sqrt{\underline{v}.\underline{v}} = \sqrt{v_i v_i}$$

If $\underline{v}$ is a first order tensor and $\underline{\underline{A}}$ a second order one :

$$\underline{u} = \underline{\underline{A}}.\underline{v} \Leftrightarrow u_i = A_{ij} v_j$$

Scalars are not underlined.

The superscript * characterises unit vector :

$$\underline{u}^* \Rightarrow \left|\underline{u}^*\right| = 1$$

Abbreviations

FEM	Finite Element Method
BEM	Boundary Element Method
MSM	Mécanique des Structures et des Matériaux
MK	Marciniak and Kuczinsky's approach
SEM	Scanning Electron Microscope
TEM	Transmission Electron Microscope

Symbols

$\dot{(\,)} = \frac{\mathrm{d}(\,)}{\mathrm{dt}}$	derivative with respect to time
$\int (\,)\,\mathrm{d}(\,)$	integration
x^e	variable associated with elasticity
x^p	variable associated with plasticity
$\overline{a}$	effective variable in damage model, value of one variable in the equivalent virgin state
$\underline{\hat{\alpha}}$	deviatoric tensor
$\underline{\overset{\nabla}{\alpha}}$	objective Jaumann time derivative
Δa	increment of variable a
$(\underline{A})_m$	mean value of tensor $\underline{A} = (1/3)\, A_{ii}$

Latin letters

a_1, a_2, a_3	scalar values in Bodner's damage model or Zhu's damage approach
A	material constant in numerous functions
A	set of equations in Boudeau-Gelin's approach
A_1, A_2	recovery coefficients of isotropic or directional hardening in damage Bodner's model
A_k	thermodynamic forces associated with internal variable α_k in the general thermodynamic formulation
A_d	damaged surface area taking into account area of micro-cracks, voids, microstress concentration iteraction between micro-cracks...
A_t	total cross sectional area of a unit cell cut by a plane
b	ratio between the diagonal of the smallest finite element and the notch radius in meshes dedicated to experiments on aluminum rods
$\underline{b}$	displacement discontinuity vector in Dragon's approach
B_0	initial damage strengthening threshold
B	increase of damage strengthening threshold force associated with scalar damage variable β in anisotropic damage model
B	hardening / softening variable of the loading damage surface in Fichant's model
c	ratio between maximal and minimal finite element edge in meshes dedicated to experiments on aluminum rods
c	square of the average internal length in Geer's model
$c^d\ c^p\ c^r$	material constants in Hayakawa & Murakami's model
$\underline{\underline{C}}^e$	tensor of elastic moduli
d	scalar deviatoric damage variable in Zhu's and Bodner's model
d	scalar variable defined in Fichant's model
d_n	damage variable in direction $\underline{n}$
D	unique damage scalar variable in isotropic damage model
D_0	assumed limit plastic-shear strain rate in Bodner's model
D_1	directional hardening coefficient in Bodner's model
$\underline{\underline{D}}$	second order damage tensor in anisotropic damage model, defined by its 3 principal values d_1, d_2, d_3 in principal axes
$\underline{\underline{D}}^c$	rate of deformation, c means cinematic variable , not damage

e	specific internal energy
E	isotropic Young's modulus
E	void shape parameter in Rice & Tracey's model
E,F,G,H,L,M	material parameters in Hill's model
E_0	initial isotropic Young's modulus in damage model
$\overline{E}$	effective Young's modulus value
E_{eq}, E_m	hardening parameters respectively coming from equivalent and mean plastic macroscopic strain rate in Leblond's version of Gurson's model
E_t	tangent modulus of effective stress-plastic strain curve
f	microvoid volume fraction or porosity
f	loading surface in Fichant's model
f	axial force in Souza Neto's comparison of Gurson's and Lemaître's models
f^*	specific coalescence function in Gurson's model
f_0	initial microvoid volume fraction
f_c	microvoid volume fraction due to coalescence
f_{cr}	critical void volume fraction at onset of coalescence
f_F	porosity at final failure
f_g	microvoid growth volume fraction
f_n	nucleated microvoid volume fraction
f_N	potential nucleated microvoid volume fraction
f_u	ultimate value of f^* at rupture
f_v	volume fraction of inclusions
F	pseudo dissipation potential
F	triaxiality function in damage extension of Bodner's model
F_1	applied force in direction 1
F_d	damage dissipation potential
F_p	yield surface (equal to plastic dissipation potential in associate models)
F_T	triaxiality function to account for multiaxial stress state by a scalar indicator
F_1, F_2	functions defined by Leblond to improve Gurson's model
$\underline{\underline{F}}$	deformation gradient
g	function used to calibrate Bodner's model
g	function of Rousselier's model
$g(\underline{y})$	weighting function defining the intensity and the radius of the spatial non-local effect in Geer's model
G	energy released per unit extension of crack front per unit thickness in fracture mechanics
G	elastic shear modulus
G^d	damage Gibs' potential
G^e	elastic Gibs' potential

G^p	plastic Gibs' potential
$\overline{G}$	effective elastic shear modulus
G_0	initial elastic shear modulus in damage model
$Gibs$	themodynamic potential of Gibs
$\Delta G_{(max)}$	maximum activation enthalpy
H	height of the unit cell in Benzerga's approach
$\underline{\underline{H}}$	fourth order anisotropic Hill's tensor
i,j	orthotropy axes in Vacher's application of Marciniak and Kuczinsky's approach model
$\underline{I}$	second order unity tensor
$\underline{\underline{I}}$	fourth order unity tensor
J	well known parameter in fracture mechanics, rate of change of potential energy per unit cracked area
$\underline{J}$	damage characteristic tensor in anisotropic Zhu's model
J_2	second stress invariant = $\frac{1}{2}\hat{\underline{\sigma}} : \hat{\underline{\sigma}}$
K	isotropic part of the total scalar hardening variable in Bodner's model
K	material parameter in Swift's law
K_0	initial isotropic hardness in Bodner's model
K_I K_{II} K_{III}	stress intensity factor for crack opening modes *I, II, III* respectively
K_{IC}	critical value of the stress intensity factor, value at fracture
K_1	maximum or limiting isotropic hardness in Bodner's model
K_2	minimum or stable isotropic hardness in Bodner's model
l_c	material length scale for rupture
$l_{c(0)}$	(initial) intervoid length in a porous material
l_{10} l_{20} l_{30}	initial plate dimensions in directions 1 2 3 , superscripts *a* or *b* can define one zone of the plate
$l_1 l_2 l_3$	updated plate dimensions in directions 1 2 3
L	distance between the centers of 2 cavities in the transverse direction
$\underline{L}$	velocity gradient
$\underline{\underline{L}}$	fourth order damage tensor used to define the damage surface in Hayakawa & Murakami's model
m_1	hardening exponent of isotropic hardness in Bodner's model
m_2	hardening exponent of directional hardness in Bodner's model
M	point where instability occurs in Boudeau & Gelin's approach

$\underline{\underline{M}}$	fourth order damage tensor used to define the yield surface in Hayakawa & Murakami's model and Zhu's model
n	strain rate sensitivity coefficient in Bodner's model or classical strain hardening exponent in elastoplastic model
$\underline{n}$	unit normal direction to the defect in Marciniak & Kuczinsky's model or to the necking direction in Boudeau & Gelin's approach
$\underline{n}$	unit normal direction
o	origin of axes
p	plastic variable for general isotropic hardening model
p	parameter of the modified damage isotropic Zhu's model
$\underline{p}_i$	unit principal direction i
q, q_1, q_2, q_3	Tvergaard's parameters to improve Gurson's model
$\underline{q}$	heat flux
r	polar coordinate, distance from the crack tip in fracture mechanics
r	exponent of equivalent plastic strain rate in damage model
r	Lankford coefficient
r_H	Lankford coefficient computed with Hill's model
r_1	recovery exponent of isotropic hardness in Bodner's model
r_2	recovery exponent of directional hardness in Bodner's model
R	increase of plastic radius or plastic hardening threshold
R	spherical void radius
R_0	initial spherical void radius
$\dot{R}_k$	radius rate in principal strain direction k
R_1 R_2 R_3	ellipsoidal void radii, the subscript 0 also means initial value
s	stress function exponent in damage model
s	specific entropy
S	second Piola Kirchoff's uniaxial stress
S^k	micro-crack surface in Dragon's approach
S_N	Gaussian standard deviation of the normal distribution of inclusions
t	time
t	unit direction parallel to the defect in Marciniak Kuczinsky's model or to necking in Boudeau & Gelin's model
T	triaxiality ratio σ_m/σ_{eq}
T	temperature

$T_i = \sigma_{ij} n_j$	components of the normal stresses acting at the boundaries along an arbitrary contour for *J*-integral evaluation
u	axial displacement in Souza Neto's comparison of Gurson's and Lemaître's models
u_i	components of the displacement vector in *J*-integral evaluation
$\underline{u}$	direction of the stress tensor in Bodner's model
$\underline{u}$	vector of unknowns in Boudeau-Gelin's approach
$\underline{u}^0$	solution vector in Boudeau & Gelin's approach
$\delta\underline{u}$	perturbation of the solution vector in Boudeau & Gelin's approach
$\delta\underline{u}^0$	amplitude of the perturbation in in Boudeau & Gelin's approach
V	elementary representative volume
V_A	elementary apparent volume of the material (matrix +void)
V_M	elementary apparent volume of the matrix
$w = R_3/R_1 = R_3/R_2$	void shape factor ($w = 1$ sphere, $w = \infty$ cylinder, $w < 1$ oblate void)
W	strain energy density
W^p	plastic work
$\dot{W}^p$	plastic work rate or plastic power
W^t	total plastic and damage energy used in Chaouadi's approach
$\underline{x}, \underline{y}$	coordinates of a material point
$\underline{X}$	back stress due to kinematic hardening
Y or $\underline{Y}$	damage energy release rate in isotropic or anisotropic damage models
Z	total scalar hardening variable in Bodner's model
$x\,y\,z$	principal strain direction in Marciniak and Kuczinsky's model
xy	plane coordinates in fracture mechanics
$X\,Y\,Z$	principal stress directions in Marciniak and Kuczinsky's model
Z_D	directional part of the total scalar hardening variable in Bodner's model

Greek letters

α	triaxiality function parameter
α	material constant in Rice & Tracey's model
α	angle between a tensile test direction and the material Rolling Direction
α_k	internal variable in general thermodynamic formulation
$\underline{\alpha}$	internal variable related to kinematic hardening
α, β	material parameters of damage evolution law in Geer's model
β	strain ratio in Hora's criterion
β	scalar damage variable in anisotropic damage model
$\underline{\beta}$	directional hardening, symmetric tensor in Bodner's model
γ	scalar value derivative of the stress according to plastic work in Bodner's model
$\underline{\gamma}$	center of the plastic yield surface in Zhu's model
δ	volumetric damage variable in Zhu's and Bodner's model
$\varepsilon_1 \ \varepsilon_2 \ \varepsilon_3$	principal strains
$\varepsilon_{eq}\ (\varepsilon_{eq}^{p})$	von Mises equivalent (plastic) strain $\sqrt{\frac{2}{3}\varepsilon_{ij}\varepsilon_{ij}}$
$\dot{\varepsilon}_{eq}$	von Mises equivalent plastic strain rate
ε_{eq}^{d}	damage equivalent strain
$\dot{\varepsilon}_k^{p}$	plastic principal strain rate in direction k
ε_m	mean strain
ε_N	mean effective plastic strain of the matrix at incipient nucleation
ε_{ps}	prestrain strain applied in one direction before a second sollicitation
ε_f	equivalent fracture strain
ε_0	assumed initial strain in Swift's type law
$\underline{\varepsilon}$	strain tensor
$\underline{\dot{\varepsilon}}$	strain rate tensor
$\underline{\varepsilon}^{e(p)}$	elastic (plastic) strain tensor
$\underline{\tilde{\varepsilon}}(\theta)$	dimensionless function depending on polar coordinate θ in fracture mechanics
$\underline{\overline{\varepsilon}}$	effective strain tensor
$\underline{\hat{\varepsilon}}$	deviatoric strain tensor
η	time dependent part of the instability in Boudeau & Gelin's approach

θ	integration scalar in Bodner's integration scheme
θ	angle relative to the crack plane in fracture mechanics
κ	monotonically increasing deformation history parameter in Geer's model
$\dot{\kappa}$	rate of the deformation history parameter
$\lambda_{(o)}$	(initial) void distribution parameter in Benzerga's work
$\dot{\lambda}_p \quad \dot{\lambda}_d$	plastic and damage Lagrange multipliers
ν	Poisson's ratio
ξ	spatial part of the instability in Boudeau & Gelin's approach
ρ	specific mass
$\overline{\sigma}$	uniaxial reference effective yield stress of the fully dense matrix material
$\sigma_1 \sigma_2 \sigma_3$	principal stresses
σ_0	elastic stress limit
σ_D	damage threshold stress in Bodner's model
σ_{eq}	von Mises equivalent stress $= \sqrt{\frac{3}{2}\hat{\sigma}_{ij}\hat{\sigma}_{ij}}$
σ'_{eq}	equivalent stress affected by damage in Hayakawa and Murakami's model
σ_m	hydrostatic (mean) stress = $(1/3)\sigma_{ii}$
$\overline{\sigma}_{eq}$	equivalent effective stress, yield stress of the fully dense matrix
σ_F	updated plastic limit stress
σ_h	plastic stress computed by Hill's model
σ_s	global saturation stress
σ_y	initial yield stress
σ_{1s}	saturation stress of directional hardening in Bodner's model
$\underline{\sigma}$	Cauchy stress tensor
$\underline{\tilde{\sigma}}(\theta)$	dimensionless function depending on polar coordinate θ in fracture mechanics
$\underline{\tilde{\sigma}}$	stress divided by specific mass in Rousselier's model
$\underline{\overline{\sigma}}$	effective stress tensor
$\underline{\hat{\sigma}}$	deviatoric Cauchy stress tensor
$\overset{\nabla}{\underline{\hat{\sigma}}}$	Jaumann stress rate
$\Sigma_1 \quad \Sigma_2$	stresses that replace $\overline{\sigma}$ in Leblond's version of Gurson's model
τ	tensile effect coefficient (ratio between deviatoric and isotropic damage)

χ	bulk modulus
χ_0	initial value of the bulk modulus
$\underline{\Omega}$	antisymmetric part of the velocity gradient tensor or total spin
ψ	Helmholtz free energy per unit mass
$\psi^{(0)e}$	elastic free energy function (in the undamaged, virgin material)
ψ^{d}	damage contribution to free energy
ψ^{ed}	elastic damage contribution to free energy
$\psi^{(0)p}$	plastic contribution to free energy (in the undamaged, virgin material)

1. INTRODUCTION

For more than 20 years, there has been a tremendous amount of research work in the area of elasto-plastic and elasto-visco-plastic damage continuum theories (Gurson 1977, Tvergaard 1982, Lemaître 1985, Perzyna 1986, Gologanu *et al.* 1993, van der Giessen & Tvergaard 1994a). The goal of these studies is the prediction of fracture during forming processes or structural loading for materials like metals, concrete, polymers, rocks... Thanks to the numerous improvements of numerical methods (Finite Element Method -FEM-, or Boundary Element Method -BEM-, or new meshless methods...), scientists are now able to simulate processes as different as forging, extrusion, rolling, deep drawing, wire drawing, cutting... By means of parametric studies, numerical approaches allow optimizations of industrial processes and a deeper understanding of industrial problems. Such a numerical optimization process is often quicker and cheaper than the way of trials and errors. These advantages have progressively convinced the industrial world, and, in some fields like automotive industry or can production for instance, numerical simulations are routinely used. This success has increased the request for reliable constitutive models and rupture criteria in order to produce accurate results and to allow their interpretation with regard to defect prediction.

Zhu's Ph.D. thesis (Zhu 1992) presents a review of the two common approaches of rupture prediction: classical behavior laws coupled with calculation of rupture criteria and continuum damage theory producing constitutive laws coupled with damage. As he has demonstrated, the second approach is more attractive: it allows the prediction of different fracture types, the rupture zone is well identified and crack growth can be followed. According to Lemaître 1985, using uncoupled constitutive equations gives rise to small errors on stresses and strains if the loading is far from the rupture conditions, but the errors may be of the order of 10 to 50 % close to failure. So, MSM research team has concentrated its work on damage models. Even if this field still requires improvements (more sophisticated fracture criteria than threshold value of damage variable, general solution to avoid mesh dependence...) different formulations for the damage theory already exist. They have been developed in order to describe the behavior of materials submitted to high temperature creep, high cycle fatigue, creep-fatigue interaction, spalling and ductile fracture....

There are mainly four kinds of damages: brittle, ductile, creep and fatigue damages. Such a characterization of damage assumes that the material is not the only factor to be considered; in addition, for the same material, damage evolution may be triggered by very different physical mechanisms that fundamentally depend on loading type, loading rate, temperature, as well as environmental factors such as exposure to corrosive substances or nuclear radiation. Therefore, rather than the material alone, the material-process-environment triad must be considered in the study of internal damage.

For many metallic materials at low temperature, **brittle** damaging occurs mainly in the form of cleavage of crystallographic planes in presence of negligible inelastic deformations. At high temperature, brittle damage can also be observed in association with creep processes. In that case, the decohesion of interatomic bonds is concentrated at grain boundaries. At low stresses, this phenomenon is accompanied by relatively small strains.

Ductile damage, on the other hand, is normally associated with large plastic deformations in the neighborhood of crystal defects. The decohesion of interatomic bonds is initiated at the boundary interface between inclusions, precipitates and particles of alloying elements leading to the formation of microscopic cracks and cavities. Further evolution of local plastic deformations may cause the cavities to grow and eventually coalesce, resulting in final rupture. This mechanism is schematically illustrated in Figure 1-1.

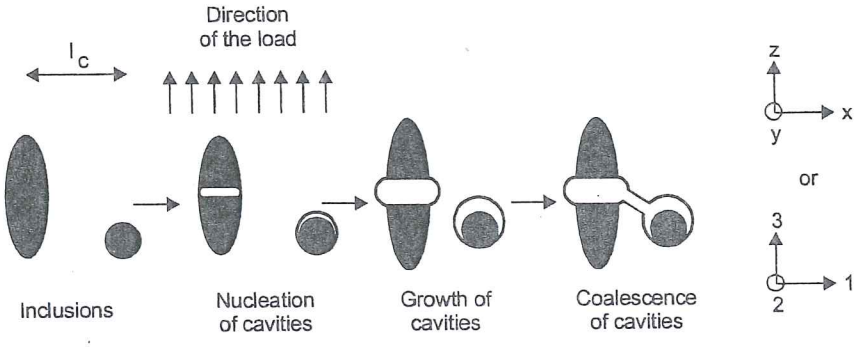

Figure 1-1 : Modeling of ductile fracture and definition of axis (adapted from Rousselier 1987).

The models developed in Liège and presented in Chapters 6 and 7 account for ductile fracture during forming processes; so the following review mainly deals with this specific topic.

Fatigue damage is normally observed in mechanical components subjected to a large number of load and/or temperature cycles. Although fatigue damage occurs at stress amplitudes below the plastic yield limit, the nucleation of micro-cracks is attributed to the accumulation of dislocations observed in connection with cyclic plastic deformation due to stress concentration near microscopic defects. A large number of complex interactive physical mechanisms take place from crack nucleation to complete failure. The understanding of fatigue degradation processes in metals remains a challenging issue in the field of material science. As roughly summarized by Lemaître 1985, the high-cycle fatigue loading, for which the number of cycles to failure is higher than 10^5, does not produce any significant macroscopic plastic strain. This damage is essentially due to transcristalline micro-cracking.

In order to represent the strain rate increase that characterizes tertiary **creep**, Kachanov 1958 replaced the observed uniaxial stress by an effective stress computed by means of a scalar damage internal variable. This was the first Continuum Damage Mechanics model. Later, Rabotnov 1963 proposed a physical significance for this damage variable: the reduction of the cross-section area due to micro-cracking. Then, Leckie & Onate 1981 used a sequence of even rank irreductible tensors to represent the void distribution on the grain boundaries in the context of creep-damage theories.

Another typical classification of damage models is deduced from their scales: the microscale, the mesoscale and the macroscale, as presented in Table 1-1 reproduced from Eckstein 1997.

Scale	Defects	Models
MICRO Atoms, molecule chains	 Vacancies and dislocations	Physics and material sciences
MESO Grains	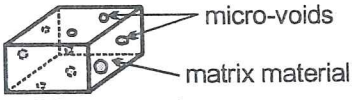 Micro-cracks, pores	Micromechanics
MACRO Test specimen structures	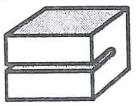 Macro-cracks, shear bands	Continuum theories

Table 1-1 Classification of damage models (from Eckstein *et al.* 1997).

The **microscale** description of damage characterizes the material at the atomic level. The simulation technique of molecular dynamics is based on the motion of a given number of atoms, governed by their mutual interactions described by means of continuous interatomic potentials. It requires the numerical integration of Hamilton's equation of motion. These models study samples of micron size on parallel computers and are therefore not appropriate for engineering applications. However, such approach significantly improves the understanding of the physical principles underlying the elementary processes involved in fracture. For instance, atomistic modeling explains why, depending on material, the dislocation nucleation models of Rice or Peierls are confirmed or not. In fact, the reason lies in different ratios of unstable stacking energy and surface energy (Gumbsch 1995). Another example is a better understanding of the transition between ductile and brittle rupture (Abraham 1995).

The **mesoscale** approach consists in evaluating the behavior of an elementary cell the scale of which lies between that of a subgrain (microscopic) and that of the specimen (macroscopic). For instance, finite element simulations predict the behavior of a

representative cell containing a simple cavity or an inclusion (Luo & Sthalberg 1998), embedded in an elasto-plastic or elasto-visco-plastic matrix, for all kinds of loading conditions, such as torsion, tension or various mechanical states with a constant triaxiality ratio. Figure 1-2 shows one example. Such an approach allows comparisons of void growth between mesoscopic analysis, experiments and macroscopic models like Gurson-Tvergaard's model or Gologanu's model, as presented by Brethenoux et *al.* 1997.

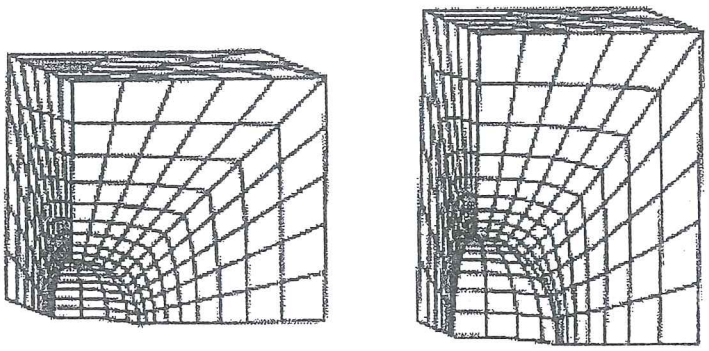

Figure 1-3 : Example of a mesoscopic mesh approach, evolution of a simple cavity; (from Brethenoux *et al.* 1997).

Boyer & Staub 1997 also use the mesoscopic approach to check void growth models such as Rice & Tracey's 1969 or Thomason's 1990. In Gologanu *et al.* 1993, mesoscopic finite element simulations, still limited to one cavity cell, suggest a slight modification of the damage model proposed by Gologanu. van der Giessen & Tvergaard 1994a, 1994b use the planar analysis of a unit cell containing many grains to study the effect of random variations in microstructure on failure events in a metal subjected to creep at high temperatures. Their model accounts for intergranular failure by cavity nucleation and growth to coalescence, or by grain boundary sliding.

As a researcher situated at the limit between two worlds, the metallurgical one and the mechanical one, and, within the latter, being more concerned by the particular sub-domain of numerical simulation, the mesoscale approach seems under-exploited. The advantages of this method are, for instance, to avoid restrictive assumptions usually used in analytical models (spherical or simple shape of void, matrix linear hardening ...) and to give a good account of ductile damage phenomena (nucleation, growth and coalescence) for all kinds of loading conditions. This last point is fundamental, when one is aware of the experimental difficulties to reproduce the mechanical states frequently applied to some metal pieces. It can be the only way to fit with accuracy the model parameters for shear state. It represents a very efficient tool for validating analytical models, for understanding the coalescence phenomena and for choosing adequate formulations. It can also be regarded as a rather easy way to reach some microscopic parameters like volume fraction of initial void when compared to SEM analysis or complete inverse modeling (Lauro *et al.* 1997). In conclusion, the

mesoscopic approach seems a promising way to increase the understanding of damage mechanism, to help with the development and validation of analytical models and hence to improve macroscopic modeling.

Finally the **macroscale** models are characterized by the homogenization of the material behavior. The presence of a large number of micro-defects is considered as smeared throughout the solid, leading to continuum damage theories. Evolution laws for damage variables can be defined by means of phenomenological models (Zhu 1992, Habraken *et al.* 1997) or deduced from micro-mechanical observations (Perez *et al.* Andrés 1997). These types of continuum damage models provide a computationally efficient investigation tool for large-scale structures and offer the advantage of being already implemented in commercial finite element codes, like for instance a Gurson's type law in ABAQUS (Picart *et al.* 1997). Numerous research teams prefer to work with their home made code, in which new or well-known damage models can be easily added. The damage laws implemented in the LAGAMINE code will be presented in Chapters 6 and 7 (Zhu *et al.* 1992, Zhu *et al.* 1995, Wang *et al.* 1996, Habraken *et al.* 1997, Zhang *et al.* 1998). Other examples are Gurson's type law implemented in the ASTRID code (Lazzaretto *et al.* 1996) or a mixed Gurson-Perzyna's law implemented in the METAFOR code (Stainier 1996). A historical review of the development of continuum damage mechanics is presented by de Souza Neto *et al.* 1998.

The book by Voyiadijs & Kattan 1999 about advances in damage mechanics in metal and metal matrix composites summarizes well the state of the art of this field. It offers the interest of presenting a connection between the models applied for metals and composites.

Nowadays, damage mechanics has become an efficient way to solve practical problems. For instance, Doghri 2000 includes a chapter on this topic in his recent introduction to the mechanics of deformable solids and structures.

The goal of next chapters is not to provide a complete overview of damage mechanics applied to metals. However, it has been tried to gather the information necessary to understand damage mechanics; it helps to seize the advantages and limitations of the models developed in Liège. Following this idea, Gurson's model and its further developments are presented in Chapter 2. This macroscopic model with its microscopic bases has met a great success, justified by its good performance as demonstrated by comparisons between simulation results and experimental fractures.
In Chapter 3, thermomechanical damage models are described. Because Lemaître's model is widely used and constitutes the basis of the work performed in MSM department, it is recalled in details.
Gurson and Lemaître's models represent examples of the model families respectively based on micromechanics and continuum thermodynamics. The constitutive models based on variational bounds, like the one of Ponte Castenada & Zaideman 1994 for instance, are not presented in details not for a lack of interest but because they are less

commonly used for metals. This approach is briefly summarized in section 2.2, which compares Gurson's and Hashin-Shtrikman's yield surfaces.

To take advantage of damage simulation results, one must be able to detect where and when fracture will happen. So Chapter 4 gathers interesting rupture criteria. However, this field still requires further research and it seems that no general unique criterion exists.

A well-known problem in FEM damage simulations is the mesh dependency of the results. This problem cannot be forgotten in any work dedicated to damage; so Chapter 5 briefly summarizes the research on this tropic.

Chapter 6 and 7 present the work performed by the MSM team under Habraken supervision. Each of them is dedicated to one specific application: respectively the study of aluminum rods in Chapter 6 and steel sheets in Chapter 7. The different models developed and applied in these cases are described as well as their results. The used models belong to the field of macroscopic continuum damage mechanics and present different characteristics:

- isotropic damage, isotropic elasto-plastic-law,
- isotropic damage, isotropic elasto-visco-plastic-law,
- anisotropic damage, anisotropic elasto-plastic-law.

Finally Chapter 8 gives some conclusions and perspectives.

References

Abraham F.F. (1996) Parallel molecular dynamics investigation fracture. *Computer simulation in materials science*, Kluwer Academic Publishers, 211-226.

Boyer, J.C., Staub, C., (1997) A ductile damage model including shear stress effects. *Advanced Methods in Materials Processing Defects*, Predeleanu, M., Gilormini, P., Eds., Elsevier, 13-22.

Brethenoux, G., Mazataud, P., Bourgain, E., Muzzi, M. & Giusti, J. (1997) A mesoscopic approach of ductile damage during col forming processes, *Advanced Methods in Materials Processing Defects*, Predeleanu, M., Gilormini, P., Eds., Elsevier, 23-32.

Doghri, I., (2000) Mechanics of Deformable Solids, Linear, Nonlinear, Analytical and Computational Aspects, Springer Ed.

Eckstein, A., Basar, Y. & Konke, C. (1997) Damage analysis of ductile metallic shells. *Computational plasticity – Fundamentals and Applications*, COMPLAS V, Owen, D.R.J, Onate, E., Huiton, E., Eds, CIMNE, Barcelona.

Gologanu, M., Leblond, J.B, Devaux, J., (1993) Approximate models for ductile metals containing non-spherical voids – case of axisymmetric prolate ellipsoïdal cavities, *J. Mech. Phys. Solids*, **41-11**, 1723-1754.

Gumbsch P., Atomistic modeling of failure mechanisms, *Computer simulation in materials science*, Kluwer Academic Publishers, 227-244.

Gurson, A.L. (1977) Continuum theory of ductile rupture by void nucleation and growth. *J. Engng. Materials Technology*, **99**, 2-15.

Habraken, A.M., Charles, J.F., Cescotto, S. (1997) Calibration and validation of an anisotropic elasto-plastic damage model for sheet metal forming, in *Damage Mechanics, in Engineering Materials*, Voyiadjis, G.Z., Ju, J.W., Chaboche, J.L., Eds., Elsevier, 401-420.

Kachanov, L.M. (1958) Time of the rupture process under creep condition, *Izv. Akad. Nauk SSSR, Otd. Tekhn. Nauk*, **8**, 26-31.

Krajcinovic, D., (2000) Damage mechanics : accomplishments, trends and needs, *International Journal of Solids and structures*, **37**, 267-277.

Lazzarotto, L., Picart, P. Oudin, J. (1996) Sensitivity of Material Parameters in the Finite Element Computation of Microvoid Nucleation and Growth, *Int. J. of Damage Mechanics*, **5**, 259.

Lauro, F., Barrière, T., Bennani, B., Drazetic, P., J. Oudin (1997) Damage framework for the prediction of material defects : identification of the damage material parameters by inverse technique, *Advanced Methods in Materials Processing Defects*, Predeleanu, M., Gilormini, P., Eds., Elsevier, 165-174.

Leckie, F.A., Onate, E.T. (1981) Tensorial nature of damage measuring internal variables, in Proceedings of the IUTAM *Symposium on physical nonlinearities in structures*, Springer, 140-155.

Lemaître, J. (1985) Coupled elastoplasticity and damage constitutive equations, *J. Comp. Meth. in Appl. Mech. and Eng.* **51**, 31-49.

Luo, C. , Stahlberg, U. (1998) FEM simulation of void formation close to an inclusion in a uniform matrix during plastic deformation, *NUMIFORM 98, Simulation of Materials Processing :Theory, Methods and Applications,* Huetink, J., Baaijens, F.P.T., Eds., Balkema, 379-384.

Peres Aparicio, J.L., de Andres, A., Ortiz, M. (1997) 3D interface element applied to the simulation of crack growth with plasticity. *Computational Plasticity – Fundamentals and Applications*, COMPLAS V, Owen, D.R.J, Onate, E., Huiton, E., Eds, CIMNE, Barcelona, 2011-2018.

Perzyna, P. (1986) Internal state variable description of dynamic fracture of ductile solids, *Int. J. Solids & Struct.*, **22**, 797-818.

Picart, P., Piechel, G. & Oudin, J. (1997) Damage influence in the finite element computations for large strains elastoplastic mechanical structures, *Advanced Methods in Materials Processing Defects*, Predeleanu, M., Gilormini, P., Eds., Elsevier, 175-184.

Ponte Castaneda, P., Zaidman, M. (1994) Constitutive models for porous materials with evolving microstructure, *J. Mech. Phys. Solids*, **42-9**, 1459-1497.

Rousselier, G. (1987) Ductile fracture models and their potential in local approach of fracture, *Nuclear Engineering and Design*, **105**, 97-111.

Rabotnov, Y.N., (1963) On the equations of state for creep. *Progress in Applied Mechanics*, Prager Anniversary Volume, New-York, Mac Millan, 307.

Rice, J.R., Tracey, D.M. (1969) On the ductile enlargement of voids in triaxial stress fields, *J. Mech. Phys. Solids*, **17**, 201-217.

de Souza Neto, E.A., Peric, D., Owen, D.R.J. (1998) Continuum modelling and numerical simulation of material damage at finite strains, *Archives of Computational Methods in Engineering*, **5-4**, 311-384.

Stainier, L. (1996) Modélisation numérique du comportement irréversible des métaux ductiles soumis à grandes déformations avec endommagement. Thèse de docteur en sciences appliquées, Université de Liège.

Thomason, P.F. (1990) Ductile fracture of metals, Pergamon Press.

Tvergaard, V. (1982) Material failure by void coalescence in localized shear bands, *Int. J. Solids & Struct.* **18**, 659-672.

Van der Giessen, E., Tvergaard, V. (1994a) Development of final creep failure in polycrystalline aggregates. *Acta Metall. mater.*, **42-3**, 959-973.

Van der Giessen, E., Tvergaard, V. (1994b) Effect of random variations in microstructure on the development of final creep failure in polycrystalline aggregates. *Modelling Simul. Mater. Sci. Eng.***2**, 721-738.

Voyiadijs, G.Z., Kattan, P.L., (1999) Advances in Damage Mechanics : Metals and Metal Matrix Composites, Elsevier.

Wang, X.C., Habraken, A.M. (1996) An elastic-visco-plastic damage model : from theory to application, *supplément au Journal de Physique*, **6**, 549-558.

Zhang, L.H., Habraken, A.M., Wang, X.C. (1998) Validation of an Elasto-Visco-Plastic Model of Bodner Type Coupled with Damage. *NUMIFORM 98, Simulation of Materials Processing : Theory, Methods and Applications*, Huetink, J., Baaijens, F.P.T., Eds., Balkema, 291-296.

Zhu, Y.Y. (1992) Contribution of the local approach of fracture in solid dynamics, Ph. D. Thesis, University of Liège, Department MSM.

Zhu, Y.Y., Cescotto, S. and Habraken, A.M. (1992) A fully coupled elastoplastic damage modeling and fracture criteria in metalforming processes, *J. of Mater. Processing Technology* **32**, 197-204.

Zhu, Y.Y., Cescotto, S., Habraken, A.M. (1995) Modelling of fracture initiation in metalforming processes, *Materials Processing Defects*, Gosh, S.K., Predeleanu, M., Eds, 155-170, Elsevier Science B.V.

2. GURSON'S MODEL

2.1. Description of Gurson's model and its further developments

Ductile fracture results from initiation, growth and coalescence of cavities as already summarized in Figure 1-1. In fact, Gurson has first derived his model from an approximate limit analysis of a hollow sphere made of rigid perfectly plastic material (representing a typical volume element in a porous medium) and subjected to some axisymmetric loading. Then, in a purely phenomenological and macroscopic way, he has extended his result to the case of a matrix exhibiting isotropic hardening. Finally, Gurson's yield function (Gurson 1977) improved by Tvergaard 1981 for ductile porous metals is defined by:

$$F_p = \frac{\sigma_{eq}^2}{\overline{\sigma}_{eq}^2} + 2q_1 f \cosh\left(\frac{3}{2} q_2 \frac{\sigma_m}{\overline{\sigma}_{eq}}\right) - (1 + q_3 f^2) = 0 \qquad (2\text{-}1)$$

with

σ_{eq} = macroscopic von Mises equivalent of Cauchy's stress, in the context of large strains,

$= \sqrt{\frac{3}{2} \underline{\hat{\sigma}} : \underline{\hat{\sigma}}}$ where $\underline{\hat{\sigma}}$ is the deviatoric stress tensor,

σ_m = macroscopic mean stress = 1/3 tr $\underline{\sigma}$,

f = microvoid volume fraction or porosity ,

$$f = (V_A - V_M)/V_A \qquad (2\text{-}2)$$

where V_A is the elementary apparent volume of the material,
V_M is the elementary volume of the matrix,

f_0 = initial microvoid volume fraction,

q_1, q_2, q_3 constant coefficients later introduced by Tvergaard (Tvergaard, 1981, 1982) but not used in the initial Gurson's law ($q_1=q_2=q_3=1$),

q_1 = parameter to account for interactions between voids,

q_2 = parameter to account for void shape,

q_3 = often defined as q_1^2, this parameter also takes into account void interaction,

$\overline{\sigma}_{eq}$ = yield stress of the fully dense matrix material.

The equivalence between the plastic power dissipated into the material and into the corresponding matrix enables to define the effective values:

$$(1-f)\overline{\sigma}_{eq}\dot{\overline{\varepsilon}}_{eq} = \underline{\sigma} : \underline{\dot{\varepsilon}}^p \qquad (2\text{-}3)$$

where $\dot{\bar{\varepsilon}}_{eq}$ is an average plastic strain rate in the fully dense matrix, also called effective plastic strain rate. $\bar{\sigma}_{eq}$, $\dot{\bar{\varepsilon}}_{eq}$ are scalar variables while $\underline{\sigma}$, $\underline{\dot{\varepsilon}}^{p}$ are Cauchy stress and plastic strain rate macroscopic tensors.

The additional parameters q_i ($q_1 \cong 1.5$; $q_2 \cong 1$; $q_3 \cong q_1^2$) were proposed by Tvergaard 1981 to bring predictions of shear band bifurcation based on Gurson's constitutive relation into closer agreement with corresponding results of a totally numerical analysis of a periodic array of voids. Perrin & Leblond 1990, using a self-consistent method and their improved version of Gurson's model, find q_1 between 1.35 and 1.38 and $q_2 = 1$. They also report that the experimental values q_1 of generally lie in the range from 1.5 to 2.0.

Note three properties of relation (2-1) :

- it reduces to the isotropic von Mises' yield criterion for $f=0$,
- the dependence on void volume fraction is simple when $\sigma_m = 0$ as in pure shear:

$$F_p = \frac{\sigma_{eq}^2}{\bar{\sigma}_{eq}^2} + 2q_1 f - 1 - q_3 f^2 = 0 \qquad (2\text{-}4)$$

- the dependence on stress triaxiality is exponential.

In Gurson's type models, damage is directly linked with the microvoid volume fraction f. Its evolution follows the three phases of void nucleation (f_n), growth (f_g), and coalescence (f_c). The final rate of microvoid volume fraction is given by additivity :

$$\dot{f} = \dot{f}_n + \dot{f}_g + \dot{f}_c \qquad (2\text{-}5)$$

- **The nucleation** of new microvoids is due for instance to decohesion of matrix - inclusion or matrix-second phase interfaces, or to hard particle fracture. Considering a Gaussian inclusion distribution, an assumption is that the microvoid nucleation rate is mainly controlled by the equivalent plastic strain and defined by the relationship proposed by Chu & Needleman 1980:

$$\dot{f}_n = \frac{f_N}{S_N\sqrt{2\pi}} \exp\left\{-\frac{1}{2}\left(\frac{\bar{\varepsilon}_{eq} - \varepsilon_N}{S_N}\right)^2\right\} \dot{\bar{\varepsilon}}_{eq} \qquad (2\text{-}6)$$

where

f_n = nucleated microvoid volume fraction,

f_N = potential nucleated microvoid volume fraction in relation, for instance, with the inclusion volume fraction,

ε_N = mean effective plastic strain of the matrix at incipient nucleation,

S_N = Gaussian standard deviation of the normal distribution of inclusions,

$\bar{\varepsilon}_{eq}$ = equivalent effective plastic strain in the matrix (see relation (2-3)).

For steel sheets, according Chu & Needleman 1980 or Lazzaretto *et al.* 1996, the possible values of the parameters are: $f_N = 0.04$; $0.01 \leq S_N \leq 0.2$; $0.3 \leq \varepsilon_N \leq 0.7$.

The interested reader can refer to the review paper by Montheillet & Moussy 1986 to have a description of the most common nucleation modes and models.

- **The growth of existing microvoids**: in Gurson's model, the growth rate equation comes from the apparent volume change, the mass conservation and the matrix plastic incompressibility. It is easily derived from relation (2-2):

$$\dot{f}_g = \frac{V_M \dot{V}_A}{V_A^2} = (1-f)\,tr\underline{\dot{\varepsilon}}^p \tag{2-7}$$

- **The coalescence of neighboring microvoids** yields to final material failure. As summarized in Pardoen's 1998 bibliographical review, numerous coalescence modes exist and experimental observations are difficult. This short presentation is limited to one possibility, proposed by Tvergaard & Needleman 1984, which is frequently used (Koplik & Needleman 1988, Brunet *et al.* 1997, Lauro *et al.* 1997). In this approach, f_c is not used as an additive part of the porosity but a specific coalescence function f^* replaces the porosity f in relation (2-1) .The aim of this parameter change is to model the complete vanishing of the carrying stress capacity due to void coalescence, at a realistic void volume fraction :

$$f^* = f \qquad \text{if } f < f_{cr}$$

$$f^* = f_{cr} + \frac{f_u - f_{cr}}{f_F - f_{cr}}(f - f_{cr}) \qquad \text{if } f > f_{cr} \tag{2-8}$$

where

f_u = the ultimate value of f^* at the occurrence of ductile rupture, also related to the material parameter q_1 introduced by Tvergaard ($f_u = 1/q_1$),

f_{cr} = the critical void volume fraction at coalescence onset, generally in the range [0.1-0.25] (Tvergaard 1982, Needleman & Tvergaard 1984),

f_F = the porosity at final failure.

As demonstrated by Koplik & Needleman 1988, this latter improvement f^* as well as the q_i coefficients of Tvergaard are necessary to enable Gurson's model to recover results from a mesoscopic approach (cell model of an array of voids loaded with different constant triaxiality ratios) near rupture. This article also shows a limit of Gurson's approach: a same initial void volume fraction f_0 can correspond to different cell geometries which are then characterized by different f_{cr} values (more details will be presented in section 4.1.).

As checked by Leblond, Perrin and Devaux 1995, Gurson's model is incompatible with the classical, exact solution of the problem of a hollow rigid hardenable sphere hydrostatically loaded. Another drawback of Gurson's model is the following one: for any loading path corresponding to a fixed triaxiality, it predicts that the "porosity-macroscopic equivalent plastic strain" curve depends only on the initial porosity f_o

and on the triaxiality T ($T = T_m / T_{eq}$) but not on the hardening exponent. This fact disagrees with both experiments and numerical simulations of the behavior of porous hardenable elementary cells (Leblond *et al.* 1995). These authors propose the following modified yield function :

$$F_p = \frac{\sigma_{eq}^2}{\Sigma_1^2} + 2qf\ cosh\left(\frac{3}{2}\frac{\sigma_m}{\Sigma_2}\right) - (1+qf^2) = 0 \qquad (2\text{-}9)$$

where the stresses $\Sigma_1 = F_1(f_0, E_{eq}, E_m)$ and $\Sigma_2 = F_2(f_0, E_{eq}, E_m)$ are directly determined from the analysis of a rigid hardenable hollow sphere subjected to an axisymmetric proportional prestraining. E_{eq}, E_m are two overall hardening parameters, respectively depending on the deviatoric and hydrostatic parts of the macroscopic plastic strain rate. Functions F_1 and F_2 are tabulated by integrating analytical expressions derived by Leblond *et al.* 1995. Two types of hardening are considered : isotropic, as in the original Gurson's model, and kinematic, as in Mear & Hutchinson's 1985 variant of Gurson's model. The adjustable factor q, introduced by Tvergaard 1981 to bring predictions into closer agreement with numerical analysis of a periodic array of voids is retained in Leblond & Perrin's model. This model helps to check that this parameter q depends only on the geometry of voids and not on the hardening exponent. Pardoen 1998 has performed an extended analysis of the behavior of a copper specimen. His numerous comparisons between experiments and simulations with Gurson's model (2-1) or Gurson-Leblond-Perrin's model (2-8) demonstrate the superiority of the latter model.

Gologanu *et al.* 1993 derive their model from the analysis of an ellipsoidal volume containing a co-focal ellipsoidal cavity. They propose another improvement of Gurson's approach. After some approximations, their theory can be reduced to a Gurson like criterion adapted to materials containing axisymmetric prolate ellipsoidal cavities with parallel orientations. The modifications of the classical Gurson-Tvergaard's criterion (2-1) are the following ones:

- a new internal parameter is introduced: the *void shape factor*, and its evolution rule;
- the hydrostatic stress is replaced by a stress taking into account the stress field anisotropy;
- a factor, function of porosity f, eccentricities e_1 and e_2 of the inner and outer ellipsoids, replaces q_2;
- the evolution of e_1 and e_2 depends *on the void shape factor*.

Since Zhu's model presented in Chapter 7 concerns anisotropy in both plastic and damage behavior, it is worth noticing the works of Doege *et al.* 1997a, 1997b or Brunet *et al.* 1997, Brunet *et al.* 2000. Both authors and co-workers use an anisotropic version of Gurson's model where the equivalent von Mises' stress in equation (2-1) is replaced by the equivalent value given by Hill's anisotropic model. This anisotropic Gurson's extension is empirical. However, Benzerga *et al.* 1997 propose an analysis of the problem of a hollow sphere made of a rigid perfectly

plastic material obeying Hill's criterion and deduce an anisotropic plastic potential quite similar to the one used by Doege and Brunet. Other descriptions of an anisotropic yield locus, such as Barlat & Lian 1989 have also been coupled with the modified Gurson-Tvergaard's model by Brunet *et al.* 1997.

Zhu's models (sections 6.3 and 7.2) and Bodner's damage model (section 6.2) take into account the decrease of elastic parameters due to damage, while the classic Gurson's approach neglects this phenomenon. So, it is interesting to note that Stainier 1996 has proposed a modification of Gurson's model to account for it. As in other well-known models like Perzyna 1986 or Eftis & Nemes 1991, he uses Mackenzie's 1959 relations to represent the degradation of elastic shear and bulk moduli with void growth. The law proposed by Stainier 1996 is a damage elasto-visco-plastic model since Perzyna potential is used with the plastic surface proposed by Gurson. Needleman & Tvergaard 1987 had already proposed such a viscous extension of Gurson's law.

An advantage of Gurson's model is the easy way to link it with microscopic fracture criteria. If spherical voids are assumed, their updated radius R is easily computed from porosity f and initial radius R_0 :

$$\frac{R}{R_0} = \left(\frac{f}{f_0}\right)^{1/3} \tag{2-10}$$

Following Pardoen's 1998 review about growth models (Rice & Tracey 1969, Worswick & Pick, 1990), the following equations, used as post-processor of the FEM analysis results, can approximate the updated ellipsoidal shape of the void:

$$\frac{dR}{R} = A\, exp\left(\frac{3\sigma_m}{2\sigma_{eq}}\right) d\varepsilon_{eq} \tag{2-11}$$

$$\frac{\dot{R}_k}{R} = \frac{\dot{R}}{R} + (1+E)\dot{\varepsilon}_k \tag{2-12}$$

where A is a material constant initially evaluated by Rice at 0.283 for a rigid plastic material, E is a void shape parameter and R_k is the void radius in the principal direction k.

2.2. Comparison between Gurson's and Hashin-Shtrikman's yield surfaces

As summarized in Ponte Castaneda & Zaidman 1994, an approach to account for void interactions can be associated with the effective properties of composites with random microstructures. Scientists in this field obtain bounds for the effective potentials of porous or rigidly reinforced materials with isotropic microstructures, using an extension of Hashin-Shtrikman's 1963 variational principles. For instance, this homogenization technique allows to recover Eshelby's 1957 estimates for a

material with dilute concentrations of aligned ellipsoidal inclusions dispersed in a matrix. So, using a lower bound of the effective potential of nonlinear composite materials, the particular case of a rigid-perfectly plastic matrix material with aligned ellipsoidal voids is expressed in terms of an upper bound effective yield function, hereafter called Hashin-Strickman's yield function (HS). The internal variables used in this HS function are the void volume fraction f and the ratios of the ellipsoidal pore radii: R_3/R_1 and R_2/R_1. The classical relation (2-6), deduced from matrix incompressibility, is used as evolution law for f. The rates of change of the void radii ratios are related to the strain rate within the voids, that can be estimated thanks to Hashin-Shtrikman's assumptions.

Figure 2-1 compares sections of the HS yield surface, computed with fixed values of porosity and void shape to sections of Gurson's yield surface, based on the assumption of spherical voids (GS) or cylindrical voids (GC). The void shape factor is defined by $w=R_3/R_1=R_3/R_2$; $w=1$ or $=\infty$ respectively means spherical or cylindrical voids, while values less (greater) than 1 characterize oblate (prolate) voids.

The axes are defined on Figure 1-1. For small values of porosity (Figure 2-1a. and b.) and highly triaxial loading ($T=\sigma_m/\sigma eq$), Gurson's yield surfaces for spherical (GS) and cylindrical (GC) voids are significantly smaller than the corresponding HS yield surface ($w=1$ and ∞ respectively). This indicates that the HS yield surface is not particularly useful for high triaxiality values. For relatively low values of the triaxiality variable, the yield surfaces GS, GC, HS $w=1$ or ∞ are in close agreement. Recalling that HS surfaces are upper bounds, the fact that the GS surface lies outside the HS yield surface for $w=0.1$ suggests that the GS model is not adequate for oblate voids. The HS model becomes a better option for the whole range of void shapes, from oblate to prolate, provided the triaxiality remains small ($|T|<4/3$).

For moderately large value of the porosity (Figure 2-1c. and d.), HS and Gurson's yield surfaces for both spherical and cylindrical voids are in fairly good agreement, even for high triaxiality. Again, Gurson's model provides rather poor estimates for the yield surfaces of porous materials with flat aligned voids.

Finally, comparing Figures 2-1a., b. and Figures 2-1c., d., one can observe that increasing porosity has a definite softening effect on the porous solid.

The HS surface can be computed simultaneously with the evolution of the void shape and porosity (Ponte Castaneda & Zaidman 1994). Such an approach has demonstrated that the effect of void shape can be as significant as porosity, especially in case of low triaxiality. It was also found that the predictions of shear localization are sensitive to the evolution of porosity, which acts as a hardening-softening mechanism in compression-tension. It is also sensitive to the anisotropy parameters, which typically act in opposite fashion.

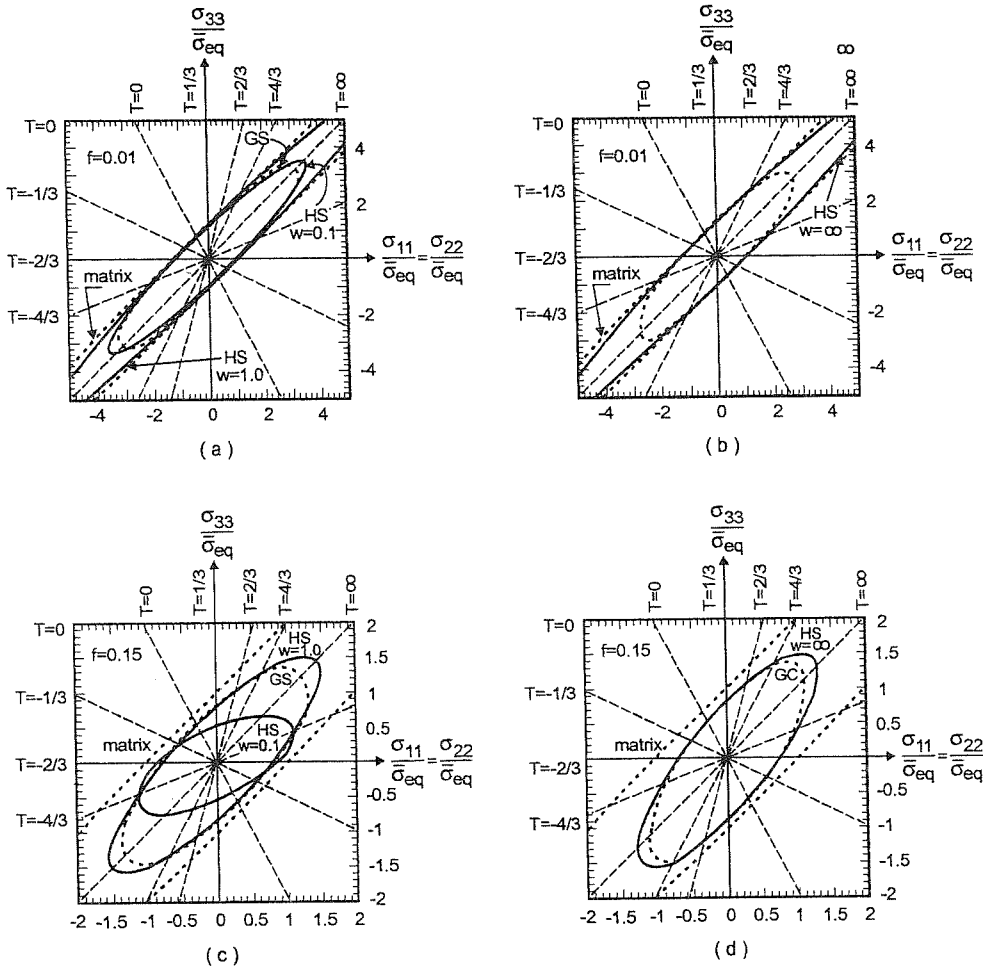

Figure 2-1 Comparison of cross sections of HS and Gurson's yield surfaces for porous materials with aligned spherical (w=1), cylindrical (w=∞) and oblate (w=0.1) voids (from Ponte Castenada & Zaidman 1994).

HS for w =1 and 0.1 versus Gurson with spherical voids (GS) at f=0.01
HS for w = ∞ versus Gurson with cylindrical voids (GC) at f=0.01
HS for w =1 and 0.1 versus Gurson with spherical voids (GS) at f=0.15
HS for w = ∞ versus Gurson with cylindrical voids (GC) at f=0.15

2.3. Conclusions about the use of Gurson's model

The microscopic physical bases of their development as well as their accuracy in fracture prediction explain the great success of Tvergaard-Gurson's model or its extensions. In practice, the model summarized by relations (2-1) to (2-7) requires 8 microscopic parameters:

- f_0 : initial void volume fraction,
- q_1,q_2, ($q_3=q_1^2$) : Tvergaard's material coefficients,
- nucleation parameters: ε_n, S_n, f_n,
- coalescence description: f_{cr}, f_F, ($f_u=1/q_1$).

One must add macroscopic parameters defining the hardening behavior of the matrix, to these 8 microscopic parameters. So, to retain the physical advantage of the model, the user should use optic and electronic microscopic analysis and accurate relative density measurements, obtained for instance by the double weight method, in order to reach the microscopic material parameters. Even with such an equipment, the deduction of f_0 is not always straightforward. A classical approximation is to choose it equal to the volume fraction of inclusions f_v. In some cases, this value can be estimated from the chemical composition of the material (Mudry 1982). However, due to the frequent high anisotropy of ductile fracture, different f_0 can be used depending on the direction of the main loading or the direction of the cracks to be examined. Mudry 1982 has observed that the formed cavities size basically depends on the dimensions d_x d_y of inclusions perpendicular to the load direction z (see Figure 1-1). He proposes to use:

$$f_0 = f_v \frac{(d_x d_y)^{1/2}}{d_z} \tag{2-13}$$

Some well-equipped researchers effectively define the parameters of Gurson's model by microscopic measurements (Rousselier *et al* 1989, Pardoen 1998, Benzerga *et al* 1999). However most mechanical engineers using Gurson's approach have no access to such techniques. So, they have to rely on bibliographical information like the one proposed by Chu & Needleman 1980 or Lazzaretto *et al.* 1996a, which does not always fit their materials. Note that, in his Ph. D. thesis, Wilsius 1999 proposes tables with Gurson-Tvergaard-Needleman parameters for a large set of materials.
This gives mechanical engineers an order of magnitude about values of the model microscopic parameters. In some cases, they try to fit microscopic parameters on macroscopic measurements from damage tests (notched tensile test or other ones) or, less convincingly, from a global tensile curve already used to find the macroscopic parameters of the model (apparent stress-strain curve function). In the latter case, an open question is: "Has their approach any advantage when compared to the use of phenomenological models like the one proposed by Lemaître 1985, in which, at least, the damage function is based on macroscopic measures of the decrease of apparent Young's modulus?" For Gurson's type law, some authors have studied the sensitivity of the microscopic material parameters in regard to the finite element simulation results. For Lazzarotto *et al.* 1996a and 1996b, the initial volume fraction f_0, the effective plastic strain at incipient nucleation ε_N and the potential nucleated microvoid volume fraction f_N are the most sensitive microscopic material parameters. For instance, in cold forging processes, modifications of the initial porosity induce significant variations of the required axial load and of the filling ratio in die cavities. However Picart *et al.* 1997 verify that an accurate characterization of f_0 is not

necessary for small values of the initial porosity. Both preceding studies use no coalescence description (parameters f_{cr}, f_F, f_u). Nevertheless, the work of Koplik & Needleman 1988 demonstrates the importance of f_{cr} to recover the sudden drop of macroscopic stress-strain curves, the parameter f_F being essential to obtain a good approximation of the curves of void volume fraction versus strain, for $f > f_{cr}$.

By means of the development of general inverse modeling techniques, mechanical engineers with no metallurgical microscopic equipment try to reach microscopic parameters with accuracy. It is well known that inverse techniques applied to non linear finite element simulations to identify constitutive law parameters are not straightforward. The unicity of the parameter set provided by such approach is not guaranteed. One must rely on of a set of experimental results sensitive to all the parameters. When strong differences exist between parameters sensitivities, the method convergence can be low. A good example is presented by Lauro *et al.* 1997 : they work on a notched tensile test and adopt the variation of the inner radius in function of the longitudinal elongation as macroscopic response. Their cost function, expressed in a least square sense, measures the difference between FEM simulations and experimental responses and they use a classical optimizer module to find the material parameters minimizing their cost function. They first take some bibliographic values for the microscopic parameters and fit the macroscopic parameters. Then, in a second run, the macroscopic parameters are fixed and they search for some microscopic ones (ε_N, f_N, q_1) related only to void nucleation and growth because their experiment is not able to produce reliable data on the coalescence process. This choice is also suggested by their sensitivity analysis. They report that the optimization of these 3 microscopic parameters has required 292 iterations, which means that the FEM modeling of their notch experiment must be CPU time efficient to avoid unacceptable CPU time.

Another example is available in Kleinermann's 2000 thesis; this scientist applies inverse analysis to identify all the microscopic parameters of Gurson's model except the initial porosity. The macroscopic parameters are known. The assumed experimental data also concern a notched tensile test. The tensile load, the contraction of the notch and the axial displacement of the notch boundary are recorded. These 3 functions of time are used in the cost function. The high number of parameters as well as the different sensitivity of the results provide a difficult problem for the inverse method. Kleinermann's 2000 computation has requested nearly 3 weeks of CPU time or the equivalent of 378 times the direct problem CPU time.

Considering the available mechanical equipment in MSM, the lack of metallurgical investigation technique (SEM, TEM) in this team and the heavy work to develop efficient inverse modeling, one can understand from the preceding paragraphs why phenomenological models of Lemaître's type have been preferred to Gurson's model.

Another element to explain this choice is the fact that the advantage of the microscopic foundation of Gurson's type models is restricted to specific loadings

such as uniaxial or multiaxial tensile states. The reality often deals with complex mechanical states with non-negligible shear components, where the superiority of Gurson's type law is not certified. Another disadvantage of Gurson's model compared to Lemaître's model is its lack of damage accumulation in cyclic loading, when compressive states decrease the porosity accumulated during tensile phases as shown in section 3.3. The last strong argument in favor of damage macroscopic models is their relatively easy identification on the basis of simple mechanical tests. This enables to find quickly and at low cost the parameters required to model a new material. In conclusion, the present thesis is limited to macroscopic damage models of the phenomenological type, identified without global inverse modeling tools.

References

Barlat, F., Lian, J. (1989) Plastic behaviour and stretchability of sheet metals. Part 1 : a yield function for orthotropic sheets under plane stress conditions, *Int. J. of Plasticity*, **5**, 51.

Benzerga, A., Besson, J., Pineau, A. (1997) Modèle couplé du comportement-endommagement ductile de tôles anisotropes. *3ème colloque national en calcul des structures*, 20-23 mai, Giens, France.

Benzerga, A., Besson, J., Pineau, A. (1999) Coalescence-controlled anisotropic ductile fracture. *J. Eng. Mat. Eng.* **121**, 221-229.

Brunet, M., Mguil-Touchal, S., Morestin, F. (1997) Numerical and experimental analysis of necking in 3D sheet forming processes using damage variable, *Advanced Methods in Materials Processing Defects*, Predeleanu, M. & Gilormini, P., 205-214.

Brunet, M., Morestin, F, Walter, H., Numerical Analysis of Failure in Sheet Metal Forming with Experimental Validation (2001), *Numerical Modelling in Damage Mechanics, Euromech 417,* University of Technology of Troyes, France, *Journal of Finite Elements to appear in Spring.*

Chu, C.C., Needleman,A. (1980), Void-nucleation affects in biaxially stretched sheets. *J. Eng. Mat. Techn.*, **102**, 1980, 249-256.

de Borst, R. (1991) Simulation of strain localization : a reappraisal of the Cosserat continuum, *Engineering Computations*, **8**, 317-332.

Doege, E., Bagaviev, A. & Dohrmann, H. (1997a) Application of an anisotropic extension of Gurson model to practical engineering problems, *Computational Plasticity – Fundamentals and Applications*, CIMNE, Barcelona, 1453-1458.

Doege, E., Bagaviev, A. & Dohrmann, H. (1997b) Formability analysis based on the anisotropically extended Gurson model, *Advanced Methods in Materials Processing Defects*, Predeleanu, M. & Gilormini, P., 281-288.

Eftis, J., Nemes, J.A. (1991) Evolution equation for the void volume growth rate in viscoplastic damage constitutive model. *Int. J. of Plasticity*, **7**, 275-293.

Eshelby, J.D. (1957) The determination of the elastic field of an ellipsoidal inclusion and related problems. *Proc. Roy. Soc. London*, **A241**, 376-396.

Gologanu, M., Leblond, J.B., J. Devaux (1993) Approximate models for ductile metals containing non-spherical voids – case of axisymmetric prolate ellipsoïdal cavities, *J. Mech. Phys. Solids*, **41-11**, 1723-1754.

Gurson, A.L. (1977) Continuum theory of ductile rupture by void nucleation and growth. *J. Engng. Materials Technology*, **99**, 2-15.

Hashin, Z., Shtrikman, S., (1963) A variational approach to the theory of the elastic behavior of multiphase materials. *J. Mech. Phys. Solids,* **11**, 127-140.

Kleinermann, J.P. (2000) Identification paramétrique et optimisation des procédés de mise à forme par problèmes inverses, Thèse de Doctorat, Université de Liège. .

Koplik, J. , Needleman, A. (1988) Void growth and coalescence in porous plastic solids. *Int. J. Solids Structures*, **24-8**, 835-853.

Lazzarotto, L., Picart, P. Oudin, J. (1996a) Sensitivity of Material Parameters in the Finite Element Computation of Microvoïd Nucleation and Growth, *Int. J. of Damage Mechanics*, **5**,259.

Lazzarotto, L., Picart, P. Oudin, J. (1996b) Benchmarks for finite element modeling of cold forging processes with elasto-plastic microvoided materials. *Computational Materials Science*, **5**, 167-176.

Lauro, F., Barrière, T., Bennani, B., Drazetic, P. and J. Oudin (1997) Damage framework for the prediction of material defects : identification of the damage material parameters by inverse technique, *Advanced Methods in Materials Processing Defects*, Predeleanu, M. & Gilormini, P., Eds. Elsevier 165-174.

Leblond, J.B., Perrin, G., Devaux, J. (1995) An improved Gurson-type model for hardenable ductile metals, *Eur. J. Mech. A/Solids*, **14**, 499-527.

Lemaître, J. (1985) Coupled elastoplasticity and damage constitutive equations, *J. Comp. Meth. in Appl. Mech. and Eng.* **51**, 31-49.

Mackenzie, J.K. (1959) The elastic constants of a solid containing spherical holes, *Proc. Phys. Soc.*, **63B**, 2-11.

Mear , H.E., Hutchison, J.W. (1985) Influence of yield surface curvature on flow localization in dilatant plasticity, *Mech. Mat.*, **4**, 395-407.

Montheillet, F., Moussy, F. (1986) Physique et mécanique de l'endommagement F. Montheillet and F. Moussy eds., GRECO, Editions de Physique, les Ulis, France.

Mudry, F. (1982) Etude de la rupture ductile et de la rupture par clivage d'aciers faiblement alliés, Thèse d'état, Université Technologique de Compiègne.

Needleman, A., Tvergaard, V. (1987) An anlysis of ductile rupture modes at a crack tip, *J. Mech. Phys. Solids*, **35-2**, 151-183.

Pardoen, T., (1998) Ductile fracture of cold-drawn copper bars : experimental investigation and micromechanical modelling, Doctorat en Sciences Appliquées, Université de Louvain-La-Neuve.

Perrin G., Leblond, J.B. (1990) Analytical study of a hollow sphere made of plastic porous material and subjected to hydrostatic tension-Application to some problems in ductile fracture of metals, *Int. J. of Plasticity*, **6**, 677-699.

Perzyna, P. (1986) Internal state variable description of dynamic fracture of ductile solids, *Int. J. Solids & Struct.*, **22**, 797-818.

Picart, P., Piechel, G. & Oudin, J. (1997) Damage influence in the finite element computations for large strains elastoplastic mechanical structures, *Advanced*

Methods in Materials Processing Defects, Predeleanu, M. & Gilormini, P., Eds. Elsevier, 175-184.

Ponte Castaneda, P., Zaidman, M. (1994) Constitutive models for porous materials with evolving microstructure, *J. Mech. Phys. Solids*, **42-9**, 1459-1497

Rice, J.R. , Tracey, D.M. (1969) On the ductile enlargement of voids in triaxial stress fields, *J. Mech. Phys. Solids*, **17**, 201-217.

Rousselier, G., Devaux, J.C., Mottet, G., Devesa, G. (1989) A methodology for ductile fracture analysis based on damage mechanics : an illustration of a local approach of fracture, *Nonlinear Fracture Mechanics : vol. II – Elastic-Plastic Fracture, ASTM STP 995*, J.D. Landes, A. Saxena, J.G. Merkle Eds, *American Society for Testing and Materials*, Philadelphia, 332-354.

Stainier, L. (1996) Modélisation numérique du comportement irréversible des métaux ductiles soumis à grandes déformations avec endommagement. Thèse de Docteur en Sciences Appliquées, Université de Liège.

Tvergaard, V. (1981) Influence of voids on shear band instabilities under plane strain conditions. *Int. J. Fract.*, **17**, 389-407.

Tvergaard, V. (1982) Material failure by void coalescence in localized shear bands, *Int. J. Solids & Struct.* **18**, 659-672.

Tvergaard, V., Needleman, A. (1984) Analysis of a cup and cone fracture in a round tensile bar. *Acta Metallica*, **32**, 157-169.

Wilsius, I., (1999) Etude expérimentale et numérique de la déchirure ductile basée sur des approches locales en mécanique de la rupture, Ph. D. Thesis Université des Sciences et Technologie de Lille.

Worswick, M.J. & Pick, R.J. (1990) Void growth and constitutive softening in a periodically voided solid. *J. Mech. Phys. Solids*, **38**, 601-625.

3. THERMODYNAMIC DAMAGE MODELS

In the present state of development of Continuum Damage Mechanics, it has been verified that, in general, the loss of microscopic information resulting from the phenomenological approach is compensated by the gain in analytical, experimental and computational tractability of such models.

The application field of coupled mechanical and damage constitutive equations is very large. For instance, Lemaître 1985 presents an elastic model coupled with damage for brittle failure of concrete or high-cycle fatigue of metals, an elasto-plastic model coupled with damage for ductile fracture or low-cycle fatigue, and an elasto-visco-plastic model coupled with creep and fatigue damages. As underlined by Desoyer 1995, one might apply Continuum Damage Mechanics (CDM) during quite a long time. According to material and loading type, first damage steps are induced by various mechanisms (void nucleation followed by growth for metallic alloys, or meso crack appearance followed by propagation in brittle rocks...) and require appropriate models. Then, the ultimate damage steps (void coalescence, strain localization...) are problems still open, calling for new bridges between Continuum Mechanics and Fracture Mechanics.

In this Chapter, the concepts of the thermodynamic approach to damage are summarized and some of the numerous models, that can be applied to ductile fracture of metallic alloys, are presented.

3.1. General thermodynamic formulation

An interesting summary of the well established rules in the continuum mechanics literature is proposed by de Souza Neto *et al.* 1998. Here, only the principles required for the model presentations of Chapters 6 and 7 are presented.
The basic concepts of thermodynamics of continuous media are:

- mass conservation;
- momentum balance;
- first principle = conservation of energy;
- second principle = irreversibility of entropy production.

Clausius-Duhem's inequality results from the combination of the first and the second principles :

$$\underline{\sigma} : \underline{\dot{\varepsilon}} - \rho(\dot{\psi} + s\dot{T}) - \frac{1}{T}\underline{grad}\ T.\underline{q} \geq 0 \tag{3-1}$$

where $\underline{q}$ is the heat flux, ρ the specific mass, ψ the free energy per unit mass, also called Helmholtz' free energy, defined by :

$$\psi = e - Ts \tag{3-2}$$

with e the specific internal energy, s the specific entropy, T the temperature.

The starting point of thermodynamics with internal variables is the hypothesis that, at any instant of a thermodynamic process, the thermodynamic state of a given material point can be completely determined by the knowledge of a finite number of state variables (kinematic variables such as the deformation gradient or the elastic strain $\underline{\varepsilon}^e$, the temperature T and its gradient), and internal variables α_k associated with dissipative mechanisms. Each α_k can be of scalar, vectorial or tensorial nature. One model is characterized by the choice of the variables. For instance, maintaining a general approach, the free energy is assumed to have the form:

$$\psi = \psi\ (\ \underline{\varepsilon}^e, T, \alpha_k\ ) \tag{3-3}$$

Consequently, its rate is given by:

$$\dot{\psi} = \frac{\partial \psi}{\partial \underline{\varepsilon}^e} : \dot{\underline{\varepsilon}}^e + \frac{\partial \psi}{\partial T}\dot{T} + \frac{\partial \psi}{\partial \alpha_k}\dot{\alpha}_k \tag{3-4}$$

Assuming additive decomposition of strain rate:

$$\dot{\underline{\varepsilon}} = \dot{\underline{\varepsilon}}^e + \dot{\underline{\varepsilon}}^p \tag{3-5}$$

the Clausius-Duhem inequality becomes:

$$(\underline{\sigma} - \rho\frac{\partial \psi}{\partial \underline{\varepsilon}^e}) : \dot{\underline{\varepsilon}} + \rho\frac{\partial \psi}{\partial \underline{\varepsilon}^e} : \dot{\varepsilon}^p - \rho(\frac{\partial \psi}{\partial T} + s)\dot{T} - \rho\frac{\partial \psi}{\partial \alpha_k}\ \dot{\alpha}_k - \frac{1}{T}\underline{grad\ T}.\underline{q} \geq 0 \tag{3-6}$$

Since this inequality must hold for any thermomechanical process and, among others, for arbitrary $\dot{\varepsilon}$, $\dot{T}$, the expressions between parentheses must be null. This yields the well-known expressions:

$$\underline{\sigma} = \rho\frac{\partial \psi}{\partial \underline{\varepsilon}^e} \qquad s = -\frac{\partial \psi}{\partial T} \tag{3-7}$$

The thermodynamic forces associated with each internal variable α_k are defined by:

$$A_k = \rho\frac{\partial \psi}{\partial \alpha_k} \tag{3-8}$$

For an isothermal process, Clausius-Duhem's inequality can be written:

$$\underline{\sigma} : \dot{\underline{\varepsilon}}^p - A_k\dot{\alpha}_k \geq 0 \tag{3-9}$$

In order to define a constitutive model, equations for $\dot{\alpha}_k$ must be derived. As the above inequality must be verified, this fact imposes some restrictions on the possible constitutive relations. An effective way of ensuring Clausius-Duhem's inequality consists in postulating the existence of a scalar pseudo dissipation potential, a convex function of all thermodynamical forces $\underline{\sigma}$, A_k, using the state variables $\underline{\varepsilon}^e, \underline{\varepsilon}^p, \alpha_k$ as parameters.

$$F = F(\underline{\sigma}, A_k ; \underline{\varepsilon}^e, \underline{\varepsilon}^p, \alpha_k) \tag{3-10}$$

A generalized normality rule is then applied :

$$\underline{\dot{\varepsilon}}^p = \frac{\partial F}{\partial \underline{\sigma}} \quad \dot{\alpha}_k = -\frac{\partial F}{\partial A_k} \tag{3-11}$$

For phenomena that do not explicitly depend on time, a multiplicator $\dot{\lambda}$ is added. For instance, for plasticity, F can be chosen equal to the yield surface F_p, and constitutive equations are written using a plasticity multiplicator λ_p calculated from the consistency condition $\dot{F}_p = 0$.

$$\underline{\dot{\varepsilon}}^p = \dot{\lambda}_p \frac{\partial F_p}{\partial \underline{\sigma}} \tag{3-12}$$

It should be noted that the constitutive description by means of convex potentials as explained above is not a consequence of thermodynamics but rather a tool for formulating constitutive equations without violating thermodynamics. Indeed, it is obvious that a constitutive model defined by (3-3), (3-7), (3-11) a priori satisfies the dissipation inequality.

The version of the above general principles taking into account the multiplicative split of the deformation gradient $\underline{F}$ can be found in Souza Neto *et al.* 1998. MSM hypoelastic formulation, that uses additive splitting of the strain rate and neglects the plastic spin, is historical. It assumes that elastic strains are small by comparison with plastic ones, which is acceptable in the metallic ductile rupture fields. Cauchy's stress and Jaumann's derivative are used with the assumption of neglecting the scale factor ($det\ \underline{F}^1$) that should affect Cauchy's stress. In 1987, these choices were classical for all codes taking into account large plastic strains as presented by Charlier 1987. The hyperelastic formulation, using multiplicative split of the deformation gradient (Weber & Anand 1990, Simo 1992), and Piola Kirchoff's stress or Cauchy's is now often used (Owen *et al.* 1995, MARC commercial code, EPIM3D code developed by Menezes 1994). However, even if this approach seems more elegant, it is not demonstrated that it simplifies the coding, provides robustness and yields such a better accuracy. So, as long as small elastic strains field are concerned, the traditional hypoelastic approach is applied in MSM.

Even if kinematic description and integration schemes are fundamental for any Finite Element Code, these topics are not treated here as the LAGAMINE choices have already been presented in several Ph.D. theses (Charlier 1987, Li 1995).

3.2. Thermodynamic damage models

3.2.1. Introduction

The material behavior is modeled by constitutive equations taking into account its progressive deterioration. The local loss of material integrity of a representative volume element is modeled by *continuous* (in space and time) variables defined at macro-scale and referred to as *the damage variables*. The notion of a continuous representation of -intrinsically discontinuous- material damage stems from the work of Kachanov 1958 on tertiary creep and was further developed by Rabotnov 1963. "Damage" can be defined as a collection of permanent microstructural changes concerning material thermomechanical properties (e.g. stiffness, strength, anisotropy, etc.) brought in a material by a set of irreversible physical microcracking processes resulting from the application of thermomechanical loadings (Talreja 1985).

Following this definition, the damage variable is not limited to a void volume fraction and to the well-known nucleation, growth and coalescence approach. For instance, it covers the decrease of stiffness cohesion between a matrix and an inclusion or the effect of micro-stress concentration. The word of micro-cracking process in Talreja's definition could even be replaced by internal micro-structural evolution if one looks at the effect of dislocation density modification and at the appearance of substructures. These changes modify the material response and result in softening behavior.

A large part of the experimental analysis of damage does not look at the microscopic level but measures the effect of damage on macroscopic variables such as stress and strain fields, optical wave reflection, acoustic wave transmission... A review of these techniques (photoelasticity, interferometry methods, acoustic emission, optical particle tracking, digital image processing...), applied to damage investigation, can be found in Geers 1997.

The classical technique, used in MSM research, to evaluate damage variables consists in measurements of Young's modulus decrease by means of accurate extensometers and/or electrical-resistance strain gages. Lemaître & Chaboche 1985 have already proposed such an approach to measure damage. It is interesting to note that Geoffroy *et al.* 1993 provide a microscopic explanation, without any connection to void growth assumption, to apparent Young's modulus decrease with strain hardening in steel sheets. In this article, four typical steels (interstitial free steel, aluminum killed deep drawing quality steel, high strength Niobium alloyed steel and rephosphorized steel for structural parts) have been studied by two different laboratories of the SOLLAC group. The first lab measures Young's modulus with an instrumented tensile test machine (strain gauge cell with 0.4N resolution and electronic extensometer with 5.10^{-2} micrometers resolution); the other one

ultrasonically, by measuring the resonant frequency of the material when a longitudinal wave is propagated through the specimen by a magneto-oscillator.

Their conclusion leads them to make a distinction between "Young's modulus" and "tangent elasticity modulus". Their "Young's modulus" is measured at very low magnitude of strains (10^{-6}) and high strain rates by the ultrasonic approach. Their "tangent elasticity modulus" results from the tensile test method. In this latter case, strains reach 2, 5 and 10 %; strain rates are not given but they report slow cross head speed of 2 mm/min, which corresponds to a rate 100 times slower than with ultrasonic approach.

The comparisons of their measurements on as-received samples and after 5 or 10 % pre-strain in tension allow to conclude that *"Young's modulus"* (as defined hereabove) *is a constant intrinsic mechanical property* and *"the tangent elasticity modulus" depends on deformation speed, strain and composition.* The four steels exhibit a strong decrease of "tangent elasticity modulus" when the applied stress increases. They propose the following explanation:

- in the ultrasonic approach, interstitial atoms cannot migrate and the measure is more intrinsic;
- in the tensile test on pre-strained steel, the material can be considered as a visco-elastic material described by a Kelvin-Voigt's rheological model (see Figure 3-1). The pure elastic behavior is represented by the spring E_2 submitted to strain ε_2; the visco-elastic behavior is represented by spring E_1 and damper η; the associated strain is ε_1 and the total material strain is $\varepsilon_1 + \varepsilon_2$.

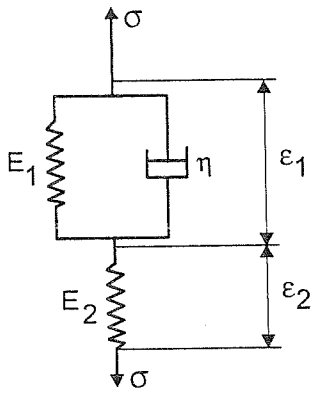

$$(1 + E_1 / E_2)\sigma + \eta / E_2 . \dot{\sigma} = E_1 . \varepsilon + \eta \dot{\varepsilon}$$

Figure 3-1 Kelvin-Voigt's rheological model (from Geoffroy *et al.* 1993).

Steel behavior is visco-elastic because the carbon and alloying elements act as pins for dislocations. As long as the applied stress remains at low level, the dislocations

cannot glide so they bend between atoms (see Figure 3-2a). If relaxed, dislocations return to their initial state. The residual strain is equal to zero but some energy has been dissipated. This phenomenon is observed at a stress level lower than real plastic stress when linear elasticity disappears before appearance of real permanent strain as shown on Figure 3-2b. This small quantity of energy is dissipated to bend the pinned dislocations.

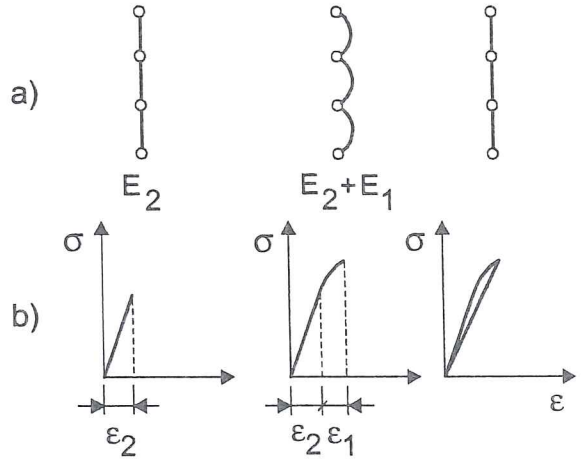

Figure 3-2 Pinned dislocations submitted to bending and unbending
a) visualisation of the phenomenon,
b) associated stress-strain curve (from Geoffroy *et al.* 1993).

Looking at the differential equation associated to Kelvin-Voigt's model, one can check that, at high strain rate, only the spring E_2 is activated and defines the tangent modulus. This fact recoups "Young's modulus" from ultrasonic measurements. At low strain rate, the material behavior results from both springs E_1 and E_2 and its stiffness is lower than "Young's modulus". When the steel sheet has been submitted to a pre-strain, dislocations multiply and this phenomenon is amplified. The "elastic tangent modulus" decreases sharply when "Young's modulus" remains the same as in as-received conditions.

In general, the literature makes no distinction between "Young's modulus" and "elastic tangent modulus". Scientists measuring "Young's modulus" decrease at different strain states by cyclic tensile tests determine in fact the "elastic tangent modulus". According to the above study, the macroscopic damage variable associated to this decrease is from a microscopic point of view an increased density of dislocations pinned on carbon and alloying elements. This explanation holds surely at incipient plasticity where a strong decrease of elastic tangent modulus is observed (see section 6.2.7). The continuous decrease after a few percents of plastic strains probably also results from additional phenomena such as void nucleation, growth and coalescence.

Hereafter, some traditional choices of damage variables are described. The damage variable d_n in the normal direction $\underline{n}$ defined by Lemaître & Chaboche 1985 is the following ratio:

$$d_n = \frac{A_d}{A_t} \tag{3-13}$$

A_t = total cross sectional area of a unit cell cut by a plane normal to direction $\underline{n}$,
A_d = damaged surface area taking into account the area of microcracks or/and voids, the microstress concentration and the interaction between microcracks.

If the phenomenon of damage is regarded as isotropic, it can be defined by a scalar D, which represents the same ratio as above but for any plane direction cutting the cell unit. In fact, the area which effectively resists the stress is $(1\text{-}D)A_t$.

A second-order damage tensor $\underline{D}$ has been proposed by Dragon 1985 :

$$\underline{D} = \frac{1}{2V}\sum_k \int_{S^k} (\underline{b} \otimes \underline{n} + \underline{n} \otimes \underline{b})^k dS^k \tag{3-14}$$

where $\underline{b}$ = displacement discontinuity vector,
$\underline{n}$ = unit normal vector across the k^{th} microcrack surface S^k,
V = representative volume.

As reported by Ju 1989, Krajcinovic has pointed out that such definition is thermodynamically incorrect, because it leads to energy dissipation during unloading. This tensor is nevertheless a good mean to add flexibility due to open microcracks.

Bruhns & Schiesse 1996 use a description of voids on grain boundaries with tensorial Fourier's series that they limit for practical purpose to second order tensors. Their final internal damage variables are a scalar one (the void volume fraction) and a tensorial one.

The second concept very often used in thermodynamic damage modeling is *the definition of effective values.* This concept was introduced by Kachanov in 1958 for the purpose of modeling fracture due to creep. He defines the effective stress by :

$$\underline{\bar{\sigma}} = \underline{\sigma} / (1 - D) \tag{3-15}$$

where D is the isotropic damage internal variable presented above, the value of which is 0 in the undamaged case. This effective stress is in fact the stress relative to the effective area $(1\text{-}D)A_t$. So, equilibrium imposes relation (3-15). The assumption of strain equivalence between a damaged material and a sound, equivalent virgin material is defined by:

$$\underline{\bar{\varepsilon}} = \underline{\varepsilon} \tag{3-16}$$

This assumption associated with the concept of effective stress leads to the fact that the constitutive relations of the damaged material are derived from those of the undamaged material by replacing $\underline{\sigma}$ by $\overline{\underline{\sigma}}$ and $\underline{\varepsilon}$ and by $\overline{\underline{\varepsilon}}$.
Remark that, without assuming the concept of effective stress, the model by Bruhns & Schiesse 1996 recovers relation (3-15) as their weighted Cauchy's stress tensor can finally be expressed by this relation. Rousselier *et al.* 1989 use $\underline{\sigma}/\rho$ in their plastic potential and not $\underline{\sigma}$ to take into account the variation of ρ, reflecting damage and elastic deformation.

As summarized by Zhu 1992, Simo & Ju 1987, who work with a stress-based formulation of elasto-plastic damage constitutive laws, propose an effective strain concept and an assumption of stress equivalence :

$$\overline{\underline{\varepsilon}} = (1-D)\underline{\varepsilon} \qquad \overline{\underline{\sigma}} = \underline{\sigma} \tag{3-17}$$

And finally, Cordebois & Sidoroff 1979 assume that the damaged material state can be replaced by a fictitious undamaged material state which is characterized by effective stresses and strains in the sense that the complementary elastic energy involved in the two states should be equal. This gives:

$$\overline{\underline{\varepsilon}} = (1-D)\underline{\varepsilon} \qquad \overline{\underline{\sigma}} = \underline{\sigma}/(1-D) \tag{3-18}$$

These equivalence principles help to define the expression of the free energy and the pseudo dissipation potential functions used in the models.

Different damage models are presented in the next sections. An unified notation has been adopted and is summarized in Table 3-1.

State variables		Associated thermodynamic forces	
ε^e	elastic strain	σ	Cauchy stress
p	isotropic hardening state variable, often equal to ε_{eq}	R	increase of the initial plastic threshold σ_y
$\underline{\alpha}$	kinematic hardening state variable	$\underline{X}$	back stress
D	isotropic scalar damage variable in isotropic damage model	Y	scalar damage energy release rate in isotropic damage model
$\underline{D}$	second order damage tensor in anisotropic damage model	$\underline{Y}$	damage energy release rate tensor in anisotropic damage model
β	isotropic scalar damage variable in anisotropic model.	B	increase of initial damage strengthening threshold B_0.

Table 3-1 Definition of state variables and associated thermodynamic forces.

3.2.2. Lemaître's model

This section presents the isotropic, isothermal version of Lemaître 1985 model. It assumes decoupling between elasticity and damage on one hand and plastic hardening on the other hand. The specific free energy is expressed by :

$$\psi = \psi^{ed}(\underline{\varepsilon}^e, D) + \psi^p(\underline{\alpha}, p) \tag{3-19}$$

where

$$\psi^{ed} = \frac{1}{2\rho}(1-D)\underline{\varepsilon}^e : \underline{\underline{C}}^e : \underline{\varepsilon} \tag{3-20}$$

- ψ^{ed} = elastic damage contribution to free energy, with $\underline{\underline{C}}^e$ the tensor of elastic moduli,
- ψ^p = plastic contribution to free energy,
- p = scalar, internal variable of isotropic hardening, associated with R, the increase of the radius of the yield surface,
- $\underline{\alpha}$ = an internal variable related to kinematic hardening; its dual associated force $\underline{X}$ is a kinematic tensorial variable, which represents the translation of the yield surface in stress space. It is a second order tensor.

According to (3-7), the elasticity law can be derived as:

$$\underline{\sigma} = \rho\frac{\partial \psi}{\partial \underline{\varepsilon}^e} = (1-D)\underline{\underline{C}}^e : \underline{\varepsilon}^e \tag{3-21}$$

One can verify that the effective stress $\underline{\overline{\sigma}}$, defined by (3-15), respects the classic elastic behavior. This relation (3-21) has very important experimental consequences. It justifies the experimental characterization of the damage state. Damage determination is reduced to the measurement of the degradation of the current effective elastic modulus with respect to the virgin state.

Using relation (3-8), the associated force of the damage variable, generally called Y is computed by:

$$Y = \rho\frac{\partial \psi}{\partial D} = -\frac{1}{2}\underline{\varepsilon}^e : \underline{\underline{C}}^e : \underline{\varepsilon}^e \tag{3-22}$$

which gives to $-Y$ the meaning of an elastic strain energy release rate associated with a unit damage growth. $-Y\dot{D}$ is the power dissipated in the creation of surfaces of separation. $-Y$ corresponds to the variation of internal energy density due to damage growth at constant stress; so it is commonly termed as the "damage energy released rate". As recalled by de Souza Neto *et al.* 1998, Rice 1968 considers $-Y$ as the continuum "damage" analogue of the J-integral used in linear fracture mechanics. Using (3-21) and (3-22), Lemaître's model yields :

$$-Y = \frac{\sigma_{eq}^2}{2(1-D)^2}\left[\frac{2}{3}(1+\nu)+3(1-2\nu)(\frac{\sigma_m}{\sigma_{eq}})^2\right] \tag{3-23}$$

According to the general thermodynamic formulation, one must now define a pseudo dissipation potential and apply normality rules to compute the rates of the state variables. Lemaître 1985 assumes that the pseudo dissipation potential is written as the sum of 2 functions, F_p and F_d, respectively related to plasticity and damage. As underlined by Hayakawa & Murakami 1998, such a choice can be justified by physics considerations. They assume that the dissipation associated with plastic deformation in polycrystalline materials is mainly produced by the dislocation motion under applied stress, while the damage dissipation is governed by the release of internal energy due to the development of microscopic cavities. This explains why these dissipation mechanisms are represented by two different potential functions. The presence of the damage internal variable in the equation of F_p is related to the fact that damage leads to a reduction of the load carrying area and induces stress concentrations around defects which finally result in the reduction of the yield surface.

$$F = F_p(\underline{\sigma}, \underline{X}, R; \underline{\varepsilon}^p, \underline{\alpha}, p, D) + F_d(Y; D) \tag{3-24}$$

The pseudo potential of plasticity is taken as the plasticity criterion function or, in other words, the associate flow rule is assumed. The von Mises' criterion is used to define the effective stress. Only isotropic hardening is taken into account for the sake of simplicity. So the coupling between plasticity and damage is introduced by :

$$F_p = \frac{\sigma_{eq} - R}{1-D} - \sigma_y \tag{3-25}$$

where σ_y is the initial yield stress of the material. Then, adding a multiplicator $\dot{\lambda}$ because damage elasto-plastic models do not explicitly depends on time, a generalized normality rule is applied.

$$\dot{\underline{\varepsilon}}^p = \dot{\lambda}\frac{\partial F_p}{\partial \sigma} = \frac{3}{2}\frac{\dot{\lambda}}{1-D}\frac{\hat{\underline{\sigma}}}{\sigma_{eq}} \qquad \dot{p} = -\dot{\lambda}\frac{\partial F_p}{\partial R} = \frac{\dot{\lambda}}{1-D} = (\frac{2}{3}\dot{\underline{\varepsilon}}^p : \dot{\underline{\varepsilon}}^p)^{1/2} \tag{3-26.a, b}$$

with the simple expression of the strain hardening curve:

$$R = \rho\frac{\partial \psi}{\partial p} = Kp^{1/M} \tag{3-27}$$

where K and M are material constants. The multiplicator $\dot{\lambda}$ is derived from the consistency condition $\dot{F}_p = 0$ (for details, see Lemaître 1985).

A general form of the damage pseudo potential, that can be used to represent brittle, fatigue, ductile or creep damage, is a power function of Y:

$$F_d = \frac{A}{(s+1)(1-D)}(\frac{-Y}{A})^{s+1} \tag{3-28}$$

This choice, the generalized normality rule and relation (3-26.b) leads to:

$$\dot{D} = \dot{\lambda}\,\frac{\partial F_d}{\partial Y} = \frac{\dot{\lambda}}{(1-D)}\left(\frac{-Y}{A}\right)^s = \left(\frac{-Y}{A}\right)^s \dot{p} \tag{3-29}$$

According to Lemaître, multidimensional experiments show that $s \equiv 1$, so the only material coefficient necessary for damage modeling is A. Thus the isotropic elastic-damage-plastic model proposed by Lemaître only requires 5 parameters : E, ν, K, M, A.

As already mentioned, this section purpose is not to describe the computational aspects such as time integration schemes or tangent modulus computation. Some information about these very important topics, for those who want to implement a damage model in a finite element code, can be found in Simo & Ju 1987, Doghri 1995, Doghri 2000, de Souza Neto *et al.* 1998.

3.2.3. Three choices of free energy function or its complementary Gibbs' function

As reported by Ju 1989, Lemaître's choice to uncouple plasticity and damage processes contradicts the fact that plastic variables also contribute to the initiation and growth of microcracks. So, he proposes another free energy function, which yields another expression of the thermodynamic force associated with the scalar damage variable D:

$$\psi = (1-D)\left[\psi^{0e}(\underline{\varepsilon}^e) + \psi^{0p}(p,\underline{\alpha})\right] \tag{3-30}$$

$$Y = \rho\frac{\partial \psi}{\partial D} = -\rho\left[\psi^{0e}(\underline{\varepsilon}^e) + \psi^{0p}(p,\underline{\alpha})\right] \tag{3-31}$$

where ψ^{0e}, ψ^{0p} respectively represent the elastic and plastic free energy functions of an undamaged (virgin) material. So, $-Y$ represents the damage energy release rate that controls the microcracks. It is related to the local debonding energy required to initiate and propagate these cracks. As underlined by Ju 1989, $(\psi^{0e} + \psi^{0p})$ is actually the local counterpart of the global J-integral fracture energy in nonlinear elasto-plastic fracture mechanics.

Rousselier 1987 applies the thermodynamic formulation and what he calls "the principle of simplicity" for choosing his functions. He proposes for the specific free energy :

$$\psi = \psi^e(\underline{\varepsilon}^e) + \psi^d(D) + \psi^p(p) \tag{3-32}$$

At this level, this choice seems to uncouple elasticity, damage and plasticity. However, as he works with a stress weighted by the specific weight: $\underline{\sigma}/\rho$, the coupling appears in both elastic and plastic descriptions.

When Helmholtz's free energy is used, the damage conjugate forces are expressed as functions of the elastic strain tensor. Thus, the examination of the validity of the theory requires experiments governed by the elastic strain. In the case of elastic-plastic-damage materials, such experiments are difficult as the elastic strain cannot be easily determined due to the change of elastic properties with damage development. So Hayakawa & Murakami's 1998 work with Gibbs' thermodynamic potential which is assumed to consist of 3 terms :

- the complementary energy due to elastic deformation $G^e(\sigma,\underline{D})$
- the lattice distortion energy related to dislocation structure $G^p(p)$
- the surface energy due to cavity nucleation $G^d(\beta)$

where $\underline{D}$ is a damage second order tensor and β is a scalar variable related to damage development. The need for a tensorial damage state variable is linked to the anisotropy of the cases studied by these authors. As Lemaître does, they assume a strong coupling of the elastic complementary energy with damage but a small influence on the other terms. So damage coupling only appears in the first term.

3.2.4. Three choices of the pseudo potential function

Murakami *et al.* 1998 and Hayakawa & Murakami 1998 report a research on spheroidized graphite cast iron FCD400. Their experiments were concerned with verification of the existence of the damage surface and with validation of the assumption of associated flow rule and normality rule of damage evolution, i.e. the existence of the damage potential. The experimental results show that the shape of the damage and yield surfaces does not always remain similar but may depend on the current damage state. Furthermore, the development of damage is also dependent on plastic deformation. Thus, the proposed damage potential F_d is not only a function of the damage internal variable but also of the internal state variable controlling isotropic hardening.

Hayakawa & Murakami's model describes the material state by 3 variables: a second rank symmetric damage tensor $\underline{D}$, a scalar isotropic hardening variable p and a scalar β, which controls the further development of damage. Their conjugate forces are respectively $\underline{Y}$, R and B. The yield surface is defined as:

$$F_p(\underline{\sigma},R;\underline{D},p)=\sigma_{eq}^I-(\sigma_y+R)=0 \tag{3-33}$$

with

$$\sigma_{eq}^I=\sqrt{\frac{3}{2}\underline{\hat{\sigma}}:\underline{\underline{M}}(\underline{D}):\underline{\hat{\sigma}}} \tag{3-34}$$

where $\underline{\hat{\sigma}}$ is the deviatoric stress tensor and $\underline{\underline{M}}$ is defined by :

$$\left[\underline{\underline{M}}(\underline{D})\right]_{ijkl}=\frac{1}{2}(\delta_{ik}\delta_{jl}+\delta_{il}\delta_{jk})+\frac{1}{2}c^p(\delta_{ik}D_{jl}+D_{il}\delta_{jk}+\delta_{il}D_{jk}+D_{il}\delta_{jk}) \tag{3-35}$$

It is a fourth rank symmetric tensor with the damage tensor $\underline{D}$ as an argument and c^p a material constant. The above linear function postulates moderate effects of $\underline{D}$ on plastic deformation.

The yield function derivatives multiplied by a plastic multiplicator $\dot{\lambda}_p$ give the plastic strain rate $\underline{\dot{\varepsilon}}^p$ and the rate of the isotropic hardening variable $\dot{p}$. This plastic multiplicator $\dot{\lambda}_p$ is determined from the consistency condition $\dot{F}_p = 0$. The loading/unloading conditions are defined by Kuhn-Trucker's relations :

$$\dot{\lambda}_p \geq 0, \quad F_p \leq 0, \quad \dot{\lambda}_p F_p = 0 \tag{3-36}$$

Hayakawa & Murakami tensile and torsion tests consolidate the assumptions of a damage potential and corresponding normality rule. The proposed damage surface is found identical to the damage potential :

$$F_d\ (\underline{Y}, B; \underline{D}, \beta\ ) = Y_{eq} + c^r\, p\, tr\underline{D}\, tr\underline{Y} - (B_0 + B) = 0 \tag{3-37}$$

$$Y_{eq} = \sqrt{\frac{1}{2}\underline{Y} : \underline{\underline{L}}(\underline{D}) : \underline{Y}} \tag{3-38}$$

$$\left[\underline{\underline{L}}(\underline{D})\right]_{ijkl} = \frac{1}{2}(\delta_{ik}\delta_{jl} + \delta_{il}\delta_{jk}) + \frac{1}{2}c^d\,(\delta_{ik}D_{jl} + D_{il}\delta_{jk} + \delta_{il}D_{jk} + D_{il}\delta_{jk}) \tag{3-39}$$

where c^r, c^d are material constants, as well as B_0 which specifies the size of the initial damage surface. The choice of $\underline{\underline{L}}$, linear function of damage tensor $\underline{D}$, was justified because, from experimental results, the material damage in the studied elastic-plastic material was not so significant. As in plasticity, the evolution equations of the damage variables $\dot{\underline{D}}$, $\dot{\beta}$ are given by the derivatives of the damage function multiplied by a damage multiplicator $\dot{\lambda}_d$. Again the latter is computed thanks to the consistency condition $\dot{F}_d = 0$ and the loading/unloading conditions for the damage evolution are specified by Kuhn-Tucker's conditions :

$$\dot{\lambda}_d \geq 0, \quad F_d \leq 0, \quad \dot{\lambda}_d F_d = 0 \tag{3-40}$$

This model is very interesting. To the 5 material constants c^r, c^d, c^p, B_o, σ_y presented here, 10 other constants are required to define the complementary energy used to derive $\underline{\dot{\varepsilon}}^e$, $\underline{Y}$, R, B. This Gibbs thermodynamic potential has been briefly described at the end of preceding section 3.2.3. So, finally, this model is defined by 15 variables. It is quite general as the yield surface and the damage surface shape and size are affected by damage. Damage anisotropy is taken into account by a second rank symmetric damage tensor $\underline{D}$. For instance, Figure 3-3 presents the damage surface in the space of tensile stress σ and shear stress τ.

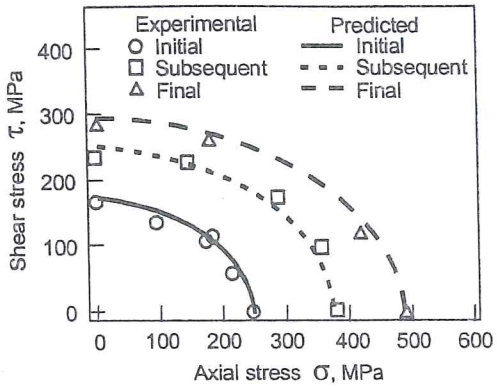

Figure 3-3 Damage surfaces in a combined stress space for a spheroidized graphite cast iron (from Hayakawa & Murakami 1998).

The aspect ratio σ/τ of the initial damage surface is 1.46, in contrast to the ellipse of the initial yield surface of von Mises type the aspect ratio of which is $\sqrt{3}$. This difference may be explained as follows: while plastic yielding is governed by deviatoric stresses, the influence of hydrostatic stresses cannot be neglected for damage development due to the nucleation and growth of microcracks. On the other hand, the aspect ratio of the updated damage surface is 1.62, closer to the aspect ratio of von Mises' yield surface. This can be explained by the fact that the increasing plastic deformation of the ferrite matrix gradually governs the damage process. The aspect ratio of the final damage surface is very close to $\sqrt{3}$. This provides information to define the elastic–damage complementary energy the derivative of which allows to compute the damage conjugate force $\underline{Y}$.

Rousselier 1987 proposes a pseudo dissipation potential divided into two terms:

$$F = F_1(\tilde{\sigma}_{eq}, R) + F_2(\tilde{\sigma}_m, Y) \tag{3-41}$$

where $\underline{\tilde{\sigma}} = \underline{\sigma}/\rho$ is used. R and Y follow above definitions. The functions F_1, F_2 are respectively related to plasticity (von Mises' criterion) and damage:

$$F_1 = \tilde{\sigma}_{eq} + R(p) \tag{3-42}$$

$$F_2 = Y(D)\, g(\tilde{\sigma}_m) \tag{3-43}$$

The choice of F_2 is as simple of possible. Taking into account mass conservation and neglecting elastic volume change yields :

$$\dot{\rho} + 3\rho\dot{\varepsilon}^p_m = 0 \tag{3-44}$$

Then, assuming that, in first approximation, $\rho=\rho(D)$ and applying the normality rule :

$$\underline{\dot{\varepsilon}}^p = \dot{\lambda}\,\partial F / \partial(\underline{\tilde{\sigma}}) \quad \text{and} \quad \dot{D} = \dot{\lambda}\,\partial F / \partial Y \tag{3-45}$$

one gets :

$$\frac{\partial g / \partial \tilde{\sigma}_m}{g} = -\frac{\partial \rho / \partial D}{Y\rho} \tag{3-46}$$

The two members of the latter equation being functions of different variables $\underline{\tilde{\sigma}}$ and D, the only possibility is that they are equal constants, which produces after integration:

$$F = \frac{\sigma_{eq}}{\rho} - R(p) + Y(D)\ c^d\ exp(\frac{\sigma_m}{\rho\sigma_1}) \tag{3-47}$$

If one assumes $Y(D) = \sigma_1 f$, where f is the microvoid volume fraction the growth of which can be linked to Rice and Tracey's relation (2-10), this pseudo potential is very close to Gurson's criterion (2-1). This model is interesting as it contains only 7 parameters: E, ν, K, M (if relation 3-27 is assumed), σ_1, c^d, f_0, and proves that phenomenological models based on thermodynamics can recover Gurson's model. An extension of this model, adapted to large strains, has been used by Eckstein *et al.* 1997, Eckstein & Basar 2000. Rousselier's model is quite popular, it is used for instance by Baaser & Gross 2000 or Besson *et al.* 2000.

Gelin & Danescu 1992 work with a symmetric second order tensor $\underline{D}$ in order to describe anisotropic damage. They propose to decompose the stress tensor into a part $\underline{\sigma}^D$, normal to $\underline{D}$, and a part parallel to $\underline{D}$:

$$\underline{\sigma} = \underline{\sigma}^D + \frac{\underline{\sigma} : \underline{D}}{\underline{D} : \underline{D}} \underline{D} \tag{3-48}$$

They use a generalized von Mises' yield condition:

$$F_p(\underline{\sigma}, \underline{D}, R) = \underline{\sigma} : \underline{\sigma} + c^d\ \underline{\sigma}^D : \underline{\sigma}^D - \frac{(\sigma_y + R)^2}{\underline{D} : \underline{D}} \tag{3-49}$$

Finally, their damage evolution equation, defining the objective damage derivative, is:

$$\overset{\nabla}{\underline{D}} = \dot{\lambda} \left[-\frac{\underline{\sigma} : \underline{D}}{\underline{D} : \underline{D}} \underline{\sigma}^D + \left(\frac{\sigma_y + R}{\underline{D} : \underline{D}} \right)^2 \underline{D} \right] \tag{3-50}$$

The consequences of their choices are :

- the damage norm is increased by the part of the stress that may produce the plastic flow,
- supposing that the stress tensor has a fixed orientation, the damage tensor tends to achieve an orientation normal to the stress,
- plastic anisotropy and softening are induced due to the damage tensor,
- the symmetry of the elastic response is not changed qualitatively in the presence of damage.

3.2.5. The strain decomposition

Ju 1989 uses a split of the total strain tensor into "elastic-damage (reversible)" and "plastic-damage (irreversible)" parts. However he does not try to express separately the reversible and irreversible damage strains from the elastic and plastic strains. So he finally uses simple additive relation (3-5) as Lemaître.

Further steps are proposed by Bruhns & Schiess 1996, who propose three strains: elastic, plastic and damage strains. Voyiadjis & Park 1998 go even further as they split the strain into four terms: ε^e elastic, ε^p plastic, $\varepsilon^{d'}$ recoverable damage and $\varepsilon^{d''}$ irreversible damage strains. Their approach is represented by Figure 3-4 for a uniaxial stress-strain curve. The microscopic events supporting damage strain splitting are the following ones:

- $\varepsilon^{d'}$ "recoverable" damage strain due to the reduction of elastic stiffness tensor,
- $\varepsilon^{d''}$ "irreversible" damage strain tensor due to the lack of closure of microcracks and microvoids during unloading.

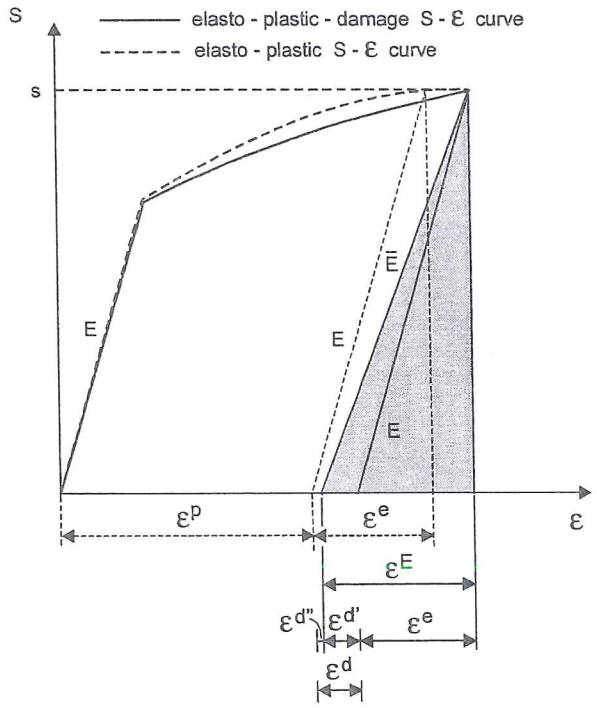

Figure 3-4 Schematic representation of elasto-plastic damage strain increments in the case of a uniaxial stress-strain curve with second Piola Kirchhoff stress S and the Lagrangian strain ε (from Voyiadjis & Park 1998).

Voyiadjis & Park 1998 propose a kinematics of damage for elasto-plastic behavior with finite strains. The multiplicative decomposition of the deformation gradient and the additive decomposition of the Lagrangian strain tensor are used to deduce separately each strain.

3.2.6. Microcrack opening and closing

This state of the art cannot forget the very useful concept, introduced by Ortiz 1985 and Ju 1989, to consider different mechanisms under tensile and compressive states. They use the spectral decomposition of tensors and retain the positive spectral projection to define functions such as, for instance, the elastic free energy. For a second order tensor $\underline{A}$, with principal values a_i and unit principal directions $\underline{p}$, Ju defines the positive spectral projection $\underline{A}^+$ as :

$$\underline{A}^+ = \sum_{i=1}^{3} H(a_i)\, \underline{p} \otimes \underline{p} \tag{3-51}$$

where H is the Heaviside step function. In their respective damage models, several authors replace tensors such as strain $\underline{\varepsilon}$ (Ju 1989), stress $\underline{\sigma}$ (Zhu 1992), damage associated force $\underline{Y}$ (Gallerneau 1995) by their positive projections.

3.2.7. Crack induced anisotropy

The present literature review is not dedicated to quasi-brittle materials. However, it is interesting to note that brittle approach can be quite close to ductile one. For instance, in the model proposed by Fichant *et al.* 1996 or 1998, the concepts of effective stress and damage surface are also applied. Their model is based on the approximation of the relationship between the effective stress in the damage material and the macroscopic stress. Given a vector normal to a microplane in the material, the microplane stress is proportional to the effective stress. The coefficient of proportionality is expressed as a function of the damage in the direction defined by the vector normal to the microplane. The macroscopic stress-strain relationship is obtained according to the principle of virtual work, with a kinematic constraint. The micro-strain on each plane is equal to the macroscopic strain. So the microplane strains represent the projections of the macroscopic strain tensor but the microplane stresses are not equal to the resolved components of the macroscopic stress tensor. The constitutive relation can be viewed as a simplified micro-plane type model (Bazant & Ozbolt 1990) where the behavior of the damaged material is discretised in a finite set of directions.

The damage surface and its evolution are summarized here because the approach of Fichant *et al.* 1996, 1998 could be extended to ductile materials. The simplest approximation, which does not yield to isotropy, corresponds to an ellipsoidal damage surface characterized by three principal directions and the values of three damage scalars along these directions. Initially, the damage surface is reduced to a point:

$$d(\underline{n})=0 \tag{3-52}$$

where d is a scalar quantity which introduces the effect of damage in the relation between the effective stress tensor and the macroscopic stress. It is known for a finite set of directions $\underline{n}$. The evolution of damage is controlled by a loading surface f:

$$f(\underline{n}) = \underline{n}.\underline{\varepsilon}.\underline{n} - \varepsilon_d - B(\underline{n}) \tag{3-53}$$

with B a hardening/softening variable which is interpolated in the same fashion as the damage surface and ε_d is a damage threshold strain value. The evolution of the damage surface is defined by:

$$\text{if } f(\underline{n}^*) = 0 \text{ and } \underline{n}^*.\dot{\underline{\varepsilon}}.\underline{n}^* > 0 \text{ then}$$

$$\dot{d}(\underline{n}^*) = \left[\frac{\varepsilon_d (1 + a(\underline{n}^*.\underline{\varepsilon}.\underline{n}^*)}{(\underline{n}^*.\underline{\varepsilon}.\underline{n}^*)^2} exp(-a(\underline{n}^*.\underline{\varepsilon}.\underline{n}^*) - \varepsilon_d \right] (\underline{n}^*.\dot{\underline{\varepsilon}}.\underline{n}^*) \tag{3-54a, b}$$

$$\dot{B}(\underline{n}^*) = \underline{n}^* \dot{\underline{\varepsilon}} \underline{n}^* \tag{3-54c, d}$$

$$\text{else } \dot{d}(\underline{n}^*) = 0 \quad \dot{B}(\underline{n}^*) = 0$$

Note that the vectors $\underline{n}^*$ are the three principal directions of the incremental strain whenever damage grows. The parameters of this damage model are the initial value of $B(\underline{n})$, which is assumed to be initially isotropic since the undamaged material is isotropic, and the parameter a. The first parameter can be related to the tensile strength of the material, if one assumes that damage in uniaxial tension occurs at the peak stress, and the second one will be related to the fracture energy of the material. The new damage surface is the combination of two ellipsoidal surfaces: one surface corresponding to the initial damage, and the other one corresponding to the incremental growth of damage.

These two surfaces do not have the same principal axes and the resulting surface has not the same principal directions as the total strain tensor, except when the principal directions of strains and damage do not rotate during the strain increment. So principal directions of strains and stresses are not necessarily the same. This approach, initially coupled only with elastic behavior (Fichant *et al.* 1996) has been adapted to an elasto-plastic case (Fichant *et al.* 1998). Applied to concrete, this model allows structural analysis of bending of beams, compression, shear and tension-shear of concrete panels.

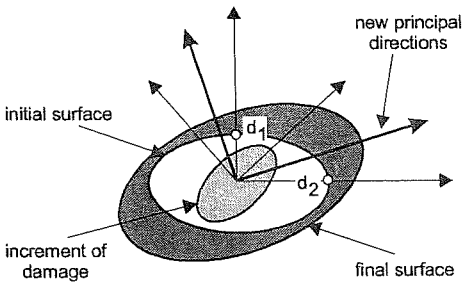

Figure 3-5 Evolution of the damage surface in plane 12 (from Fichant *et al.* 1998).

3.3. Comparison of models

Gelin & Danescu 1992 summarize quite well the main differences between micro-macro damage models, as the one proposed by Gurson or Ponte Castenada, and phenomenological approaches with internal variables. They point out that to build a Gurson's type approach generally involves five different steps:

1. Definitions of strain and stress at macroscale.
2. The choice of a particular geometry for the cell and the void. Very often one adds as much symmetry as possible to allow analytical study.
3. A lower bound result. This is a point in which different approaches give different results.
4. A particular velocity field used to describe the void growth.
5. An optimization procedure. Since the lower bound result only gives a lower bound, it is expected that the real form of the macroscopic potential is found, or at least approximated, by maximizing this lower bound.

These steps are required to find the macroscopic yield function. In fact, the crucial role played by the choice of the velocity field and the geometry of the cell in Gurson's type models is the counterpart of the evolution equations of the internal damage variable or the pseudo potential function choice in phenomenological model. For such approaches, these functions are deduced according to thermodynamics limitations and experimental observations.

In contrast to Gurson's model, the evolution of the damage variables of Lemaître's type damage model is associated with a dissipative mechanism. The simple problem of a uniaxially stressed bar subjected to cyclic loading (Figure 3-6) has been simulated by FEM codes using Lemaître's and Gurson's damage models by de Souza Neto *et al.* 1998.

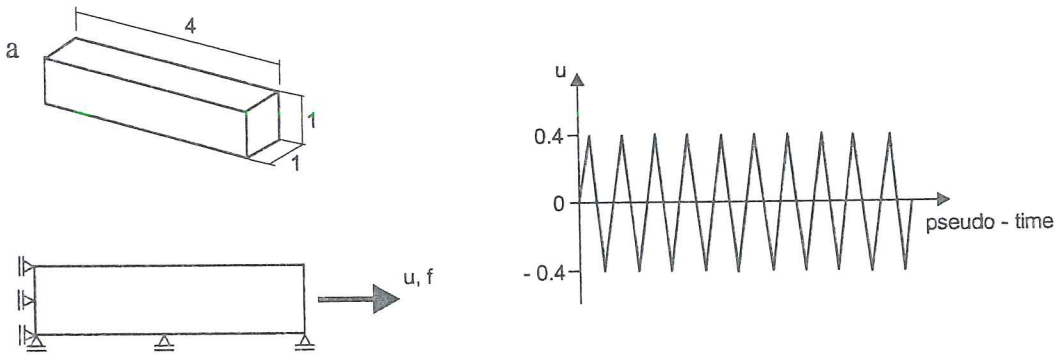

Figure 3-6 Bar geometry and loading (from de Souza Neto *et al.* 1998).

Figure 3-7 presents the axial reaction force f obtained in the simulations versus the imposed displacement u. With Lemaître's model simulation, the reaction force is progressively decreasing over the cycles. This is a direct result of damage

accumulation and consequent material softening. The elastic unloading after the end of the last cycle also proves the degradation of the elastic modulus. In contrast, the reaction forces obtained with Gurson's model are practically constant over the cycles. Indeed for this model, damage growth resulting from the extension of the bar is compensated by damage healing that occurs during compression. In this case, no cumulative damage occurs and the damage variable returns to its initial value after each cycle. This does not correspond to the experimental observation of progressive damaging in cyclic tests with ductile materials.

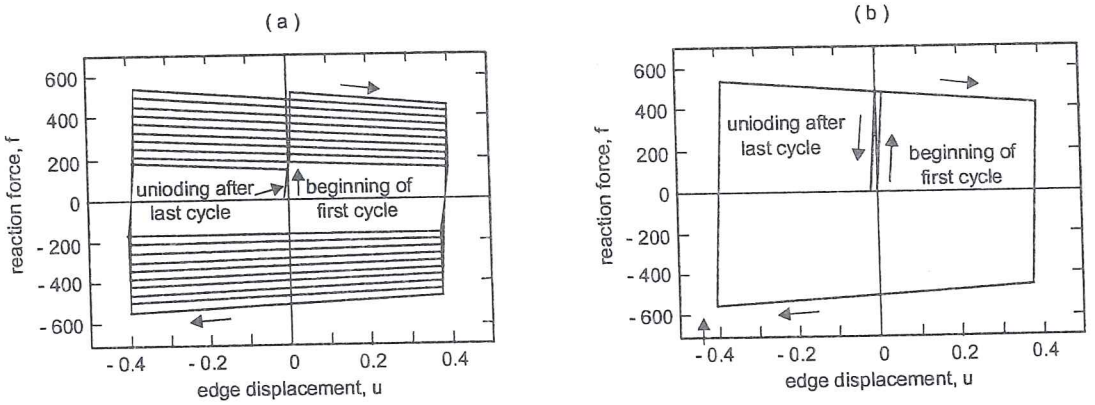

Figure 3-7 Bar cyclic extension/compression without hardening, force-displacement curves obtained with: (a) Lemaitre's model; (b) Gurson's model (from Souza Neto *et al.* 1998).

3.4. Summary

Chapter 3 describes thermodynamics damage models. It does not expand over their integration scheme or their link with physical metallurgy but provides examples of choices such as internal variables and pseudo potential functions.

As this thesis is focused on ductile rupture, very few references are dedicated to brittle models, nothing is devoted to fatigue. However, it is important to note that thermodynamics damage models also predict fracture appearance in such cases.

The « French school » of damage models is presented by means of Lemaître & Chaboche 1985. However, it is worth to underline that this approach is now applied all over the world : see for instance Bruhns & Schiesse 1996 in Germany, Geers 1997 in the Netherlands, Ju 1989 in United States, Hayakawa & Murakami 1998 in Japan.

The principles presented here help the reader to understand the context of the models used in Chapters 6 and 7.

References

Baaser, H., Gross, D., (2000) 3D simulation of ductile crack growth, a numerical realisation, Euromech 417, *Numerical Modelling in Damage Mechanics*, University of Technology of Troyes, France, 27-29.

Bazant, Z.P., Ozbolt J. (1990) Nonlocal microplane model for fracture, Damage and size effect in structures, ASCE, *J. of Eng. Mech.*, **116**, 2485-2505.

Besson, J., Brocks, W., Chabanet, O., Steglich, D., (2000) Ductile rupture of aluminium sheet materials, Euromech 417, *Numerical Modelling in Damage Mechanics*, University of Technology of Troyes, France, 30-31.

Bruhns, O.T., Schiesse, P. (1996) A continuum model of elastic-plastic materials with anisotropic damage by oriented microvoids. *Eur. J. Mech. A/Solids*, **15-3**, 367-396.

Charlier, R. (1987) Approche unifiée de quelques problèmes non linéaires de mécaniques des milieux continus par la méthode des éléments finis (grandes déformations des métaux et des sols), contact unilatéral de solides, conduction thermique et écoulements en milieux poreux. Université de Liège, thèse de doctorat en sciences appliquées.

Cordebois, J.P., Sidoroff, F. (1979) Damage induced elastic anisotropy, *Euromech*, **115**, Villars de Lans, France.

Desoyer, T. (1995) Contribution à la modélisation de l'endommagement diffus et localisé, Mémoire pour l'obtention de l'habilitation à diriger les recherches, Université de Poitiers.

Doghri, I., (1995) Numerical implementation and analysis of a class of metal plasticity models coupled with ductile damage, *Int. J. Num. Meth. Engin.*, **38**, 3403-3431.

Doghri, I. (2000), Mechanics of Deformable Solids, Springer.

Dragon, A., (1985) Plasticity and ductile fracture damage : study of void growth in metals, *Eng. Fract. Mech.*, **21**, 875-885.

Eckstein, A., Basar, Y. & Konke, C. (1997) Damage analysis of ductile metallic shells. *Computational plasticity – Fundamentals and Applications,* Owen, D.R.J, Onate, E. Hinton, E., editors, CIMNE, Barcelona.

Eckstein, A., Basar, Y. (2000) Ductile damage analysis of elasto-plastic shells at large inelastic strains, *Int. J. Num. Meth. Engin.*, **47**, 1663-1667.

Fichant, S., Pijaudier-Cabot G., La Borderie, C. (1996) Continuum damage modelling with crack induced anisotropy, *Numerical Methods in Engineering,* John Wiley & Sons

Fichant, S., La Borderie, C., Pijaudier-Cabot G. (1998) A comparative study of isotropic and anisotropic descriptions of damage in concrete structures, *Damage mechanics in engineering materials*, Voyiadjis, G.S., Ju, J.W., Chaboche, J.L. Eds, Elsevier 259-274.

Gallerneau, F. (1995) Etude et modélisation de l'endommagement d'un superalliage monocristallin revêtu pour aube de turbine, Thèse Docteur en sciences et génie des matériaux, Ecole Nationale Supérieure des Mines de Paris.

Geers, M.G.D., (1997) Experimental Analysis and Computational Modelling of Damage and Fracture, Ph. D. thesis, Technische Universiteit Eindhoven.

Gelin, J.C., Danescu, A., (1992) Constitutive model and computational strategies for finite-strain elasto-plasticity with isotropic or anisotropic ductile damage, *Proc. of the third Int. Conf. Computational plasticity*, D.R.S. Owen *et al.* editors, Pineridge Press, 1413-1424.

Geoffroy, J.L., Cambien, I., Mareuse, D., (1993) Assessment of intrinsic elastic constants by mean of both tensile test and resonance frequency measurements, *IDDRG 93: Working group Nr.3.*

Hayakawa, K., Murakami, S. (1998) Space of damage conjugate force and damage potential of elastic-plastic-damage materials, *Damage Mechanics in Engineering Materials*, Voyiadjis, G.S., Ju, J.W., Chaboche, J.L. Eds, Elsevier, 27-44.

Ju, J.W. (1989) On energy-based coupled elastoplastic damage theories : constitutive modelling and computational aspects, *Int. J. Solids & Structures*, **25-7**, 803-833.

Kachanov, L.M. (1958) Time of the rupture process under creep condition, *Izv. Akad. Nauk SSSR, Otd. Tekhn. Nauk*, **8**, 26-31.

Lemaître, J. (1985) Coupled elastoplasticity and damage constitutive equations, *J. Comp. Meth. in Appl. Mech. and Eng.*, **51**, 31-49.

Lemaître, J., Chaboche, J.L. (1985) Mécanique des matériaux solides, Dunod, Paris.

Li, K. (1995) Contribution to the finitie element simulation of three-dimensional sheet metal forming, Université de Liège, thèse de doctorat en sciences appliqués.

Martins Meneze, K.F., (1994) Modélisation tridimensionnelle et simulation numérique des processus de mise en forme, Application à l'Emboutissage des Tôles Métalliques, version française, Faculdade de ciências e tecnologia da Universidade de Coimbra Departamento de engenharia mecânica.

Murakami, S., Hayakawa, K., Liu, Y. (1998) Damage evolution and damage surface of elastic-plastic-damage materials under multiaxial loading, *Int. J. of Damage Mechanics*, **7**, 103.

Ortiz, M. (1985) A constitutive theory for the inelastic behaviour of concrete. *Mech. Mater.*, **4**, 67-93.

Owen, D.R.J., Peric, D., de Souza Neto, E.A., Jianguo, Y., Dutko, M., Crook, A.J.L. (1995) Advanced computational strategies for 3-D large scale metal forming simulations, *NUMIFORM 95, Simulation of materials processing: theory, methods and applications*, Shen & Dawson Eds, Balkema Press, Rotterdam.

Rabotnov, Y.N., (1963) On the equations of state for creep. *Progress in Applied Mechanics*, Prager Anniversary Volume, New-York, Mac Millan, 307.

Rice, J.R. (1968) A path independent integral and the approximate analysis of strain concentration by notches and cracks, *J. Appl. Mech.*, **35**, 379-386.

Rousselier, G. (1987) Ductile fracture models and their potential in local approach of fracture, *Nuclear Engineering and Design*, **105**, 97-111.

Rousselier, G., Devaux, J.C., Mottet, G., Devesa, G. (1989) A methodology for ductile fracture analysis based on damage mechanics : an illustration of a local approach of fracture, *Nonlinear Fracture Mechanics : vol. II – Elastic-Plastic Fracture, ASTM STP 995,* J.D. Landes, A. Saxena, J.G. Merkle Eds, American Society for Testing and Materials, Philadelphia, 332-354.

Simo, J.C., Ju, J.W. (1987) Strain – and stress – based continuum damage models. I. Formulation, *Int. J. Solids & Structures*, **23-7**, 821-840.

Simo, J.C. (1992) Algorithms for static and dynamic multiplicative plasticity that preserve the classical return mapping schemes of the infinitesimal theory, *Comp. Method. in Appl. Mech. & Eng.*, **99**, 61-112.

de Souza Neto, E.A., Peric, D., Owen, D.R.J. (1998) Continuum modelling and numerical simulation of material damage at finite strains, *Archives of Computational Methods in Engineering*, **5-4**, 311-384.

Taljera (1985) A continuum mechanics characterization of damage in composite materials. *Proc. R. Soc. Lond. Ser. A*, **399**, 195-216.

Voyiadijs, G.Z., Park, T., (1998) Kinematics of Large Elastoplastic Damage Deformation, *Damage Mechanics engineering Materials*, Eds. Voyiadijs, G.Z., Ju, J-W.W., Chaboche, J.L., Elsevier.

Weber, G., Anand, L. (1990) Finite deformation constitutive equations and a time integration procedure for isotropic, Hyper elastic-viscoplastic solids, *Comp. Meth. In Appl. Mech. & Eng.*, **79**, 173-202.

Zhu, Y.Y. (1992) Contribution to the local approach of fracture in solid dynamics, Ph. D. thesis, University of Liège, MSM Department .

4. RUPTURE CRITERIA USED WITH CONTINUUM DAMAGE MODELS

To write a compilation of all failure criteria is an impossible task due to the incredible amount of work in this field. The present review is limited to criteria applied to **ductile fracture** and compatible with finite elements using continuum damage models. As final rupture quickly follows void coalescence, this study includes coalescence criteria. Fracture criteria can be divided into four families:

- simple damage criteria;
- criteria deduced from stress and strain fields;
- complex criteria issued from microscopic observations or mesoscopic approach and taking into account the microscopic phenomena;
- criteria attempting to bridge classical fracture mechanics and damage continuum mechanics.

For each family, a few criteria are proposed together with their advantages and weaknesses as well as their suitability for use in macroscopic damage models.

4.1. Simple damage criteria

For isotropic damage models with only one scalar variable, it seems straightforward to define its threshold value thanks to one experiment conducted until rupture. The fracture criterion is then fulfilled when the damage variable reaches this level :

- Gurson's type model : $f = f_{cr}$ if coalescence is not modeled,
  $f = f_F$ if coalescence is modeled.
- Lemaître's type model : $D = D_{rupture}$

Such easy fracture criteria are very current and have been used successfully by, among others, Picart *et al.* 1997, Doege *et al.* 1997, Lemaître 1985, Zhu 1992, Tvergaard 1982, Rousselier *et al.* 1989, Brocks *et al.* 1995, Eckstein *et al. 1997*. The advantage of such an approach is its simplicity. Its drawback is a poor accuracy as different rupture types are detected by the same threshold value. To detect chevron crack in drawing, Komori 1998 uses critical void volume fraction coupled with critical axial stress.

The mesoscopic approach allows an interesting verification of such limit values. For instance, assume that the internal damage variable is the void volume fraction or porosity like in classical Gurson's model. The FEM discretization of an elementary cell with one void can be submitted to different loadings (torsion, triaxial loading deduced from notched tensile test,...). Such FEM simulations will produce porosity-equivalent strain curves, showing for each loading a vertical branch clearly localizing the porosity and equivalent strain at the rupture onset. This validates the use of a critical value of the void volume fraction as a criterion of final material failure.

Brethenoux *et al.* 1996 present experimental fracture strains close to the ones computed by means of their mesoscopic models. For their studied materials (steel grade 22MnCrB5, 27CrMo4, 42CrMo4), very low values of critical porosity are deduced (0.01 to 0.06).

Koplik & Needleman 1988 present numerical computations of the behavior of a cell model and also the corresponding predictions based on improved Gurson's model (version with Tvergaard coefficients and function f^*). Their cell model simulates a three-dimensional periodic array of spherical voids in an isotropically hardening elastic-viscoplastic matrix. This cell model is submitted to both axial and radial stresses ($T = \sigma_m / \sigma_{eq}$ = 1, 2 or 3). The cell model calculations show a shift from a general axisymmetric deformation state to a mode of uniaxial straining of the ligament between neighboring voids. The plastic deformation localizes on this ligament and this event is associated with the accelerated void growth accompanying coalescence. Figure 4-1 illustrates that the same void volume fraction can characterize various geometries and Figure 4-2 shows the macroscopic stress-strain curves deduced from the cell model with b_0/R_0= 8 or 1. The exact cell material properties and the definitions of macroscopic effective stress and strain are given in Koplik & Needleman 1988.

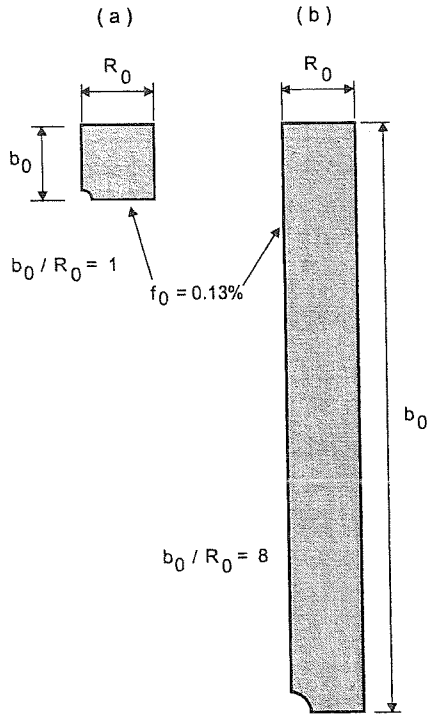

Figure 4-1 Two cell geometries with identical initial void volume fraction (adapted from Koplik & Needleman 1988).

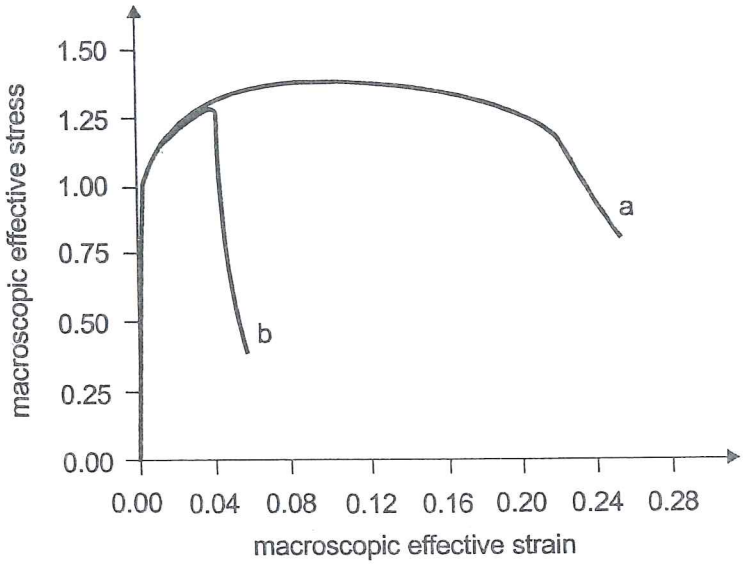

Figure 4-2 Macroscopic effective stress-strain curves according to cell geometry defined by Figure 4-1 (from Koplik & Needleman 1988).

Before the stress drop, the stress-strain response is identical. However the maximum stress reached and the shift to a uniaxial straining mode is sensitive to the void distribution. For a square cell, the authors show good agreements between Gurson's and cell models (Figure 4-3). They also verify that f_{cr} value, at which the onset of coalescence appears, varies slowly with the stress triaxiality and the matrix strain hardening, but depends strongly on the initial void volume fraction. Brocks *et al.* 1995's researches confirm that the void volume fraction at void coalescence f_{cr} does not significantly depend on the triaxiality if the initial volume fraction of primary voids is small and if there are no secondary voids. The strain rate does not affect f_{cr} either.

In conclusion, the simple threshold value of void volume fraction in Gurson's model appears to be valid if the whole parameter set is accurately fitted. As actual materials are non periodic, the definition of f_{cr} is even more difficult. Section 4.4 summarizes recent information on the dependence of f_{cr}.

Results of cell calculations performed by Brocks *et al.* 1995 indicate that a single internal variable, as the void volume fraction, is not sufficient to characterize the fracture processes in materials containing two different size scales of void nucleating particles.

In case of multiple scalar damage variables, threshold values can be applied on each damage variable as performed by Zhu 1992. However, the existence of interactions between these variables is an open question. For tensor damage variables, one could use a tensor norm to define one scalar threshold value (Zhu 1992). Experimental verification is however still lacking.

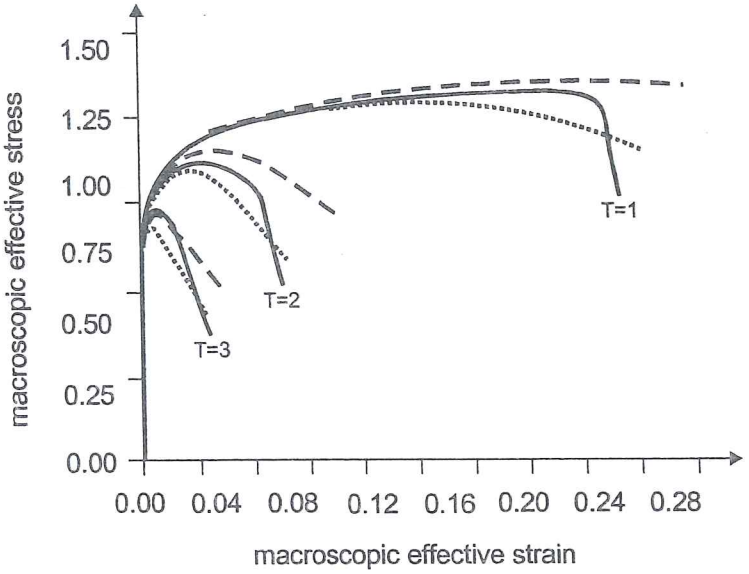

Figure 4-3 Comparison of macroscopic stress-strain curves:
cell model response, (——),
initial Gurson's model (- - - -),
modified Gurson's model with q_1, q_2 & f^* (……)
(from Koplik & Needleman 1988).

4.2. Criteria based on stress or strain field analysis

Using improved Gurson's law (with Tvergaard coefficient q_1 and function f^*) to simulate ductile rupture in notched bars, Needleman & Tvergaard 1984 correctly identify the experimental failure strain when the computed porosity reaches a constant value of $f_{cr}=0.15$.

They find that, as long as deviations from a constant triaxiality history are not too big, the onset of failure can also be represented by a curve relating effective strain with stress triaxiality. Later, the research performed by Chiou 1996, using an extension of Gurson's model, seems to prove that the critical porosity value is not a constant. However, Chiou proposes, like Needleman & Tvergaard 1984, to use a fracture strain related to the triaxiality ratio. The fracture criterion is :

$$\varepsilon_{eq} \leq \varepsilon_{rupture} = A \quad exp(-B\frac{\sigma_m}{\sigma_{eq}}) \tag{4-1}$$

Table 4-1 compiles the review performed by Zhu 1992 and Esche *et al.* 1996.

Criterion name	Formula	Origin, Physical assumptions
Gosh 1976 version of Zhu, Cescotto, Habraken 1992	$(\sigma_1+\sigma_2+\sigma_3)(\sigma_1-\sigma_3)=C$	This criterion is based on the statistical process of shear joining of voids.
Freudenthal 1950	$\int_o^{\varepsilon_f}\sigma_{eq}d\varepsilon_{eq}=C$	The absorbed energy per unit volume characterizes the critical fracture state.
Cockroft & Latham 1968	$\int_o^{\varepsilon_f}\sigma_1 d\varepsilon_{eq}=C$	This maximum tensile work criterion assumes that the maximum principal tensile stress rather than the effective stress causes fracture initiation.
Brozzo, de Luca, Rendina 1972	$\int_o^{\varepsilon_f}\frac{2\sigma_1}{3(\sigma_1-\sigma_m)}d\varepsilon_{eq}=C$	This criterion improves the preceding one by including the effect of hydrostatic stress.
MC Clintock 1968 Version of Oh, Chen, Kobayashi 1979	$\int_o^{\varepsilon_f}\left\{\frac{2}{\sqrt{3}(-n)}sinh\left[\frac{\sqrt{3}(1-n)}{2}\frac{\sigma_3-\sigma_1}{\bar{\sigma}_{eq}}\right]+\frac{\sigma_3-\sigma_1}{\bar{\sigma}_{eq}}\right\}$	This criterion is based on the analysis of the expansion of cylindrical cavities in a plastic material under a triaxial state of stress of fixed orientation.
Rice & Tracey 1969	$\int_o^{\varepsilon_f}B\,exp\left(\frac{A\sigma_m}{\sigma_{eq}}\right)d\varepsilon_{eq}=C$	Spherical voids in a plastic material are assumed to grow exponentially with the triaxiality. This criterion is widely used.
Oyane 1972	$\int_o^{\varepsilon_f}\left(1+\frac{\sigma_m}{A\sigma}\right)\varepsilon_{eq}^B d\varepsilon_{eq}=C$	This criterion is derived from the equation of plasticity theory for porous material.

Norris, Reaugh, Moran, Quinones 1978 Version of Atkins1981	$\int_o^{\varepsilon_f} \left(\frac{1+\frac{d\varepsilon_1}{d\varepsilon_2}\cdot\frac{1}{2}}{1-A\sigma_m} \right) d\varepsilon_{eq} = C$	Empirical criterion which considers the effect of principal strain ratio and hydrostatic stress.

Table 4-1 Some fracture criteria, where:

C	is the critical value of the scalar damage value, computed as a function of the stress and strain deformation history,
A	is a material constant,
σ_m	is the hydrostatic stress,
σ_{eq}	is the von Mises' stress,
$\sigma_1\ \sigma_2\ \sigma$	are the principal stresses,
$\varepsilon_1\ \varepsilon_2$	are the principal strains,
ε_f	is the effective equivalent fracture strain,
n	is the material hardening exponent,

(adapted from Zhu 1992 and Esche *et al.* 1996).

As concluded in both reviews, the drawbacks of the above criteria are their accuracy dependency on the mode in which failure takes place and the difficulty to find accurate material constants. In fact, the critical damage values are not purely material constants but rather depend to some degree on the type of boundary conditions. Their advantage is an easy implementation in the Finite Element code. A more complete review can be found in Wilsius 1999.

4.3. Criteria based on stress or strain fields dedicated to sheet metal forming

This section is specifically dedicated to sheet metal forming. Different approaches were considered to detect the localized necks that are quickly followed by rupture:

1. experimental work to define the material limits (Forming Limit Diagram FLD);
2. analytical work based on Marciniak & Kuczynski's 1967 approach (MK), which requires the assumption of an initial defect and allows to predict FLD;
3. analytical plastic instability criteria which require no additional data or defect assumption and allow to predict necking in any conditions.

4.3.1. Forming Limit Diagram (FLD)

A forming limit diagram (FLD) divides the plane of major principal strain versus minor principal strain into a safe zone and a failure zone. Commonly, such diagram is experimentally determined by means of proportional loadings, which keep a constant ratio between the major and minor principal strains throughout the deformation process (depending on the authors, such a loading is called a radial, linear or direct strain path). Figure 4-4, relative to an isotropic material, presents the restrained, stretched, failure and safe zones. For anisotropic material, the relation between the stress and strain ratios differs, FLD diagram keeps classical directions defined by the train increment ratio.

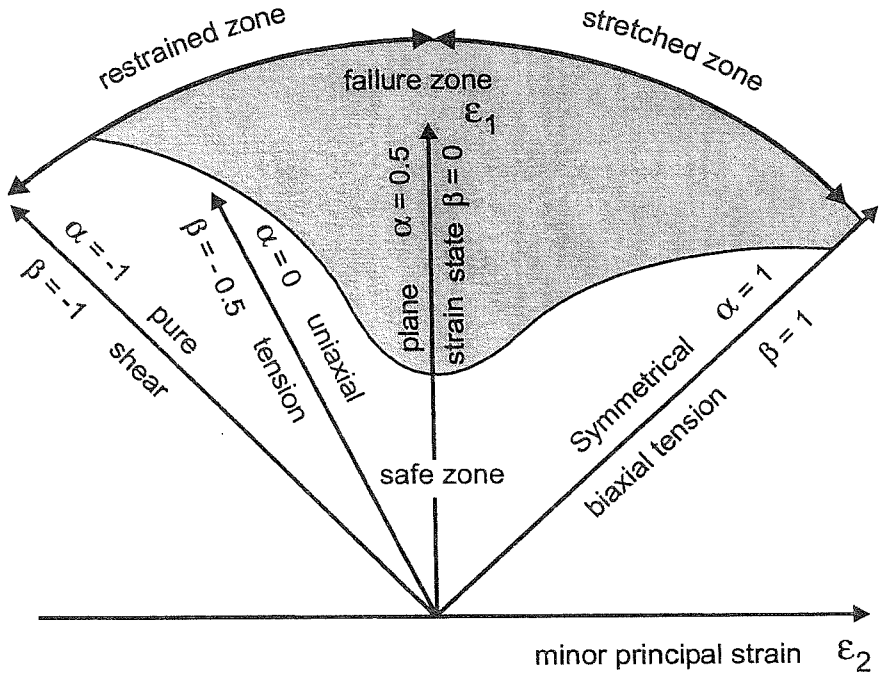

Figure 4-4 Forming Limit Diagram, where α is the stress ratio ($\alpha = \sigma_2/\sigma_1$) and β is the strain increment ratio ($\beta = d\varepsilon_2 / d\varepsilon_1$), isotropic material, (adapted from Barata da Rocha 1985).

A short historical survey of FLD is proposed by Esche *et al.* 1996.

FLD deduced from direct strain paths cannot be used in all cases, because they are not overlaid by FLD obtained by means of broken strain paths (stretching or large tensile tests followed by radial strain paths...). However, they can still serve for comparing different materials or determining the best orientation of the sheet to optimize a deep drawing operation. Arrieux 1990, Vacher *et al.* 1988 propose to employ a Stress Forming Limit Diagram, which seems to be a better intrinsic material property. The Stress FLD deduced from broken or direct strain paths are very close to each other and the one deduced from linear strains is almost always located slightly below the others. So, the current practice in deep drawing is to

implement experimentally measured Stress or Strain Forming Limit Diagrams in FEM codes. Then, the computed principal stresses or strains are compared to these limit curves which allows to detect fracture. Such an approach can be used with a law which is coupled or not with damage. Note that the intrinsic property of Stress FLD can be very dependent on the quality of the stress calculation procedure (Boudeau 1995).

Vacher *et al.* 1988 introduce in fact a Forming Limit Stress Surface as they include the effect of the angle between the principal strains and the material orthotropy directions (Figure 4-5). One of the main problems with this approach is the impossibility of using this surface if the angle θ between principal strains and orthotropy directions varies during the forming process.

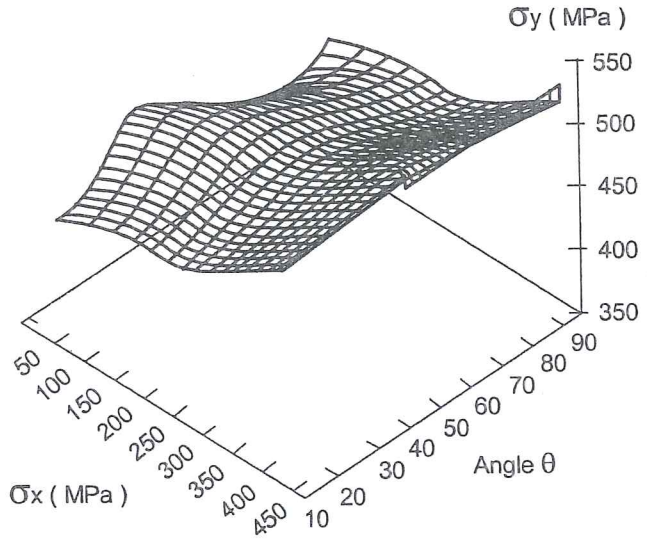

Figure 4-5 Forming Limit Stress Surface in and off axis solicitations, with direct paths, mild steel for deep drawing SEDDK A151 (from Vacher *et al.* 1988).

The FLD predictions also provide a very sensitive way to check analytical approaches coupled or not with FEM and adapted to different descriptions of the material behavior. The following references give only a small idea of the important effort dedicated to theoretical FLD prediction: Narasimhan & Wagoner 1991, Qiu *et al.* 1995, Boudeau *et al.* 1996a, Banabic 1996, Hora *et al.* 1996, Vegter *et al.* 1998, Cayssials 1998 and 1999, Hoferlin *et al.* 1998,Vegter *et al.* 1999, ... This proves the interest in FLD from the automotive or can deep drawing industries. Note that the model proposed by Cayssials 1998 and 1999 is very effective for classical steels. Coupling plastic instability theory with a damage approach, Cayssials's model accurately predicts FLD with data as simple as yield stress, hardening exponent, Lankford coefficient, and thickness of the metal sheet.

A complete review of approaches using MK model or analytical criteria to predict FLD is available in Esche *et al.* 1996. This represents a large amount of research as,

once the general computation principles are defined, they can be applied for numerous constitutive models: isotropic or not, with or without strain rate sensitivity, coupled to damage or not ... The following paragraph presents Marciniak & Kuczynski's approach. Then two examples of FEM models coupled with analytical stability criteria (Hora-Brunet and Boudeau-Gelin criteria) are summarized.

4.3.2. Marciniak & Kuczynski's approach.

Since localized necking under biaxial stretching of a uniform and homogeneous sheet is impossible when flow theories of plasticity with smooth yield loci are used, Stören & Rice 1975 pointed out that the development of a vertex on the yield locus is responsible for the onset of localized necking in thin sheets under biaxial tension. Marciniak & Kuczynski 1967 attempt to resolve this 'paradox' by another way. They assume pre-existing inhomogeneities in the sheet. Their method provides a well-known way to predict FLD by analytical developments (Barata da Rocha *et al.* 1984, Zhou & Neale 1995, Banabic 1996, Hoferlin *et al.* 1998, Vacher *et al.*1998, Vegter *et al.* 1999...) or even by FEM simulations (Narasimhan & Wagoner 1991, Qiu *et al.* 1995, Habraken *et al.* 1998, ...). The analytical way is summarized here. This approach postulates that an initial geometric imperfection exists in the form of a narrow band across the width of the sheet. As depicted in Figure 4-6, the initial thickness l_{30}^{b} of the band (zone b) is slightly less than the initial thickness l_{30}^{a} of the rest of the sheet (zone a).

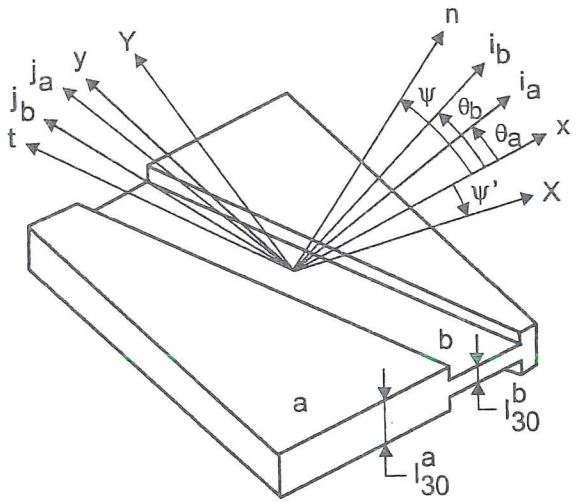

Figure 4-6 Marciniak and Kuczynski's model
X,Y principal stress directions; *x, y* principal strain directions; $i_a j_a$, $i_b j_b$ principal orthotropy axis in zone *a* and *b; n, t* initial orientation of the geometric defect (from Vacher *et al.* 1998).

The applications of MK method differ according to the orientation of the band, the imposition of principal stresses or strains at the edges of the sheet, the orientation of the material orthotropy axes. In their computation, Vacher *et al.* 1998 handle four

angles as defined in Figure 4-6. Generally, orthotropy axes and principal stresses or strains directions are set parallel and the orientation of the band is chosen. The simplest case (Zhou & Neale 1995, Banabic 1996) is to assume the band aligned with the minor-strain direction.

As studied by Barata da Rocha *et al.* 1984, for planar isotropic material and stretched zone of FLD, the critical neck orientation is effectively parallel to minor strain axis. Doghri & Billardon 1995 study the localization condition for homogeneous plane problems without shear. It depends on the material model and the stress-state but the orientation of the localization band only depends on the biaxiality ratio. Using a different approach, they recover the results of Hill 1950 for a tensile test. In this loading case, an angle of 54.7° separates the normal to the localization band from the normal to the tensile direction. This neck orientation is then assumed in the computation on FLD stretched zone by Vegter *et al.* 1999. The conservative approach used by Hoferlin *et al.* 1998 for predicting FLD is to compute the limit strains with various values of the initial band angle and to designate the minimum strain as the predicted forming limit. However Wu *et al.* 1998 have verified by simulations and experiments that FLD predictions are not very sensitive to the groove orientation.

Once these orientation choices are done, one must define the initial thickness ratio l^b_{30}/l^a_{30} . This ratio value (0.995, 0.986, ...) is often used as fitting parameter to get close to experimental results. Then, all authors apply the same procedure deduced from physical conditions:

- they impose principal stresses or strains in zone *a;*
- the yield locus and hardening law are respected in zones *a* and *b;*
- the normality rule is applied to derive strain from yield locus;
- the plastic incompressibility is used;
- the equilibrium across band boundary (1 or 2 equations according to its orientation) is respected;
- the equality of strain parallel to the band across its boundary is imposed;
- necking is assumed when the maximal principal strain rate in zone *b* is larger than the one in zone *a* by a factor of 10, 100, or even 1000 depending on the authors.

To be clear, the approach used by Hoferlin *et al.* 1998 is reproduced hereafter. The adopted choice of coordinates is presented on Figure 4-7. The stability analysis of plastic flow proceeds by an incremental loading of the homogeneous zone. During each increment, the strain rate tensor $\underline{\dot{\varepsilon}}^a$ is assumed to be constant and such that its principal directions are aligned with *X, Y, Z* axes. Furthermore, the major strain is assumed to occur along *X*-axis and the strain rate mode is characterized by the ratio β between $\dot{\varepsilon}^a_{xx}$ and $\dot{\varepsilon}^a_{yy}$. At each increment, the problem consists in determining the strain rate tensor $\underline{\dot{\varepsilon}}^b$ describing the plastic flow in the groove. For convenience, this latter is computed in the local reference frame *t, n*. In the following analysis, plastic

flow localization is supposed to occur when the maximal principal value of $\underline{\dot{\varepsilon}}^b$ is larger than $1000\,\dot{\varepsilon}^a_{xx}$. The corresponding strains $(\varepsilon^a_{xx}, \varepsilon^a_{yy})$ accumulated at that moment in the homogeneous zone are the limit strains. The analysis is actually repeated for different values of ψ ranging from 0 to 90° and the limit FLD point is obtained after minimization of ε^a_{xx} versus ψ.

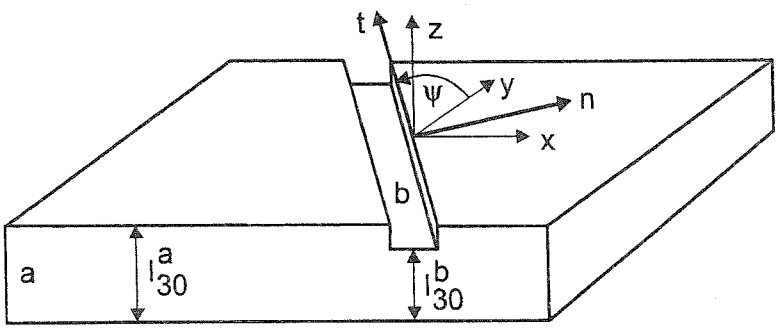

Figure 4-7 Marciniak and Kuczynski's model applied by Hoferlin *et al.* 1998. *xyz* principal strain directions, *x* is either the rolling direction or the transverse direction, *z* normal direction of the sheet; *n,t* initial orientation of the geometric defect (from Hoferlin *et al.* 1998).

The unknowns of the problem are the groove spin tensor $\underline{\Omega}$ and the groove strain rate tensor $\underline{\dot{\varepsilon}}^b$:

$$\underline{\dot{\varepsilon}}^b = \begin{bmatrix} \dot{\varepsilon}^b_{nn} & \dot{\varepsilon}^b_{nt} & 0 \\ \dot{\varepsilon}^b_{nt} & \dot{\varepsilon}^b_{tt} & 0 \\ 0 & 0 & \dot{\varepsilon}^b_{zz} \end{bmatrix} \quad \text{and} \quad \underline{\Omega} = \begin{bmatrix} 0 & \Omega^b_{nt} & 0 \\ -\Omega^b_{nt} & 0 & 0 \\ 0 & 0 & 0 \end{bmatrix} \tag{4-2}$$

The 5 unknowns of above equations are constrained by the following relations describing plastic incompressibility and geometrical compatibility:

$$\dot{\varepsilon}^b_{nn} + \dot{\varepsilon}^b_{tt} + \dot{\varepsilon}^b_{zz} = 0 \tag{4-3}$$

$$\dot{\varepsilon}^b_{tt} = \dot{\varepsilon}^a_{tt} \tag{4-4}$$

$$\Omega^b_{nt} = \dot{\varepsilon}^a_{nt} - \dot{\varepsilon}^b_{nt} \tag{4-5}$$

Finally, only 2 independent unknowns remain $(\dot{\varepsilon}^b_{nn}, \dot{\varepsilon}^b_{tt})$. They are solutions of the force equilibrium non linear equations (4-6) where stresses and strains are related by yield locus, normality rule and hardening law:

$$\sigma^b_{nn} l^b_3 = \sigma^a_{nn} l^a_3 \quad \text{and} \quad \sigma^b_{nt} l^b_3 = \sigma^a_{nt} l^a_3 \tag{4-6}$$

The updated thickness is computed by:

$$l_3^b = l_{30}^b \exp\left(-\int_0^t \dot{\varepsilon}_{xx}^b dt - \int_0^t \dot{\varepsilon}_{yy}^b dt \right) \quad (4\text{-}7)$$

The numerical necking prediction from the MK model depends on the value given to the initial geometrical defect. However it is often accepted to fit this parameter by one experiment and then to keep it constant for the other FLD points. As confirmed by numerous authors, Banabic 1996, Boudeau *et al.* 1998, Hoferlin *et al.* 1998, Narasimhan & Wagoner 1991, Vegter *et al* 1999, Zhou & Neale 1995, the initial yield shape and its evolution, the choice of a hardening law and the strain sensitivity formulation affect the FLD prediction produced by the MK method with fixed geometrical defect.
The use of MK method as a criterion to detect necking in general FEM deep drawing simulations is seldom considered because this method implies to solve a highly non linear problem at each incremental step and then leads to very long computation times (Boudeau *et al.* 1996a, Vacher *et al.* 1998). In conclusion, MK method is only dedicated to FLD prediction for direct or broken paths.

4.3.3. Hora & Brunet's criterion

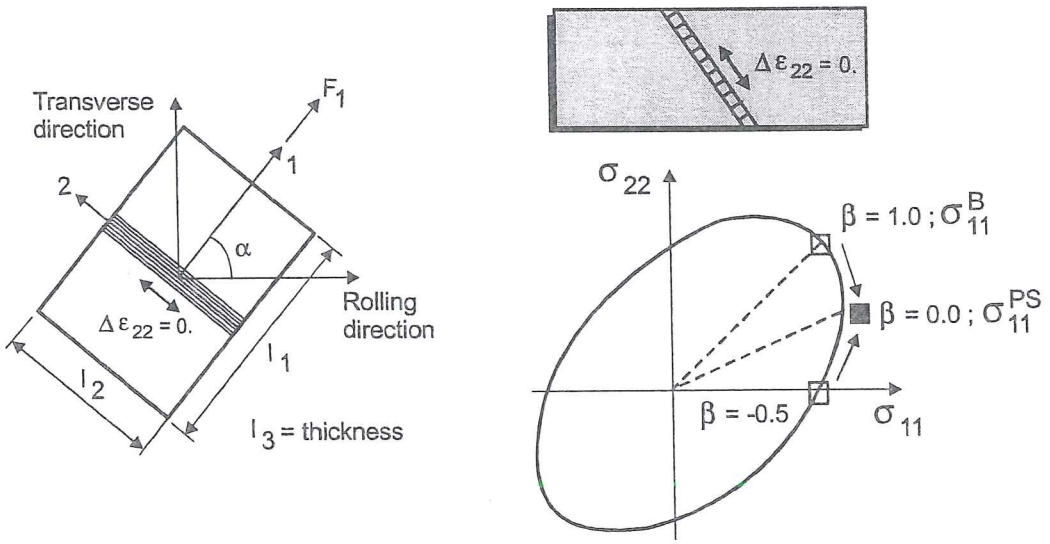

Figure 4-8 Model of sheet behavior when localized necking occurs (adapted from Hora *et al.* 1996).

The necking criterion proposed by Hora *et al.* 1996 has the great interest of not adding any parameter to the constitutive law to detect rupture. This criterion is based on physical considerations on the transition between a diffuse necking and a strain localization leading to necking and rupture. The strain ratio $\beta = \Delta\varepsilon_2 / \Delta\varepsilon_1$ (see Figure 4-8) has an evident influence on the internal damage of metal sheets. At the same level of deformation, it is generally noted that the damage increment is the largest in plane strain state. This indicates that plane strain is the most dangerous strain state for which strain localization is most likely to appear. Progressive development of

plane strain state after diffuse necking may be the common origin of strain localization appearance in tension-tension and tension-compression stress states. In both regions, the strains evolve towards the plane strain state such that $\Delta\varepsilon_2=0$, $\beta=0$ when localized necking occurs. The final criterion form is deduced from the following steps:

- assume plane stress state;
- Figure 4-8 defines the force F_1 and the directions 1 and 2. The sheet initial dimensions are l_{10}, l_{20}, l_{30} with l_1, l_2, l_3 being their updated value;
- the principal Cauchy stress σ_1, with $F_1 = \sigma_1 l_1 l_2$, and the natural strains are used:

$$\varepsilon_2 = ln\,(l_2/l_{20}) \qquad \varepsilon_3 = ln\,(l_3/l_{30}) \tag{4-8}$$

- so, the load instability ($dF_1<0$) gives:

$$\frac{d\sigma_1}{\sigma_1} + d\varepsilon_2 + d\varepsilon_3 \le 0 \tag{4-9}$$

- neglecting the elastic strain part, the plastic incompressibility leads to:

$$\frac{d\sigma_1}{d\varepsilon_1} \le \sigma_1 \tag{4-10}$$

- since the state of strain evolves towards plane strain due to the change of related stress state, there is an additional hardening effect such that :

$$d\sigma_1 = \frac{\partial\sigma_1}{\partial\varepsilon_1} d\varepsilon_1 + \frac{\partial\sigma_1}{\partial\beta} d\beta \tag{4-11}$$

- the final necking criterion takes the form:

$$\frac{\partial\sigma_1}{\partial\varepsilon_1} + \frac{\partial\sigma_1}{\partial\beta}\frac{d\beta}{d\varepsilon_1} \le \sigma_1 \tag{4-12}$$

Hora *et al.* 1996 apply this criterion on von Mises or general non-quadratic yield loci, while Brunet *et al.* 1997, 1998 compute it for anisotropic extensions of Gurson's model with Hill, Barlat or Lian's yield locus. The use of Gurson's type model requires some adaptation; for instance, relation (4-10) based on incompressibility is modified. Hora and Brunet's results demonstrate the efficiency of this criterion to determine strain Forming Limit Diagrams (Figure 4-9). This criterion is able to detect rupture for arbitrary paths by a direct implementation in FEM codes and does not require any arbitrary defect value as in MK approach. This model is unfortunately limited to 2D stress state.

Remark the similarity of this concept with the parameter P introduced by Sowerby & Duncan 1971 and telling that, for biaxial strain state, the higher is the P-ratio, the larger is the limiting strain. This P parameter is defined as the ratio between the

plane strain and the balanced biaxial flow stresses (see Figure 4-8, $P=\sigma_{11}^{PS} / \sigma_{11}^{B}$). Considering a MK model submitted to biaxial stretch ($\varepsilon_{11} = \varepsilon_{22}$) with a groove parallel to the "minor" strain axis and neglecting hardening, the stress states in the groove and in the homogeneous zone belong to the same yield locus. As deformation proceeds, the ratio between the thickness of the groove and the homogeneous zone decreases. Consequently, in order to fulfill the force equilibrium along the groove interface, the stress in the groove has to increase. Therefore it rotates towards the plane strain yield point ($\beta=0$) where the normal to the yield locus is "horizontal" (parallel to σ_{11}). Since the strain rate in the vertical direction (parallel to σ_{22}) remains constant (MK hypothesis), it implies an infinite horizontal strain rate in the groove, *i.e.* plastic flow localization or necking. So, the additional shape hardening of the yield surface, indicated by the β parameter in Hora and Brunet's approach, was already present in the P–ratio approach. Note that, when isotropic hardening occurs, the rotation of the stress point toward plane strain-state is slowed down. Finally, if kinematic hardening is introduced, it reduces the effect of the shape hardening (Hiwatashi *et al.* 1998).

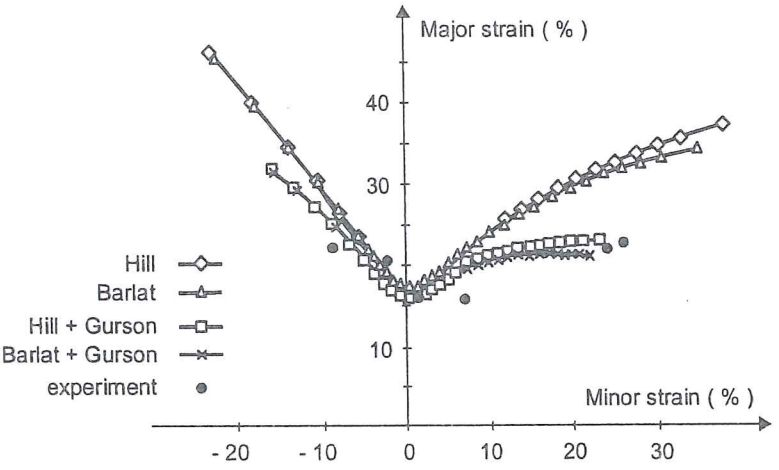

Figure 4-9 Experimental and theoretical FLD predicted by Hora-Brunet's criterion applied to Hill's or Barlat's models coupled or not with damage, Al5182 (from Brunet *et al.* 1998).

4.3.4. Boudeau-Gelin's criterion.

Since 1992, Boudeau and Gelin have presented a criterion, which considers the necking phenomenon as an instability phenomenon. The proposed method is the linear perturbation technique largely employed in physics and engineering sciences. It consists in perturbing the equilibrium and examining if the perturbed solution remains close to the initial one or, on the contrary, increases indefinitely when time goes on. The particularities of this approach are that it does not require to study the evolution of an assumed defect and that the analysis can be done at any instant regardless of the previous one. Initially, developed in plane stress state, this approach

has been extended to 3D stress state (Boudeau *et al.* 2001). For 2D stress state, Boudeau & Gelin 1994 can be summarized by the following steps:

- The equilibrium of a material point is locally governed by nine equations defining nine variables represented by the vector $\underline{u}$:

$$\underline{u} = \{ \sigma_{11}, \sigma_{22}, \sigma_{12}, \sigma_{eq}, \dot{\varepsilon}_{11}, \dot{\varepsilon}_{22}, \dot{\varepsilon}_{12}, \dot{\varepsilon}_{33}, \dot{\varepsilon}_{eq} \}$$

  Note that σ_{eq} and $\dot{\varepsilon}_{eq}$ are not the equivalent von Mises' expressions but are related to the anisotropic yield locus formulation (see respectively sections 3.5.5 and 2.2 of part B). The nine relations to fulfill are the following ones:

  - The hardening law defining the plastic reference yield curve σ_F, for instance:

$$\sigma_F = K(\varepsilon_o + \varepsilon_{eq}^p)^n (\dot{\varepsilon}_{eq}^p)^m \qquad (4\text{-}13)$$

  - The yield surface: $F_p(\underline{\sigma}, \sigma_F) = 0$ (4-14)

  - The plastic flow law (3 equations): $\underline{\dot{\varepsilon}}_p = \dot{\lambda}_p \dfrac{\partial F_p}{\partial \underline{\sigma}}$ (4-15)

  - The equilibrium:

$$(l_3\ \sigma_{11})_{,1} + (l_3\ \sigma_{21})_{,2} = 0 \qquad (4\text{-}16a)$$

$$(l_3\ \sigma_{12})_{,1} + (l_3\ \sigma_{22})_{,2} = 0 \qquad (4\text{-}16b)$$

  - The plastic incompressibility assumption: (4-17)

$$\dot{\varepsilon}_{33} = -\dot{\varepsilon}_{11} - \dot{\varepsilon}_{22}$$

  - The compatibility of the strain rate: (4-18)

$$\dot{\varepsilon}_{11,22} + \dot{\varepsilon}_{22,11} = 2\dot{\varepsilon}_{12,22}$$

- The elastic strain is neglected.
- The above set of equations defines a non linear system: $A(\underline{u})=0$.
- If $\underline{u}^0$ is a solution of $A(\underline{u})=0$, its stability, in the sense of linear perturbation technique, is verified using the perturbed solution $\underline{u}$:

$$\underline{u} = \underline{u}^0 + \delta\underline{u} \qquad (4\text{-}19)$$

  with $\delta\underline{u} = \delta\underline{u}^0 \exp(\eta t) \exp(\xi\, o\underline{M} \,.\, \underline{n})$

  where $\delta\underline{u}^0$ is the amplitude of the perturbation;
  η is the temporal part of the instability;

ξ is the spatial part of the instability;
M is the point where instability could occur;
o is the center of the global frame (o,x,y);
$\underline{n}$ is the normal to the direction $\underline{t}$ along which necking could occur.

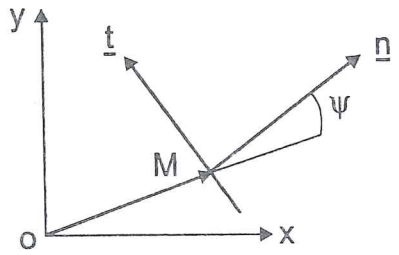

Figure 4-10 Representation of $\underline{oM}$, $\underline{n}$, $\underline{t}$ vectors in global frame x,y, (from Boudeau & Gelin 1996a).

- The above system is linearized, and the perturbed solution must satisfy:

$$A(\underline{u}^0, \eta, \xi).\ \delta\underline{u}^0 = \underline{0} \tag{4-20}$$

A non trivial solution only exists if:

$$det\ A(\underline{u}^0, \eta, \xi) = 0 \tag{4-21}$$

Knowing $\underline{u}^0$ and fixing ξ, this equation allows computing η. If the real part of η becomes positive, instability occurs.

The numerical implementation has been carried out in the FE code developed by Gelin's laboratory (Boudeau & Gelin, 1994). It has been extended to 3D stress state in Boudeau *et al.* 2001. The code does not consider strain rate sensitivity in the hardening law. However, this parameter is required for the establishment of the necking criterion. At last, the strain rate sensitivity parameter will be imposed to be equal to 0. Above equations are transformed into an incremental form and a loop on various orientations of the necking zone ψ is necessary to find the lowest root η with positive real part. Numerous numerical results, compared to experimental ones, show the validity of such an approach (Boudeau *et al.* 1992, 1994, 1996, 2001). The necking phenomenon is detected even when no critical thinning is observed. The investigations also prove the ability of this criterion to detect the formation of wrinkles too. The two kinds of instability can be distinguished by the sign of the two principal stresses in the sheet plane, but also by the range of the instability parameter η. For necking, this parameter is in the range 0.01 to 0.1, while it reaches unit value in case of wrinkling. This criterion has been applied with the classical Hill's yield locus but also with a polycrystalline model taking into account crystallographic slips, work hardening at microstructural level and lattice rotations, which induce texture evolution (Boudeau *et al.* 1996b, 1998, 2001). Note that Cayssials' 1998 "new" criterion is very similar to Boudeau-Gelin's approach.

4.3.5. Conclusion

To detect necking in sheet FEM simulations, the use of criteria such as Brunet-Hora's or Boudeau's ones seems promising. Such approaches require no additional assumption and are closely connected to stress and strain fields, which should be more sensitive in any finite element code than the global thickness reduction. Moreover, these approaches are adapted to complex strain paths as demonstrated by their authors. Interesting applications can be found in Knockaert 2001.

4.4. Criteria based on microscopic phenomena analysis

The study of the coalescence of cavities in porous plastic solids is important for the definition of macroscopic models describing the mechanical behavior of ductile metals. Unfortunately, a number of factors contribute to make it a difficult problem, notably the fact that coalescence is sensitive to many parameters such as void shape, spacing and distribution, nucleation of cavities, presence of smaller, secondary voids, etc... The hereafter collected criteria result from the application of a mechanical theory, like the upper-bound theorem, localization condition or just geometric conditions, applied on representative cell models (matrix + voids or matrix + inclusions).

The work of Rice & Tracey 1969 based on the study of a cell model with initial spherical void yields an approximate relation, where void growth rate is linked to triaxiality ratio. First, a variational principle was established by Rice and Tracey to characterize the flow field in a plastic rigid incompressible material containing internal voids and subjected to a remote uniform stress-strain field. Then, an approximate Rayleigh-Ritz procedure is applied to the enlargement of an isolated spherical void in a non-hardening material and approximate relations are deduced for linear hardening material. This work establishes that, for any remote strain field, the ratio of the void enlargement rate over the remote strain rate is amplified by a factor rising exponentially with triaxiality ($T = \sigma_m/\sigma_{eq}$). Recalling relation (2.11), already presented in section 2.1, it covers the simple case of a tension remote field and gives the average spherical growth rate:

$$\frac{dR}{R} = A\, exp\left(\frac{3\sigma_m}{2\sigma_{eq}}\right) d\varepsilon_{eq} \qquad (4\text{-}22)$$

The first work of Rice & Tracey set A to 0.283; however further research shows that this factor should be increased (Marini 1985). In practice the factor A is adjusted to fit the experimental data obtained with different triaxialities.

The ellipsoidal shape can be estimated by the general relation (2.12) using a void shape parameter E or, in the case of linear isotropic hardening materials, is directly given by:

$$\dot{R}_k = \left(\frac{5}{3} \dot{\varepsilon}_k^p + \frac{3}{4} \frac{\sigma_m}{\sigma_{eq}} \dot{\varepsilon}_{eq}^p \right) R \qquad (4\text{-}23)$$

where $\dot{R}_k$ denotes radial velocities of the void boundary at points aligned with the remote principal directions, $\dot{\varepsilon}_k^p$ are the principal plastic strains. As reported by Boyer & Staub 1997, relation (4-23) gives useful estimates of the change in shape and volume of an initial spherical void. Some extensions have already been proposed by Thomason 1990. However, this type of approach does not handle pure shear stress states.

The critical ratio $(R/R_0)_c$ can be used as rupture criterion. The determination of this value links numerical FEM simulation and fracture mechanics experiments. A large literature review of $(R/R_0)_c$ is proposed by Wilsius 1999.

It is worth to mention Rice & Tracey's relation since principal radii of ellipsoidal voids are necessary to use coalescence criteria of Brown & Embury or Thomason for instance.

Based on a number of experimental studies, Brown & Embury 1973 found that after nucleation, cavities elongate along the major tensile axis and that two neighboring cavities coalesce when their length has grown to the order of magnitude of their spacing. This local failure occurs by the development of slip planes between the cavities or simply by necking of the ligament. As presented by Pardoen 1998, Brown & Embury's criterion can be of practical application in numerical macroscopic computations :

- the porosity f is computed by a Gurson's type model, relation (2-10) allows to estimate the updated void radius; relations (2-11) and (2-12) assume an ellipsoidal void growth and help to compute characteristic sizes of the ellipse (R_1, R_3) (see Figure 1-1 for axes definition).
- the updated distance l_c between the centers of neighboring voids is deduced from the local strain ε_1 and the initial intervoid length l_{c0}:

$$l_c = l_{c0} \ exp(\varepsilon_1) \qquad (4\text{-}24)$$

- Brown & Embury's criterion is fulfilled if: $l_c = 2\sqrt{R_1^2 + R_3^2}$ (4-25)

Koplik & Needleman's 1988 work, already described at section 4.1, verifies that this criterion provides a good approximation in case of a triaxiality ratio $(T = \sigma_m / \sigma_{eq})$ close to 1 and of predominant axial stress loading. However, they show that it detects coalescence too late at a higher triaxiality value ($T = 2$). The experimental and numerical work of Pardoen 1998 confirms this conclusion. The cell model easily explains this observation: the void initially grows into a prolate ellipsoid as expected from predominant axial stress, then suddenly turns back to more oblate shapes as coalescence results in a strong straining and necking of the horizontal ligament

separating nearby cavities. Of course, the intensity of the lateral stresses and hence the triaxiality value modify this event appearance.

As verified by Brocks *et al.* 1995, the critical void volume fraction f_{cr} decreases with increasing triaxiality. Gologanu *et al.* 1994 also use a cell model to study lower triaxiality cases (T = *1/3; 2/3; 1*) and different loading characteristics such as predominant lateral axisymmetric stress or axial stress. In the case of predominant axial stress and high value of triaxiality (T = *2/3 and 1*), their conclusions recover those of Koplik & Needleman's work. However in the case of no lateral stress and T=*1/3*, which corresponds to uniaxial tension, the shape parameter (equal to $ln(R_3/R_1)$, where R_3 and R_1 respectively denote the semi-axes of the void along the vertical-axial and horizontal-transversal direction) can be observed to increase without any apparent bound. This means that the cavity grows into cylindrical hole, the porosity tends towards some asymptotic value and no coalescence occurs in pure tensile state. Note that tensile bars (for which T=*1/3*) usually fail after necking, which locally increases the stress triaxiality. In the case of predominant lateral stresses, intervoid straining and coalescence were observed to occur along vertical columns (see Figure 4-11b) instead of horizontal layers (see Figure 4-11a). Since the overall weakening effect resulting from the formation of a damaged zone is considerably less dramatic in the case of a column than in that of a layer, the macroscopic equivalent stress at fracture decreases in a much more gradual way than in the case studied by Koplik & Needleman (see Figure 4-3). In conclusion, the cell model helps to understand the limits of Brown & Embury's criterion.

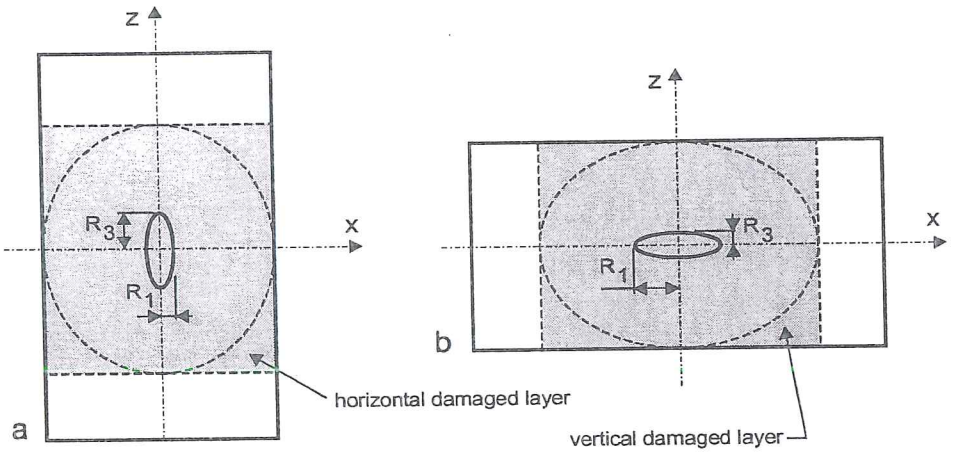

(a) predominant axial stress (b) predominant transversal stress

Figure 4-11 Composite cell models to simulate the coalescence event with sound material (not shaded) described by von Mises criterion and highly porous material (shaded) represented by Gurson-Gologanu's model accounting for void shape effects (from Gologanu *et al.* 1994).

Thomason's criterion (Thomason 1985a, 1985b, 1993) is issued from a sophisticated micromechanical model of void coalescence. For a non-hardening rigid plastic solid,

which contains a regular three-dimensional distribution of spherical microvoids in the initial state, this model considers that the necking of ligaments separating the cavities results from the attainment of a maximal load withstood by these ligaments. Recall that Koplik & Needleman 1988 cell computations give further support to Thomason's idea about this fracture mechanism. The updated size and shape of microvoids are computed by Rice-Tracey's equations. The limit load depends on the current yield stress of the matrix, the updated shape of the voids, their size and spacing, which are related to the strain state. This load, estimated by means of the upper-bound theorem[1], is then compared to the maximal principal stress effectively applied (Figure 4-12). When both terms are equal, failure is predicted. In three dimensions, assuming axisymmetry and ellipsoidal void growth and collecting various results from Thomason, Pardoen 1998 expresses this criterion by the following equation:

$$\left(\frac{0.1}{\left(\frac{R_3}{\frac{l_c}{2} - R_1} \right)^2} + \frac{1.2}{\sqrt{\frac{R_1}{\frac{l_c}{2}}}} \right) (1 - f_0)^{-1} \left(1 - \left(\frac{3\sqrt{\pi}}{4} f_0 \right)^{2/3} \left(\frac{R_1}{R_{10}} \right)^2 \exp \varepsilon_3 \right) = \frac{\sigma_{max\ princ}}{\overline{\sigma}_{eq}} \qquad (4\text{-}26)$$

where l_c is the current transversal distance (see Figure 1-1) between the centers of two cavities, ε_3 is the longitudinal strain, $\sigma_{max\ princ}$ is the value of maximal principal stress and $\overline{\sigma}_{eq}$ is the current yield stress of the matrix.

Figure 4-12 from Pardoen 1998 illustrates how the two sides of equation (4-26) behave in the case of the finite element simulation of a notch test. He uses the improved version of Gurson's model proposed by Leblond *et al.* 1995 to compute the macroscopic stress-strain state. The updated radii of cavities are computed as explained above for Brown & Embury's criterion. As shown by Figure 4-12, at the beginning of void growth, the applied stress state is much lower than the stress state required to cause plastic failure of the ligament (left-hand side of equation (4-26)). As void size increases, the stress state required to induce ligament failure decreases to a point where it becomes equal to the applied stress and the fracture strain is predicted.

[1] From the upper-bound theorem for rigid-plastic non-hardening solids, an overestimated plastic load for incipient internal necking of the intervoid matrix is obtained by equating the rate of internal energy dissipation, for a kinematically admissible velocity field, to the rate of work of the external loads.

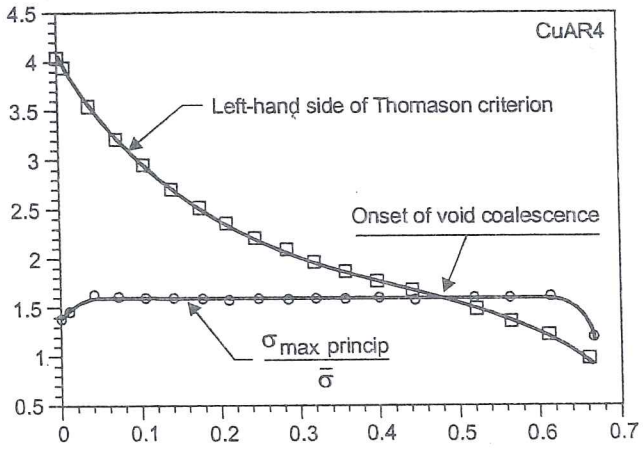

Figure 4-12 Example of Thomason's criterion application; variations of both sides of equation (4-26) are locally computed thanks to FEM simulation of a notch test (from Pardoen 1998).

To be clear, Thomason's criterion for coalescence is purely based on geometrical consideration and upper-bound theorem. To be used, it requires other models that provide the evolution of the porosity, the void shape and the stress and strain fields.

Pardoen's 1998 work dedicated to experimental and numerical study of copper bars concludes that, among the four void growth models studied (Rice & Tracey's approach coupled with von Mises' law, Gurson-Tvergaard's model, Gurson-Leblond-Perrin's model, Lemaître's model) and the four void coalescence criteria (threshold value of damage parameter, Brown & Embury's criterion, Thomason's criterion and a criterion based on the decrease of macroscopic stress), *the Gurson-Leblond's void growth model coupled with the Thomason's void coalescence criterion was found the most pertinent for modeling the porosity variation and cracking initiation in copper bars.*

Another aspect of Thomason's work concerns his study on ductile fracture by the growth and coalescence of microvoids of non-uniform size and spacing (Thomason 1993). The theoretical void-growth strains at ductile fracture for a wide variation in void diameters and spacing show that, for a given volume fraction of voids, the minimum ductile-fracture strain occurs when the voids are of uniform size and spacing. Such a result is quite interesting as most of the models are developed on the assumption of uniform void size and spacing and should accordingly give safe predictions. However, this conclusion is opposite to common physical sense and to the work of Benzerga *et al.* 1999 or Koplik & Needleman 1988 commented in this thesis. Thus Thomason's results are probably of limited generality since they were reached by means of a two-dimensional plane strain model of void growth and coalescence in a rigid/plastic solid.

Another coalescence model considers the coalescence as a bifurcation behavior in a pressure-sensitive material. As summarized by Benzerga *et al.* 1999, various scientists have followed such approach. The first trials to apply strain-localization

analyses on simulations performed with Gurson's models lead to excessive ductility predictions. To find results in correlation with experiments for axisymmetric loading with predominant axial stress, Leblond & Perrin 1991 use a doubly periodic array of voids (Figure 4-13). Let us remark that such an assumption is connected to the one chosen by Gologanu and represented on Figure 4-11. The non-homogeneity of the void distribution during deformation has been confirmed by experimental observations (Pineau 1981).

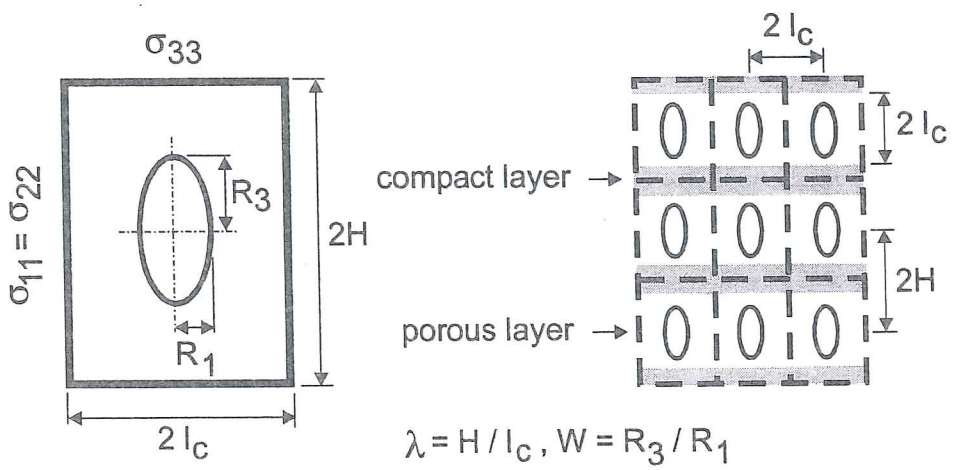

Figure 4-13 Axisymmetric unit cell submitted to macroscopic stress (σ_{11} σ_{22} σ_{33}), definition of compact and porous layers and geometric parameters (from Benzerga *et al.* 1999).

According to Leblond & Perrin 1991, the overall behavior of the material is supposed to obey a Gurson like criterion. Coalescence arises from the progressive concentration of voids in some highly porous layers separated by compact regions (Figure 4-13). Coalescence is detected by the localization condition of Rudnicki & Rice 1975 applied on a mesoscopic stress state present in this porous layer. This mesoscopic stress state must be compatible with the macroscopic one and is computed according a Gurson's criterion written with a local porosity. Such final coalescence condition is of course not straightforward.

Benzerga *et al.* 1999 compares the hereabove described Leblond-Perrin model coupled with a localization criterion and three models coupled with Thomason's criterion. The first one is a simple law with fixed porosity and perfect plasticity which uses Rice and Tracey's assumptions to model void shape modifications. The second one is the classical Gurson's model with spherical voids and the third one, proposed by Gologanu *et al.* 1994, takes void shape into account. Some conclusions from Benzerga *et al.* 1999 are now summarized.

For highly clean materials ($f_0 < 0.01\%$), the onset of coalescence (f_{cr}) is almost independent of the stress state for mean to high triaxiality ($T>1.5$); however for higher initial porosity, the dependence is not negligible (Figure 4-14). This figure

helps to understand why, depending on the studied cases, authors like Koplik & Needleman 1988, Brocks *et al.* 1995, Brethenoux, *et al.* 1997 ... have concluded to different influence of triaxiality on the critical porosity.

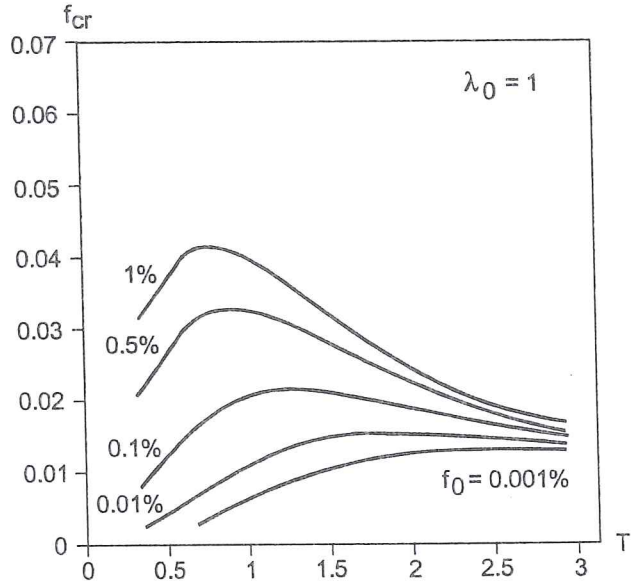

Figure 4-14 Critical porosity-triaxiality curve according to Thomason's criterion and Gurson's model (from Benzerga *et al.* 1999).

The coalescence models predict a drastic effect of void distribution (λ_0) on the critical porosity (Figure 4-15), as already checked on Figure 4-2 from Koplik & Needleman 1988. High λ_0 means that porous layers are separated by large sound layers.

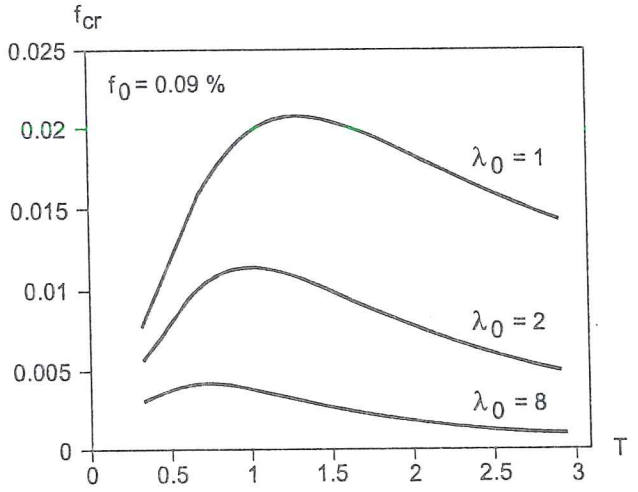

Figure 4-15 Critical porosity-triaxiality curve according to Thomason's criterion and Gurson's model for various initial void distributions (from Benzerga *et al.* 1999).

For initial spherical voids, the assumption of spherical void growth leads to underestimate both critical porosity f_{cr} and strain at coalescence. However, for high triaxiality ($T=3$), frequently encountered at a blunted crack tip in plane strain conditions, the void shape evolution has little effect. The effect of inclusion morphology appears to be negligible at high triaxiality ($T=10/3$) but crucial for low triaxiality.

To complete this section about microscopic phenomena analysis, one cannot forget the work at the atomic level. Using massive parallel computers, scientists like Abraham 1996 use *molecular dynamics simulation technique* to learn about fracture process in ductile or brittle materials. This technique is based on the motion of a given number of atoms governed by their mutual interatomic interactions described by continuous interatomic potentials. It requires the numerical integration of Hamilton's equation of motion. For instance, Abraham models the fracture of two-dimensional notched solids under tension using a million of atoms. Even if his results such as the order of magnitude of the fracture strain or the crack tip speed do not agree with experimental values, ductile or brittle fractures are effectively reproduced. Such approaches are still far from producing macroscopic fracture criteria, but help to understand fracture events more deeply. As developed by Ceder 1999, the gap between time scale and length scale of atomistic level (10^{-13} sec, 10^{-10} m) to macroscopic properties (10^{4} sec, 1 m) can only be overcome with knowledge of the relevant phenomena at each scale. According to Ceder's point of view, even if practical results of atomistic computations can already be presented in the designing of rechargeable Lithium batteries, the field of mechanical properties seems to need further investigation.

4.5. Criteria issued from fracture mechanics

Presenting the links between continuum damage mechanics and fracture mechanics was one aim of the Symposium on "Continuous Damage and Fracture" (Benallal, 2001) held in Cachan on October 2000 to celebrate Professor Jean Lemaître's 66th birthday. Such a symposium underlines the connections between these two fields that are now of common use not only in the academic world but also in the industry. For instance, Mudry 2000 has given practical examples in his presentation.

Chaouadi 1996 from Katholieke Universiteit Leuven, Marchal 1997, Pardoen 1998 from Université Catholique de Louvain, and Wilsius 1999 from Université des Sciences et Technologie de Lille are Ph.D. theses that cover fracture mechanics, continuum damage ductile fracture models and important experimental work. Their state-of-the-art summaries of fracture mechanics are used here to present its general concepts, then to underscore the interest of its coupling with continuum damage mechanics.

4.5.1. Fracture Mechanics

Materials possess a fracture resistance, which is an intrinsic property. Fracture propagation occurs when the loading imposed to the crack exceeds the material fracture resistance. As presented on Figure 4.16, a crack can experience three loading modes or a combination of these modes.

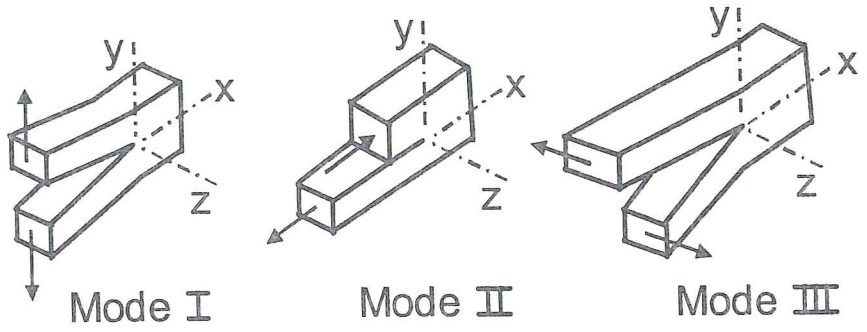

Figure 4-16 Fracture modes; mode I: opening mode, mode II: sliding mode, mode III: tearing mode (from Chaouadi 1996).

In practice, mode I is the most severe. Typical stress-strain zones appear at the crack tip in a finite cracked specimen; they are represented on Figure 4-17.

Linear elastic fracture mechanics is shown on Figure 4-17a. For mode *I*, the stress and strain fields near the crack tip are defined by:

$$\underline{\sigma} = \frac{K_I}{\sqrt{2\pi r}}\underline{\tilde{\sigma}}(\theta) \qquad \underline{\varepsilon} = \frac{K_I}{\sqrt{2\pi r}}\underline{\tilde{\varepsilon}}(\theta) \tag{4-27}$$

where r and θ are the polar coordinates, with r the distance from the crack tip and θ the angle relative to the crack plane, $\underline{\tilde{\sigma}}(\theta)$ and $\underline{\tilde{\varepsilon}}(\theta)$ are functions, dependent on the angle θ. Similarly, the same expressions can be obtained for mode *II* and *III*. That means that one parameter, the stress intensity factor K, is sufficient to determine the material stress or strain field near the crack tip. The critical condition for fracture corresponds to a critical value of stress intensity factor, K_{IC} for mode *I*. This parameter is related to G, the energy released per unit extension of crack front per unit thickness of the body, also called crack extension force:

$$G = \frac{K_I^2}{E} \text{ (plane stress)} \qquad G = \frac{K_I^2}{E(1-\nu^2)} \text{ (plane strain)} \tag{4-28}$$

The stress and strain distributions ahead of a crack are similar for any geometry and loading provided similar K are reached. This is true when small scale yielding prevails: the plastic zone is very small compared to the geometrical dimensions. Such situations are found in brittle materials or for very low load levels.

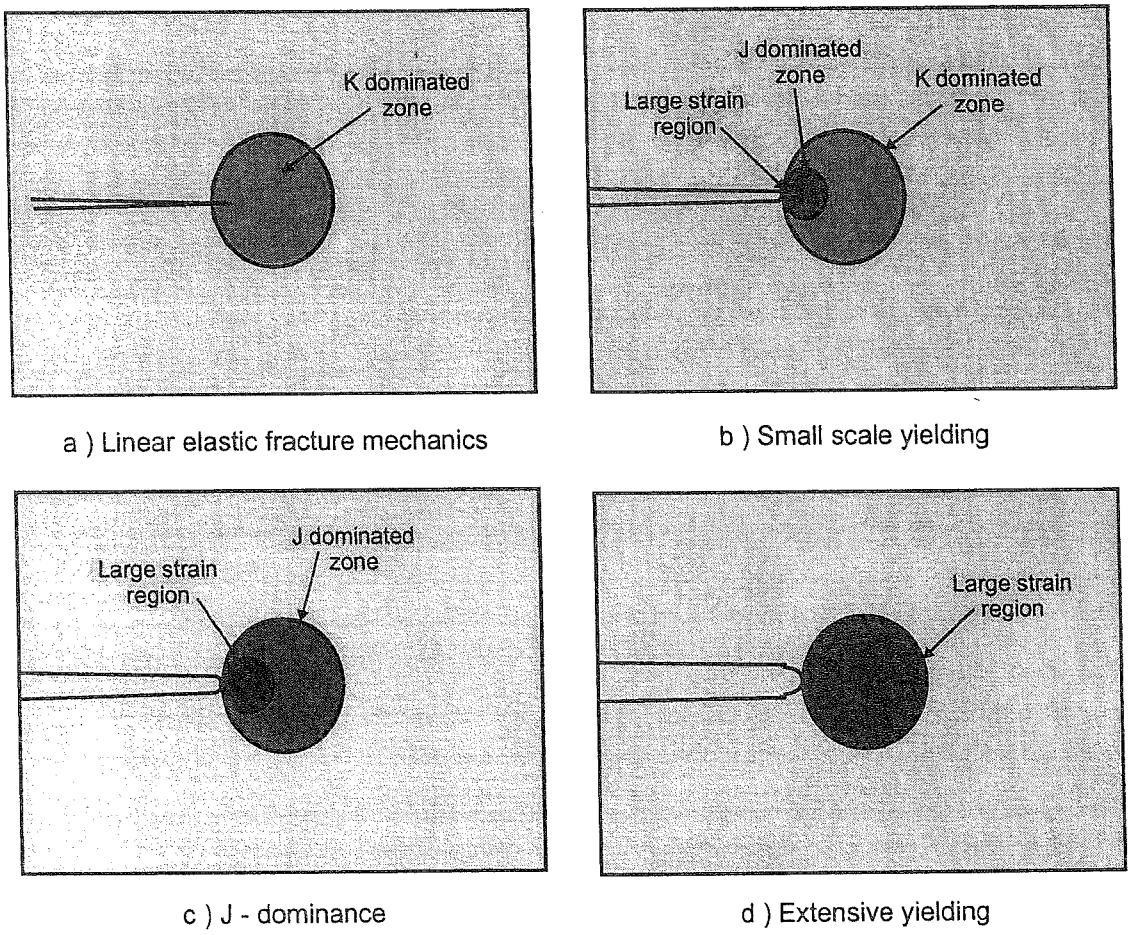

Figure 4-17 Typical stress-strain zones at the crack tips for different types of material (from Anderson 1995).

When working with *elastic plastic fracture mechanics*, the *J*-integral parameter appears. Rice 1968 defines the *J*-integral for non-linear elastic material by:

$$J = \int_{\Gamma} \left(W dy - T_i \frac{\partial u_i}{\partial x} \right) ds \qquad (4\text{-}29)$$

where $W = \int_0^{\varepsilon_{ij}} \sigma_{ij}\, d\varepsilon_{ij}$ is the strain energy density, u_i are the components of the displacement vector, n_j is the component j of a unit vector perpendicular to the contour line, Γ is the path followed in anti-clockwise direction, $T_i = \sigma_{ij} n_j$ are the components of the normal stresses acting at the boundaries, x, y and s coordinates are defined on Figure 4.18. Rice derived this parameter from a non-linear elastic material, so its application to elastic-plastic material assumes radial loading without unloading.

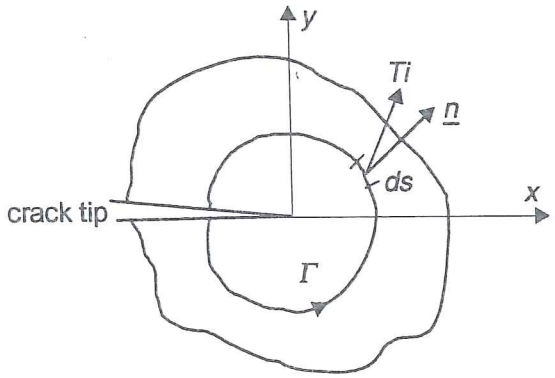

Figure 4-18 *J*-integral evaluation along an arbitrary contour (from Chaouadi 1996).

The interesting properties of *J*-integral are:

- *J*-integral is path independent except very near the crack tip.
- *J* can be interpreted as a pseudo energy release rate. *J* should be considered as the difference of the energies absorbed by 2 specimens with crack sizes a and $a+\Delta a$ loaded up to a given displacement u rather than as the variation of the potential energy of the sample for an increment of crack advance (see Figure 4-19).

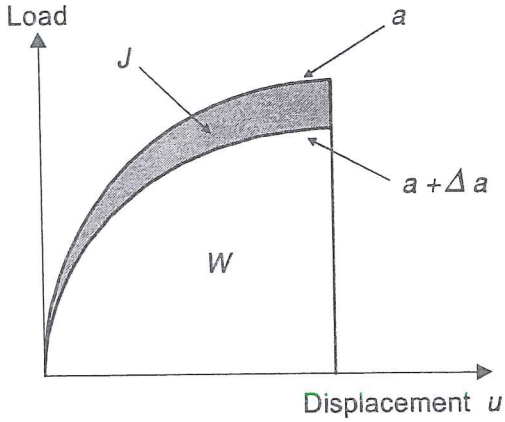

Figure 4.19 Energy release rate interpretation of *J* (from Pardoen 1998).

- The stress and strain fields ahead of a crack tip can be represented by functions known as the HRR fields. These relations due to Hutchinson 1968 and Rice & Rosengren 1968 use material constants such as the yield stress and strains, *J*-integral and dimensionless functions tabulated by Shi 1983. The HRR (Hutchinson-Rice-Rosengren) singularity fields define the stress and the strain fields ahead of a crack tip for loading levels such that the plastic zone size is small in comparison to the specimen dimension (see Figure 4-17b). HRR fields are accurate in the *J* dominated zone except very near the crack tip (large strain zone). This means that the fields in crack tip region are independent on specimen geometry and loading type.

Since World War II, testing standards to measure fracture toughness have been established (see ASTM, American Society for Testing and Materials, and ESIS, European Structural Integrity Society). Wilsius 1999 summarizes the methods generally applied to measure J and Figure 4-20 presents sample geometries commonly used. In small scale yielding situations, where the plastic zone does not influence the elastic stress field, J-integral is equal to G and relation (4-28) directly gives the link between J-integral and K stress intensity factor.

The case shown on Figure 4-17c presents a large plastic zone with respect to specimen dimension. In such a case, the geometry can induce a highly constrained crack, corresponding to high stress triaxiality near the crack tip. In this condition, the HRR fields still apply. So J-integral alone still suffices to characterize the stress and strain fields in the zone called "J-dominance".

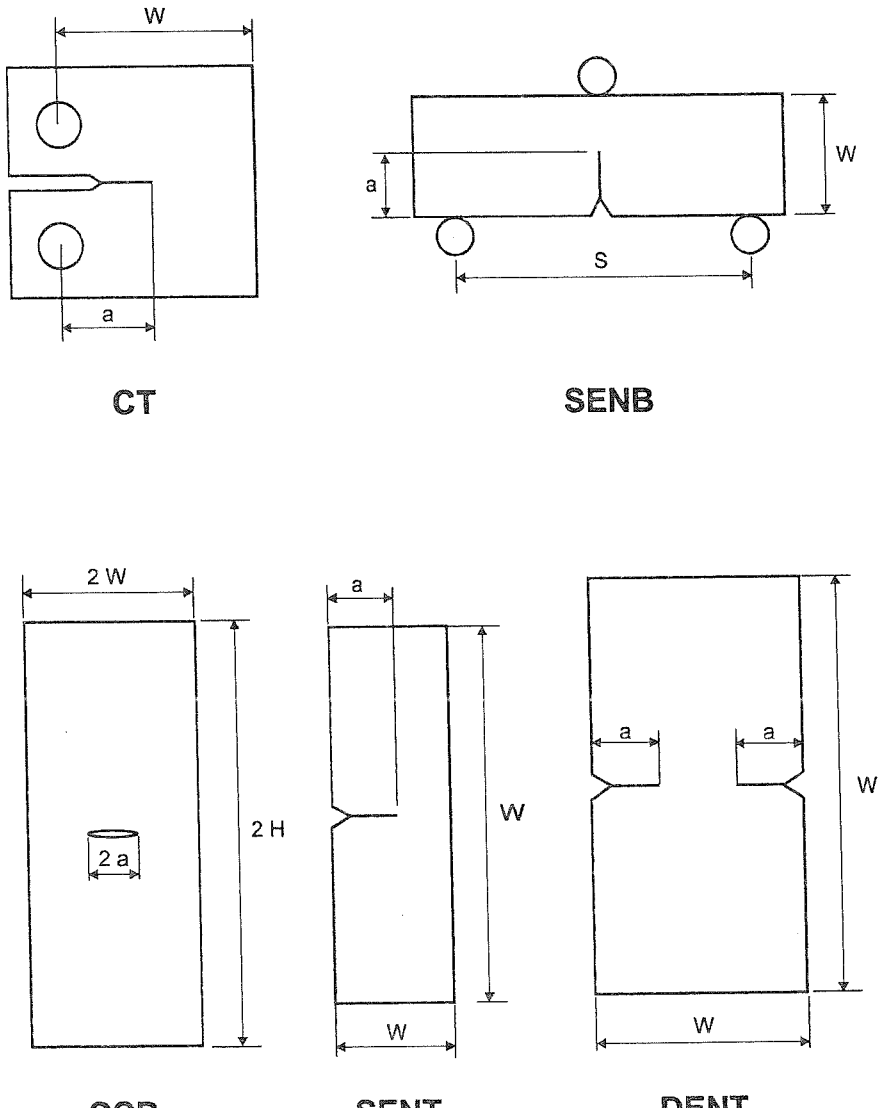

Figure 4.20 Fracture samples used to characterize fracture toughness estimated by J-integral (from Wilsius 1999).

For less constrained crack, Figure 4-17d shows an extensive finite strain region at the crack tip. In this case, J-integral alone cannot characterize univocally the stress and strain fields anymore because they exhibit size and geometry dependence.

Brocks *et al.* 1995 underlines the geometry dependence of the toughness results:

$$J_{CCP} \geq J_{DENT} \geq J_{SENT} \geq J_{SENB} \geq J_{CT} \tag{4-30}$$

where the geometries CCP, DENT, SENT, SENB and CT are defined of Figure 4-20. So additional parameters are required to characterize the fracture; common choices are either Q parameter or T parameter. Q is the difference field between a FEM solution and a reference field (HRR field for instance). T characterizes the stress conditions, including specimen geometry effect, on stress triaxiality under well contained yielding. Wilsius 1999 reviews the determination methods of T and Q.

The thickness of engineering structures is usually larger than the size of the laboratory samples with which the fracture toughness is determined. When J uniquely characterizes the crack tip field in specimen and structure, the onset of crack initiation can be identified, when one reaches a same critical value J_{IC}. However, in other cases, different fracture toughness values appear between specimen and real piece, so additional parameters are required. This leaves a field where fracture mechanics and continuum mechanics can cooperate.

4.5.2. Continuum damage mechanics criteria imbued from fracture mechanics

Considering fracture mechanics where critical values of J-integral or K stress intensity factor determine fracture occurrence, the concept of critical energy as an intrinsic property of the material appears. A lot of authors, such as Lemaître 1986, Rabier 1989, Chaboche 1988, Bruhns & Schiesse 1996, use a critical value of the elastic energy release rate, often called Y in the damage models (see section 3.2.2) as fracture criterion.

Another example is given by Chaouadi's 1996 work devoted to the fracture of steels for reactor pressure vessels in the ductile regime. Like many other scientists (Cotterel & Reddel 1977, Atkins & Mai 1985, Knockaert *et al.* 1996), Chaouadi proposes an energy criterion. He first validates it using notch experiments, then applies it to predict crack toughness data, in cases where experiments are not possible. He assumes that the total energy is a constant at rupture. Neglecting the elastic part, this energy consists in two terms: the plastic strain work and the void expansion work. This latter damage energy is simply evaluated by the hydrostatic stress multiplied by the hydrostatic strain related to Rice & Tracey's relation (4-22). This gives:

$$W^t = \int_0^{\varepsilon} \sigma_{eq}\, d\varepsilon_{eq}^p + 3A\sigma_m\, exp(\frac{3}{2}\frac{\sigma_m}{\sigma_{eq}})\, d\varepsilon_{eq}^p \tag{4-31}$$

where A is a "constant" reflecting the particle distribution in the material, it can be replaced by a statistical distribution. Numerous comparisons with tensile experiments on notched tests show that a critical value of W^t, independent of the sample geometry or the stress triaxiality appears. So this critical energy is an intrinsic material property. To reach this conclusion, Chaouadi has introduced a critical length: a distance over which the energy should reach its critical value to initiate the crack. The evaluation of this distance shows that it is always larger than the blunting affected region. A correlation between W^t and J-integral is established with the objective to define fracture toughness derived from the tensile test. In practice, the size of irradiated samples available from nuclear power plants does not allow valid toughness measurements and Chaouadi's approach, using total energy, allows extrapolating reasonable values.

Pardoen 1998 proposes another thesis using both fracture mechanics and continuum damage mechanics. He works on cold-drawn copper bars of 10 or 20 mm diameter and studies two states of the material: the As-Received state, called "CuAR" and the annealed state, called "CuA". He reaches J-integral by means of tensile tests on circumferentially cracked bar (CBR) geometries, which is an approach not yet standardized. He finds that for CuAR material, the J-integral is valid (path independent) and dominant (no constraint effects) until cracking, in spite of large scale yielding. However for CuA material, which is very ductile, even if CRB geometry provides highly constrained fracture, path independence of J-integral is not valid. Pardoen checks that the J-Q approach cannot be applied in this case. So, fracture mechanics does not provide an efficient way to predict fracture. To solve this problem, Pardoen, as Chaouadi, tries to find an energy criterion with success. He assumes that the work density spent in the Fracture Process Zone (FPZ) until crack initiation is a material constant. Broberg 1975 has proposed the occurrence of a physical uncoupling between an "essential" work for fracture, consumed in a crack tip zone (FPZ), and a "non-essential" work, dissipated around FPZ. This means that the FPZ zone is defined more precisely as the smallest zone where specific work until fracture is constant, independent of specimen geometry. Marchal's 1997 thesis particularly investigates and develops the "essential" work of fracture. In Pardoen's thesis, the FPZ is assumed to cover the major part of the ligament area in deeply cracked specimens CuA or, in other words, all work spent in the test would be "essential". Numerical simulations and experiments confirm this assumption and the efficiency of this energy criterion to predict fracture for different sizes of specimen.

The last example presented here is Wilsius 1999. This thesis proposes a synthesis of criteria to detect rupture and a practical introduction to fracture mechanics, which summarizes not only the theory but also the methods to measure introduced variables. Wilsius studies three materials with very different volume fraction of inclusions: a CMn steel with welding, an aluminum alloy 2024 T351 and a NiCr 12 NC6 steel. Classical fracture tests to determine toughness and classical tensile tests to reach material behavior are performed. Three different models are applied to simulate toughness tests:

- a rigid plastic von Mises' approach coupled with Rice & Tracey's criterion (see relation 4.22);
- Rousselier's model (see section 3.2.3);
- Gurson-Tvergaard-Needleman (see Chapter 2).

To reach a good simulation of fracture tests, Wilsius shows that the mesh size at the crack tip is an important parameter. The set of material parameters describing material behavior and enabling to recover the curve "*J*-integral versus fracture opening" strongly depends on this information. The fracture criteria used to simulate the fracture development are either Rice & Tracey's criterion or a critical value of the damage parameter. These simulations also require the use of a characteristic length (different from the element size) where the criterion is fulfilled to determine crack propagation. This research shows that continuum damage mechanics can reproduce the curves measured in fracture mechanics.

4.5.3. Summary of links between Fracture Mechanics and Continuum Damage Mechanics

Energy criteria suggested by fracture mechanics are interesting to use in continuum mechanics. For ductile rupture with large plastic zone, the critical value of one parameter proposed by fracture mechanics cannot provide a solution to detect fracture anymore. So, a continuum damage approach can complete fracture mechanics to find efficient ways to predict fracture in these cases.

Note that an important feature appears in this section: a material length scale. The critical density energy or the critical damage value must be reached not at a single point but in a zone to induce crack propagation. This feature seems logical when one looks at numerical simulations near the crack tip with refined finite elements. Such refined simulations are necessary if one intends to study crack propagation, as cracks introduce singularities in the stress and strain fields at a very small length scale.

The rupture criteria described in previous sections were more dedicated to the detection of the initiation of rupture, which explains why this length scale did not so clearly appear.

References

Abraham F.F. (1996) Parallel molecular dynamics investigation fracture. *Computer simulation in materials science*, Kluwer Academic Publishers, 211-226.

Arrieux, R. (1990) Détermination théorique et expérimentale des courbes limites de formage en contraintes, Thèse de docteur d'état en sciences, Institut national des sciences appliquées de Lyon et l'université Claude Bernard Lyon I.

Anderson, T.L. (1995) Fracture Mechanics – Fundamentals and Application, CRC Press, Boca Raton.

Atkins, A.G. (1981) Possible explanation for unexpected departures in hydrostatic tension-fracture strain relations. *Metal Sci*, **15**, 81-83

Atkins, A.G., Mai, Y.W., (1985) Elastic and Plastic Fracture, Ellis Horwood Limited, Chicheester, England.

Banabic, D. (1996) Forming limit diagrams predicted by using the new Hill's yield criterion, *Proceedings of the 3rd Int. Conf. Numisheet' 96 Numerical Simulation of 3-D Sheet Metal Forming Processes – Verification of Simulations with Experiments*, ed. Lee, Kinzel, Wagoner, the Ohio State University.

Barata da Rocha, A., Barlat, F., Jalinier, J.M. (1984) Prediction of the forming limit diagrams of anisotropic sheets in linear and non-linear loading, *Mat. Sci. Eng.*, **68**, 151-164.

Barata da Rocha, A. (1985) Mise en forme des tôles minces, instabilité plastique, anisotropie et endommagement, Thèse de Doctorat, Institut National Polytechnique de Grenoble.

Bauvineau, L. (1996), Approche locale de la rupture ductile: application à un acier au carbone –manganèse, Thèse de Doctorat, Ecole Nationale Supérieures des Mines de Paris.

Benallal, A., (2000), Continuous Damage and Fracture, Elsevier.

Benzerga, A., Besson, J., Pineau, A. (1999) Coalescence-controlled anisotropic ductile fracture. *J. of Eng. Mat. & Techn.* (soumis pour publication).

Boudeau, N., Gelin, J.C. (1992) Finite element simulation of the ductile fracture in 3-D sheet metal forming process, *Journal of Materials Processing Technology*, **32**, 521-530.

Boudeau, N., Gelin, J.C. (1994) Prediction of the localized necking in 3D sheet metal forming processes from FE simulations. *J. of Materials Processing Technology*, **45**, 229-235.

Boudeau, N., (1995) Prédiction des instabilités élasto-plastiques. Application à l'emboutissage, Ph. D. Thesis, Université de Franche – Comté, France.

Boudeau, N., Gelin, J.C. (1996a) Post-processing of finite element results and prediction of the localized necking in sheet metal forming, *J. of Materials Processing Technology*, **60**, 325-330.

Boudeau, N.,Salhi, S., Gelin, J.C. (1996b), Necking in sheet metalforming, prediction from finite element simulations and computations based on crystalline plasticity, *NUMISHEET 96 Numerical Simulation of 3-D Sheet Metal Forming Processes – Verification of Simulations with Experiments,* ed. Lee, Kinzel, Wagoner,,the Ohio State University.

Boudeau, N., Gelin, J.C., Salhi, S. (1998) Computational prediction of the localized necking in sheet forming based on microstructural material aspects, *Computational Materials Science*, **11**, 45-64.

Boudeau, N., Lejeune, P., Gelin, J.C. (2001) Damage in sheet metal forming : prediction of necking phenomena, *Journal of Finite Elements*, Hermes, to appear.

Boyer, J.C., Staub, C., (1997) A ductile damage model including shear stress effects. *Advanced Methods in Materials Processing Defects*, Predeleanu, M., & Gilormini, P., Eds Elsevier, 13-22.

Brethenoux, G., Mazataud, P., Bourgain, E., Muzzi, M. & Giusti, J. (1997) A mesoscopic approach of ductile damage during cold forming processes, *Advanced Methods in Materials Processing Defects*, Predeleanu, M., & Gilormini, P., 23-32.

Broberg, K.B. (1975) On stable crack growth, *J. Phys. Mech. Solids* **23**, 215-237.

Brocks, W., Sun, D.Z., Honig, A. (1995) Verification of the transferability of micromechanical parameters by cell model calculations with visco-plastic materials, *Int. J. Plasticity*, **11-8**, 971-989.

Brown, L.M. , Embury, J.D. (1973) The initiation and growth of voids at second phase particles. *Proceedings of the 3rd Int. Conf. on the Strength of Metals and Alloys, ICSMA3*, Cambridge, England, 164-169.

Brozzo, P. de Luca, B. & Rendina, R. (1972) Eine neue Methode zur Vorhersage der Umformbarkeit von Metallfeinblechen. *Proc. 7th Biennial Congress IDDRG*, 9-13.Cayssials, F. (1998) A new method for predicting FLC, *IDDRG, Conference Geneval*, Brussel 6/98.

Bruhns, O.T., Schiesse, P. (1996) A continuum model of elastic-plastic materials with anisotropic damage by oriented microvoids. *Eur. J. Mech. A/Solids*, **15-3**, 367-396.

Brunet, M., Mguil-Touchal, S., Morestin, F. (1997) Numerical and experimental analysis of necking in 3D sheet forming processes using damage variable, *Advanced Methods in Materials Processing Defects*, Predeleanu M. & Gilormini P. Eds, 205-214.

Brunet, M., Mguil-Touchal, S., Morestin, F. (1998) Analytical and experimental studies of necking in sheet metal forming processes, *J. of Materials Processing Technology*, **80-81**, 40-46.Cayssials, F., (1999) The new version of the Sollac model, *Working Group of the IDDRG 99*, Birmingham.

Cayssials, F. (1998) A new method for predicting FLC, IDDRG, Conference Geneval, Brussel 6/98.

Cayssials, F., (1999) The new version of the Sollac model, Working Group of the IDDRG 99, Birmingham.

Ceder G. (1999) Designer materials, *Res metallica'99*, Chair Framework Agreement, KUL, MTM-Bekaert, Sidmar, Union Minière.

Chaboche, J.L., (1988a) Continuum damage mechanics. Part I – General concepts, *J. Appl. Mech.*, **55**, 59-64.

Chaboche, J.L., (1988b) Continuum damage mechanics. Part II – Damage growth, crack initiation, and crack growth, *J. Appl. Mech.* **55**, 65-72.

Chiou, J.M. (1996) A study of ductile damage in metal forming. Ph. D. thesis, the University of Birmingham.

Chaouadi, R. (1996), Micromechanically based damage modelling of crack initiation in reactor materials, Ph. D. Thesis Katho. Universiteit Leuven.

Cockroft, M.G. & Latham, D.J. (1968) Ductility and the workability of metals, *J. Inst. Met.*, **96**, 33-39.

Cotterell, B., Reddel, J.K., (1977) The essential work of plane stress ductile fracture. *Int. J. Fract.* **13**, 267-277.

Doege, E., Bagaviev, A. & Dohrmann, H. (1997) Formability analysis based on the anisotropically extended Gurson model, *Advanced Methods in Materials Processing Defects*, Predeleanu, M. & Gilormini P., 281-288.

Doghri, I. Billardon, R.(1995), Investigation of localization due to damage in elasto-plastic materials, *Mechanics of Materials,* **19**, 129-149.

Eckstein, A., Basar, Y. & Konke, C. (1997) Damage analysis of ductile metallic shells. Computational plasticity – *Fundamentals and Applications*, Owen, D.R.J, Onate, E. Hinton, E., editors, CIMNE, Barcelona.

Esche Sven K, Kinzel Gary L., Altan, T. (1996) Review of failure analysis in sheet metal forming simulations. *Proceedings of the 3rd Int. Conf. Numisheet' 96 Numerical Simulation of 3-D Sheet Metal Forming Processes – Verification of Simulations with Experiments*, ed. Lee, Kinzel, Wagoner, the Ohio State University.

Freudenthal, A.M. (1950) The inelastic behaviour of engineering materials and structures, John Wiley & Sons, New-York.

Gologanu, M., Leblond, J.B., Devaux, J. (1994) Numerical and theoretical study of coalescence of cavities in periodically voided solids, *Computational Material Modeling, ASME*, AD-vol. **42/PVP**-Vol. 294.

Gosh, A.K., (1976) A criterion for ductile fracture in sheets under biaxial loading, Metallu. Trans. , **7A**, 523-533.

Habraken, A.M., Radu, J.P., Duchêne. L., Wauters, M. (1998) Simulation of Materials processing : Theory, methods and Applications, *Proceedings of the sixth international conference on numerical methods in industrial forming processes – Numiform '98, June*, Huétink, J., Baaijens, F.P.T., Balkema, A.A., Eds.

Hill, R. (1950) *The Mathematical Theory of Plasticity*, Clarendon Press, UK.

Hiwatashi, S., Van Bael, A., Van Houtte, P., Teodosiu, C. (1998) Prediction of forming limit strains under strain-path changes : application of anisotropic model based on texture and dislocation structure. *Int. J. of Plasticity*, **14-7**, 647-669.

Hoferlin, E., Van Bael, A., Hiwatashi, S., Van Houtte, P. (1998) Influence of texture and microstructure on the prediction of forming limit diagram, *19th RISO Symposium on Materials Science*, 7-11 Sept. 1998.

Hora, P., Tong, L., Reissner, J. (1996) A prediction method for ductile sheet metal failure in f.e. simulation, Proceedings of the 3rd Int. *Conf. Numisheet' 96 Numerical Simulation of 3-D Sheet Metal Forming Processes – Verification of Simulations with Experiments*, ed. Lee, Kinzel, Wagoner, the Ohio State University.

Hutchinson, J.W. (1968) Singular behaviour at the end of a tensile crack in a hardening material, *J. Mech.A/Solids*, **16**, 13-31.

Knockaert, R., Doghri, I., Marchal, Y., Pardoen, T., Delannay (1996) Experimental and numerical investigation of fracture in double-edge notched steel plates. *Int. J. Fract.* **81**, 383-399.

Knockaert, R. (2001), Etude expérimentale et numérique de la localisation de la déformation lors de la mise en forme de produits minces, Thèse de Doctorat, Ecole Nationale Supérieure des Mines de Paris, Sophia Antipolis.

Koplik, J., Needleman, A. (1988) Void growth and coalescence in porous plastic solids. *Int. J. Solids Structures*, **24-8**, 835-853.

Komori, K. (1998) Simulation of chevron crack in drawing : effect of parameter in fracture criterion, *Simulation of Materials Processing: Theory, Methods and Applications*, Numiform, Huetink & Baaijens Eds, Balkema.

Leblond, J.B., Perrin, G. (1991) Analytical study of the coalescence of cavities in ductile fracture of metals, *Plasticity 3rd Symposium*, 233-236.

Leblond, J.B., Perrin, G., Devaux, J. (1995) An improved Gurson-type model for hardenable ductile metals, *Eur. J. Mech. A/Solids*, **14**, 499-527.

Lemaître, J. (1985) Coupled elastoplasticity and damage constitutive equations, *J. Comp. Meth. in Appl. Mech. and Eng.* **51**, 31-49.

Lemaître, J. (1986), Local approach of fracture, *Eng. Fracture Mech.*, **25**, 523-537.

Marchal, Y. (1997), Mechanics and Physics of the ductile fracture of thin plates, Thèse de doctorat, Université de Louvain-La-Neuve.

Marciniak, Z., Kuczynski, K., (1967) Limit strains in the processes as stretch-forming sheet metal, *Int. J. Mech. Sci.*, **9**, 609-620.

Marini, B., Mudry, D., Pineau, A. (1985), Experimental study of cavity growth in ductile rupture, *Eng. Fracture Mech.*, **22/6**, 989-996.

Narasimhan, K., Wagoner, R.H. (1991) Finite element modeling simulation of in-plane forming limit diagrams of sheets containing finite defects. *Metallurgical Transaction A*, 22A, 1991, 2655.

Needleman, A., Tvergaard, V. (1984) An analysis of ductile rupture in notched bars, *J. Mech. Phys. Solids*, **32**, 461-490.

Mudry, F.(2000), Some examples of the use of continuous damage and fracture mechanics in the steel industry, *Continuous Damage and Fracture*, Benallal, A, editor, Elsevier.

Pardoen, T. (1998) Ductile fracture of cold-drawn copper bars : experimental investigation and micromechanical modelling, Doctorat en sciences appliquées, Université de Louvain-La-Neuve.

Oh, S.I., Chen, C.C. & Kobayashi, S. (1979) Ductile fracture in axisymmetric extrusion and drawing. *J. Eng. Ind. Trans. ASME*, **101**, 36-44.

Oyane, M. (1972) Criteria of ductile fracture strain. *Bull. Jpn. Soc. Mech. Eng.*, **15**, 1507-1513.

Picart, P., Piechel, G. & Oudin, J. (1997) Damage influence in the finite element computations for large strains elastoplastic mechanical structures, *Advanced Methods in Materials Processing Defects*, Predeleanu, M. & Gilormini, P., Eds. Elsevier, 175-184.

Pineau, A. (1981) Review of fracture micromechanisms and a local approach to predicting crack resistance in low strength steels., *Advances in Fracture Research*, Pergamon Press, 553-577.

Qiu, Y., Neale, K.W., Makinde, A., MacEwen S.R. (1995) Numerical modelling of metal formability using polycrystal plasticity, *IDDRG Genval*, juin 1998.

Rabier, P. J. (1989) Some remarks on damage theory, *Int. J. Engng. Sci.*, **27**, 29-54.

Rice, J.R. (1968) A path independent integral and the approximate analysis of strain concentration by notches and cracks, *J. Appl. Mech.*, **35**, 379-386.

Rice, J.R. , Tracey, D.M. (1969) On the ductile enlargement of voids in triaxial stress fields, *J. Mech. Phys. Solids*, 17, 201-217.

Rice, J.R., Rosengren, G.F. (1968), Plane strain deformation near a crack tip in a power-law hardening material, *J. Mech. Phys. Solids,* **16**, 1-12.

Rousselier, G., Devaux, J.C., Mottet, G., Devesa, G. (1989) A methodology for ductile fracture analysis based on damage mechanics : an illustration of a local approach of fracture, *Nonlinear Fracture Mechanics : vol. II – Elastic-Plastic Fracture, ASTM STP 995,* J.D. Landes, A. Saxena, J.G. Merkle Eds, American Society for Testing and Materials, Philadelphia, 332-354.

Rudnicki, J.W., Rice, J.R. (1975) Conditions for the localization of deformation in pressure-sensitive dilatant materials, *J. Mechs. Phys. Solids*, **23**, 371-394.

Shi, C.F. (1983) Tables of Hutchinson-Rice-Rosengren singular field quantities, *Report MRL E-147,* Brown University.

Sowerby, R., Duncan, J.L. (1971) Failure in sheet metal in biaxial tension, *Int. J. Mech. Sci.*, **13**, 217-229.

Storen, S. & Rice, J.R. (1975) Localized necking in thin sheets, *J. Mech. Phys. Solids*, **23**, 421-441.

Thomason, P.F. (1985a) Three-dimensional models for the plastic limit-load at incipient failure of the intervoid matrix in ductile porous solids, *Acta Metall.*, **33**, 1079-1085.

Thomason, P.F. (1985b) A three-dimensional model for ductile fracture by the growth and coalescence of microvoids, *Acta metall.*, **33**, 1087-1095.

Thomason, P.F. (1990) Ductile fracture of metals, Pergamon Press.

Thomason, P.F. (1993) Ductile fracture by the growth and coalescence of microvoids of non uniform size and spacing, *Acta Metall. Mater*, **41-7**, 2127-2134.

Tvergaard, V. (1982) Material failure by void coalescence in localized shear bands, *Int. J. Solids & Struct.* **18**, 659-672.

Vacher, P., Arrieux, R., Tabourot, L. (1998) Analysis of a criterion of deep drawing operation capability for thin orthotropic sheets, *Journal of Materials Processing Technology*, **78**, 190-197.

Vegter, H., An Y., Pijlman H.H., Carlee B.D., Huetink J. (1998), Advanced material models in simulation of sheet forming processes and prediction of forming limits, *1st ESAFORM Conference on Material Forming*, Sophia Antopolis, Eds. Chenot, Agassant, Montmitonnet, Vergnes, Billon.

Vegter, H., An Y., Pijlman H.H., Huetink J. (1999), Different approaches to describe the plastic material behaviour of steel and aluminium-alloys in sheet forming, *2nd ESAFORM Conference on Material Forming*, Guimaraes, Portugal, Covas J.A. Ed.

Wilsius, I., (1999) Etude expérimentale et numérique de la déchirure ductile basée sur des approches locales en mécanique de la rupture. Ph. D. Thesis Université des Sciences et Technologie de Lille.

Wu, P.D., Neale, K.W., Van Der Giessen, E. (1998) Effects of strain paths on sheet metal limit strains, Material Instabilities in Solids, John Wiley & Sons Ltd, de Borst R. & Van der Giessen EK, Eds.

Zhou, Y., Neale, K.W. (1995) Prediciotns of Forming limit Diagrams using a rate sensitive crystal plasticity model, *Int. J. Mech. Sc.*, 37-1, 1-20.

Zhu, Y.Y. (1992) Contribution to the local approach of fracture in solid dynamics, Ph. D. thesis, University of Liège, MSM Department .

Zhu, Y.Y., Cescotto, S. and Habraken, A.M. (1992) A fully coupled elastoplastic damage modeling and fracture criteria in metalforming processes, *J. of Mater. Processing Technology* **32**, 197-204.

5. MESH DEPENDENCE IN DAMAGE MODELING

5.1. Introduction

To model the behavior of a structure or a specimen up to rupture, a descending branch in the stress-strain curve is introduced, at a generic stage of the deformation process, to simulate the loss of load-carrying capacity at progressive straining. Examples of such models applied to ductile metals were given in Chapters 2 and 3; however this approach also appears in soils or more brittle materials like concrete, polymers, ceramics, ... So, the global answer, "load-deflection curve", is translated into local description by a "softening" stress-strain relation.

A mathematical consequence of such softening models is that, at certain threshold levels of loading, in the static case, the governing differential equations locally lose their elliptic character. In the dynamic case, a change of the hyperbolic equations into an elliptic set is typically observed. Consequently, the boundary or initial value problem becomes ill-posed and analytical as well as numerical solutions become meaningless. For instance, the numerical solution appears to be fully determined by the refinement and the direction of the mesh discretization. For instance, de Vree *et al.* 1995 apply a simple elastic isotropic model of local damage to a square plate with a central hole. This plate is supported along one side and a prescribed displacement is defined along the opposite side. Because of symmetry, only the upper right quarter of the plate is discretized with 5 different meshes (Figure 5.1).

Figure 5-1 Meshes for the quarter plate (from de Vree *et al.* 1995).

The results of the local damage approach are clearly mesh dependent as shown by the force-displacement curves presented on Figure 5.2.

Typical differences in the distributions of the damage variable determined by a coarse and a refined mesh are visualized on Figure 5.3. Mesh refinement leads to

a vanishing energy dissipation and the deformation localizes in an zone of decreasing volume.

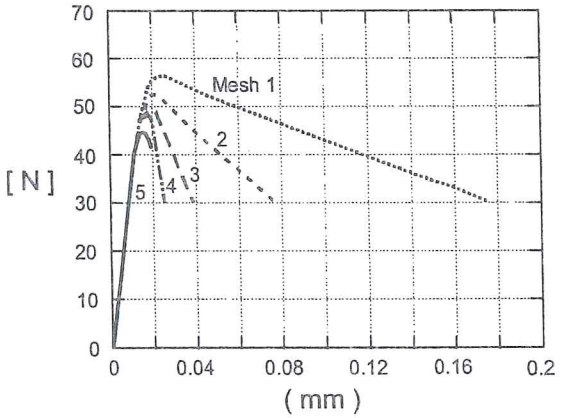

Figure 5-2 Force- displacement curves, local damage model (from de Vree *et al.* 1995).

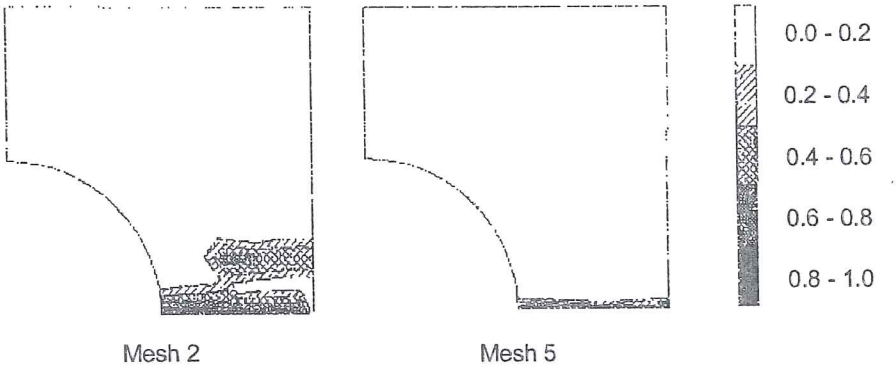

Figure 5-3 Damage distribution, local damage model (from de Vree *et al.* 1995).

Starting in the early 1980s, a tremendous amount of activity has been devoted to remedying this deficiency of the standard continuum approach.

A good review of all possible solutions was proposed by de Borst *et al.* 1998 and presented for instance during de Borst's 1999 plenary lecture at the 5th United States National Congress on Computational Mechanics; or one can also read the review by Desoyer 1995. Both authors underline that softening materials can predict strain localization, which in most engineering materials precedes failure by the emergence of narrow zones of intense straining. For rate insensitive materials, localization is interpreted as a bifurcation phenomenon (Rice 1976): for a given homogeneous strain rate, the material constitutive equation allows for a

non homogeneous solution to develop. A material instability occurs and strain localization takes place. Standard, rate independent continuum models are able to determine the behavior in the pre-localization regime and some properties at incipient localization, such as the direction of shear bands in tensile tests or in biaxial and triaxial states (Doghri & Billardon 1995). However in the post-localization regime, or in the softening branch of the material behavior, a possible change appears for the character of the governing set of partial differential equations. Numerical solutions suffer from spurious mesh sensitivity and become meaningless.

Scientists (Belytscko & Fish 1989, Wang 1993) have first tried to "enrich" finite elements but this does not tackle the basic problem of loss of ellipticity. Upon mesh refinement, the solution converges to a localization zone with zero dimension. No energy is dissipated and the results become meaningless. A more efficient approach is to modify the FEM formulation or the constitutive law of the material in such a way that, even when localization occurs, the problem remains well posed. Different ways to achieve this second approach have been followed:

The Non-Local Approach. It basically consists in using classical laws with non-local variables computed by a weighted average over a volume of material with characteristic dimension l. This length introduced in the formulation proves to be an essential feature to restore the objectivity of the numerical models during localization (Bazant & Chang 1984). The choices of the characteristic volume (size and shape), weighting function and variables on which averaging is made are not simple.

The Cosserat Continuum Theory. In this approach, moment and rotation degree of freedom are used in addition to the classical stress components and translation degrees of freedom. It constitutes an elegant way to induce an internal length in the material constitutive law (de Borst 1991). It may be justified in the case of granular materials like sand. For polycrystalline materials, one can link rotations to grain motion (Lippman 1995). Unfortunately, this approach is totally effective in pure shear, only when the rotations are predominant. For instance, Sluys 1992 shows that, for a compression test, only partial regularization is achieved.

The Viscous Regularization. Some authors (Simo 1989, Loret 1990, Zhu 1992) use classical continuum theory but they include some viscous effects in the material constitutive equations. It appears that the mesh independency can be achieved but is conditional to the amount of viscosity introduced in the model.

The Gradient Approach. The basic idea is to introduce some gradients of the pertinent state variables in the formulation of constitutive laws. Bazant 1984 has presented the non-local gradient formulation with a Laplacian of strain and has applied this formulation in solving a one dimensional localization problem. Aifantis 1988, 1992 show that the introduction of the second gradient of deformation into the expression of the flow stress for plastic materials can

preserve ellipticity of the governing equations. de Borst & Mulhaus 1992 have presented the formulations and algorithms for the gradient plastic continuum in a two-dimensional and three-dimensional finite element context, where the yield strength depends not only on the effective plastic strain but also on its Laplacian. This method has been widely used in plastic models (Pamin 1994, Li & Cescotto 1996), in elastic damage models (Geers 1997) or elastic-plastic-damage models (Zbib & Aifantis 1988); it keeps efficiently ellipticity of the equations when localization occurs.

It seems that all the different proposed numerical solutions and the physical reality have in common the existence of an internal material length scale parameter. It characterizes the range and the amplitude of the micromechanical non-local bindings between the material particles. This length scale parameter can only be identified when inhomogeneous deformations occur; so standard material tests do not suffice. Structural tests must be considered and the length scale parameter must be determined by inverse modeling (Geers 1997). Note that it is interesting to couple non-local continuum damage model to random field theory and stochastic finite-element analysis. This yields a probabilistic formulation of the damage evolution (Carmeliet 1996). This approach introduces two different length parameters: the characteristic length of the non-local damage model and the correlation distance of the random field.

The Euromech 417 conference entitled "Numerical Modelling in Damage Mechanics" held in Troyes or the Symposium on "Continuous Damage and Fracture" (Benallal, 2000) held in Cachan, both in October 2000, help to summarize the state-of-the-art. They demonstrate clearly that the non-local and gradient approaches have the largest range of applications and solve efficiently the problem of mesh dependency. So these solutions will be shortly presented hereafter.

If the softening effect is not too strong and in applications where the non-homogenous strain and stress fields induce well localized shear zone, one can hope to avoid more or less mesh dependent results. It is then possible to detect fracture location and to identify the fracture moment of occurrence (pre-localization regime). For instance, Brunet *et al.* 1997, with his anisotropic extension of Gurson's model, but also Picart *et al.* 1997, Lazzaretto *et al.* 1996, with a classic isotropic Gurson's model, or Hartley *et al.* 1997, with a Lemaître's type law, look for fracture occurrence and do not bother with mesh dependence problems. It is difficult to know if these authors have checked the mesh independence of their results with their particular data or if the regularization issued from damage strain rate dependence preserves the ellipticity of their equations. However for metal modeling, the work of Stainier 1996 with Gurson's law and Castagne 1998 with Lemaître's type model proved the importance of the mesh dependence on results. To follow crack development it is really not possible to neglect this problem.

In the applications of Chapter 6, the conclusion is that, because of the non homogeneous field, the fracture location is well predicted but its occurrence instant is mesh dependent, at least in cases of strong damage localization like the notch test with sharp radius or the notched bending rod test. In the research described in section 6.2, even if the material viscosity is low, it generally seems to be sufficient to prevent strain localization before experimental crack appears. This was not the case with Castagne's 1998 work, summarized in section 6.3, where a damage elasto-plastic model was fitted on the same set of experiments. Her elasto-plastic simulations clearly show bifurcations long before experimental cracks appear.

5.2. Non-Local approach

In this method, the length range of the microscopic interaction forces is taken into account at macroscale, by expressing the material constitutive law in terms of one or more non-local variables defined as suitably weighted averages of their local values over the interaction domain.

The case of a simple isotropic elastic local model of damage is presented here. The stress-strain relation is given by:

$$\underline{\sigma} = (1 - D)\,\underline{\underline{C}}^{e} : \underline{\varepsilon} \tag{5-1}$$

where the scalar damage variable D is limited by:

$$0 \le D \le 1 \tag{5-2}$$

This damage parameter D is coupled to the deformation history of the material through the use of a monotonically increasing deformation history parameter κ. Geers' 1997 choice is presented here:

$$\kappa(\underline{x},t) = max\left[\varepsilon^{d}_{eq}(\underline{x},\tau)\ with\ \tau \le t\ ),\kappa_{i}\right] \tag{5-3}$$

where ε^{d}_{eq} is a damage equivalent strain derived from the different strain components of the local strain tensor. The chosen mathematical function for ε^{d}_{eq} offers various possibilities to quantify the effect of the local strain on the damage process, and constitutes one of the characteristics of the failure behavior. $\underline{x}$ identifies the position of the point in consideration, t is the time, κ_i is the threshold value for damage initiation at time $t = 0$. The evolution of κ can be mathematically expressed by Kuhn Tucker's relations:

$$\dot{\kappa} \ge 0 \quad \varepsilon^{d}_{eq} - \kappa \le 0 \quad \dot{\kappa}\,(\varepsilon^{d}_{eq} - \kappa) = 0 \tag{5-5}$$

An example of damage evolution law is:

$$D = 1 - \frac{\kappa_i}{\kappa}((1-\alpha) + \alpha\, e^{-\beta(\kappa - \kappa_i)}) \tag{5-6}$$

where α and β are material parameters.

In the non-local version of this model, the damage equivalent strain is just replaced by a non-local equivalent strain, which characterizes the deformation in a material volume surrounding the focused point:

$$\bar{\varepsilon}^{d}_{eq}(\underline{x}) = \frac{1}{V}\int_{V} g(\underline{y})\,\bar{\varepsilon}^{d}_{eq}(\underline{x}+\underline{y})\,dV \tag{5-7}$$

where $\underline{x}$ characterizes the position of the analyzed point, $\underline{y}$ the relative positions of the material points in a surrounding volume V. The function $g(\underline{y})$ is a weighting function defining the intensity and the radius of the spatial non-local effect. It introduces the material internal characteristic length scale. It should satisfy:

$$\frac{1}{V}\int_{V} g(\underline{y})\,dV = 1 \tag{5-8}$$

The definitions of the non-local variable(s), weight function and interaction domain have important consequences in finite element implementations. For instance, depending on the choice of non-local variables, the corrector phase in standard finite element iterative procedure, typically carried out separately at each Gauss point, may cease to be local. The choice of a non symmetric weight function implies that the consistent tangent matrix becomes non-symmetric. These two drawbacks are suppressed in the final proposal by Comi & Perego 2001. In this article, they first choose as non-local variable the elastic energy release rate. It has the advantage that the constitutive calculations can be separately conducted during the corrector phase but suffers the drawback of yielding a non-symmetric consistent tangent matrix. Following the thermodynamically founded, non-local theory recently developed by Borino *et al.* 1999, a second version of the model is proposed. A new term is added in the dissipation rate density: a non-local residual. It represents the energy due to the intrinsic non-locality of the developing damage mechanism. This energy is exchanged between the considered material point and other points belonging to its interaction domain. In the final proposal by Comi & Perego 2001, the non-local nature, originally conferred to the damage variables, is transferred to their conjugate variables, the energy release rates, on the basis of an energy equivalence, which helps to eliminate the so-called non-local residual. The explicit expression of the finite element tangent stiffness matrix for this new non-local model has been derived and is symmetric.

5.3. Gradient approach

5.3.1. Gradient damage method

As proposed by Bazant *et al.* 1984 and applied for instance by Geers 1997, Peerlings 1999, one way to reach gradient theory is to expand the local damage equivalent strain ε_{eq}^{d} into a Taylor series, then to compute its integral (5-7) in a material volume surrounding the focused point. Neglecting the high-order terms, this substitution allows to transform relation (5-7) into:

$$\bar{\varepsilon}_{eq}^{d} = \varepsilon_{eq}^{d} + c\nabla^2 \varepsilon_{eq}^{d} \tag{5-9}$$

The remaining gradient parameter c represents the square of the average internal length. It only depends on the selected weighting function and the averaging volume V. In practice, if no term of the Taylor series was neglected and the same weighting function was applied, the integral (5-7) and differential (5-9) formulation should be fully equivalent. However, neglecting higher-order gradient coefficients is one way to choose implicitly another weighting function, so the integral and differential formulations differ. As formulation (5-9) relates explicitly $\bar{\varepsilon}_{eq}^{d}$ to the Laplacian of ε_{eq}^{d}, it inevitably requires C^1 continuity of the displacement shape functions in finite element formulations. To tackle this drawback, Peerlings *et al.* 1996 propose to use another formulation reached by some algebraic transformation of (5-9), where higher order term are dropped:

$$\bar{\varepsilon}_{eq}^{d} = \varepsilon_{eq}^{d} + c\nabla^2 \bar{\varepsilon}_{eq}^{d} \tag{5-10}$$

In practice, it can be considered as another approximation deduced from the differential formulation (5-7). It implicitly defines another weighting function than in equation (5-9). Using a Galerkin finite element scheme, Peerlings *et al.* 1996 present a consistent incremental iterative Newton-Raphson solution procedure of the discretized weak form of the governing field equations, which are the equilibrium and the non-local formulation:

$$div\,\underline{\sigma} + \underline{f} = 0$$

$$\bar{\varepsilon}_{eq}^{d} - c\nabla^2 \bar{\varepsilon}_{eq}^{d} = \varepsilon_{eq}^{d} \tag{5-11}$$

As checked by Geers 1997, this formulation, called "**constant gradient damage model**", uses a constant c parameter and suffers from some inherent deficiencies, which render the method unable to describe a discontinuous crack evolution. In the final failure stage, the damage computed by this method propagates in a direction normal to the crack, which causes widening of the damaged zone (Figure 5-4).

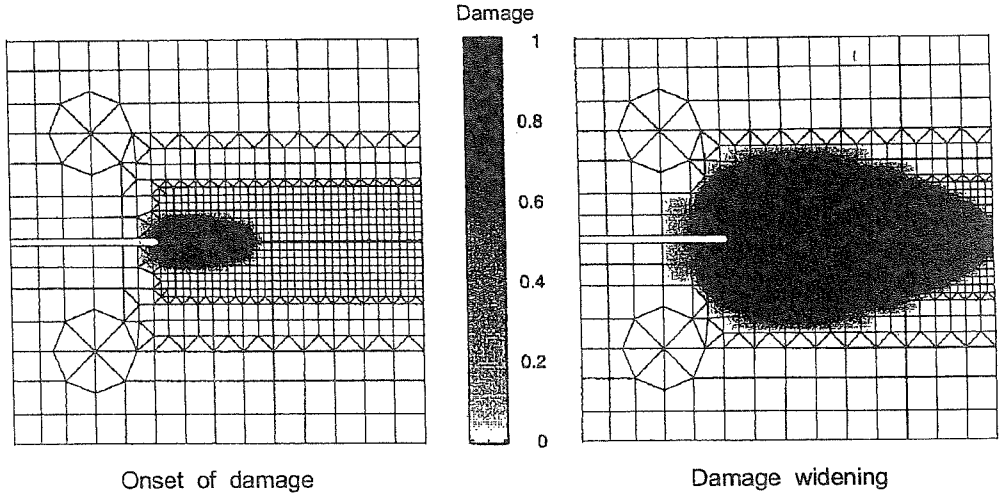

Figure 5-4 Damage distribution of a compact tension experiment on a short glass-fiber-reinforced polypropylene simulated by constant gradient damage model (from Geer's 1997).

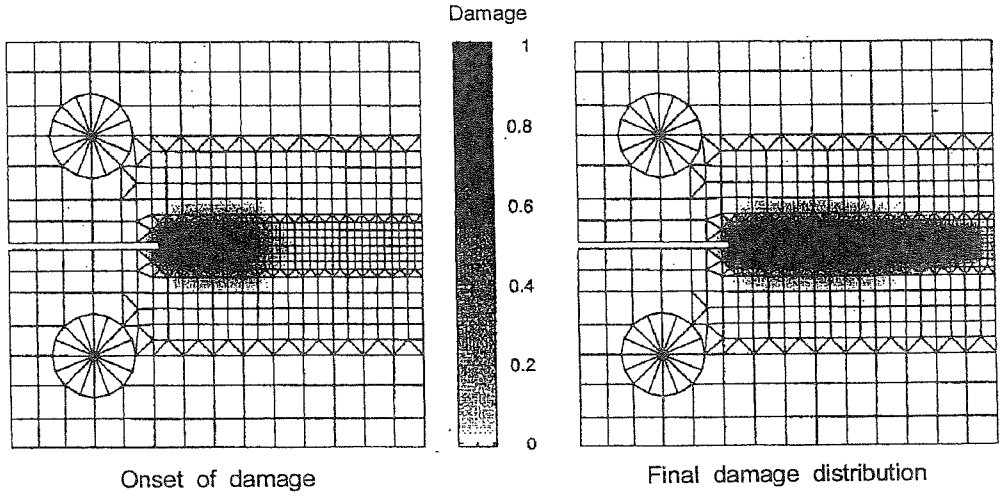

Figure 5-5 Damage distribution of a compact tension experiment on a short glass-fiber-reinforced polypropylene simulated by a strain-based transient-gradient damage model (from Geer's 1997).

In practice, damaged material should unload with the fracture propagation and a finite width of the damaged zone should be reached. This is correctly simulated with a modified formulation (Figures 5-5 and 5-6), where a new variable ζ denoted gradient activity is introduced. This parameter models the mobilized non-local coupling between particles at the micro-level. When it is equal to 0, one retrieves the local formulation. When it reaches its maximal value c, the constant gradient model is recovered. The transient behavior of ζ requires a supplementary evolution law. According to this reasoning, the non-local coupling

between the material particles is more and more mobilized as the local deformation increases and with an increasing value of ζ. The final finite element formulation satisfactorily handling this model is a three-field formulation (velocity field, non-local damage equivalent strain field and a C^0 version of variable ζ field). Details can be found in Geers 1997.

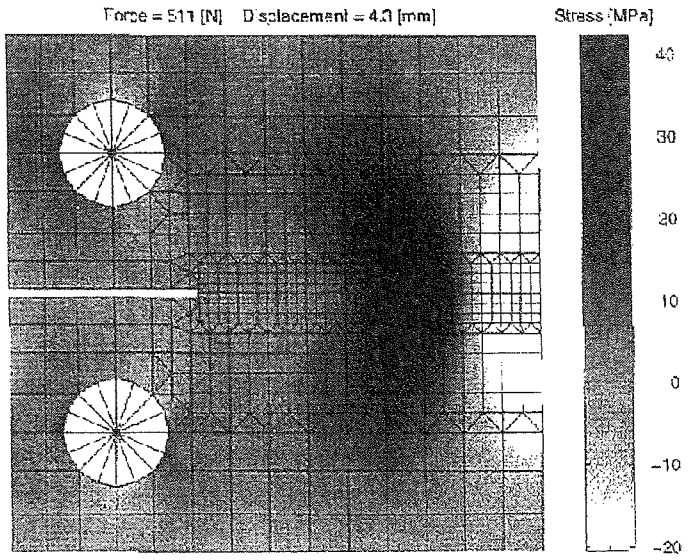

Figure 5-6 σ_{yy} stress component distribution of a compact tension experiment on a short glass-fiber-reinforced polypropylene simulated by a strain-based transient-gradient damage model (from Geer's 1997).

5.3.2. Gradient plasticity theory

The incorporation of the gradient dependence into large deformation macroscopic plasticity theory has microscopic roots, as underlined by Aifantis 1984 who considers dislocation motion and evolution. Numerous proposals have followed this research and a typical new formulation of the von Mises yield locus is:

$$F_p = \sigma_{eq} - \sigma_F(\varepsilon^p_{eq}, \nabla^2 \varepsilon^p_{eq}) = 0 \tag{5-12}$$

As the Laplacian of equivalent plastic strain is involved in the yield function, the increment of the plastic multiplier cannot be obtained at a local level (integration point). To solve this problem, the plastic multiplier is taken as an independent global variable, in contrast to the conventional approach in computational plasticity.

Pamin 1994 proposes an algorithm the fundamental feature of which is a weak (and not point-wise) satisfaction of the yield condition, which is coupled with a weak equilibrium condition. The dependence of the yield function on the Laplacian of the equivalent plastic strain induces the necessity of C^1-continuous interpolation of the plastic strain field in the finite element formulation. A new C^0-approach has been developed, in which the continuity requirement is relaxed by treating the first derivatives of the plastic multipliers as additional unknowns and connecting them to the plastic multiplier field using a penalty constraint. Pamin has examined several C^1- and C^0- continuous, rectangular and triangular elements. The behavior of these various gradient plasticity elements has been compared using a shear band test. The use of rectangular elements with reduced integration seems to give the best efficiency. This algorithm for gradient plasticity performs very well for relatively smooth strain, stress fields. However, the return mapping determined by the nodal plastic multiplier variables is not sufficiently accurate in case of stress concentrations and sudden changes of the plastic flow direction. This problem, which is a consequence of the weak fulfillment of the yield condition, causes convergence deterioration especially in the peak load regime.

Li & Cescotto 1996 propose another method. Even through the yield condition at each integration point is no longer local, it is satisfied in a point-wise fashion and at every iteration of a load step. The plastic multipliers are internal state variables locally defined at each integration point. The Laplacian of the equivalent plastic strain at an integration point is evaluated from the derivatives of the polynomial, which is interpolated by using the values of the plastic multipliers at neighboring integration points. As the plastic multipliers are not taken as independent global unknowns there is no requirement on C^1-continuous shape functions for the interpolation of the plastic multiplier.

5.4. Conclusion

Solutions exist to solve the mesh dependence and to follow crack propagation with finite element method. As underlined above, a characteristic length or internal length is necessary and is introduced in a non local computation or gradient computation. This new material data is not so easy to determine but is generally linked to microstructure information or measured by means of localization experiments. For instance, Bazant & Pijaudier-Cabot 1989 propose a characteristic length $l \approx 3\, d_a$, in which d_a is the size of the largest heterogeneity in the material. An idea from different characteristic lengths is given hereafter:

Geers 1997:	short glass-fibre-reinforced polypropylene: $l^2 = 1$ to 5 mm^2 (non local approach);
Peerlings 1999:	concrete : $l^2 = 1$ mm^2 (non local approach);
Gutierrez de la Merced 1999:	concrete : l =1.7 to 2 mm (non local approach);

Pamin 1994:	concrete : l =3 mm (non local approach);
Pardoen 1998:	copper : l =0.006 mm, inter distance between inclusions, internal length required in Thomason's rupture criterion;
Suresh 1991:	1015 steel : l =0.1 mm, a rough estimate of the maximum grain size, internal length used in non local damage model;
Wilsius 1999:	very large bibliographical review covering steels and aluminum alloys. It gives the Finite Element size required at the crack tip in order to model fracture propagation with the models of Rice & Tracey 1969, Rousselier 1987 and Gurson 1977. The range of values goes from 0.033 mm to 0.8 mm but values are generally smaller than 0.2 mm.

This quick review clearly shows that the characteristic length required in non local formulation is under the mm for metal materials. As quite a few finite elements must discretize this length scale, it leads to very refined meshes. So if real structures must be studied, very large number of elements appear and parallel computers are required. A possibility to prevent this drawback is to use remeshing techniques that refine the zones where possible cracks are detected.

If the goal is to study crack propagation, the refined meshes and non-local approach cannot be avoided with the finite element method. The crack opening appears thanks to elements without stiffness or thanks to node duplication and automatic injection of a mesh opening related to damage evolution. Specific new developments of finite elements allow no explicit meshing of the crack surfaces (Sukumar *et al.* 2000). The users of meshless method argue that one advantage of their approach is an easy study of crack propagation as no mesh adaptation is required.

In the present thesis, the main purpose is the prediction of crack appearance. Conforming to this idea of "no specific study of crack propagation", the local approach is avoided and "coarse" meshes, as compared to the internal length, are used. However, this choice already provides some difficulties of results mesh dependence.
One conclusion can be that non-local models are interesting but if real industrial parts are aimed, at this step must be coupled with parallel computer facilities.

References

Aifantis, E.C., (1984) On the microstructural origin of certain inelastic models, *Trans. ASME. J. Eng. Mater, Technol.*, **106**, 326 – 330.

Aifantis, E.C., (1988) The physics of plastic deformation, *Int. J. Plasticity*, **3**, 211-247.

Aifantis, E.C., (1992) On the role of gradients in the localization of deformation and fracture, *Int. J. Eng. Sci.*, vol. **30**, n°**10**, 1279-1299.

Bazant, Z.P. (1984) Imbricate continuum and its variational derivation, *J. Eng. Mech. ASCE*, **110**, 1693-1712.

Bazant, Z.P. ,Belytschko, T., Chang, T.P. (1984) Continuum theory for strain softening, *J. Eng. Mech. ASCE*, **110**, 1666-1692.

Bazant, Z.P. ,Chang, T.P. (1984) Instability of non-local continuum and strain averaging, ASCE, *Jnl. of Eng. Mech.*, **110-10**, 1441-1450.

Bazant, Z.P., Pijaudier-Cabot, G. (1989) Measurement of characteristic length of nonlocal continuum, *J. Engrg. Mech., ASCE*, **115(4)**, 755-767.

Belytschko, T., Fish, J. (1989) Spectral superposition on finite elements for shear banding problems, *Proc. 5th Int. Symp. On Num. Meth. In Eng.*, ed. Grüber R. *et al.*, **1**, 19-29.

Benallal, A., (2000), Continuous Damage and Fracture, Elsevier.

Brunet, M., Mguil-Touchal, S., Morestin, F. (1997) Numerical and experimental analysis of necking in 3D sheet forming processes using damage variable, *Advanced Methods in Materials Processing Defects*, Predeleanu M. & Gilormini P.,Elsevier, 205-214.

Borino, G., Fuschi, P., Plizzotto, C. (1999) A thermodynamic approach to nonlocal plasticity and related variational principles, *Journal of Applied Mechanics 1*, **66**, 952-963.

Carmeliet, J., Hens, H., Probabilistic nonlocal damage model for continua with random field properties, *J. of Engineering Mechanics*, **120 / 10**.

Castagne, S. (1998) Application d'un modèle isotrope élastoplastique couplé à l'endommagement à un aluminium. Travail de fin d'études, Université de Liège.

Comi, C., Perego, U. (2001 to appear) Numerical aspects of nonlocal damage analyses, Revue Européenne des Eléments Finis.

de Borst, R. (1991) Simulation of strain localization : a reappraisal of the Cosserat continuum, *Engineering Computations*, **8**, 317-332.

de Borst, R., Muhlhaus, H.B. (1992) Gradient-dependent plasticity : formulation and algorithmic aspect, *Int. J. Numer. Methods Eng.*, **35**, 521-539.

de Borst, R., Geers, M.G.D., Peerlings, R.H.J., Benallal, A. (1998) Some remarks on gradient and nonlocal damage theories, *Damage Mechanics in Engineering materials*, edited by Voyiadijs, G.Z., Ju, J.-W.W., Chaboche, J.-L., Elsevier.

de Borst, R. (1999) Recent issues and future prospectives in computational mechanics of materials, 5th U.S. National congress on computational

mechanics, University of Colorado, ed. Carosio, A., Smolarkiewicz, P., Willam, K., Yang, J.

de Vree, J.H.P., Brekelmans, W.A.M., van Gils, M.A.J. (1995) Comparison of nonlocal approaches in continuum damage mechanics, *Computers & Structures*, **55/4**, 581-588.

Desoyer, T., (1995), Contribution à la modélisation de l'endommagement diffus et localisé, Mémoire d'habilitation à diriger des recherches, Ecole Nat. Sup. de Mécanique et d'aérotechnique, Université de Poîtiers.

Doghri, I., Billardon, R. (1995) Investigation of localization due to damage in elasto-plastic materials, *Mechanics of Materials*, **19**, 129-149.

Doghri, I. (2000) Mechanics of Deformable Solids, Linear, Nonlinear, Analytical and Computational Aspects, Springer Ed.

Geers, M.G.D., (1997) Experimental Analysis and Computational Modelling of Damage and Fracture, Ph. D. thesis, Technische Universiteit Eindhoven.

Gurson, A.L. (1977) Continuum theory of ductile rupture by void nucleation and growth. *J. Engng. Materials Technology* **99**, 2-15.

Gutierrez de la Merced, M.A. (1999) Objective simulation of failure in heterogeneous softening solids : the use of stochastic imperfections in localization analysis, Ph. D. thesis, Technische Universiteit Eindhoven.

Hartley, P., Hall, F.R., Chiou, J.M., Pillinger, I. (1997) Elastic – plastic finite – element modelling of metal forming with damage evolution, *Advanced Methods in Materials Processing Defects*, Predeleanu, M., Gilormini, P, Elsevier.

Lazzarotto, L., Picart, P. Oudin, J. (1996) Benchmarks for finite element modeling of cold forging processes with elasto-plastic microvoided materials. *Computational Materials Science*, **5**, 167-176.

Li, X.K., Cescotto, S. (1996) Finite element method for gradient plasticity at large strains, *Int. J. Num. Meth. in Eng*, **39**, 619-633.

Lippmann, H., (1995) Cosserat plasticity and plastic spin, *Appl. Mech. Rev.*, **48**, **11 part I**, 753-762.

Loret, B., Prevost, J.H. (1990) Dynamic strain localization in elasto-visco-plastic solids, part 1. general formulation and one-dimensional examples, *Comp. Meth. Appl. Mech. Engng.*, **83**, 247-273.

Pamin, J., (1994) Gradient-dependent plasticity in numerical simulation of localization phenomena, Ph. D thesis, Technische Universiteit Delft, Delft University Press.

Pardoen, T. (1998) Ductile fracture of cold-drawn copper bars : experimental investigation and micromechanical modelling, Doctorat en sciences appliquées, Université de Louvain-La-Neuve.

Peerlings, R.H.J., de Borst, R., Brekelmans, W.A.M., de Vree, J.H.P. (1996) Gradient-enhanced damage for quasi-brittle materials. *International Journal for Numerical Methods in Engeneering*, **39**, 3391-3403.

Peerlings, R.H.J. (1999) Enhanced damage modelling for fracture and fatigue, Ph. D. Thesis, Technische Universiteit Eindhoven.

Picart, P., Piechel, G. & Oudin, J. (1997) Damage influence in the finite element computations for large strains elastoplastic mechanical structures, *Advanced*

Methods in Materials Processing Defects, Predeleanu, M. & Gilormini, P., Eds. Elsevier, 175-184.

Rice, J.R. (1976) The localization of plastic deformation. *Proc. 14th Int. congress of theoretical and applied mechanics*, 207-220, Koitier W.T. Eds.

Rice, J.R. & Tracey, D.M. (1969) On the ductile enlargement of voids in triaxial stress fields, *J. Mech. Phys. Solids*, **17**, 201-217.

Rousselier, G. (1987) Ductile fracture models and their potential in local approach of fracture, *Nuclear Engineering and Design*, **105**, 97-111.

Simo, J.C. (1989) Strain softening and dissipation : a unification of approach, *Crack and Damage*, Ed. Marzars, J., Bazant; Z.P., Elsevier, 440-461.

Sluys, L.J. , (1992) Wave propagation, localization and dispersion in softening models, Dissertation, Delft University of Technology.

Stainier, L. (1996) Modélisation numérique du comportement irréversible des métaux ductiles soumis à grandes déformations avec endommagement. Thèse de Docteur en sciences appliquées, Université de Liège.

Suresh, S. (1991) Fatigue of Materials. Cambridge University Press, Cambridge, U.K.

Sukumar, N., Moës, N., Moran, B., Belytschko, T. (2000) Extented finite element method for three-dimensional crack modelling, *Int. J. Numer. Meth. Engng*, **48**, 1549-1570.

Wang, X.C. (1993) Modélisation numérique des problèmes avec localisation de la déformation en bande de cisaillement, Thèse de Doctorat, Université de Liège.

Wilsius, I., (1999) Etude expérimentale et numérique de la déchirure ductile basée sur des approches locales en mécanique de la rupture, Ph. D. Thesis Université des Sciences et Technologie de Lille.

Zbib, H.M., Aifantis, E.C. (1988) On the localisation and postlocalization behavior of plastic deformation, I, II, III, *Res Mechanica*, **23**, 261-277, 279-292, 293-305.

Zhu, Y.Y. (1992) Contribution to the local approach of fracture in solid dynamics, Ph. D. Thesis, University of Liège, Department MSM.

6. STUDY OF ALUMINIUM RODS

6.1 Introduction

The work presented here was performed by Anne Marie Habraken with the help of Wang Xiao Chuan thanks to the Dynamic Forging Modeling project supported by the Région Wallonne. Then Zhang Li Hong and Sylvie Castagne have brought their collaboration to improve Bodner's and Zhu's models.

The manufacturing process of the studied aeronautic rod has been provided by Technical Airborne Components industry; it consists in 3 stages of rotary forging: preliminary round-round forging, round-rectangle pre-crushing and final rectangle-rectangle forging as summarized by Figure 6-1. The rotary forging process is described by Figure 6-2 showing longitudinal and transversal views and by Figure 6-3 presenting the hammer system of a forging machine.

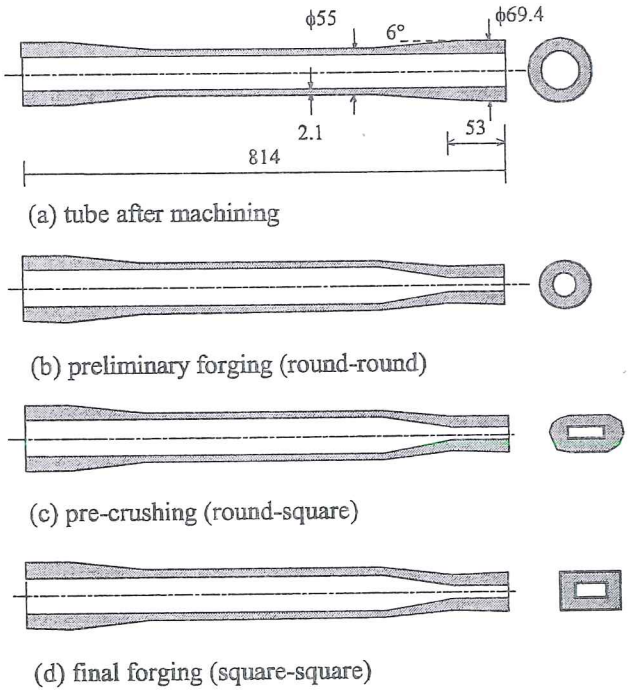

Figure 6-1 Industrial aeronautic rod manufacturing process (adapted from Wang & Habraken 1996).

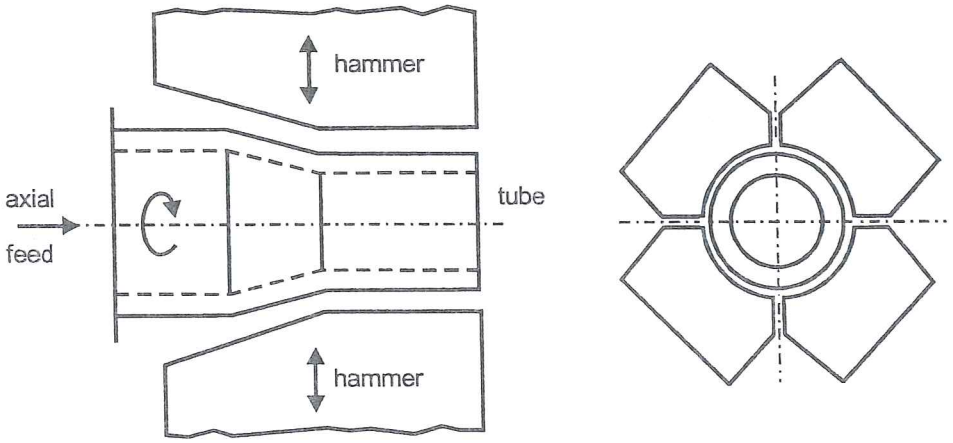

Figure 6-2 Studied rotary forging process (from Habraken & Wang 1996).

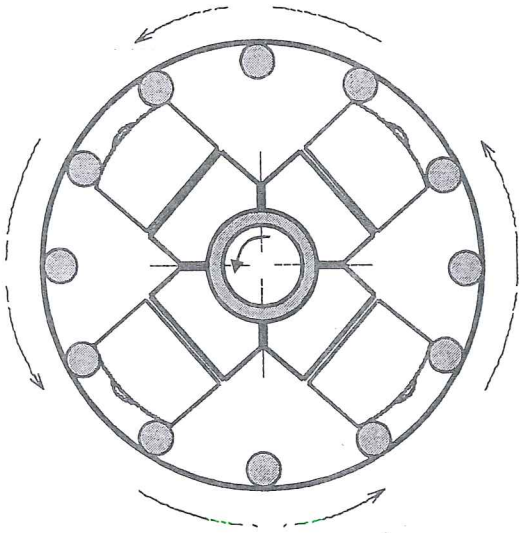

Figure 6-3 Hammer system of a forging machine (from Wang *et al.* 1995).

In fact, if relative rotation between rod and hammers exists, the circular shape of the tube is retained; otherwise the hammer shape is progressively imposed on the tube. Of course, the FE simulation requires the tools and the tube geometry and a kinetic description of the process; however the difficulties concern general choices:

- Isothermal mechanical simulation or thermomechanical one?
- Static or dynamic analysis?
- Elasto-plastic or elasto-visco-plastic assumption?
- Best strategy to represent numerically the round-round forging by an axisymmetric state?

All these points were studied and details can be found in Wang *et al.* 1994a, Wang *et al.* 1994b, Wang *et al.* 1995, Wang & Habraken 1996. The general automatic simulating procedure is summarized by Figure 6-4, and FEM results are presented on Figure 6-5.

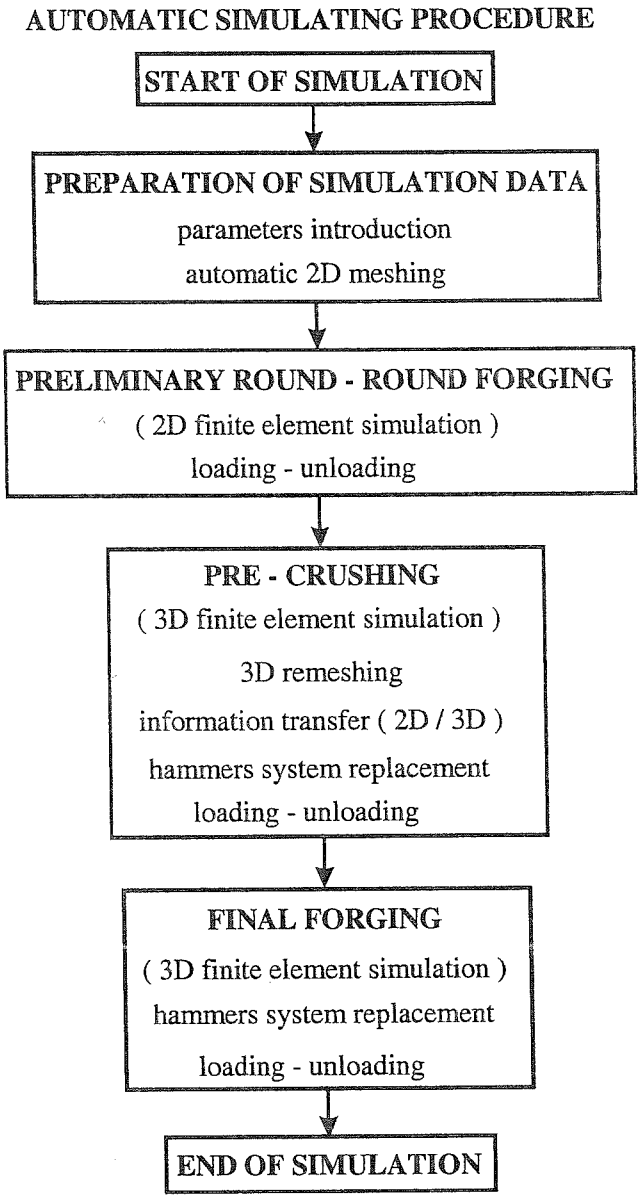

Figure 6-4 Automatic simulation procedure (adapted from Wang *et al.* 1995)

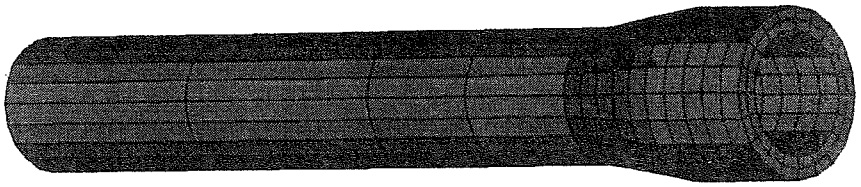

FINITE ELEMENT MESH (2D)

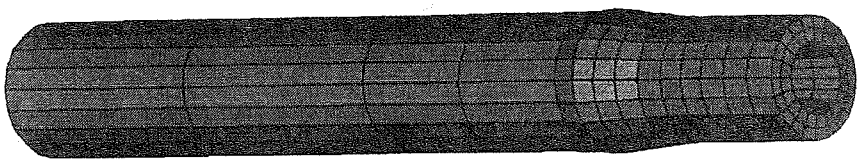

PRELIMINARY FORGING SIMULATION 2D

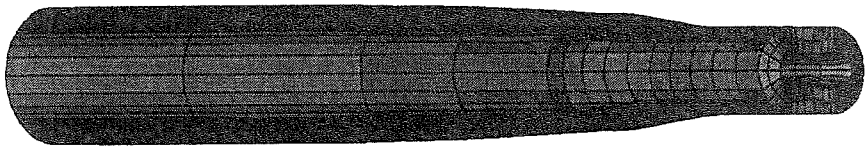

PRE-CRUSHING SIMULATION 3D

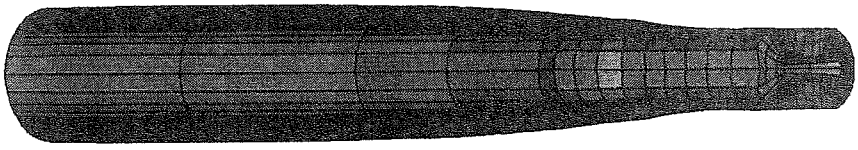

FINAL FORGING SIMULATION 3D

FE MODELLING OF FABRICATION PHASES OF AERONAUTIC RODS

Figure 6-5 Forged tube after different manufacturing steps, (adapted from Wang & Habraken 1996)

The various heat treatments applied between the forging steps prevent to really stick to the real process in this research, because the constitutive law was just identified once on the annealed state, and not 3 times, after each heat treatment. Nevertheless, it is interesting to note that Bodner's damage model presented hereafter could predict zones of maximum damage where the industry effectively observed cracks (Figure 6-6). This model allows a parametrical study, which could help to decrease damage according to process conditions.

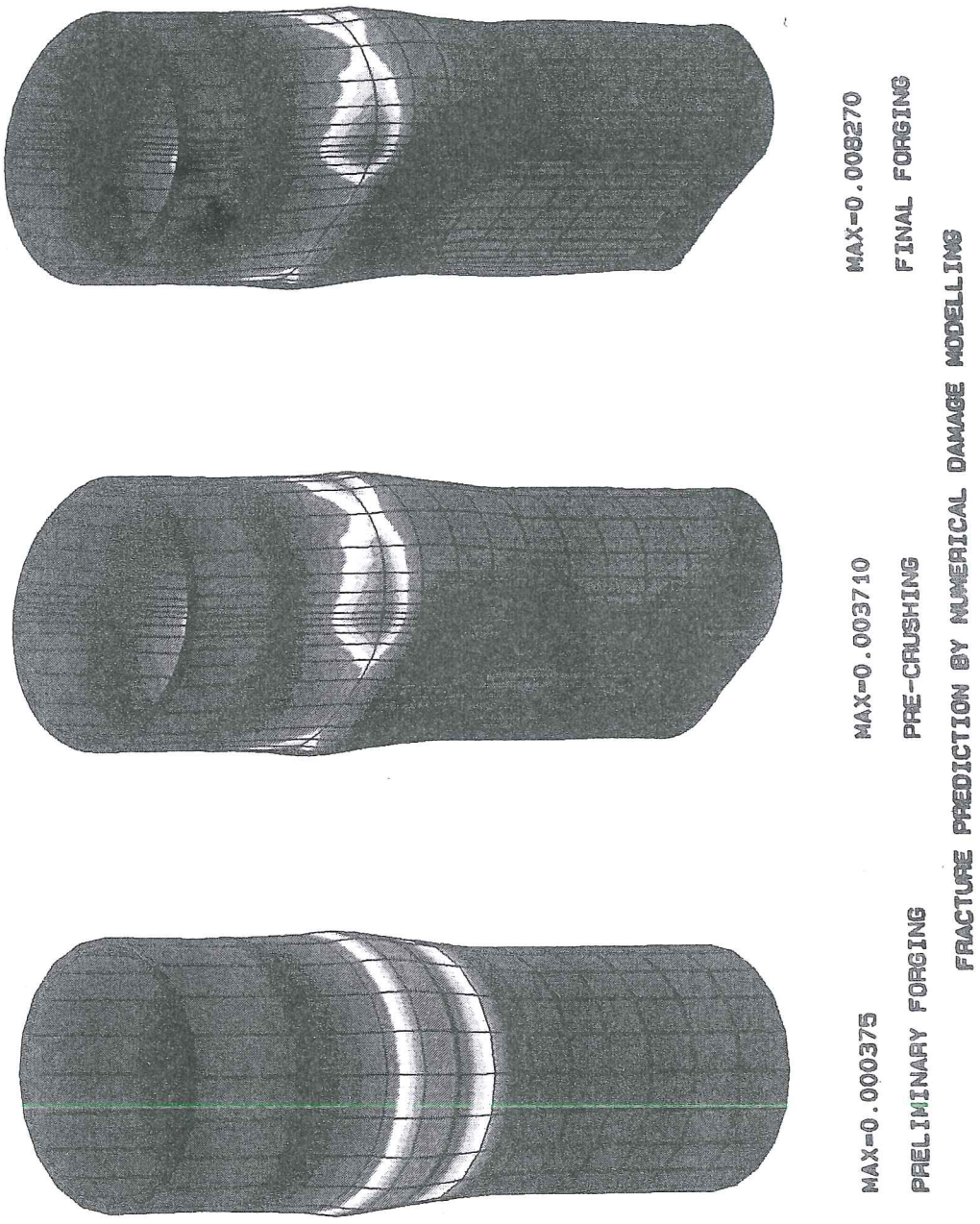

Figure 6-6 Damage distribution after different manufacturing steps (from Wang & Habraken 1996).

Note that as described in Habraken & Wang 1996, for notch test experiments and two cases of cylinder upsetting, 6 criteria from Chapter 4, table 4-1 (Freundenthal, Cockroft, Brozo, Ghosh, Oyane, Mc Clintock) have been applied with the stress and strain fields computed with Bodner's damage model. The conclusion was that for this

set of experiments it was not possible to find one criterion able to predict the right location of fracture with a unique threshold value.

The goal of this thesis is not to summarize all this project results, they can be found in the final project reports (Cescotto *et al.* 1993, Habraken *et al.* 1996). The thesis provides the description of the two damage models that were applied on the annealed state of the rod material (Aluminum alloy 2024). This material was only available in form of tubes (see Figure 6-7), which explains the chosen shape of samples for identification and validation experiments. A clear weakness of this research is the lack of microscopic investigations on the material. This task was not in the Région Wallonne project and the efforts to perform it after the end of the project have failed. Present closer links with the metallurgical department should avoid such a mistake in the future.

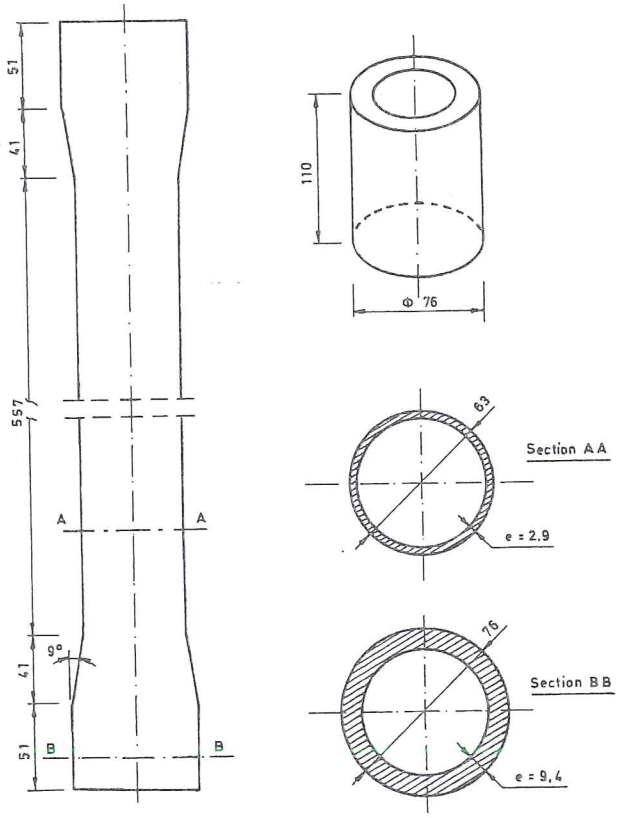

Figure 6-7 Description of the tube (Habraken & Wang 1996).

Respecting chronological order, the elasto-visco-plastic damage model of Bodner's type is first described (section 6.2) with its identification and validation, then the damage elasto-plastic law of Zhu is applied on the same experimental data (section 6.3). All the simulations are performed with 2D and 3D finite elements of mixed type (Zhu & Cescotto, 1994b, 1995b) implemented in the LAGAMINE code.

6.2. An elastic-visco-plastic-damage model

6.2.1. The model choice

The literature review by Zhu & Cescotto 1991 about elasto-visco-plastic models easily coupled with damage and able to represent material behavior in various conditions of strain rates and temperatures has pointed out the qualities of the Bodner & Partom's 1975 model. The article of Zhu & Cescotto 1994 collects the parameters of Bodner Partom's model for a large number of metals and alloys which proves the large application field of this law.

This literature analysis explains the choice of this model to be implemented in LAGAMINE. The simulations of the process of aluminum rod forging have shown that strain rate could reach 50 s^{-1}. The experimental tests demonstrate a low viscous effect at room temperature. As one particularity of Bodner's model is its application to material with low viscosity, this law has been adopted. This low viscous aspect help to regularize the problem and to prevent numerical strain localization (see Chapter 5). This was effective as proved by the problems encountered further (section 6.3) with the application of damage elasto-plastic model.

6.2.2. Bodner's constitutive law

The model is first described in its initial state without damage extension. The general formulation of Bodner's model (Bodner & Partom, 1975) is based on the additive decomposition of $\underline{\dot{\varepsilon}}$ the total strain rate tensor, symmetric part of the velocity gradient tensor, into $\underline{\dot{\varepsilon}}^e$ elastic and $\underline{\dot{\varepsilon}}^p$ inelastic components which are both non-zero for all loading and unloading conditions:

$$\underline{\dot{\varepsilon}} = \underline{\dot{\varepsilon}}^e + \underline{\dot{\varepsilon}}^p \tag{6-1}$$

The elastic behavior follows the classical Young's law, here written separately for the deviatoric Cauchy's stress tensor $\underline{\hat{\sigma}}$ and the mean stress value σ_m. As in previous sections, hereafter the superscript ^ identifies a deviatoric tensor, the superscript $^{\nabla}$ the objective Jaumann's rate and the subscript $_m$ a mean tensor value, G and χ are respectively the elastic shear and bulk moduli, computed from Young's modulus E and Poisson's ratio ν.

$$\begin{aligned} \overset{\nabla}{\underline{\hat{\sigma}}} &= 2G(\underline{\dot{\hat{\varepsilon}}} - \underline{\dot{\hat{\varepsilon}}}^p) \\ \dot{\sigma}_m &= 3\chi\dot{\varepsilon}_m \end{aligned} \tag{6-2}$$

The generalized Prandtl-Reuss' flow law is used together with the volume conservation to establish a tensorial relation between deviatoric Cauchy's stress $\underline{\hat{\sigma}}$ and inelastic strain rate $\underline{\dot{\varepsilon}}^p$:

$$\underline{\dot{\varepsilon}}^p = \frac{D_o}{\sqrt{J_2}} exp\left(-\frac{1}{2}\left(\frac{Z^2}{3J_2} \right)^n \right) \underline{\hat{\sigma}} \quad \text{with} \quad J_2 = \frac{1}{2}\underline{\hat{\sigma}} : \underline{\hat{\sigma}} \tag{6-3}$$

where D_o is an assumed limit value of plastic strain rate in shear for large J_2, n is the rate sensitivity coefficient, Z is a total scalar hardening variable, sum of an isotropic part K and a directional part Z_D:

$$Z = K + Z_D \tag{6-4}$$

The directional component Z_D is computed by the projection of $\underline{\beta}$, a directional hardening symmetric tensor, on the direction $\underline{u}$ of the stress tensor :

$$Z_D = \underline{\beta} : \underline{u} \qquad \text{with } \underline{u} = \underline{\sigma} / \sqrt{\underline{\sigma} : \underline{\sigma}} \tag{6-5}$$

When the stress direction $\underline{u}$ is strongly modified, the directional component Z_D undergoes large magnitude changes and affects material response. This is the physical meaning of the scalar directional hardening component Z_D. Let us note that such concept is also used for hardening by Phillips *et al.* 1974, Basuroychowdhury & Voyiadjis 1998.

The isotropic and directional hardening are both assumed to occur under the action of two simultaneously competitive mechanisms: a hardening process due to deformation (first term of relations 6-6 below) and a softening or recovery process evolving with time and temperature (represented by the second term of relations 6-6):

$$\dot{K} = m_1 (K_1 - K) \dot{W}^p - A_1 K_1 (\frac{K - K_2}{K_1})^{r_1} \tag{6-6a}$$

$$\underline{\dot{\beta}} = m_2 (D_1 \underline{u} - \underline{\beta}) \dot{W}^p - A_2 K_1 \left(\frac{\sqrt{\underline{\beta} : \underline{\beta}}}{K_1} \right)^{r_2} \frac{\underline{\beta}}{\sqrt{\underline{\beta} : \underline{\beta}}} + (\underline{\Omega}.\underline{\beta} - \underline{\beta}.\underline{\Omega}) \tag{6-6b}$$

where $\dot{W}^p$ is the plastic work rate. The initial value of K at zero inelastic strain is K_0; K_1 is the maximum value of K, K_2 is the minimum value of K at a given temperature at which creep is occurring. The initial and minimum value of $\underline{\beta}$ is zero corresponding to the isotropic state. m_1, A_1, r_1, m_2, A_2, r_2 are material parameters defining the hardening evolution laws. The last term of equation (6-6b) is due to Jaumann's objective correction used for large strains, where $\underline{\Omega}$ is the antisymmetric part of the velocity gradient tensor.

Bodner's model is totally defined by 14 parameters : E, ν, D_o, K_o, K_1, K_2, D_1, m_1, m_2, A_1, r_1, A_2, r_2 and n. At room temperature, the terms related to the thermal recovery can be omitted and the number of parameters is reduced to 10.

6.2.3. Damage theory

Two scalar damage variables, called d the deviatoric component and δ the volumetric component, are used to represent the average material degradation which reflects the various types of damage at the micro-scale (see section 3.2.1 for the definition of damage variables). The damage due to nucleation, growth and coalescence of voids, to micro-cracks and to other microscopic defects is globally represented by d. And δ. According to Ladevèze 1984, these two variables are necessary to modify both elastic modulus and Poisson's ratio with damage growth.

As already presented in chapter 3, the continuum damage approach assumes the existence of a "true" stress tensor $\underline{\sigma}$ computed from macroscopic loading and area measurements and an associated "effective" stress tensor $\underline{\bar{\sigma}}$ theoretically closer to the actual average microscopic stress state existing between defects. The equivalent virgin state is related to the average material state, once the defects have been dropped. It is represented by effective tensors indicated by the superscript $\bar{}$. The developed model is a phenomenological one, not directly deduced from micro-macro transition. So, contrary to Gurson 1977 or Perzyna 1986 models, a direct connection between damage variables and void volume fraction is not assumed; other defect types could be covered by these damage components. As usual, true and effective stress tensors are related through the damage variables d and δ:

$$\underline{\bar{\hat{\sigma}}} = \frac{\underline{\hat{\sigma}}}{(1-d)} \qquad \bar{\sigma}_m = \frac{\sigma_m}{(1-\delta)} \tag{6-7}$$

From the viewpoint of energy conservation (Cordebois & Sidoroff 1979), the energy equivalence seems to be of more physical significance, so the following relation is applied in the elastic part:

$$\underline{\bar{\hat{\varepsilon}}}^e = \underline{\hat{\varepsilon}}^e(1-d) \qquad \bar{\varepsilon}_m^e = \varepsilon_m^e(1-\delta) \tag{6-8}$$

So one can check from (6-7) and (6-8) that elastic energy is equal in both states. Concerning plasticity, the plastic work rate $\dot{W}^p$ is conserved, this leads to:

$$\underline{\bar{\dot{\varepsilon}}}^p = \underline{\dot{\varepsilon}}^p(1-d) \tag{6-9}$$

The damage evolution law comes from the one proposed by Lemaître 1985. It has been adapted to a multiaxial state and a two damage variables model:

$$\dot{d} = \frac{1}{2(1-d)}\left(\frac{< F(\underline{\sigma}) - \sigma_D >}{A(1-d)}\right)^s \dot{\varepsilon}_{eq}^r \tag{6-10}$$

with $<x> = x$ if $x > 0$ and $<x> = 0$ if $x \leq 0$ and where $F(\underline{\sigma})$ is a triaxiality function necessary to transform a triaxial stress state to a reference uniaxial state, σ_D is a threshold value for damage increase, A, r, s are material constant. The chosen triaxiality function is the following one which has the advantage to separate tensile, compression and shear stress states and to introduce only one new parameter α:

$$F(\underline{\sigma}) = (1-\alpha)\sqrt{3J_2} + 3\alpha\sigma_m \tag{6-11}$$

One should notice that the so-called deviatoric damage component is not strictly dependent on shear component J_2 as the triaxiality function is modified by the mean stress σ_m.

The volumic damage variable evolution is directly related to the deviatoric damage component evolution and reflects the assumption of no volumic damage increase in compression state :

$$\begin{aligned} \dot{\delta} &= \frac{\delta}{d}\dot{d} \quad \text{in tensile state } \sigma_m > 0 \\ &= 0 \quad \text{in compression state } \sigma_m \leq 0 \end{aligned} \tag{6-12}$$

It has been checked experimentally that the ratio δ/d can be assumed constant in tensile state for common materials (Gattoufi, 1984). This ratio is named τ, so finally damage is characterized by 6 parameters : A, r, s, σ_D, α, τ. This model allows to recover the well-known Kachanov's creep law for $\tau = 1$, $s = \sigma_D = 0$.

6.2.4. Damage extension of Bodner's model

According to damage theory, effective stress and strain tensors follow classical behavior law. Consequently replacing $\underline{\sigma}$ by $\overline{\underline{\sigma}}$ and $\underline{\varepsilon}$ by $\overline{\underline{\varepsilon}}$ in Bodner's relations (6-1) to (6-6) and using relations (6-7) to (6-9) between true and effective tensors, one can get the final equations:

$$\overset{\nabla}{\hat{\underline{\sigma}}} = 2G(1-d)^2(\dot{\hat{\underline{\varepsilon}}} - \dot{\hat{\underline{\varepsilon}}}^p) - 4G(1-d)(\hat{\underline{\varepsilon}} - \hat{\underline{\varepsilon}}^p)\dot{d} \tag{6-13}$$

$$\dot{\sigma}_m = 3\chi(1-\delta)^2\dot{\varepsilon}_m - 6\chi(1-\delta)\varepsilon_m\dot{\delta} \tag{6-14}$$

$$\dot{\hat{\underline{\varepsilon}}}^p = \frac{D_o}{\sqrt{J_2}(1-d)} exp\left(-\frac{1}{2}\left(\frac{Z^2(1-d)^2}{3J_2}\right)^n\right)\hat{\underline{\sigma}} \tag{6-15}$$

Z hardening variable is assumed equal in the actual damaged state and in the equivalent virgin state, since, its evolution is mainly defined by the plastic work rate which is equal in both states.

6.2.5. Numerical integration technique

The elasto-visco-plastic laws are well-known to be stiff and difficult to integrate. Another problem is related to the time consuming matrix inversions necessary to perform iterations at the constitutive law level. The integration scheme proposed by Zhu & Cescotto 1994 for their Bodner's model version has been extended to the present damage Bodner's model. In fact, this scheme applies previous work from Szabo 1985 and Dombrovsky 1992. The summary of the integration scheme has been published in Habraken *et al.* 1995; it will not be reproduced here.

6.2.6. Identification, general principle

The parameter identification procedure is summarized by Figure 6-8. The parameters for the damage evolution laws and Bodner's parameters applied on effective behavior in the equivalent virgin state are first computed separately thanks to different experimental tests. Then the model defined by this parameter set is used to simulate uniaxial tensile and compression states and to compare the model results to experimental curves. The final parameters set is reached thanks to an optimization process that modifies the less accurate experimentally defined parameters to reduce the difference between simulated and experimental values.

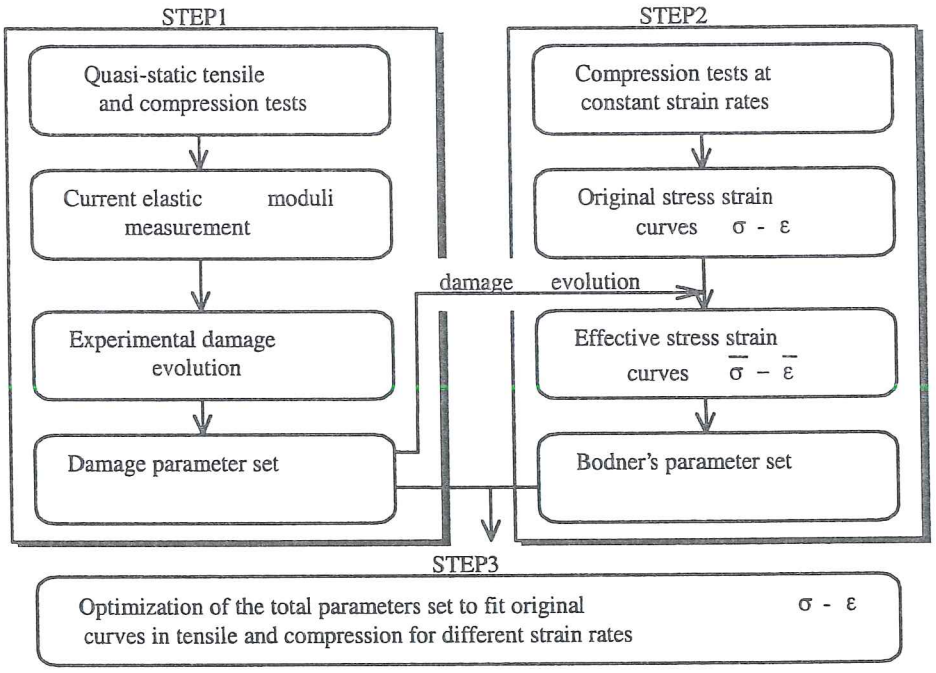

Figure 6-8 Summary of parameter identification procedure for damage Bodner's model (from Habraken *et al.* 2000).

This approach has been preferred to a global inverse procedure in order to preserve the physical meaning of each parameter.

Each step of this parameters identification procedure is now described for the chosen annealed aluminum. This material is only available under the form of tubes of limited thickness (see Figure 6-7).

6.2.7. Damage parameters identification

A. Tensile tests

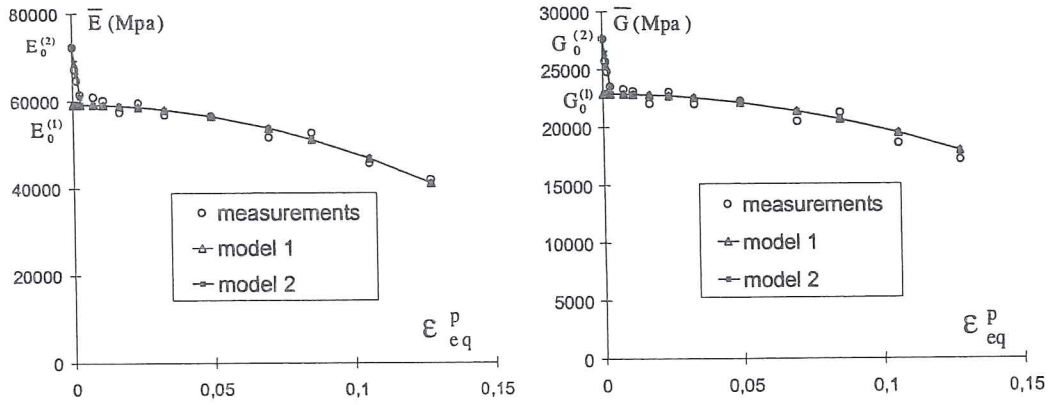

a b

Figure 6-9 Moduli measurements and models versus plastic strain for quasi-static tensile tests, a) apparent Young's modulus, b) apparent shear modulus (from Habraken *et al.* 2000).

Cyclic loading and unloading quasi-static tensile tests performed on the whole tube allow to measure Young's and shear moduli evolution. Figures 6-9a and b show the experimental results and two possible representative analytical curves which neglect or not the phenomena occurring at the beginning of plasticity. The two damage variables are directly deduced from these measures:

$$d = 1 - \sqrt{\frac{\bar{G}}{G_o}} \quad \delta = 1 - \sqrt{\frac{\bar{\chi}}{\chi_o}} \tag{6-16}$$

where $\bar{\chi}$ is the bulk modulus computed by:

$$\bar{\chi} = \frac{\bar{E}.\bar{G}}{3(3\bar{G} - \bar{E})} \tag{6-17}$$

Figure 6-10a and b show the experimental damage evolutions as well as reduced curves used further as explained in part C. of this section.

According to the classical macroscopic damage theory as described by Lemaître & Chaboche 1985, extrapolated value of Young's and shear moduli $E_o^{(1)}, G_o^{(1)}$ (see Figure 6-9) should be used. This gives damage values growing in a monotonic way from zero as represented by model 1 curves on Figure 6-10a and b. The difference between the elastic moduli $E_o^{(2)}, G_o^{(2)}$ and their extrapolated values $E_o^{(1)}, G_o^{(1)}$ is assumed to be related to plasticity entrance and not to damage as specified by Chevalier 1988 in his thesis.

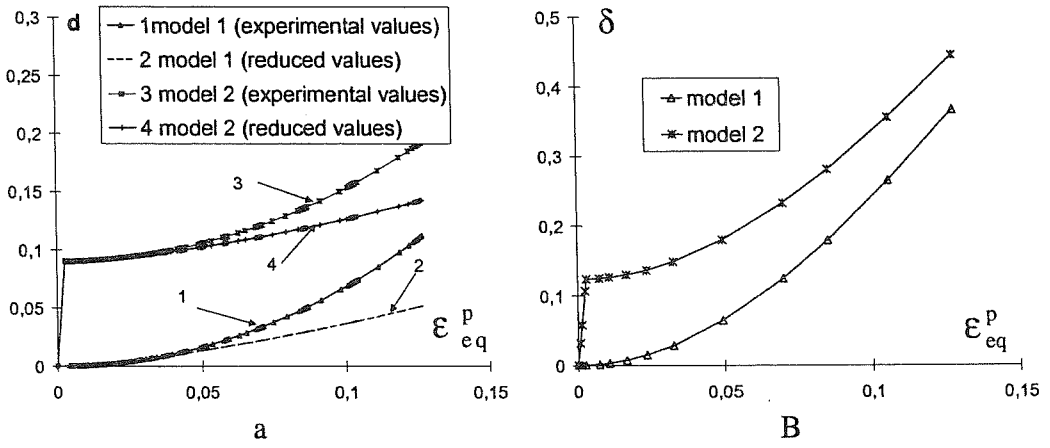

Figure 6-10 Experimental damage evolutions in tensile state according to model 1 or 2, a) deviatoric damage d, b) volumic damage, δ (from Habraken *et al.* 2000).

However looking to the damage theory proposed by Gurson 1977 or one of its late versions (Leblond *et al.* 1995), this fact could also be linked to a void nucleation rate that increases the void volume fraction very quickly at plasticity entrance and is followed by a smoother void growth rate. In the present aluminum 2024 alloy, optic microscopy has demonstrated the presence of precipitates which show a matrix decohesion after plasticity entrance. Such a phenomenon is not seldom. For instance in Pardoen's thesis 1998, which is dedicated to copper and is based on numerous electronic microscopic analyses, an initial void volume fraction is assumed to take into account the precipitate decohesion, that appears after microscopic strain.

Here, as the present research has no real microscopic part and is based on a macroscopic model, it has been decided to work with two assumptions: damage is computed according to $E_o^{(1)}, G_o^{(1)}$ or $E_o^{(2)}, G_o^{(2)}$. Of course this affects the numerical modeling and leads to verify two models: Model 1, where damage evolution is defined according to equations (6-10) and (6-12), and Model 2, where damage follows a quick linear increase at plasticity entrance and, afterwards, respects equations (6-10) and (6-12).

The constant damage ratio $\tau = \delta / d$ assumption is "reasonably" verified. Its variation is [3.24, 4.12] for Model 1 and [1.37, 2.30] for Model 2.

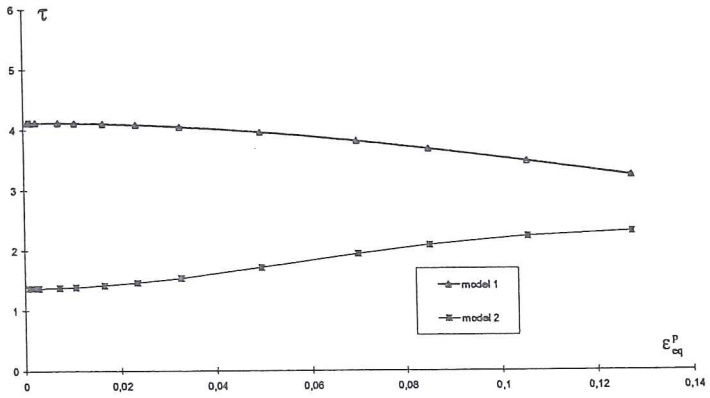

Figure 6-11 Experimental damage ratio in tensile state for model 1 and 2 (from Habraken *et al.* 1999).

B. Compression tests

First, small cubes extracted from the tube wall were compressed in order to check the isotropic behavior of the material. Then cyclic loading and unloading were performed on small cylinders (diameter 7 mm, height 7 mm) and Young modulus was deduced from the force measure and from the press table displacement corrected by the press stiffness estimated from a test without sample. The table lubrication and straightness were carefully checked to avoid barreling and non-uniform contact.

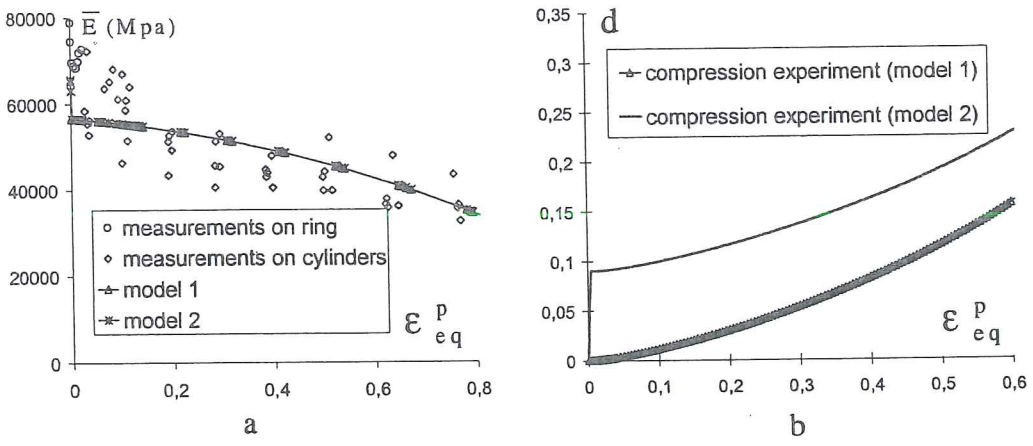

Figure 6-12 Compression state, a) apparent Young's modulus measurements versus plastic strain, b) experimental deviatoric damage (from Habraken *et al.* 2000).

The experimental results present however some dispersion (Figure 6-12a) even if the decreasing character of the modulus is corroborated. To improve accuracy, cyclic compression tests on a ring (slice of the tube) have been performed in the range of

small plastic strains. Here the sample size allows the use of strain gages and a second set of experimental points has been added on Figure 6-12a. Finally, the initial Young's modulus in compression test (78915 MPa) is slightly higher than in tensile state (72250 MPa). It has been assumed that this variance is due to different presses and different measurement techniques. To reach damage parameters in compression, thanks to relations (6-16) and (6-17), effective shear modulus measurements should be available. Practical problems, related to the sample geometry and the barreling for large strain, prevent to measure this modulus accurately. Adding the assumption of no volumic damage in compression (equation 6-12) yields the following relation:

$$d = 1-(1-D)\sqrt{\frac{E_0}{3G_0 - 3G_0(1-D)^2 + E_0(1-D)^2}} \tag{6-18}$$

where D is the classical damage parameter in a "one damage variable" model :

$$D = 1-\sqrt{\frac{\overline{E}}{E_0}} \tag{6-19}$$

So, the experimental deviatoric damage evolution is deduced from Figure 6-12a and relations (6-18), (6-19). It is presented on Figure 6-12b.

C. Damage parameters identification

Let σ be the actual value of the stress in uniaxial tests, then F the triaxiality function defined by relation (6-11) is straightforward:

$$F_T(\underline{\sigma}) = (1-2\alpha)^\theta \sigma \tag{6-20}$$

with $\theta=0$ in tensile state and 1 in compression state.

For model 1, the integration of the damage evolution law defined by equation (6-10) results in the following relation:

$$d = 1-(1-\frac{(S+2)(1-2\alpha)^{\theta s}}{2A^S}\int_o^{\varepsilon_{eq}^p}\sigma^s d\varepsilon_{eq}^p)^{1/S+2} \tag{6-21}$$

if no strain rate effect on damage evolution ($r=1$) and no threshold value ($\sigma_D=0$) are assumed. These additional hypotheses are related to the experimental damage observations (Figure 6-10a and Figure 6-12b) and to the low viscosity effect observed in section 6.2.8 for this aluminum. For model 2, the principle is identical except that the damage evolution law is first linear until damage has reached a transition value.

The problem is now reduced to a classical inverse method: knowing relation (6-21) and experimental curves (Figure 6-10a and Figure 6-12b) find the best parameters set (S, α, A), that minimizes differences between model and experiments. In fact for tensile state, the reduced values (Figure 6-10a) and not the experimental ones have been used as a target value. This choice, that slows down damage evolution in

tension in the model, was imposed because, otherwise, it was impossible to reach an effective reference curve $\overline{\sigma}_{eq}\,\overline{\varepsilon}_{eq}$ compatible with tensile and compression experimental curves (see Figure 6-13). Using a reduced damaged curve in traction leads to doubts about both experimental works and theoretical assumptions. One possible explanation is that, due to various thermal treatments applied to the aeronautic rod, the sets of rods used for the tensile tests and for all other tests were different. A posteriori microscopic investigation presents some variance according to the sample origin. Another possibility is a severe lack of accuracy in the damage measurements of tensile tests. However, this is unlikely because, as reported in Wang 1996 and Habraken, Zhang and Wauters 1997, the tests performed on the whole rod have used different types of strain gages and extensometers that yield similar results. A final possibility is the existence of a scale effect in the measurement devices or in the material. Recall that the macroscopic length of all samples covers a quite large scale as the rod diameter is 75 mm and its thickness varies from 9.4 to 2.9 mm. Notch and small compression samples were cylinders of diameter 7 mm, when all other samples were quite larger.

		Model 1	Model 2
S	Stress function exponent in damage model	2,006	2,5274
A (MPa)	Stress function constant in damage model	256.74	250
σ_D	Damage threshold stress	0	0
R	Exponent of equivalent strain rate in damage model	1	1
α	Triaxiality function parameter	0.216	0.2136
d_1	Transition deviatoric damage value (model 2)	0	0,09
ε_{eq1}	Transition equivalent strain value (model 2)	0	0,0029

Table 6-1 Parameters sets for damage models 1 and 2 (from Habraken *et al.* 2000).

Table 6-1 summarizes the final damage parameter sets provided by the inverse modeling method. One can check that tensile state is the driving mechanism for damage increase, then comes shear state, and finally compression state. So a tensile state coupled to a large triaxiality ratio leads to the fastest deviatoric damage increase.

6.2.8. Bodner's parameters identification

A. Quasi-static uniaxial tests

The damage evolution defined by the parameter sets from Table 6-1 and equations (6-7) to (6-12) allows the computation of effective curves $\overline{\sigma}_{eq} - \overline{\varepsilon}_{eq}$, once experimental curves σ_{eq}-ε_{eq} are known.

Applied to quasi-static uniaxial tensile and compression tests ($\dot{\varepsilon} = 0.004s^{-1}$), this procedure provides an effective curve $\overline{\sigma}_{eq} - \overline{\varepsilon}_{eq}$ that models the actual microscopic behavior of the material in both states (see Figure 6-13). This result was made possible only by adopting reduced values for tensile damage.

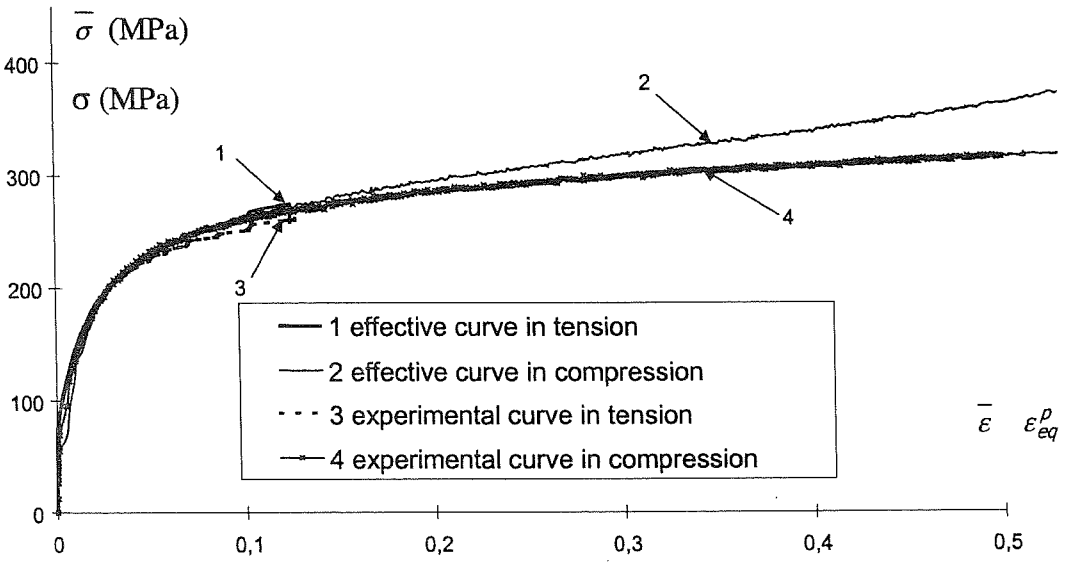

Figure 6-13 Experimental and effective stress strain curves in compression and tensile state for quasi-static experiment, Model 1 (from Habraken *et al.* 1999).

It must be noted that the plastic strain reached during tensile tests is much smaller than in compression. The range $0 \leq \varepsilon^p_{eq} \leq 0.12$ covered by tensile tests (Figure 6-9a) corresponds to the region of maximum scatter of the compression results (Figure 6-12a).

B. Compression tests at various strain rate

The experimental device being used is limited to cylindrical samples of 7 mm height for a 20 s^{-1} constant strain rate. This strain rate level already means an initial punch velocity of 140 mm/s. For 20 s^{-1} constant strain rate, an upsetting test stopped at a strain of 70% is performed in 0.035 second. So, one cannot neglect the temperature increase due to plastic dissipation during the test. Considering classical thermal coefficient for an aluminum and using an adiabatic assumption lead to a temperature increase of ≈ 80°C. The temperature dependence of the material behavior has been checked by quasi-static uniaxial compression tests at room temperature (16.5°C) and at 100°C.

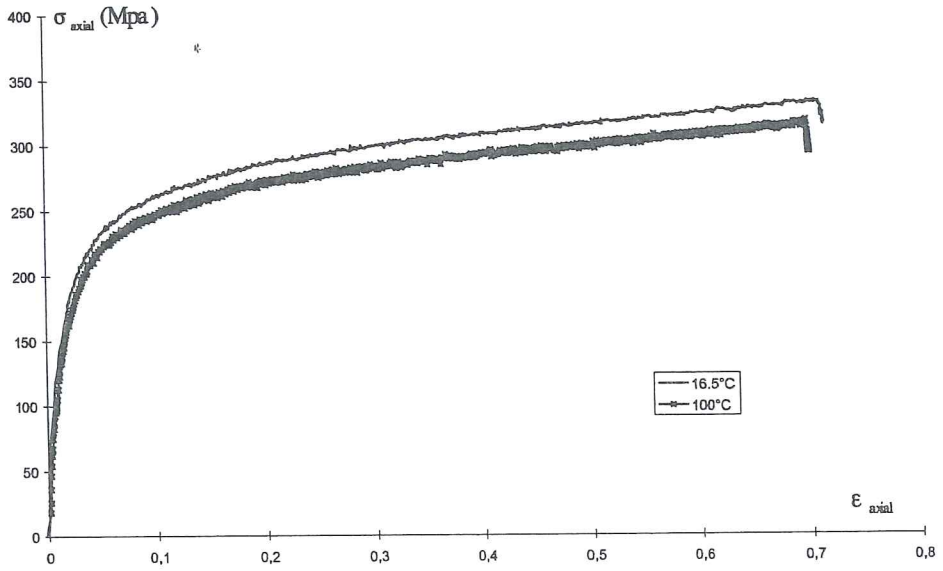

Figure 6-14 Stress strain curves for quasi-static compression tests performed at 16.5°C and 100°C (from Habraken *et al.* 1999).

So using a temperature effect issued from preceding tests, a quasi-adiabatic assumption (for tests performed at $\dot{\varepsilon} = 10\ s^{-1}$ and $20\ s^{-1}$), as well as the damage evolution law (model 1) defined in preceding sections, the effective stress strain curves (Figure 6-15b) are deduced from experiments (Figure 6-15a).

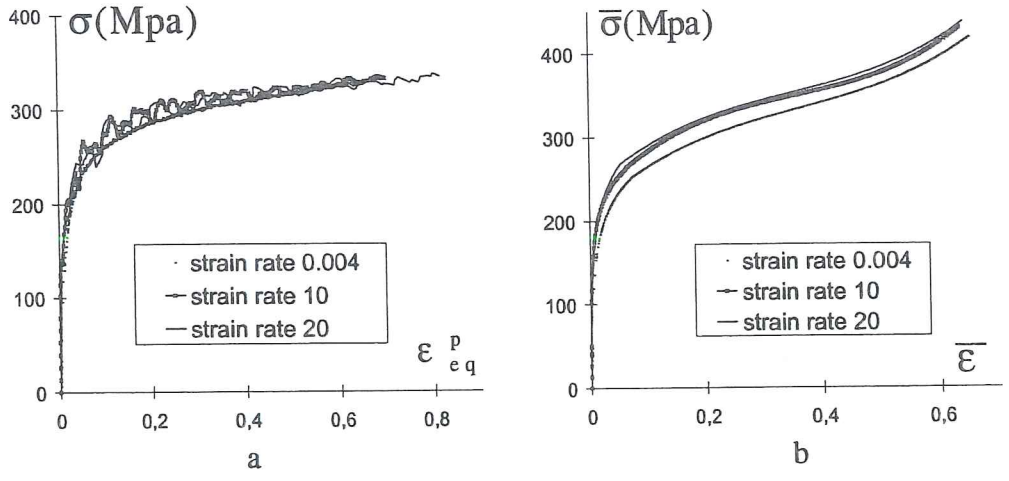

Figure 6-15 Compression at constant strain rates, a) experimental stress strain curves, b) computed effective stress strain curves (from Habraken *et al.* 2000).

Even if the stability of the performed large strain rate tests is limited, Figure 6-15a allows to verify that the viscous effect on this material is limited for the considered

strain rates. The accuracy of computed effective curves (Figure 6-15b) is poor due to the rough thermal correction and the low stability of experimental tests (Figure 6-15a).

C. Bodner's parameters identification

The applied identification procedure of Bodner's parameters partially comes from Chan *et al.* 1988. Bodner's law for a uniaxial test is expressed by the following scalar relation:

$$\frac{\sigma}{Z}=\left[2ln\left(\frac{2D_o\sigma}{\sqrt{3}\dot{\varepsilon}^p|\sigma|}\right)\right]^{-1/2n}=g \qquad (6\text{-}22)$$

where $\sigma/|\sigma|=-1$ for uniaxial compression and $\dot{\varepsilon}^p$ is constant for the selected tests. As D_o, assumed limit of plastic shear strain rate, is chosen by the user, the constant g is easily computed for each experiment once n is known. At room temperature, the thermal softening effect is negligible, so isotropic and directional hardening laws are reduced to their first term (relations 6-6a and b). Additionally for uniaxial tests, $\underline{\beta}$ the directional symmetric tensor is reduced to one non zero component equal to the directional parameter Z_D. The hardening relations are then:

$$\dot{K}=m_1(K_1-K)\dot{W}^p \quad \text{with } K(0)=K_o \qquad (6\text{-}23)$$

$$\dot{Z}_D=m_2(D_1-Z_D)\dot{W}^p \quad \text{with } D(0)=0 \qquad (6\text{-}24)$$

$$Z=K+Z_D \qquad (6\text{-}25)$$

The function $\gamma(\sigma)$, derivative of the stress with respect to plastic work, is then used to find m_1 and m_2. Its definition and previous relations (6-22 to 6-25) lead to:

$$\gamma(\sigma)=\frac{d\sigma}{dW^p}=g(m_1(K_1-K)+m_2(D_1-Z_D)) \qquad (6\text{-}26)$$

Theoretically this function defines 2 linear parts:

-for small plastic strain, isotropic hardening is equal to K_o while directional hardening is increasing:

$$K=K_o$$
$$Z_D=Z-K_o=\frac{\sigma}{g}-K_o \qquad (6\text{-}27)$$

-for large plastic strain, directional hardening has reached its saturation level D_1 while isotropic hardening is increasing:

$$Z_D = D_1$$
$$K = Z - D_1 = \frac{\sigma}{g} - D_1 \qquad (6\text{-}28)$$

This theoretical approach is represented on Figure 6-16 which also defines saturation stress σ_s and coefficient a. However, the function γ issued from the effective stress strain curves represented on Figure 6-15b is quite far from this theoretical shape, which leaves quite a large range to chose m_1 and m_2.

The value of the saturation stress σ_s can be used to find n, the strain rate sensitivity coefficient. Relation (6-22) and the definition of σ_s recalled on Figure 6-16, give :

$$ln\,\sigma_s = -\frac{1}{2n} ln(\,2\,ln\frac{2D_o}{\sqrt{3}\dot{\varepsilon}^p}\,) + ln(\,K_1 + D_1\,) \qquad (6\text{-}29)$$

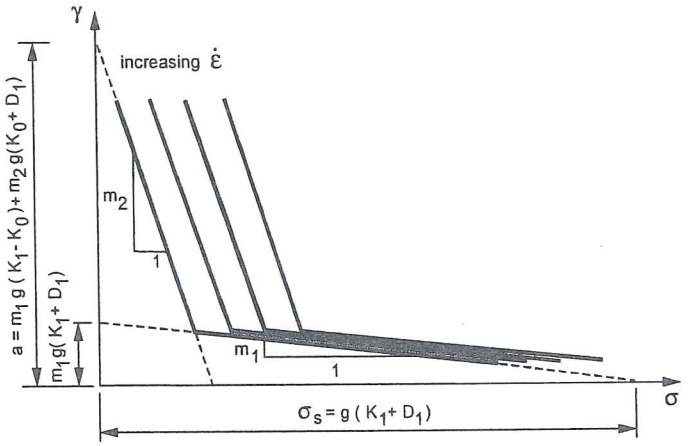

Figure 6-16 Function $\gamma(\sigma)$ for an ideal theoretical case (Habraken *et al.* 2000).

Again the performed tests do not yield co-linear points, which leaves some freedom to define the value of n. The hardening values are extracted from the stress strain curves, relation (6-22) and g value:

$$\sigma_o = g\,K_o$$
$$D_1 = \frac{\sigma_1}{g} - K_o \qquad (6\text{-}30a,b,c)$$
$$K_1 = \frac{\sigma_s}{g} - D_1$$

where σ_o is the yield stress value, σ_1 the stress at saturation of directional hardening and σ_s the stress saturation value.

The preceding procedure helps to define the range of the different parameters. The final parameters set is then obtained by optimization. At this level, Tables 6-1 and

6-2 define the whole parameters set of the models 1 and 2 and one can check that simulated curves by Bodner's damage models (1 or 2) are near experimental ones on Figures 6-17a and b representing respectively stress and damage evolution with strain for uniaxial tests. The RR' line defines the experimental rupture in tensile state.

		Damage model 1	Damage model 2
Parameter	Physical meaning	Value set	Value set
E (MPa)	Young's modulus	72250	65660
ν	Poisson's coefficient	0,31	0.31
D_o (s^{-1})	Assumed limit plastic shear strain rate	10^8	10^8
K_o (MPa)	Initial isotropic hardness	106.584	99.506
K_1 (MPa)	Maximum isotropic hardness	341.744	358.661
K_2 (MPa)	Minimum isotropic hardness	106.584	99.506
D_1 (MPa)	Maximum directional hardness	231.445	239.131
m_1	Isotropic hardening parameter	0.091	0.0125
m_2	Directional hardening parameter	0.33	0.43
N	Strain rate sensitivity coefficient	5.5126	6.8524

Table 6-1 Bodner's parameters sets to recover effective stress strain curves, models 1 and 2 (from Habraken *et al.* 2000).

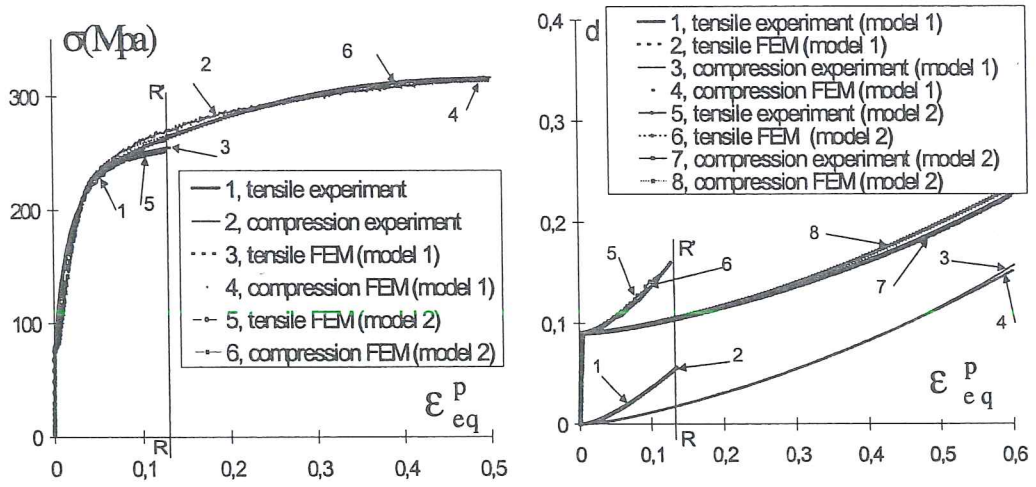

a b

Figure 6-17 Experimental and simulation results in quasi-static tensile and compression state: a) stress-strain curves, b) deviatoric damage evolution with strain, experimental reduced curve in tension (from Habraken *et al.* 2000).

6.2.9 Definition of finite element size

As underlined in chapter 5, the size of the elements used in the mesh is important. So a sensitivity analysis has been performed.

The simulated experiment consists in a tensile test on a cylindrical bar presenting a narrow part in its middle. The geometrical details are given on Figure 6-18, the test is driven by the displacement of one extremity at the constant velocity of 0.005 mm/s while the elongation of the middle part is measured between points AA'.

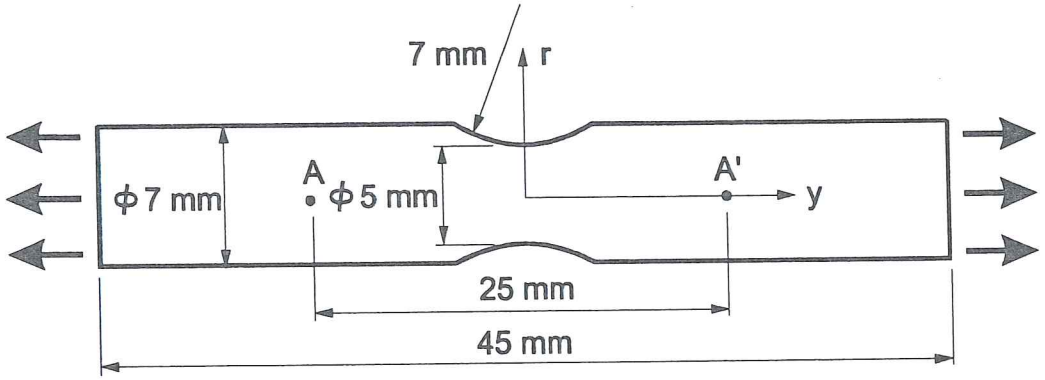

Figure 6-18 Sample description – Notch test (from Habraken *et al.* 2000).

Figure 6-19 presents the experimental global force-displacement curve for each of the four experimental tests. One can verify that the dispersion is quite low.

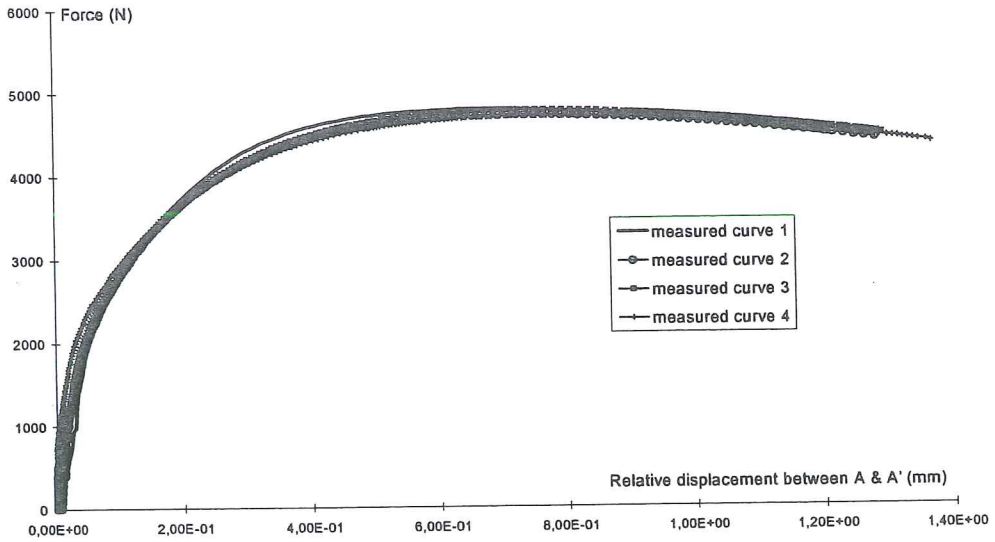

Figure 6-19 Force-displacement curve for the 4 notch test experiments.

The mesh dependence has been verified for the constitutive law using model 1 for the damage evolution rule. The simulations are performed in axisymmetrical state on one quarter of the sample by symmetry. Six different meshes (Figure 6-20) have been used to verify the stability of the simulation results. They differ by the mesh density at the notch level.

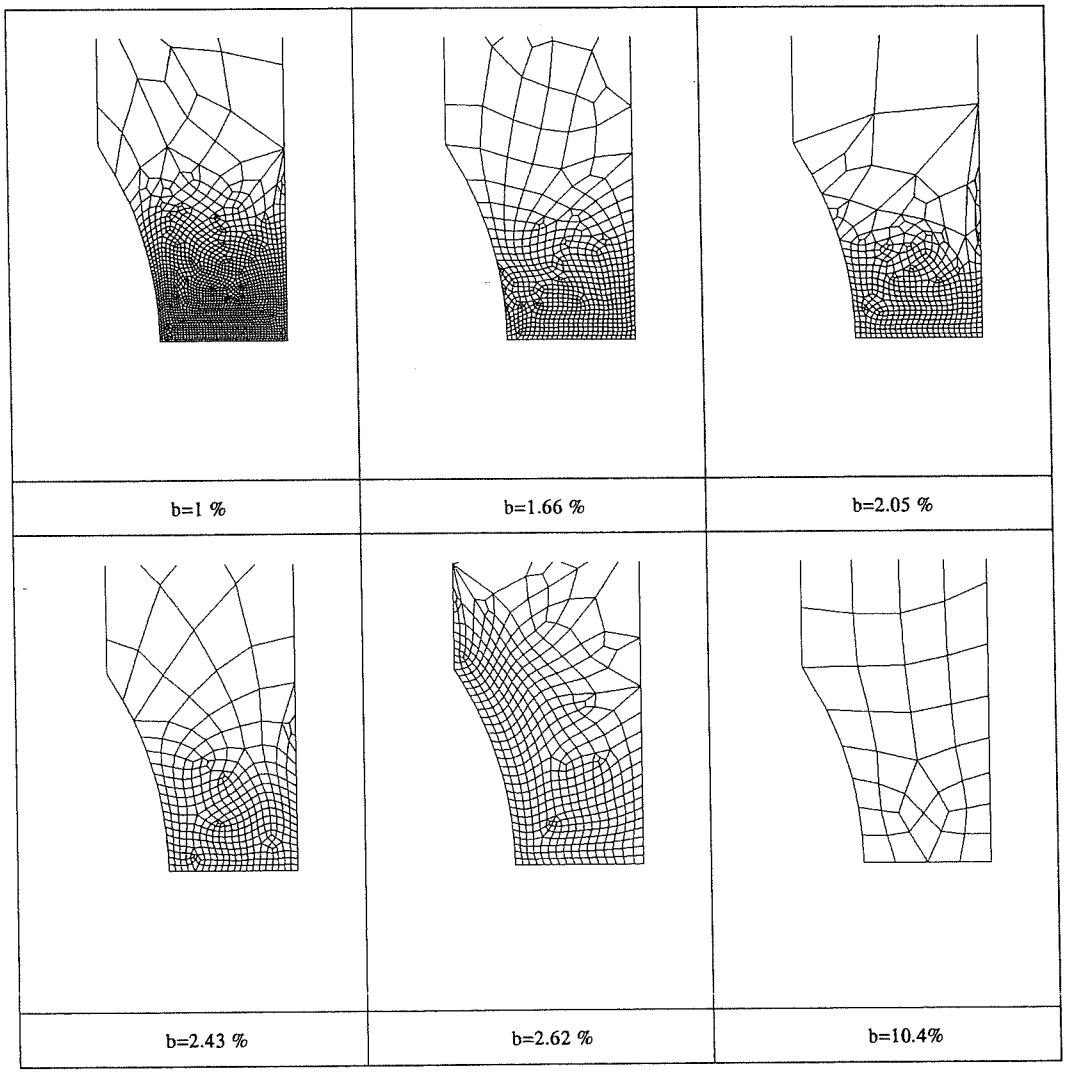

Figure 6-20 Mesh descriptions near the notch, *b* is the ratio between the diagonal of the smallest element and the notch radius (7 mm), from Habraken *et al.* 1999.

Figure 6-21 collects some of the results of the numerical simulations and one experimental curve since no significant experimental dispersion occurred. The RR' line at relative displacement of 0.96 mm represents what is called "the first experimental rupture". Because the global fracture appears quite later, this initial

rupture location could seem strange. However the force-time curve, not reproduced here, allows detecting the necking beginning for this relative displacement of 0.96 mm. For all other validation tests, the RR' line effectively identifies the moment when the first small macroscopic crack appears. According to the type of the structure, this happens nearly simultaneously or not with the global fracture. From the 4 types of tests described in following sections, the notch test is the only one presenting a clear "macroscopic" necking phase before rupture. As the present Bodner's damage model does not specifically simulate coalescence, necking beginning has been chosen as "experimental rupture" for the notch test analysis.

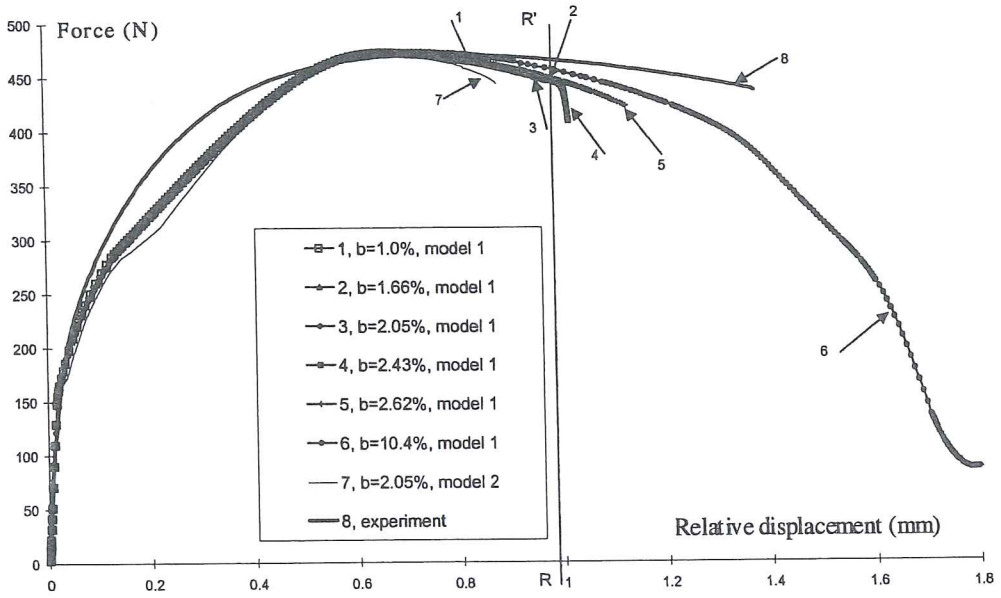

Figure 6-21 Experimental and simulation force-displacement curves, meshes are defined on Figure 6-20 (from Habraken *et al.* 2000).

Figure 6-21 global force-displacement curves show that the hardening model is not perfect, compared to the material behavior. This could have already been suspected from experimental and simulated tensile curves of Figure 6-17. Without serious modifications of the hardening description of Bodner's approach, it is not possible to improve this result. A good point is that the curve maximum is well predicted no matter model 1 or 2 is adopted for damage evolution. The mesh dependence of the result is not observed until this maximum is passed. Then depending on the mesh, the simulation stops because of non convergence, with or without noticeable slope variation in the global force elongation curve. So if this slope variation is taken as criterion for global rupture, simulation results are mesh dependent and not very consistent with experiments.

It is interesting to note that Rousselier 1987 uses the "load-diametral contraction" curve and more specifically its slope after crack initiation to determine accurately the

required finite element size. He applies finite element simulations with an elasto-plastic damaged law to notch tests. Then he argues that, numerically, the collapse of the stress happens in the strongly damaged zone. So the growth rate of cracks depends on the finite element size l_c, at the tip of the crack. In ductile fracture, a classical size is the average distance between inclusions and Mudry 1982 proposes to derive l_c from the number of inclusions per unit of volume N_V:

$$l_{c0} = 2 \sqrt[3]{N_v} \tag{6-31}$$

In the present work, the different analyzed meshes have a typical finite element size varying from 0.17 mm to 0.75 mm near the crack initiation. The number of precipitates is unknown. The final experimental slope in the "force-displacement" curve (Figure 6-19) is unavailable either due to the velocity of the breakdown related to the small size of the sample. For the other experiments like the shear test (section 6.2.10 D), the bending test (section 6.2.10 C) and the tensile test of a perforated specimen (section 6.2.10 B), the final slopes of the load displacement curve have been registered and could be used to adjust l_c. However experimental dispersion does not provide accurate information. In conclusion, Rousselier's approach to adjust finite element size has not been applied here. As the goal of the research is the rupture prediction and not the study of crack propagation, this is acceptable. Note that 2 parameters are responsible for the final slope in numerical simulations: the characteristic size l_c and the damage rate during coalescence and even after as, in the described approach, the elements still exist but with a vanishing stiffness.

Another other way to verify the mesh dependence of the results is to look at the damage variable map. This approach is often far more sensitive than a global force displacement curve. Figures 6-22a and b collect the deviatoric damage curves along r and y axes (defined on Figure 6-18) near the maximum of the global curve.

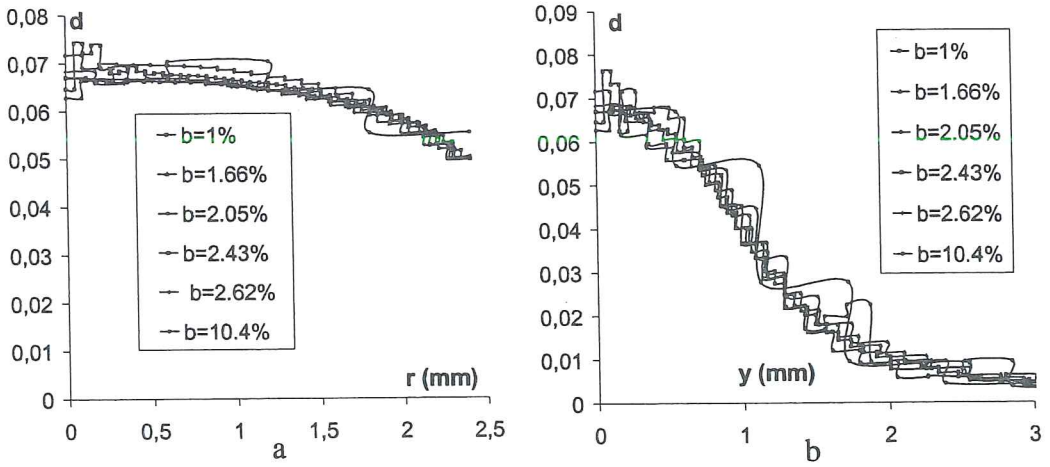

Figure 6-22 Deviatoric damage variable for an elongation of 0.65 mm of the base AA': a) along r axis, b) along y axis (from Habraken *et al.* 2000).

Figure 6-22a shows a small range of variation of the deviatoric damage value with the mesh except for the center point and the coarser mesh. The effect is slightly stronger on Figure 6-22b. Such local variations can explain why the simulation convergence is lost at different moments when damage increases. However, if some smoothing procedure is used to represent the deviatoric damage map, one will find that the level and size of the localized damage zone is quite identical for each mesh even the coarser one.

In conclusion, the damage map for this notch test simulation has a low mesh dependence. The b ratio taking into account the radius of other samples geometry will be used to have an idea of the mesh density in the following sections. In practice, for the validation simulations, the mesh refinement has been applied when the presence of discontinuities in the stress, strain or damage fields indicates errors due to too coarse discretization. As proved by the simulation of the bending test (section 6.2.10 C), the shape ratio of the element is also an important parameter.

6.2.10 Validation

The interest of a macroscopic damage approach consists in its application to different type of material loading. So four different experiments have been performed and simulated:

- tensile test of a notched specimen,
- tensile test of a perforated specimen,
- bending test,
- shear test of a perforated specimen.

Each case is studied in following sections then a general discussion is proposed in section 6.2.11.

A. Tensile test of a notched specimen

As presented on Figure 6-18, this axisymmetric tensile test has a large notch radius, which means that the damage is maximum at the center of the neck leading to a cup-cone fracture. This well-known fact (Needleman & Tvergaard, 1984) is reproduced by the performed experiments. For this test as shown by Figure 6-23, the stress field is characterized by a very high triaxiality value T of the order of 1.4. This characteristic is computed by :

$$T = \frac{\sigma_m}{\sqrt{1/2\,\underline{\hat{\sigma}} : \underline{\hat{\sigma}}}} \qquad (6\text{-}32)$$

Note that, with such triaxiality definition, the value for a uniaxial tensile experiment is $T = 0.57$. In the notch test, the high triaxiality zone covers the middle part of the section at the neck center.

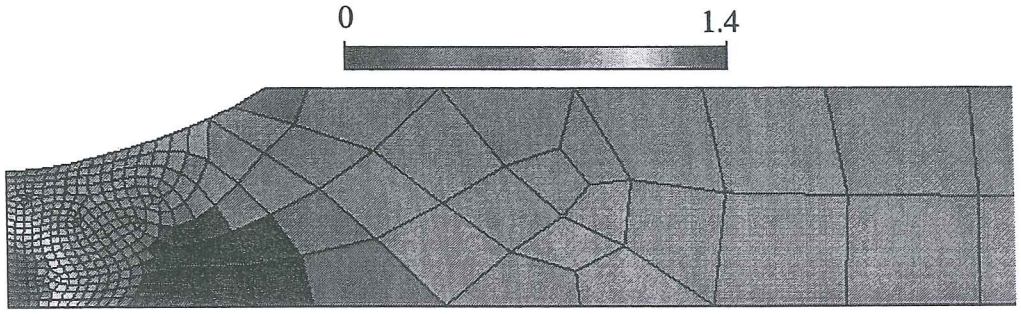

a Triaxiality *T*.

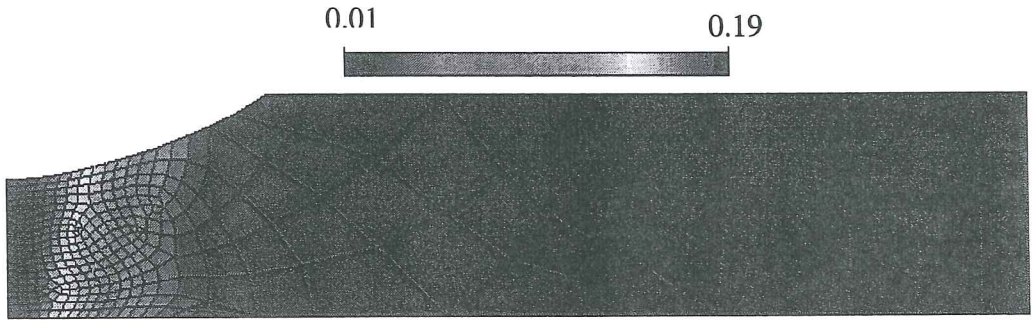

b Equivalent strain $\varepsilon_{eq.}$

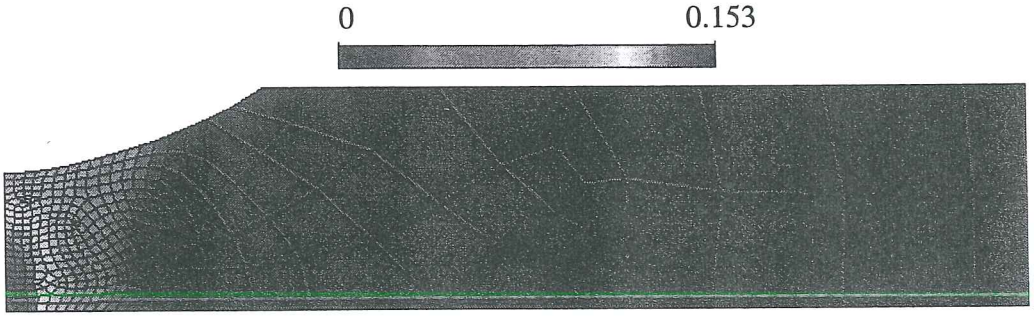

c Deviatoric damage *d*.

Figure 6-23 Notch simulation results (model 1) at RR' moment (partially published in Habraken *et al.* 2000).

The strain field confirms this high triaxial state: for a total displacement of 1.46 mm, an axial strain of 26 % and a radial strain of –12 % are reached in the neck center. The mesh used for the analysis of finite element results is the fourth one shown on Figure 6-20, characterized by a small *b* coefficient of 2.43.

Figures 6-23a, b and c respectively show the triaxiality factor, the equivalent strain and the deviatoric damage distribution of the simulation results for model 1 at the

moment identified as the "experimental rupture" (see Figure 6-21). Model 2 gives the same distribution for these 3 variables. A difference exists only on the values. For this reason, figures of results for model 2 will not be shown, neither for this example nor for the following ones, but the values will be given in Table 6-6b.

B. Tensile test of a perforated specimen

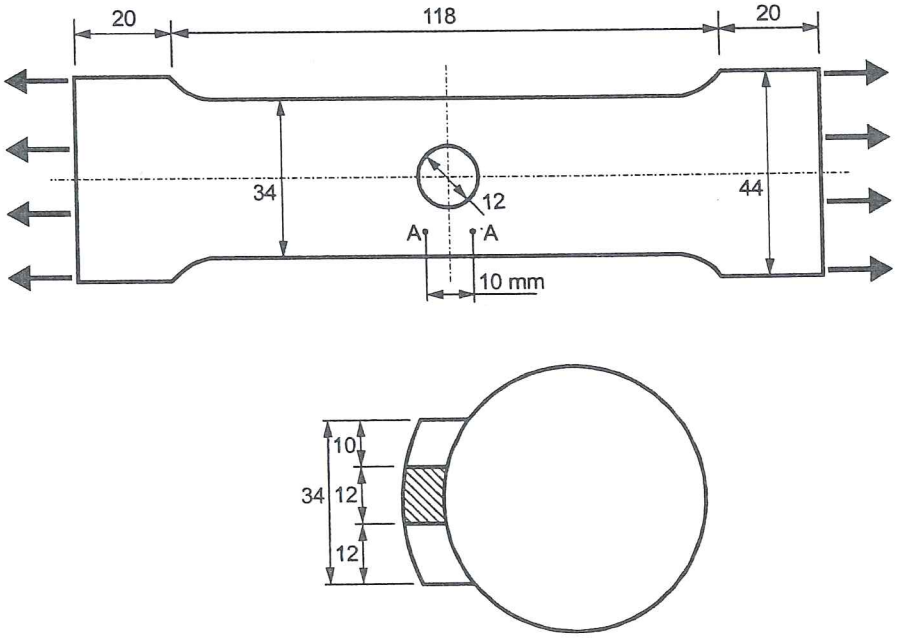

Figure 6-24 Tensile test of a perforated specimen: geometry, (from Habraken *et al.* 2000).

The sample geometry is shown on Figure 6-24. It is cut from the tube wall and is perforated in its center. The hole is not exactly in the center in such a way that one can predict on which side of the hole the fracture will begin and focus the camera on this side. A gauge length *AA'* is used for regulation: during the test, the extremity displacements are controlled so that a constant relative velocity of 0.01 mm/sec between *A* and *A'* is maintained. This is a three-dimensional problem. The specimen is discretized by 8-nodes 3D mixed finite elements (Figure 6-25). The ratio *b* between the diagonal of the smallest element and the hole radius is 9%. The ratio *c* between the maximal side and the minimal side of the smallest element is 2.3.

Numerically, it is difficult to keep a constant relative velocity between *A* and *A'* by loading. As the extremity displacements were not registered during the test, the measured tensile force has been imposed at the ends of the specimen. The relative displacement of *A* and *A'* until the maximum of the load have been verified. However to simulate the termination of the test, it has been necessary to change the loading strategy: after the maximum, the displacements of the ends of the specimen are imposed.

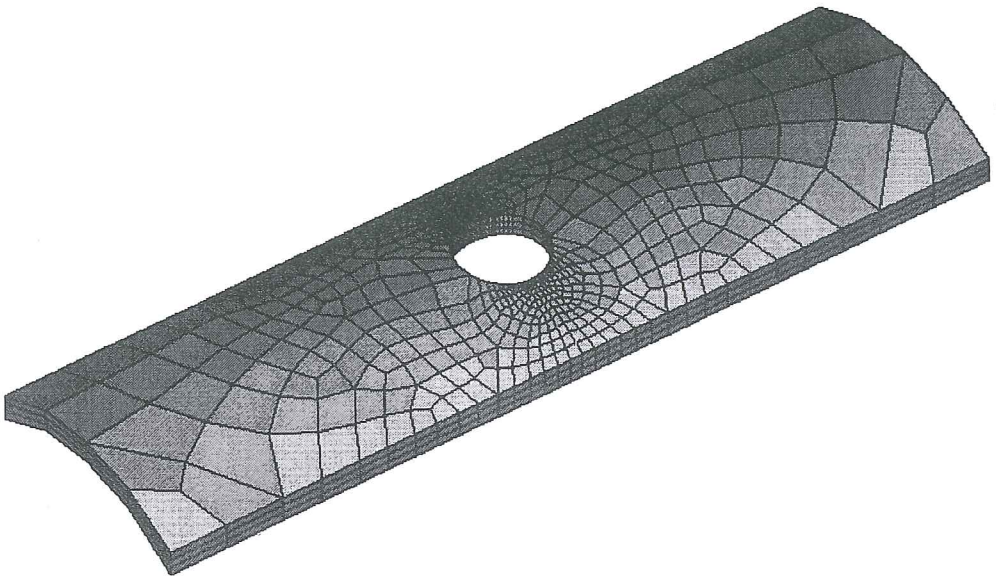

Figure 6-25 Tensile test of a perforated specimen: 3D finite element mesh (from Wang & Habraken 1996).

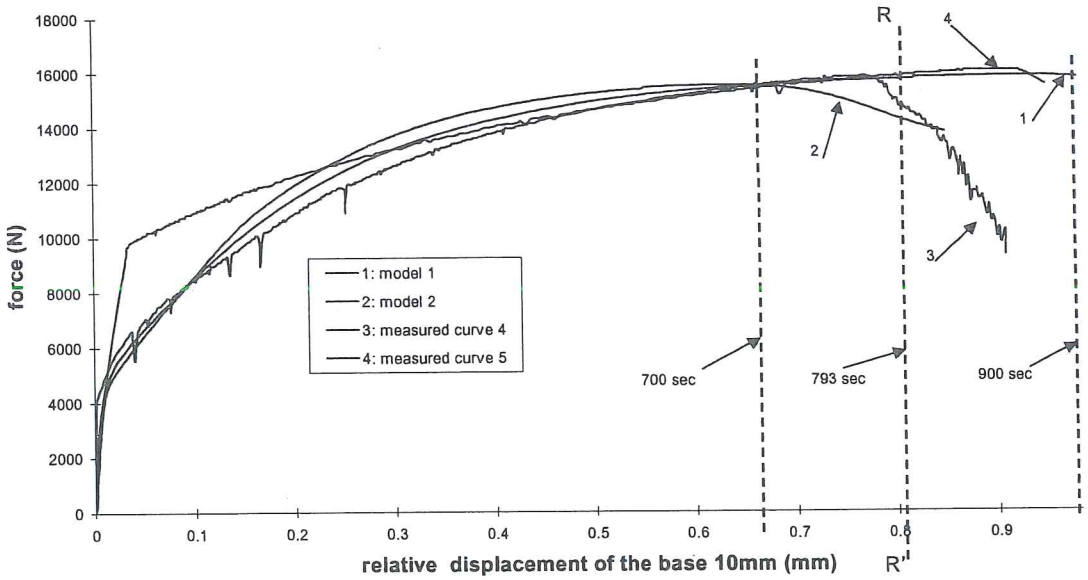

Figure 6-26 Force-relative displacement of the base AA' curves with time references (from Habraken *et al.* 2000).

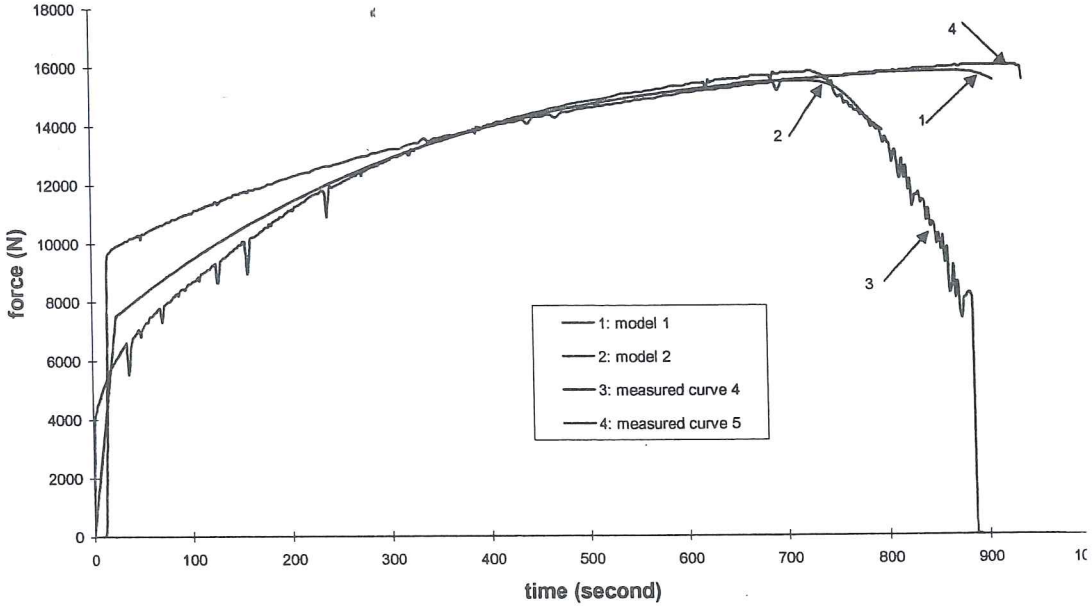

Figure 6-27 Force–time curves of the tensile test of a perforated specimen (from Habraken *et al.* 2000).

The comparison between the experimental measurements and the finite element calculations is given on Figure 6-26 for the force-displacement curves and on Figure 6-27 for the force-time curves. Generally speaking, model 2 is closer to the first test in which fracture takes place earlier, while model 1 is closer to the second test in which fracture happens later. The calculated force–time curves represent very well the drop of the experimental curve both for model 1 and model 2. But for the force-displacement curves, only model 2 follows this sudden drop trend, while model 1 shows only a little decrease of the force. This is due to a quick elongation developed at the moment of fracture.

For these simulations, at the "experimental fracture moment" (time 793 sec defined on Figure 6-26), the stress state is characterized by a relatively homogeneous triaxiality value, from 0.6 to 1.0, in the zone where deformation and damage are important. This value approaches the uniaxial tensile value "0.57".

Figures 6-28, 6-29 and 6-30 show respectively the triaxiality factor, the equivalent strain and the deviatoric damage distributions for model 1 at *RR'* moment. The equivalent strain is strongly localized at the two sides of the hole root. The largest equivalent strain reaches 26.3%. The largest axial strain, the largest radial strain and the largest circumferential strain are, respectively, 38.8%, 19% (negative) and 18.9% (negative). For the deviatoric damage, d_{max} reaches 0.15, and all values of d greater than 0.14 are located within 1.2mm from the hole root.

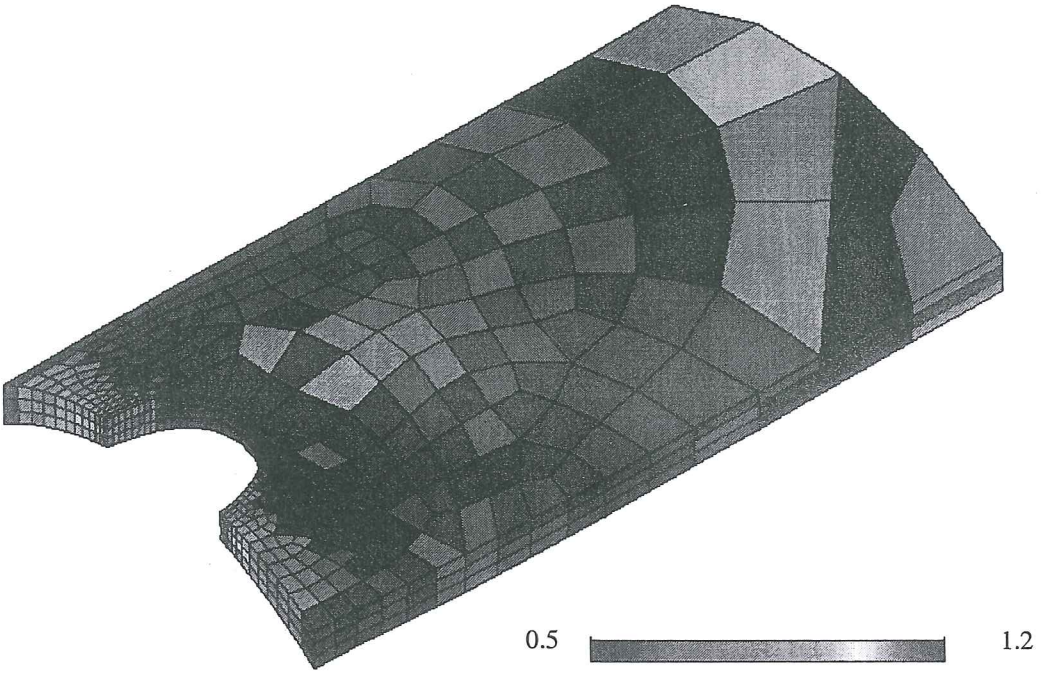

Figure 6-28 Tensile test on a perforated specimen, simulation results (model 1) at *RR'* moment, triaxiality *T*.

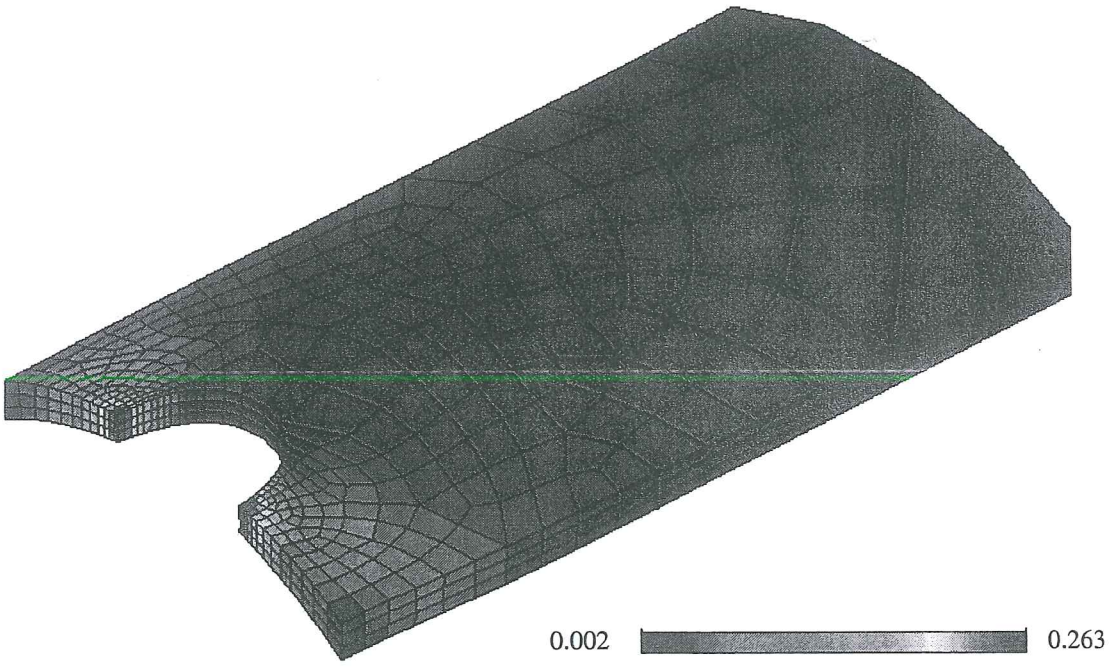

Figure 6-29 Tensile test on a perforated specimen, simulation results (model 1) at *RR'* moment, equivalent strain ε_{eq}.

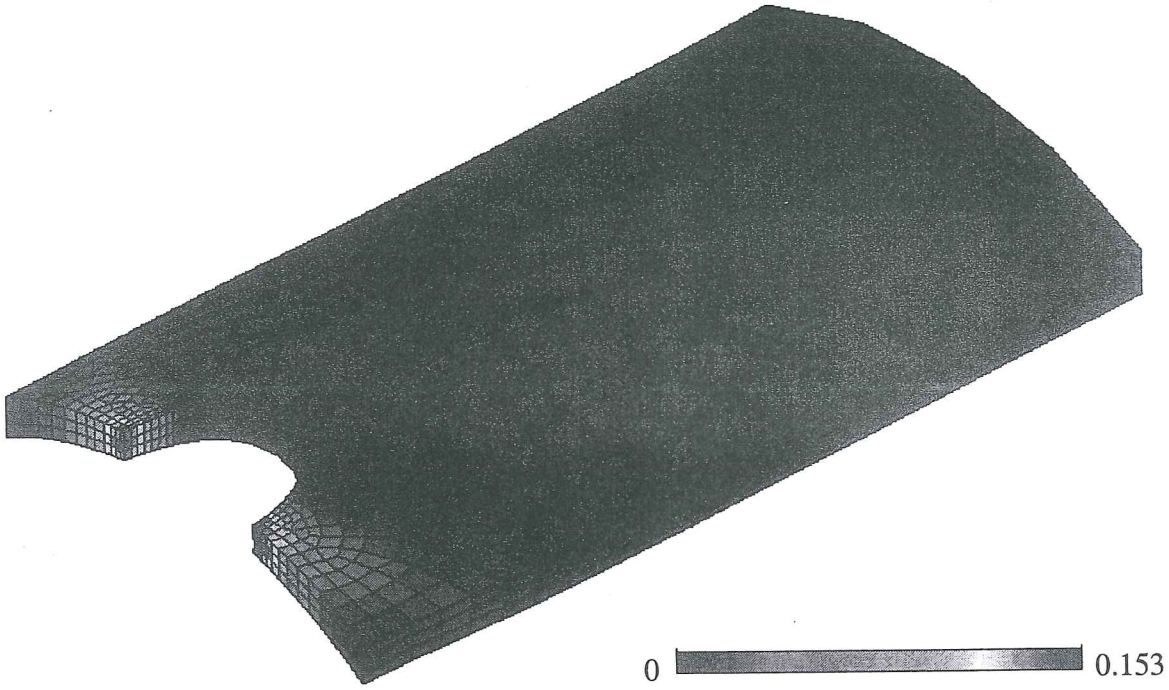

Figure 6-30 Tensile test of a perforated specimen, simulation results (model 1) at *RR'* moment, deviatoric damage *d* (from Habraken *et al.* 2000).

C. Bending test

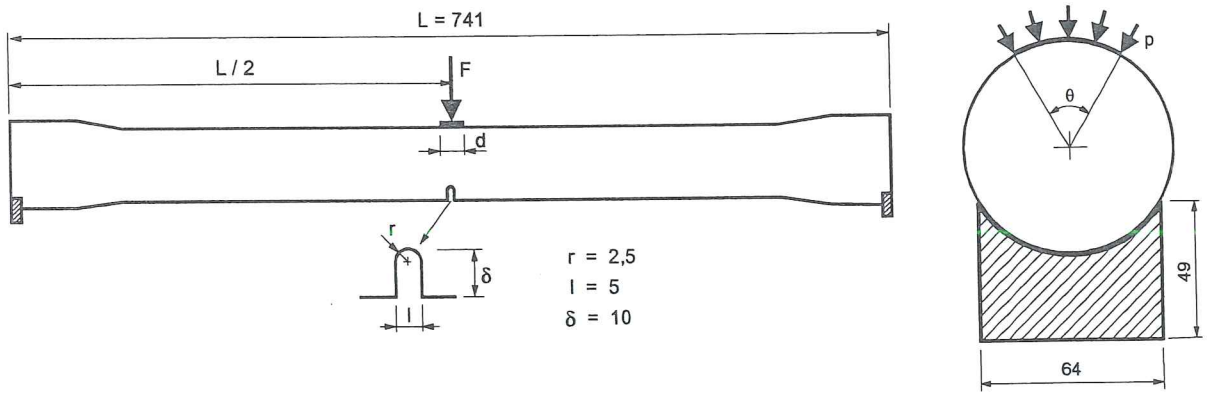

Figure 6-31 Bending test: geometry and loading (from Habraken *et al.* 2000).

The third example is a bending test. The notched whole tube is loaded and supported as a traditional three points bending, see Figure 6-31. The tube is discretized in 8-nodes 3D mixed finite elements (Fig. 6-32). The ratio *b* between the diagonal of the smallest element and the notch radius is about 12% and the ratio *c* between the maximal side and the minimal side of the smallest element is 9.5 for the first mesh with one layer of elements through the thickness (Figure 6-33a). This relatively high

c ratio leads to poorly shaped elements near the notch root. So a second mesh with two layers of elements through the tube thickness was used, its *c* ratio is 4.75, see Figure 6-33b.

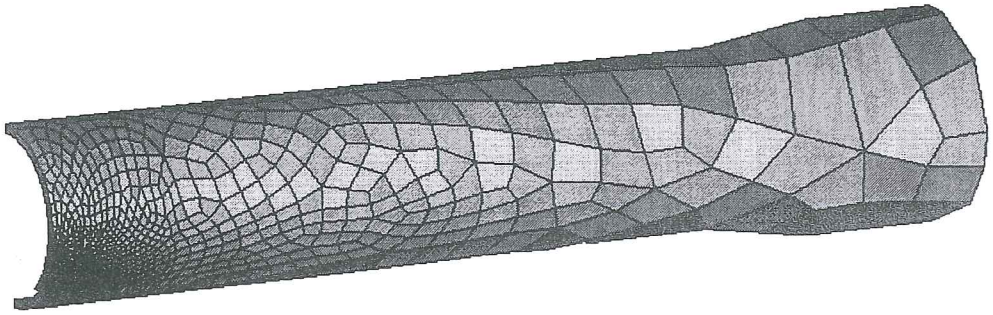

Figure 6-32 Bending test discretization, case of one element layer on the thickness, (from Habraken & Wang 1996).

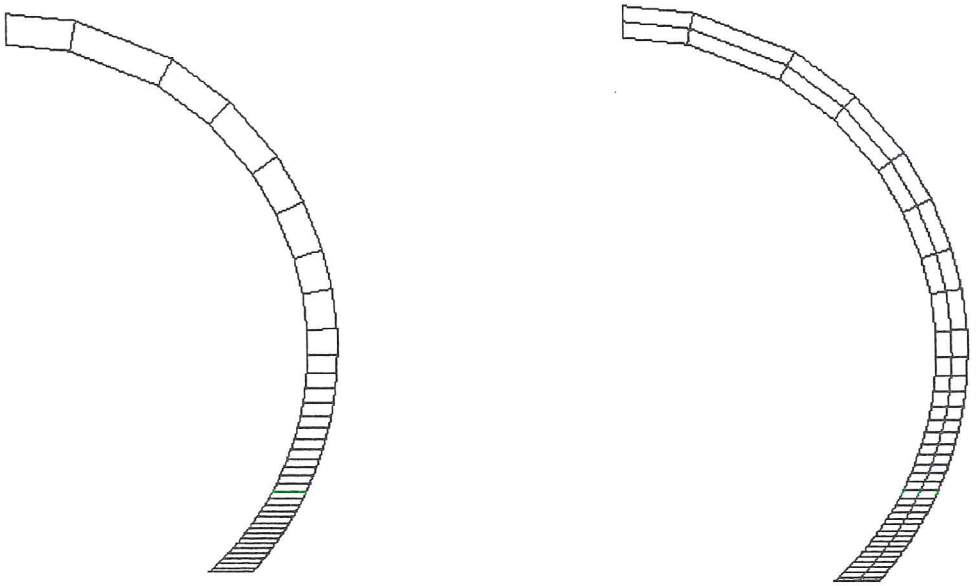

a. mesh1 b. mesh 2

Figure 6-33 Cross section in the bending test mesh: a) one layer , b) two layers.

The measured displacement of the middle section is imposed in the simulation which takes into account the problem symmetry. The numerical result of force-displacement in comparison with the experimental one is given in Figure 6-34.

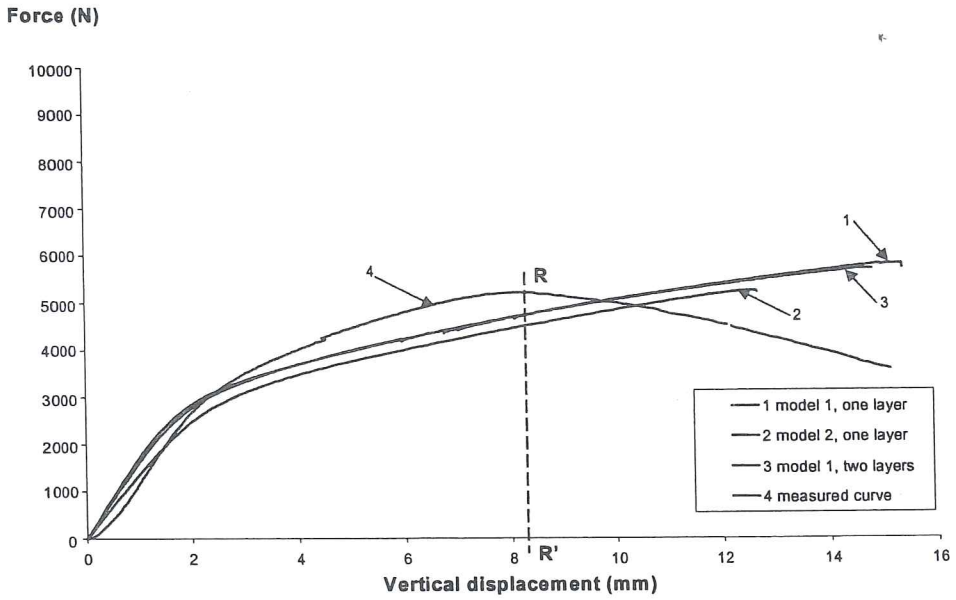

Figure 6-34 Force–displacement curves for the bending test for meshes with one and two layers of element, definition of experimental rupture, from Habraken *et al.* 2000.

The drop of the simulation curves happens much later than in the experimental breakdown. From the experimental observation, it has been checked that local fracture appears earlier than the final rupture due to the high resistance of the tube section. This fact explains why the "experimental local rupture" identified by *RR'* line on Figure 6-34 seems far from real structure fracture. Figure 6-35 shows deviatoric damage computed by model 1 with mesh 2. Strain and damage are strongly localized above the notch. When the imposed displacement reaches 8.33mm (the experimental rupture, presented by RR' in Figure 6-34), Table 6-3 presents the results for both simulations with one or two layers of elements. The shear strains are very low and not presented in the table. Clearly mesh dependence affects the simulation results. In fact in this case, the damage is highly concentrated and cannot be represented with a coarse mesh. To simulate the high damage gradient the *b* and *c* ratios should be even smaller than the smallest one used (b=12%, c=4.75%). However CPU time and storage memory prevent to go on with finer meshes. A strong damage variation between the internal layer and the external one demonstrates the necessity of low *c* ratio.

simulation	ε_{eqmax}	d_{max}	ε_x	ε_y	ε_z
mesh 1 (c=9.5)	16%	0.082	-8.9%	20.3%	-11.1%
mesh 2 (c=4.75)	29.4%	0.156	-9.6%	24.4%	-18.7%

Table 6-3 The results of bending test for mesh 1 and mesh 2 (model 1).

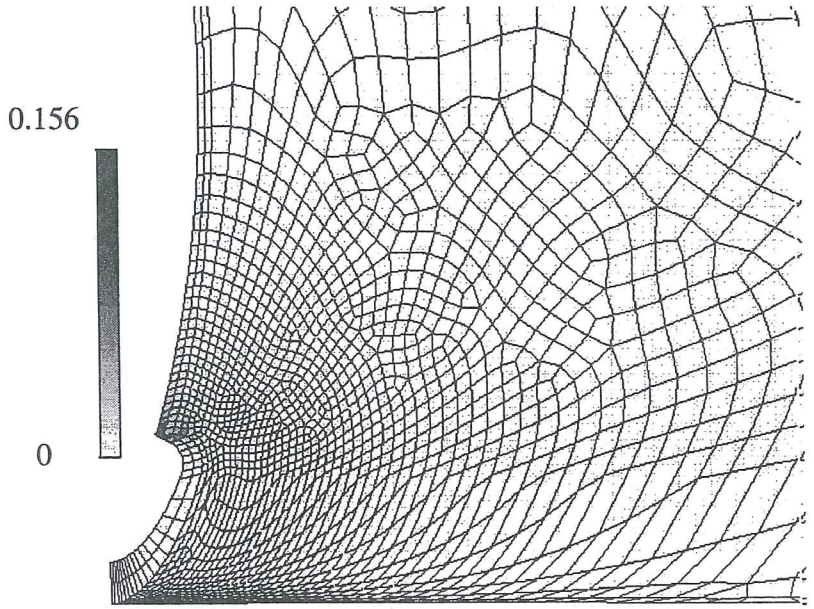

Figure 6-35 Deviatoric damage *d* computed by mesh 2 and model 1 (from Habraken *et al.* 1999).

D. Shear test of perforated tube

The fourth validation test is a shear test. As shown on Figure 6-36 and 6-37, the end of the tube is perforated for getting a shear-dominated loading. To simulate this test, two finite element meshes are used. The first mesh is shown in Figure 6-38a. Its *b* ratio is equal to 50% and its *c* ratio is equal to 2.5. As the *b* ratio is much larger than the one discussed in section 6.2.9, to get poor results with a lot of strain or damage discontinuities is not astonishing. In order to get reasonable results, a second mesh is used, shown in Figure 6-38b. It has a *b* ratio of 15% and a *c* radio of 4.1, which seems reasonable enough to analyze the results.

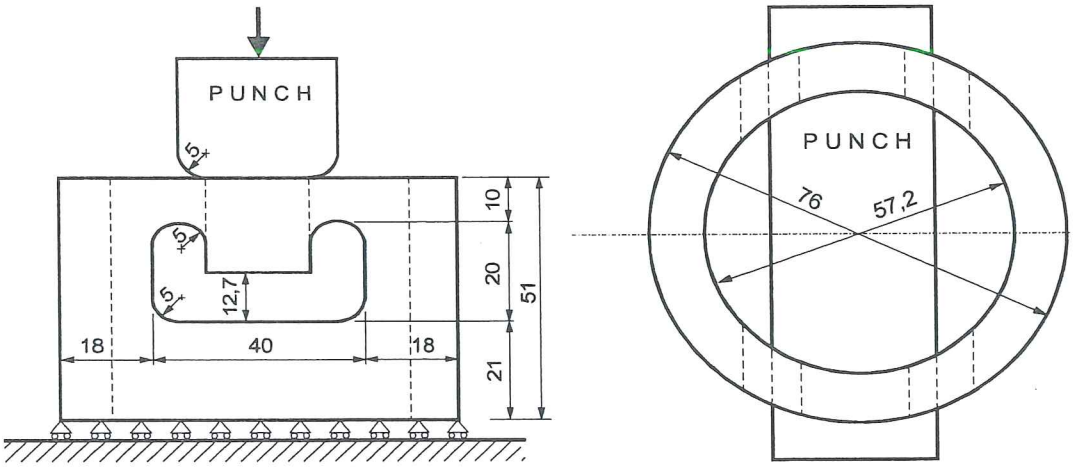

Figure 6-36 Geometry and loading of the shear test (from Habraken *et al.* 2000).

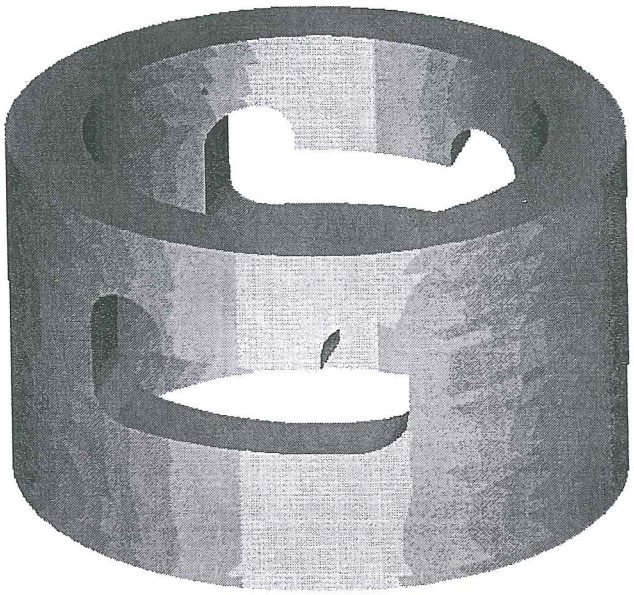

Figure 6-37 Shear test, by symmetry only 1/4 is used in computation (from Habraken & Wang 1996).

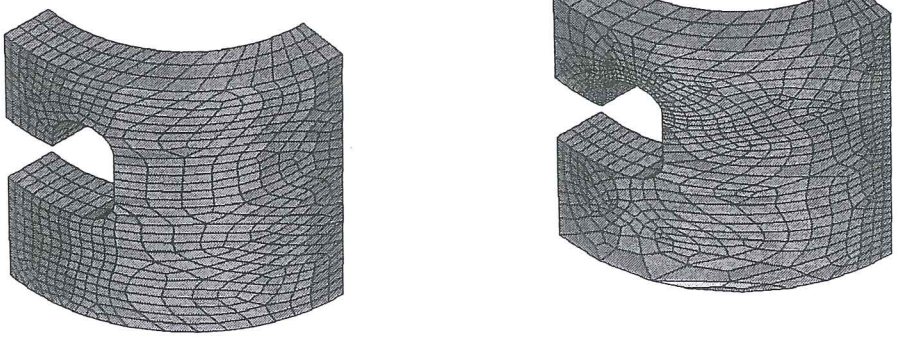

a. Shear test: mesh 1 b. Shear test: mesh 2

Figure 6-38 Finite element meshes.

Model 1		Displacement	d_{max}	$\varepsilon_{eq\ max}$	$\varepsilon_{eq\ outside}$	$\varepsilon_{eq\ internal}$
Mesh 1 b=50%	First test fracture	7.0	0.15	42.4%	14-42%	29-36%
	Second test fracture	8.3	0.22	52.4%	19-52%	36-46%
Mesh 2 b=15%	First test fracture	7.0	0.18	39.6%	14-39%	21-36%
	Second test fracture	8.3	0.27	50.7%	18-50%	28-46%

Table 6-4 Results of two meshes for shear test (model 1).

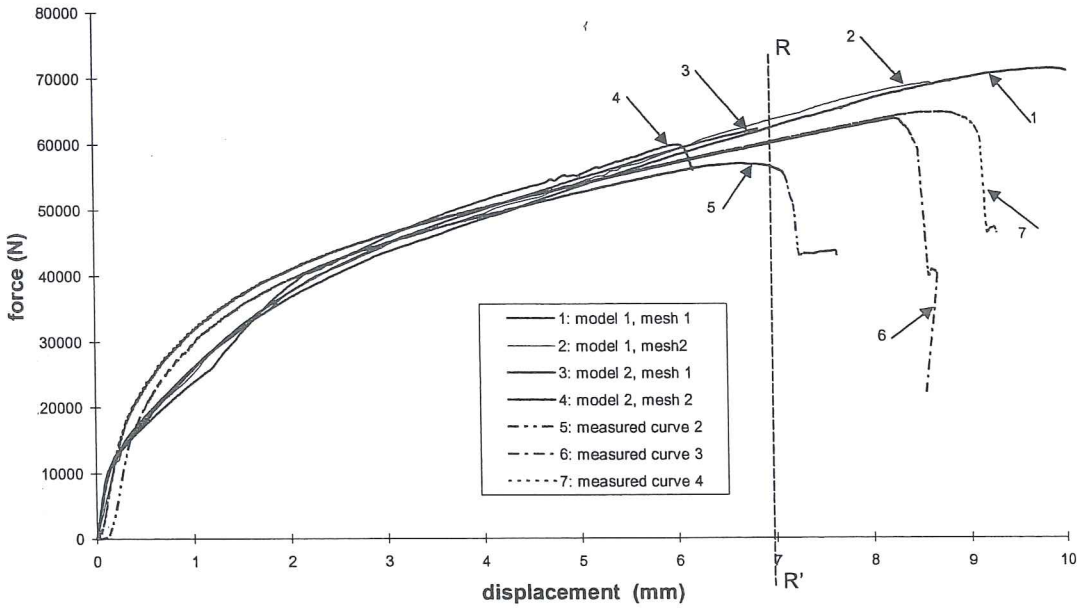

Figure 6-39 Force-displacement curves for the shear test , identification of the "experimental rupture" (from Habraken *et al.* 2000).

Figure 6-39 shows force-displacement curves of the experiments and the calculations. The drop of the simulation curves happens later than in the experiments except for the curves of model 2. Figures 40a to 40f show the triaxiality factor T, the equivalent strain ε_{eq} and the deviatoric damage d at the moment of "experimental rupture" (imposed displacement of 7mm defined on Figure 6-39, line *RR'*) for the two meshes. Some simulation results of the two meshes are summarized in Table 6-4.

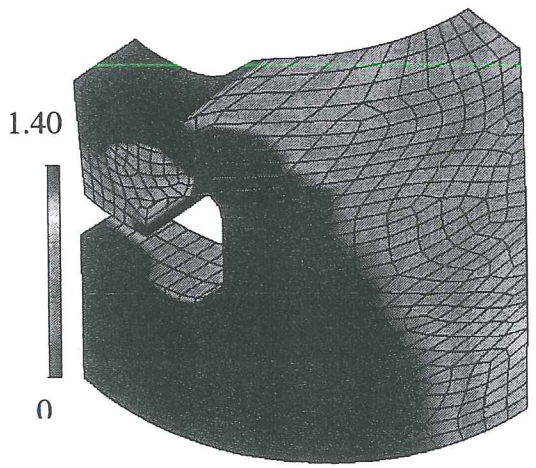

a. Triaxiality factor (mesh 1).

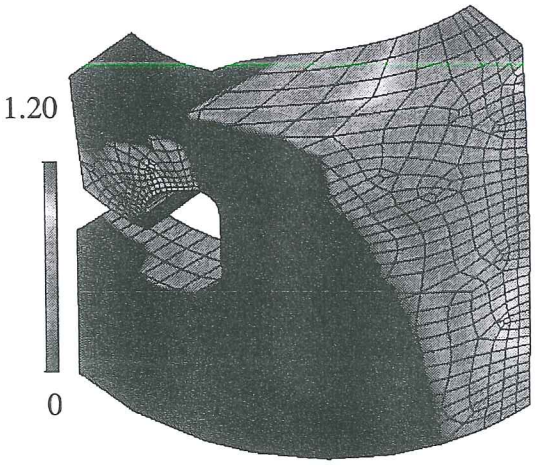

b. Triaxiality factor (mesh 2).

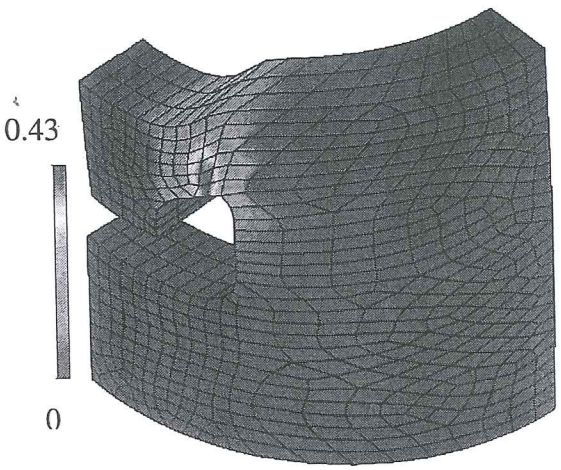

c. Equivalent strain ε_{eq} (mesh 1).

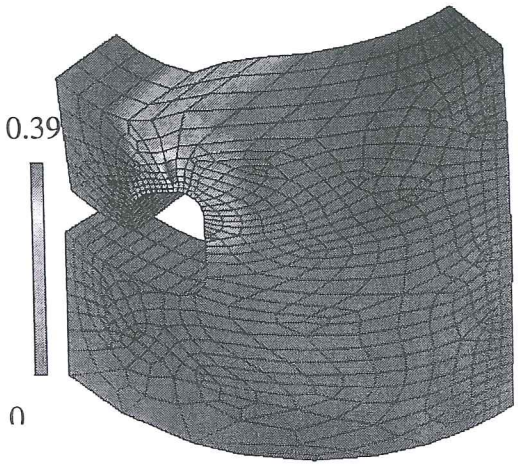

d. Equivalent strain ε_{eq} (mesh 2).

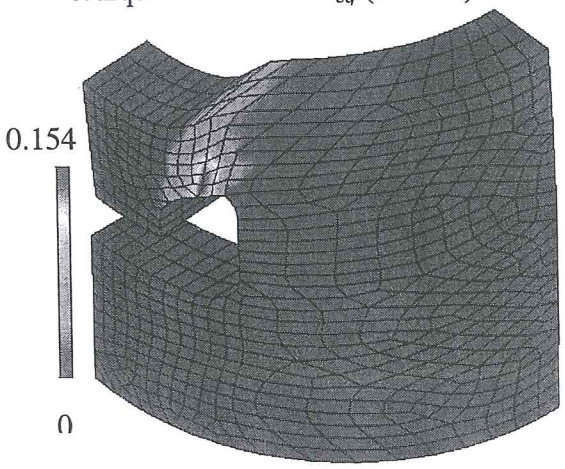

e. Deviatoric damage d (mesh 1).

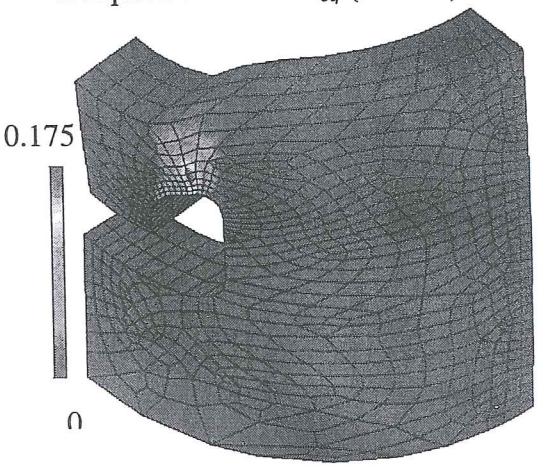

f. Deviatoric damage d (mesh 2).

Figure 6-40 Simulation results with model 1 (part f from Habraken *et al.* 2000).

The global simulation results (force-displacement curve, Figure 6-39) are not affected by the discretization, except for the curve drop as for the notch test with large radius. Both meshes and damage models predict the maximum deviatoric damage and the maximum equivalent strain at the experimental fracture location (internal face, above the notch). No matter the chosen damage model, the finer mesh simulates more accurately the damage or strain gradient; higher maxima are reached and they are more localized. Distribution of shear stress shows a maximum above the hole; however local hydrostatic stress concentration induces a strong gradient of the triaxiality factor.

6.2.11 Discussion

Four validation tests have been simulated. The characteristics of the used meshes are summarized in Table 6-5. Then, Tables 6-6 a and b gather the strain and triaxiality levels near the crack for each simulation.

Test description	Problem description	Smallest elements n>m>l	*b*=diagonal/ R_{notch}	*c*=n/l
Notch test	2D axisymmetry problem	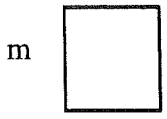	2.4%	/
Hole test	3D problem	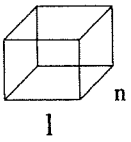	9%	2.3
Bending test mesh 1	3D problem		12%	9.5
Bending test mesh 2	3D problem		12%	4.75
Shear test mesh 1	3D problem		50%	2.5
Shear test mesh 2	3D problem		15%	5.5

Table 6-5 Validation test simulations: Finite element discretizations (from Habraken *et al.* 1999)

Test description	Characteristics	ε_{eqmax}	d_{max}
Rod tensile test	Uniaxial stress field, low triaxiality: 0.57	13%	0.06
Axisymmetric large notch bar tensile test, R=7mm	Concentrated high triaxiality in the center neck zone: 1.4	20% maximum, $\varepsilon_{eq}\geq 17$ for whole central section	d_{max}=0.154, maximum at center, $d\geq 0.14$ covers 1/3 center section
Perforated bar tensile test, R=6mm	Stress and strain maxima at the hole root, but mean to low triaxiality in the whole middle section($\approx$0.8)	26% maximum, localized at the notch root	d_{max}=0.154, maximum localized at the notch root, $d\geq 0.14$ covers 1/6 hole section
Bending test of a grooved rod , R=2.5mm (mesh 1, one-layer)	Stress and strain maxima at the groove root, but mean to high triaxiality above (0.9-1.3)	17% maximum, localized at the groove root	d_{max}=0.085, maximum strongly localized at the groove root
Bending test of a grooved rod , R=2.5mm (mesh 2, two-layer)	Stress and strain maxima at the groove root, but mean to high triaxiality above (0.9-1.4)	29% maximum, localized at the groove root, in internal layer	d_{max}=0.157, maximum strongly localized at the groove root, in internal layer
Compression test of a perforated ring (shear appearance), R=5mm (mesh 1)	Stress and strain concentration above the hole root, with strong triaxiality unhomogeneity (0.2-1.4), low triaxiality at shear zone (<0.7)	42% maximum $\varepsilon_{eq}\geq 22\%$ covers the whole section above the hole	d_{max}=0.154, maximum localized above the hole, $d\geq 0.14$ covers 1/2 section above the hole
Compression test of a perforated ring (shear appearance), R=5mm (mesh 2)	Stress and strain concentration above the hole root, with strong triaxiality unhomogeniety (0.2-1.2), low triaxiality at shear zone (<0.6)	40% maximum $\varepsilon_{eq}\geq 15\%$ covers the whole section above the hole	d_{max}=0.176, maximum localized above the hole, $d\geq 0.14$ covers 1/2 section above the hole

Table 6-6a Validation test simulations: calculation results by model 1 at "experimental" rupture, line *RR* (from Habraken *et al.* 1999).

Test description	Characteristics	ε_{eqmax}	d_{max}
Rod tensile test	Uniaxial stress field, low triaxiality: 0.57	13%	d_{max} =0.16
Axisymmetric large notch bar tensile test**, *R*=7mm	Concentrated high triaxiality in the center neck zone: 1.4	20% maximum, $\varepsilon_{eq}\geq$17% covers the 1/2 central section	d_{max}=0.48, maximum at center, $d\geq$0.36 covers 1/3 centers section, $d\geq$0.3 covers 1/2 the section
Holed bar tensile test, *R*=6mm	Stress and strain maxima at the hole root, but mean to low triaxiality in the whole middle section(≈0.8)	30% maximum localized at the notch root	d_{max} =0.5, maximum localized at the notch root, $d\geq$0.36 covers 1/6 the hole section, $d\geq$0.3 covers 1/5 the section
Bending test of a grooved rod, *R*=2.5mm (mesh1, one-layer)	Stress and strain maxima at the groove root, but mean to high triaxiality above (0.8-1.3)	11% maximum, localized at the groove root	d_{max}=0.171, maximum strongly localized at the groove root
Compression test of a holed ring (shear appearance), *R*=5mm (mesh 1)	Stress and strain concentration above the hole root, with strong triaxiality unhomogeneity (0.3-1.4), low triaxiality at shear zone (<0.7)	44% maximum, localized above the hole, $\varepsilon_{eq}\geq$20% covers the whole section above the hole, $\varepsilon_{eq}\geq$36% covers 1/2 the section	d_{max}=0.51, maximum localized above the hole, $d\geq$0.36 covers 1/3 section above the hole, $d\geq$0.3 covers 1/2 the section
Compression test of a holed ring (shear appearance), *R*=5mm (mesh 2**)	Stress and strain concentration above the hole root, triaxiality unhomogeneity (0.2-0.8), low triaxiality at shear zone (<0.6)	41% maximum, localized above the hole, $\varepsilon_{eq}\geq$18% covers the whole section above the hole, $\varepsilon_{eq}\geq$28% covers 1/2 the section	d_{max}=0.56, maximum localized above the hole, $d\geq$0.38 covers 1/3 section above the hole. $d\geq$0.28 covers 1/2 the section

Table 6-6b Validation test simulations: calculation results by model 2 at "experimental" rupture, line RR' (from Habraken *et al.* 1999).

** The drop of these simulations takes place before the 1st rupture of the test. Only the last results are given for these simulations.

From preceding validation simulations, one can check the following observations:

- The maximum damage zone detected by both models have the same location, and correspond to experimental rupture initiation.

- Higher damage values and damage gradients are produced by model 2.

- The damage value affects the global results, so global force-displacement or force-time curves from damage model 2 present dropping behavior sooner than damage model 1, however before this decrease, the curves from model 1 and model 2 are very close to each other.

- For both models, the dropping behavior of global curves is not an accurate criterion to predict global rupture as there is a clear mesh dependence. According to the validation test, the damage model and the discretization chosen, simulations predict global rupture too early, too late or in time.

- Threshold value applied on deviatoric damage seems a good rupture initiation criterion for mean to high triaxiality cases. If the mesh is reasonably refined, a threshold value of d=0.16 for model 1 and of 0.5 for model 2 should detect the rupture at the experimental moment or a little earlier in case of large shear.

- The threshold values of deviatoric damage (d=0.06 model 1; d=0.16 model 2), which could be deduced from an uniaxial tensile test, characterized by a low triaxiality factor, are not adapted for mechanical state with a mean or high triaxiality factor. The explanation of this experimental observation must be a microscopic one. In fact the Figures 4-14 and 4-15 (section 4.4, in Chapter 4) produced by Benzerga *et al.* 1999 demonstrate that such macroscopic observation could be explained by the initial void fraction or a void distribution effect. The lower critical damage value in tension could be related to a different rupture mechanism in pure tensile test as reported by Gologanu *et al.* 1994. However, as no intensive microscopic study has been performed, this assumption has not been verified.

- From all equivalent strain maps and triaxiality maps, it can be checked that simple threshold value of such variables does not allow the prediction of rupture.

6.2.12 Conclusion about the use of damage extension of Bodner's model

An extension of the elasto-visco-plastic Bodner's model to classical damage approach has been proposed. A parameter identification procedure has been developed, however its application has been difficult because the experimental

work was not straightforward and its accuracy is limited. Tensile and compression tests lead to Young's modulus of similar but not identical values. The damage measurements result from different approaches: in tensile state, cyclic loading is performed on the whole rod, while in compression state, one experiment set considers large scale rings from the rod and the other one treats small cylinders from the rod wall.

The simulations of validation experiments prove that fine meshes adapted to the sample geometry must be used. Clearly the ratio between the element diagonal and the radius defect must stay about 10 % or less and well-shaped elements with edge ratio lower or equal to 5 are necessary. Generally, the use of finer meshes with b ratio of 2 or 3% would have given results leading to better knowledge of actual material fracture as, in this work, mesh independence of results has not been reached for all the validation cases. However CPU time prevents to go on in such a direction.

As the experiments were filmed with a classical camera, this allows to roughly detect the macrocrack appearance and its evolution. Comparisons of the simulation results and the experiments show that damage is correctly localized. The analysis of the results demonstrates that a simple deviatoric damage threshold value is not very accurate to detect rupture but can be used. Staying on a macroscopic level, this research did not try to link damage variable to ductile porosity or to use some microscopic criteria like the ones proposed by Brown & Embury 1973 or Thomason 1993. The present goal to verify if this macroscopic approach is able to handle different types of fracture is fulfilled. However, it is clear that this approach raises many questions without answer. One would like to have a curve defining accurately the damage threshold value according the triaxiality state. This would require for instance:

-systematic notch test study on a macroscopic level;
-microscopic investigation to be able to use microscopic criteria;
-to perform cell models to deduce macroscopic behavior.

A microscopic study would also be necessary to define which damage model (1 or 2) is closer to the reality; however from a macroscopic point of view both models are validated. The nucleation, growth and coalescence events are represented by a unique evolution law for model 1 and by 2 functions, assumed to model respectively nucleation and both growth and coalescence for model 2. This reduces the problem of fitting numerous parameters but prevents from describing accurately the fracture development. In consequence, the experimental final slope from load-displacement curve is not well reproduced. In this research, mesh dependence is strong in the prediction of slope variation in the force-displacement curve. Some regularization method as described in Chapter 5, using the actual material characteristic length, would be better than just using finite elements of equal or smaller size than l_c as suggested by Rousselier.

6.3. An elasto-plastic damage model

6.3.1. Model description

The initial version of this model was proposed by Zhu 1992. With the help of Sylvie Castagne, this model has been applied to the experiments described in section 6.2. The poor agreement between experiments and simulations leads to model modifications described in Castagne 1998 and Castagne *et al.* (to appear). This section 6.3. appears as a summary of Castagne *et al.* (to appear), however it takes into account all the notations and principles already introduced in Chapter 3.

As in Bodner's version of damage, two scalar damage variables are introduced in the model: d, the deviatoric one and δ, the volumic one. They represent the local material degradation as explained in section 3.2.1. Contrarily to Gurson's approach (see Chapter 2), damage is not strictly connected to void volume fraction even if this is the revealing phenomenon in ductile fracture. The damage variables d and δ are not quantitatively linked to void volume fraction.

Again the hypothesis of energy equivalence is assumed to replace the damaged material state by a fictitious undamaged material state, which is characterized by effective stresses and strains $\underline{\overline{\sigma}}$ and $\underline{\overline{\varepsilon}}$. These effective tensors are related to true tensors through damage variables by identical functions as in the above Bodner's damage model:

$$\underline{\hat{\sigma}} = \frac{\underline{\hat{\sigma}}}{1-d} \qquad \overline{\sigma}_m = \frac{\sigma_m}{1-\delta} \tag{6-33}$$

$$\underline{\hat{\varepsilon}}^e = (1-d)\underline{\hat{\varepsilon}}^e \qquad \overline{\varepsilon}_m = (1-\delta)\varepsilon_m \tag{6-34}$$

where σ_m is the mean value of the stress tensor, $\underline{\hat{\sigma}}$ its deviator, $\underline{\hat{\varepsilon}}^e$ the elastic strain tensor deviator and ε_m the mean value of the strain tensor. Equations (6-33) and (6-34) imply the equality of the complementary elastic energy.

Following the thermodynamic formulation, to define a constitutive law, the first step is to choose ψ, the expression of the Helmholtz specific free energy (see equation 6-35). Zhu has applied the same proposal as Lemaître 1985, who assumes that energies related to elastic strains, plastic strains and damage growth are independent. A second assumption, hidden in Zhu's choice of ψ expression, is that elastic properties of the material depend only on the accumulated damage d and δ and not directly on the dislocation density reflected in the variable α and connected to plastic hardening.

$$\psi = \psi^e(\underline{\varepsilon}^e, d, \delta) + \psi^p(\alpha) + \psi^d(\beta) \tag{6-35}$$

where ψ^e is the elastic strain energy, ψ^p the free energy due to plastic hardening and ψ^d the free energy due to damage hardening. The elastic strain energy can be divided into the deviatoric strain energy $\hat{\psi}^e$ and the volumic dilatation energy ψ_m^e:

$$\psi^e(\underline{\varepsilon}^e, d, \delta) = \hat{\psi}^e(\underline{\varepsilon}^e, d) + \psi_m^e(\underline{\varepsilon}^e, \delta) \tag{6-36}$$

with:

$$\hat{\psi}^e(\underline{\varepsilon}^e, d) = G(1-d)^2 \underline{\hat{\varepsilon}}^e : \underline{\hat{\varepsilon}}^e \tag{6-37}$$

$$\psi_m^e(\underline{\varepsilon}^e, \delta) = \frac{9\chi(1-\delta)^2}{2}\varepsilon_m^2 \tag{6-38}$$

The true stress tensor is obtained as derivative of the free energy, see relation (3-21):

$$\begin{aligned} \underline{\hat{\sigma}} &= \rho\frac{\partial\psi}{\partial\underline{\hat{\varepsilon}}^e} = 2G(1-d)^2\underline{\hat{\varepsilon}}^e \\ \sigma_m &= \rho\frac{\partial\psi}{3\partial\varepsilon_m^e} = 3\chi(1-\delta)^2\varepsilon_m^e \end{aligned} \tag{6-39a, b}$$

Using relations (6-33), (6-34) and (6-39a,b), one can check that effective stress and strain tensors respect the classical Hooke's law. As already presented by relation (3-22), the thermodynamic forces Y_d and Y_δ associated to damage variables d and δ are given by:

$$Y_d = \rho\frac{\partial\psi}{\partial d} = -\frac{\underline{\hat{\sigma}} : \underline{\hat{\sigma}}}{2G(1-d)^3} = -\frac{2\hat{\psi}^e}{1-d} = -\frac{1}{2}\frac{d\hat{\psi}^e}{dd}$$

$$Y_\delta = \rho\frac{\partial\psi}{\partial\delta} = -\frac{\sigma_m^2}{\chi(1-\delta)^3} = -\frac{2\psi_m^e}{1-\delta} = -\frac{1}{2}\frac{d\psi_m^e}{d\delta} \tag{6-40a, b}$$

They are called "damage energy release rates". G is the shear modulus and χ is the bulk modulus. The thermodynamic formulation approach (relations 3-7 to 3-9) justifies the introduction of convex functions F, used as pseudo potentials, to satisfy the Clausius Duhem inequality. As Lemaître 1985 and Hayakawa & Murakami 1998 (relation 3-24), Zhu uses a potential decomposed into two independent components F_p and F_d representing plastic and damage criteria:

$$F_p = \sqrt{\frac{(\underline{\hat{\sigma}} - \underline{\hat{\gamma}}) : (\underline{\hat{\sigma}} - \underline{\hat{\gamma}})}{4G(1-d)^2}} - R_0 - R(\alpha) \tag{6-41}$$

$$F_d = -Y_d - \langle\tau\rangle Y_\delta - B_0 - B(\beta) = \frac{2\hat{\psi}^e}{1-d} + \langle\tau\rangle\frac{2\psi_m^e}{1-\delta} - B_0 - B(\beta) \tag{6-42}$$

where R is the force associated with plastic hardening variable α, $\underline{\hat{\gamma}}$ is the deviator of the tensor $\underline{\gamma}$, which defines the center of the plastic yield surface. The yield stress is determined by $R + R_0$ with R_0 the initial yield stress. B is the damage strengthening,

depending on the internal variable β linked to the micro-voids state. This damage strengthening is added to the initial threshold value B_0. $\langle\tau\rangle$ is defined by δ/d in tensile state and 0 in compression state since the volumic damage parameter is not affected by compression. This means it cannot decrease in compression state, it just does not increase anymore. $\langle\tau\rangle$ is considered as a constant in the model implemented by Zhu.

Classically plastic strains are deduced by a normality law and an identical assumption is done for damage evolution. Such an hypothesis has been checked experimentally by Hayakawa & Murakami 1998 (see Figure 3-3):

$$\underline{\dot{\varepsilon}}^p = \dot{\lambda}_p \frac{\partial F_p}{\partial \underline{\sigma}} = \frac{\dot{\lambda}_p \left(\underline{\hat{\sigma}} - \underline{\hat{\gamma}}\right)}{2(1-d)\sqrt{G\left(\underline{\hat{\sigma}} - \underline{\hat{\gamma}}\right) : \left(\underline{\hat{\sigma}} - \underline{\hat{\gamma}}\right)}}$$

$$\dot{d} = -\dot{\lambda}_d \frac{\partial F_d}{\partial Y_d} = \dot{\lambda}_d$$

$$\dot{\delta} = -\dot{\lambda}_d \frac{\partial F_d}{\partial Y_\delta} = \langle\tau\rangle \dot{\lambda}_d \qquad \text{(6-43a, b, c)}$$

where $\dot{\lambda}_p$ and $\dot{\lambda}_d$ are plastic and damage multipliers.

The isotropic and kinematic plastic hardening rules are expressed as follows:

$$\dot{R} = (1-m)\dot{\lambda}_p \frac{dR}{d\alpha}$$

$$\underline{\dot{\gamma}'} = 4G(1-d)^2 m \underline{\dot{\varepsilon}}^p \frac{dR}{d\alpha} + \underline{\Omega\gamma'} - \underline{\gamma'\Omega} \qquad \text{(6-44a, b)}$$

where $m \in [0,1]$ is a ratio specifying a combined isotropic-kinematic hardening rule, $\underline{\Omega}$ is the spin tensor contributing to Jaumann's derivative.

The damage hardening rule is given by :

$$\dot{\beta} = -\dot{\lambda}_d \frac{\partial F_d}{\partial B} = \dot{\lambda}_d$$

$$\dot{B} = \frac{dB}{d\beta}\dot{\beta} = \frac{dB}{d\beta}\dot{\lambda}_d \qquad \text{(6-45a, b)}$$

Finally, the plastic and the damage loading/unloading rules are expressed in Kuhn-Tucker's form by:

$$F_p \le 0, \quad \dot{\lambda}_p \ge 0, \quad \dot{\lambda}_p F_p = 0$$

$$F_d \leq 0, \quad \dot{\lambda}_d \geq 0, \quad \dot{\lambda}_d F_d = 0 \qquad \text{(6-46a, b)}$$

These relations imply that no evolution of the plasticity or damage variable occurs if F_p or F_d is negative, respectively. On the other hand, for plasticity or for damage evolution, $\dot{\lambda}_p > 0$ and $F_p = 0$ or $\dot{\lambda}_d > 0$ and $F_d = 0$ are respectively required. This model proposed by Zhu is fully described in his thesis 1992 and can also be found in the international publication Zhu *et al.* 1992, 1995.

6.3.2. Model identification

The identification consists in finding the model parameters with the help of experiments, theory analysis, curve fitting and simulations reduced to one finite element for homogeneous stress-strain states. Such simulations allow to verify the adequacy between the experimental and simulated stress-strain and damage-strain curves.

The principal data to be introduced in the model are the effective equivalent stress-plastic strain curve ($\overline{\sigma}_{eq}$-$\overline{\varepsilon}^{p}_{eq}$) and the damage strengthening threshold versus deviatoric damage curve $B(\beta)\equiv B(d)$ for a uniaxial test. To compute these curves, the evolution of the uniaxial stress and of the two damage variables versus strain must be known. With the hypothesis of elastic energy equivalence, the deviatoric and volumic damage parameters are linked to the elastic moduli by the same relations as presented in Bodner's damage model (see relations (6-16) and (6-17)). The experimental results presented on Figure 6-9 and 6-12 are used. In fact, the approach called model 1 with reduced values is assumed as damage evolution during an uniaxial tensile test (Figure 6-10a) and an uniaxial compression test (Figure 6-12b).

The knowledge of these (d-ε) curves as well as the availability of the (σ-ε) experimental curves for quasi-static tensile and compression tests (Figure 6-13) allow to determine the useful data for the model.

The equivalent effective stress, used to compute ($\overline{\sigma}_{eq}$-$\overline{\varepsilon}^{p}_{eq}$), is given for a uniaxial test by :

$$\overline{\sigma}_{eq} = \left(\frac{3}{2} \overline{\sigma'}_{ij} \overline{\sigma'}_{ij} \right)^{\frac{1}{2}} = \frac{\sigma_1}{1-d} \qquad \text{(6-47)}$$

where σ_1 is the stress in the loading direction.

As explained in Castagne 1998, the equivalent effective strain can be computed by integrating the following equation:

$$\dot{\overline{\varepsilon}}^{p}_{eq} = \left(1 - d(\varepsilon^{p}_{eq})\right) \dot{\varepsilon}^{p}_{eq} \qquad \text{(6-48)}$$

Finally a unique curve is retained taking the average between the compression and the tensile cases (Figure 6-41).

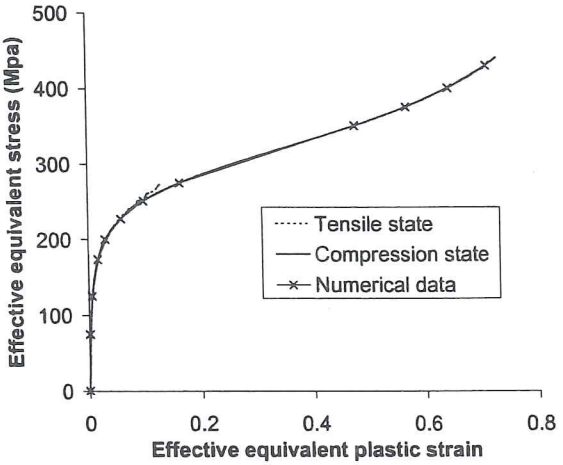

Figure 6-41 Effective equivalent stress versus effective equivalent plastic strain (from Castagne *et al.* to appear).

The second curve to be introduced to characterize the material is the (*B-d*) curve. Using equation (6-42), the following relation for a uniaxial test is obtained:

$$B_0 + B(\beta) = \left(\frac{1}{3G_0(1-d)^3} + (p)\langle\tau\rangle \frac{1}{9\chi_0(1-\langle\tau\rangle d)^3} \right) \sigma_1^2 \qquad (6\text{-}49)$$

where G_0 and χ_0 are initial elastic shear and bulk moduli, p is a weight factor explained in section 6.3.3.A. B_0, the damage threshold is given by:

$$B_0 = \left(\frac{1}{3G_0} + (p)\langle\tau\rangle \frac{1}{9\chi_0} \right) \sigma_d^2 \qquad (6\text{-}50)$$

with σ_d the initial yield stress according to the hypothesis of simultaneous plasticity and damage entrances (σ_d = 75 MPa).

Here two different curves are computed, one for the compression test and another one for the tensile test. To model fracture in tensile state, a limit value d_{coales} is introduced, it indicates voids coalescence. As soon as this value is achieved, the slope of the (*B-d*) curve is multiplied by the factor *MP* to increase the damage growth (Figure 6-42) and consequently the stress reduction. Without this modification, the curve is assumed to continue with the slope computed between the last two given points. For the compression state, no modification is introduced as no coalescence appears.

The damage ratio τ, also called tensile effect, is supposed to be a constant for the model. Actually, it varies between 1.37 and 2.30 (Figure 6-43). The constant value used in the simulations is 1.57.

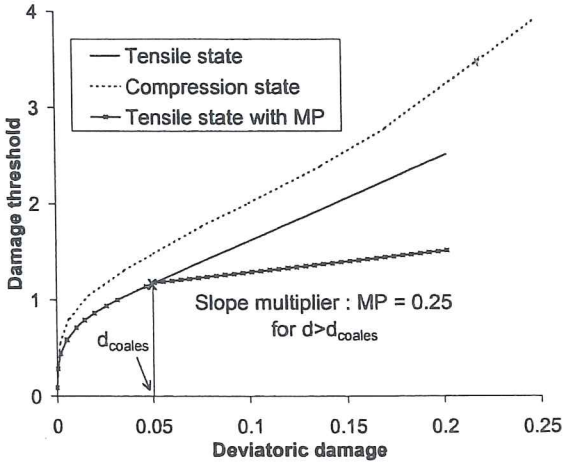

Figure 6-42 *B(d)* curve relative to tensile and compression states (from Castagne *et al.* to appear).

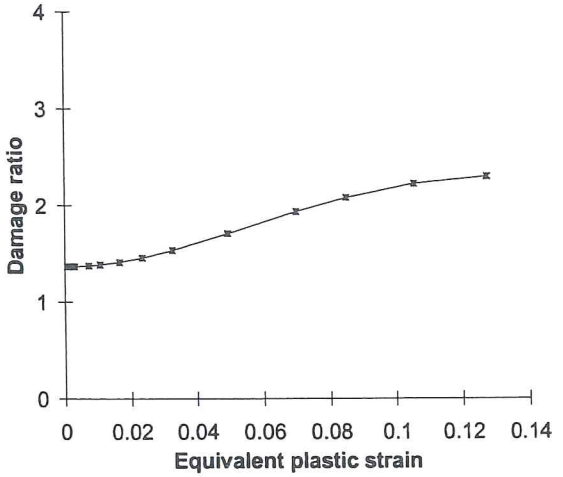

Figure 6-43 Tensile state : τ versus equivalent plastic strain (from Castagne *et al.* to appear).

Finally, the curves to be introduced in the data file are described by Figures 6-41 and 6-42. They are linearized to be written in the data file. A weight factor p will be introduced in the model (see section 6.3.3.A.). Its value has been taken into account in the calibration phase as it modifies the (*B-d*) curve in tensile state. *MP*, the slope multiplier, and d_{coales}, the coalescence level, are not easily fitted as explained in section 6.3.3. They have to be adapted according the validation experiment to obtain a better visualization of the rupture event.

Table 6-7 summarizes the final set of scalar data for the analyzed aluminum. Remark that the actual initial Young's modulus of the material is not used in the simulations.

Indeed, all the equations of the model are written using the extrapolated initial Young's modulus E_0 introduced in section 6.2.7.A.

Symbol	Description	Value
E	Material Young's modulus (not used)	72505 MPa
E_0	Extrapolated initial Young's modulus	57852 MPa
ν	Poisson's ratio	0.31
τ	Damage ratio	1.57
d_{coales}	Coalescence limit in tensile state	0.05
MP	Slope multiplier of $B(d)$ in tensile state	0.25
p	Weight factor	0.1

Table 6-7 Material data (from Castagne *et al.* to appear).

After the model identification, the deviatoric damage variable and the equivalent stress represented in Figure 6-44 are in correlation with the experimental results. The rough slope modification for the damage variable in the tensile state takes account of coalescence. In fact, the performed experiments are not accurate enough to precisely analyze the damage increase during the coalescence events. The damage evolution after the point of coalescence aims to reproduce the drastic decrease of stress (see Figure 6-44b) in order to model the presence of rupture and the loss of rigidity of elements representing these material points. Theoretically, the final slope of curves describing macroscopic fracture experiments should help to define the end of damage evolution defined by the *MP* factor (Figure 6-42). However, trials to enhance this effect lead to numerical convergence problems. The compression state also shows a stress decrease near the rupture state.

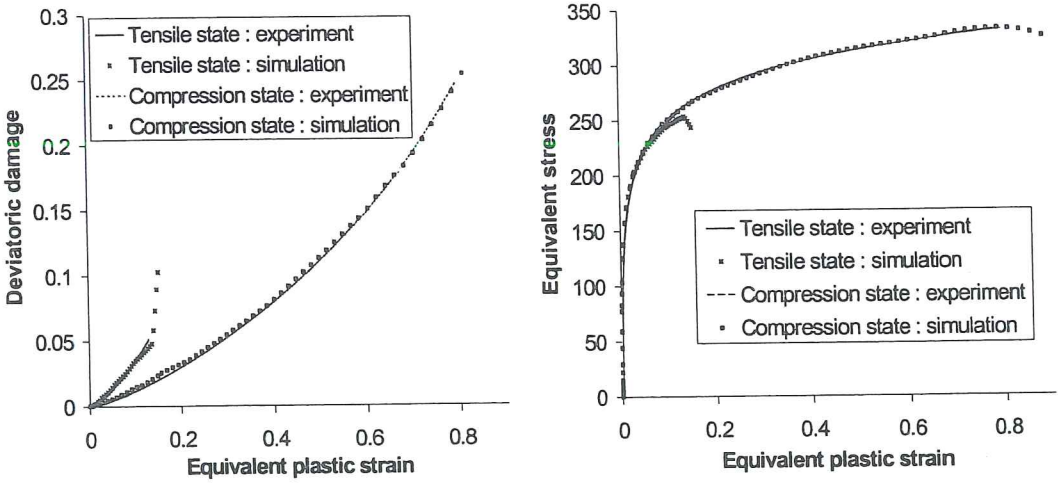

(a) Deviatoric damage variable (b) Equivalent stress

Figure 6-44 Comparison of model prediction and experiments (from Castagne *et al.* to appear).

6.3.3 Validation

This model is now applied to the same validation experiments as already presented in Bodner's damage model (section 6.2.10). The bending case is not reproduced here because the simulations have not converged due to early numerical bifurcation phenomena.

A. Tensile test of a notched specimen

First, tensile tests realized on notched cylindrical bars (Figure 6-18) are studied. The relative displacement is measured on a 25 mm basis. Three different meshes are tested in order to analyze the mesh sensitivity of the results. The experiment has been reproduced several times with very close results, which explains why only one experimental curve is presented on Figure 6-45a.

In the first simulations, very local strong damage increases with loss of convergence happened. A kinematic scalar indicator based on an idea proposed by Vilotte and used in Pierry 1997 proved the appearance of bifurcations. These localization phenomena were pointed out long before the rupture event. A viscous regularization method to improve the numerical stability as well as the suppression of the slope modification (MP) taking voids coalescence into account were introduced but this did not solve the problem.

An analysis of the damage map shows that damage increases more in the zones where triaxiality is very high. Compared to experiment, damage evolution is too important and predicts high local damage value long before rupture. This effect is enhanced when the slope of the (B-d) curve is reduced. To limit the damage growth and to allow a better convergence of the simulation, a weight factor p limiting the influence of the hydrostatic energy term ψ_m has been introduced in the model. This is equivalent to a modification of the damage surface shape (6-42):

$$F_d = \frac{2\hat{\psi}^e}{1-d} + \mathrm{p}\langle\tau\rangle\frac{2\psi_m}{1-\delta} - B_0 - B(\beta) \qquad (6\text{-}51)$$

The weight factor obtained is $p = 0.1$. It gives a correct evolution of the damage and maintains the difference of behavior between the tensile and the compression state. The graphs of Figure 6-44 were in fact drawn taking into account this factor. Indeed, the calibration has to be done with the final model.

The curve representing the force on Figure 6-45a is lower than the one obtained by the experiment although the rupture by coalescence in tensile state has been removed from the model for those simulations.

Figure 6-45b presents damage state at experimental fracture and not at the beginning of necking event as on Figure 6-23. It shows that damage increases more in some elements located at the middle of the specimen, where triaxiality is very high

(Needleman and Tvergaard, 1984) and can reach 1.6 in this example. Introducing in the model a d_{coales} would introduce a more important increase of the damage variable that could induce greater convergence problems in this high triaxiality case.

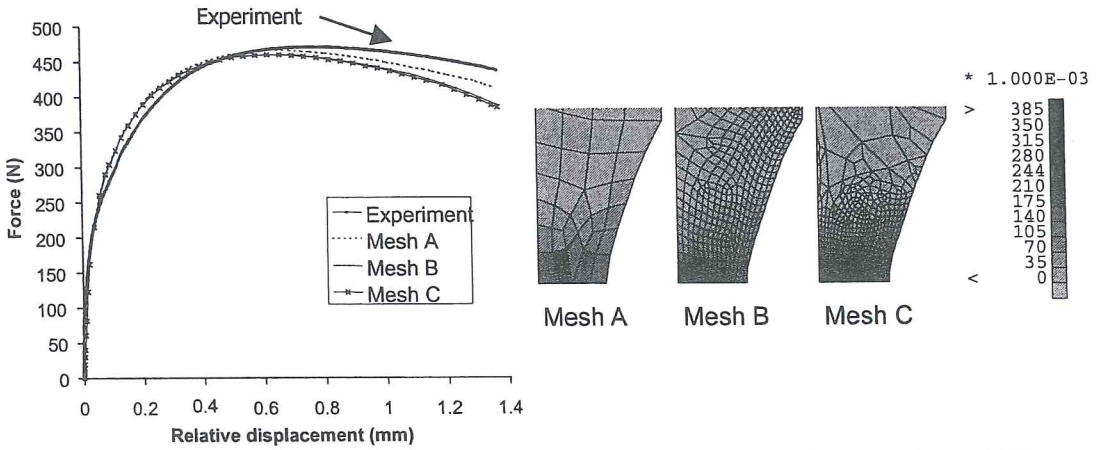

(a) Force-displacement curves

(b) Deviatoric damage for a 1.35 mm relative displacement

Figure 6-45 Results of model without d_{coales} and MP (from Castagne *et al.* to appear).

B. Tensile test of a perforated specimen

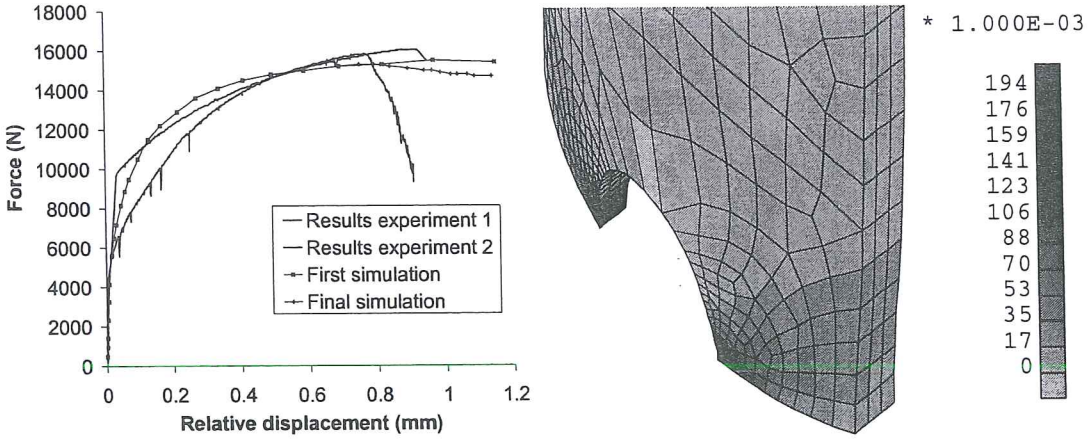

(a) Force versus relative displacement

(b) Final simulation : deviatoric damage for a 1.1 mm relative displacement.

Figure 6-46 Comparison of experimental measures and simulation results (from Castagne *et al.* to appear).

The second experiment is a tensile test on a curved bar with a hole inside (Figure 6-24). The first simulation on Figure 6-46a does not include the reduction of the (B-d) slope when coalescence of voids happens. Otherwise the final simulation has been realized with d_{coales} = 0.12 and MP = 0.25. One can observe that with the second simulation, a weak decrease of the force appears at the moment corresponding to the

experimental rupture. Figure 6-46b shows that the damage is maximum near the hole but its value remains low compared to the values obtained with the notch tests. Indeed, the maximum triaxiality here is 0.5 while it is 1.6 for the notch tests. The state described on Figure 6-46b happens a little later than the one described on Figure 6-30 and computed by Bodner's model.

C. Shear test of perforated tube

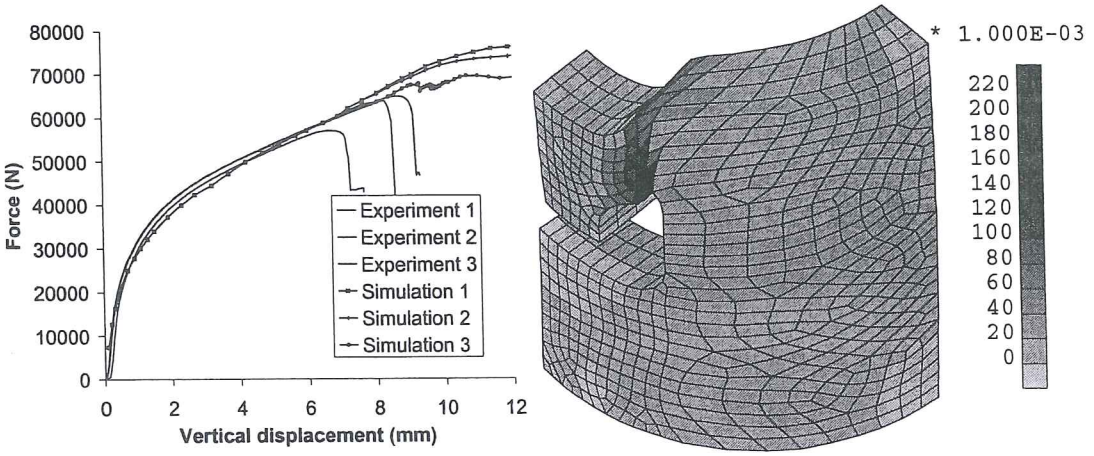

(a) Force versus vertical displacement of the tool

(b) Simulation 3, deviatoric damage for a 9.1 mm displacement of the tool

Figure 6-47 Comparison of experimental measures and simulation results (from Castagne *et al.* to appear).

On Figure 6-47a, the first simulation corresponds to a case with no coalescence, the second simulation has been computed with $d_{coales} = 0.15$ and $MP = 0.5$ and the last one with the same parameters as the second simulation from previous section (tensile test of a perforated specimen). For this last simulation, a reduction of the force can be observed at an imposed displacement of 7.7 mm, followed by oscillations. Figure 6-47b shows that damage begins near the hole as checked by the experiment; again this damage state is presented later than for the Bodner's damage model (Figure 6-40). Triaxiality reaches 0.6, which implies damage values lower than for the notch tests and similar to those observed during the perforated specimen test.

6.3.4 Damage criterion

The preceding experiment simulations show a strong dependence of damage level on triaxiality. The instant of rupture does not simply correspond to reaching a threshold value of the damage variable but must be linked to different factors.

The initial Zhu's model already contains the effect of triaxiality on damage through the volumic energy term. This parameter induces a too important damage growth, which leads to non convergence of the numerical simulations. The process followed here consists in limiting the triaxiality effect in order to avoid convergence problems. The coalescence damage level used in this model is a constant for the material. It is achieved earlier in a simulation where triaxiality is high since this factor increases the damage growth variable, even if the phenomenon is reduced with the modified model. The prediction of rupture, from a slope variation of the global force displacement curve, is not always possible : a too localized fracture can not be detected on this curve. On the other hand, d_{coales} the coalescence limit allows the detection of the micro-crack event and its consequences.

As it is not possible to define a unique threshold value of d_{coales} indicating a macroscopic rupture event, a rupture criterion coupling damage and triaxiality for instance should be determined. Nevertheless, the available tests are not numerous and accurate enough to establish this threshold value of the damage as a function of triaxiality. To get more data, new experiments on bars with various notch radii, corresponding to different triaxiality values, are required.

It is interesting to note that the difficulty to define a damage threshold value is not surprising, as, in reality, this limit depends on triaxiality. In fact Gurson's type model faces an identical problem. The general study of Benzerga *et al.* 1999 presents curves of the critical porosity f_{cr} depending on triaxiality T. Depending on the initial porosity value, f_{cr} is quite constant or increases with low (≈ 0.5) to mean values of T (0.8 – 1.2), then decreases for mean to high T values (>1.5), see Figure 4-14. This result from Benzerga *et al.* 1999 helps to understand why, depending on cases they study, authors like Needleman 1984, Koplik & Needleman 1988, Brocks *et al.* 1995, Brethenoux *et al.* 1997 have found various influences of T on critical porosity.

6.3.5 Conclusions

The initial Zhu's model does not apply to the studied aluminum alloy because the damage increases too rapidly in the zones where triaxiality is high. A modification of the law, that induces a less important damage increase, provides a solution.

The cracks initiation site is correctly predicted by this model, as well as their propagation directions. For shapes and loadings that correspond to a low triaxiality, if the damage zone is not too localized, the modified model allows to predict the sample rupture characterized by the drop in the force-displacement curve.

Additional experimental results are necessary for the establishment of a rupture criterion. When known, this criterion should predict the crack evolution according to damage and triaxiality.

Finally, the opportunity to use a non constant damage ratio τ should be investigated instead of introducing the reduction parameter p in equation (6-51). Indeed, Figure 6-43 shows the evolution of τ, which is not actually a constant for the studied material. Most of all, the analysis of the effect of the parameter p in the second term of equation (6-51) shows that it influences the value of τ in a nonlinear way.

6.4. Conclusions on the applied damage models

Sections 6.2. and 6.3. summarize a work performed at various times and with various co-workers, so it is not perfectly integrated. However, even if the damage figures are not related to the same time, it can be observed that the adapted Zhu's model is more sensitive to triaxiality than Bodner's damage version. This explains why it has not been possible to define a simple damage threshold limit to detect microcrack events for this model. As suspected, the numerical stability of the damage elasto-plastic approach is lower than the damage elasto-visco-plastic version and numerical bifurcations prevent an easy use of the model.

Different conclusions can be drawn from this work and the general literature review:

- Macroscopic damage approach can be applied to detect microcrack; however simple damage threshold value is of limited use. A criterium linking triaxiality and damage value is necessary. If one chooses to stay on a macroscopic level, systematic axisymmetric notch tests with various radii must be performed to define this limit curve, or to fit more elaborate fracture criteria by inverse modeling. Such a systematic approach would have allowed a better scientific work; however the available material shape and the cost of these experiments prevent this research extension.

- Global criteria on force-displacement are mesh sensitive if no additional regularization is applied. Non-local approaches with internal length seem to be necessary to stabilize this global information. Such non-local or gradient methods are required, if one wants to follow crack propagation.

- A microscopic material investigation, defining inclusion size and distribution, would greatly help FEM and macroscopic model users. It is necessary to be able to use rupture criteria as Thomason's or simply Rice's. It helps to adapt FEM size as explained by Rousselier. To perform a cell model analysis to define the macroscopic model parameters is not possible without knowledge of inclusion size or repartition. Even if inverse modeling based on macroscopic experiments allows fitting of models like Gurson's, a microscopic material study fixes physical variables values as initial porosity and helps to keep the advantage of the microscopic foundation of the model. In this research for instance, no discussion about the choice of model 1 or 2 in Bodner's damage approach has been possible without further microscopic information.

References

Basuroychowdhury, I.N., Voyiadijis, G.Z. (1998) A multiaxial cyclic plasticity model for non-proportional loading cases, *IJP*, **14-9**, 855-870.

Benzerga, A., Besson, J., Pineau, A. (1999) Coalescence-controlled anisotropic ductile fracture. *J. Eng. Mat. Eng.* **121**, 221-229.

Bodner, S.R. ,Partom, Y. (1975) Constitutive equations for elastic-viscoplastic strain-hardening material, *J. of Applied Mechanics*, **42**, 385-389.

Brethenoux, G., Mazataud, P., Bourgain, E., Muzzi, M. & Giusti, J. (1997) A mesoscopic approach of ductile damage during cold forming processes, *Advanced Methods in Materials Processing Defects*, M. Predeleanu & P. Gilormini, 23-32.

Brocks, W., Sun, D.Z., Honig, A. (1995) Verification of the transferability of micromechanical parameters by cell model calculations with visco-plastic materials, *Int. J. Plasticity*, **11-8**, 971-989.

Brown, L.M. , Embury, J.D. (1973) The initiation and growth of voids at second phase particles. *Proceedings of the 3rd Int. Conf. on the Strength of Metals and Alloys, ICSMA3*, Cambridge, England, 164-169.

Castagne, S. (1998) Application d'un modèle isotrope élastoplastique couplé à l'endommagement à un aluminium. Travail de fin d'études, Ingénieur Physicien, Université de Liège.

Castagne, S., Habraken, A.M., Cescotto, S. (to appear) Application of a damage model to an aluminium alloy, accepted in *Intern. Journ. of Damage Mechanics*.

Cescotto, S., Wang, X.C. & ZHU, Y.Y. (1993) Programme mobilisateur multimatériaux de la région wallonne, procédés intelligents de mise en œuvre par forgeage dynamique (forgeage rotatif), rapport final de la première phase.

Chan, K.S., Bodner, S.R., Lindholm, U.S. (1988) Phenomenological modeling of hardening and thermal recovery in metals, *J. of Eng. Mat. & Techn.*, **110**, 1-8.

Chevalier, L. (1988) Etude des caractéristiques des matériaux tréfilés après l'opération de tréfilage, Thèse de doctorat, Université de Paris 6, ENS Cachan.

Cordebois, J.P., Sidoroff, F. (1979) Damage induced elastic anisotropy, F. *Euromech*, **115**.

Dombrovsky, L.A. (1992) Increment constitutive equations for Miller and Bodner-Partom viscoplastic models, *Comp. & Struct.* **44**, 1064-1072.

Gattoufi, B. (1984) Effets de la prédéformation d, due au filage sur le comportement des métaux, Thèse de docteur de 3ème cycle, Université de Paris.

Gologanu, M., Leblond, J.B., J. Devaux (1994) Numerical and theoretical study of coalescence of cavities in periodically voided solids, *Computational Material Modeling, ASME*, AD- **42/PVP-. 294**.

Gurson, A.L. (1977) Continuum theory of ductile rupture by void nucleation and growth. *J. Engng. Materials Technology*, **99**, 2-15.

Habraken, A.M., Zhu, Y.Y., Charlier, R., Wang, X.C. (1995), A Damage Model for Elasto-Visco-Plastic Materials at Large Strains, *Computational Plasticity.*

Fundamentals and Applications, Owen, D.R.J., Onate, E., editors, Pineridge Press, Swansea UK, 1083-1094.

Habraken, A.M., Wang X.C. (1996) Programme mobilisateur multimatériaux de la région wallonne, procédés intelligents de mise en œuvre par forgeage dynamique (forgeage rotatif), rapport final de la deuxième phase.

Habraken, A.M., Zhang, L.H., Wauters, M. (1997) La calibration de l'Alu TAC, rapport interne MSM n° 230.

Habraken, A.M., Zhang, L.H., Wang, X.C., Cescotto, S. (1999) A new elastic-visco-plastic damage model for annealed aluminium, Part 1: Theory, Calibration, Part 2 Validation, internal report, MSM department, University of Liège.

Habraken, A.M., Zhang, L.H., Wang, X.C., Cescotto, S. (2000) A new elastic-visco-plastic damage model for annealed aluminium: Theory, Calibration, Validation, in *Continuous Damage and Fracture* edited by Benallal A. at Elsevier, The Data Science Library.

Hayakawa, K., Murakami, S. (1998) Space of damage conjugate force and damage potential of elastic-plastic-damage materials, *Damage Mechanics in Engineering Materials*, Voyiadjis, G.S., Ju, J.W., Chaboche, J.L. Eds, 27-44.

Koplik, J. , Needleman, A. (1988) Void growth and coalescence in porous plastic solids. *Int. J. Solids Structures*, **24-8**, 835-853.

Ladevèze, P. (1984) Sur une théorie de l'endommagement anisotrope, Rapport interne 34, LMT, Cachan, France.

Leblond, J.B., Perrin, G., Devaux, J. (1995) An improved Gurson-type model for hardenable ductile metals, *Eur. J. Mech. A/Solids*, **14**, 499-527.

Lemaître, J. (1985) Coupled elastoplasticity and damage constitutive equations, *J. Comp. Meth. in Appl. Mech. and Eng.* **51**, 31-49.

Lemaître, J., Chaboche, J.L. (1985) *Mécanique des matériaux solides*, Dunod, Paris.

Mudry, F. (1982) Etude de la rupture ductile et de la rupture par clinage d'aciers faiblement alliés, thèse d'état, Université Technologique de Compiègne.

Needleman, A., Tvergaard, V. (1984) An analysis of ductile rupture in notched bars, *J. Mech. Phys. Solids*, **32**, 461-490.

Pardoen, T. (1998) Ductile fracture of cold-drawn copper bars : experimental investigation and micromechanical modelling, Doctorat en sciences appliquées, Université de Louvain-La-Neuve.

Perzyna, P. (1986) Internal state variable description of dynamic fracture of ductile solids, *Int. J. Solids & Struct.*, **22**, 797-818.

Phillips, A., Tang J.L., Ricciuti, M. (1974) Some new observations on yield surfaces, *Acta Mechanica*, **20**, 23-39.

Pierry, J. (1997), Modélisation des bandes de cisaillement et adaptation de maillages. Application à la coupe de la roche. Université de Liège, thèse de doctorat en sciences appliquées.

Rousselier, G. (1987) Ductile fracture models and their potential in local approach of fracture, *Nuclear Engineering and Design*, **105**, 97-111.

Szabo, L. (1985) Evaluation of elasto-viscoplastic tangent matrices without numerical inversion, *Comp. & Struct.* **21**, 1235-1236.

Thomason, P.F. (1993) Ductile fracture by the growth and coalescence of microvoids of non uniform size and spacing, *Acta Metall. Mater*, **41-7**, 2127-2134.

Wang, X.C., Zhu, Y.Y., Cescotto S. (1994a) Strain-rate-sensitivity in rotary tube forging problems : finite element modelling with Bodner's constitutive model, *Proc. of 3rd Belgian Nat. Congr. of Th. & Appl. Mech.*, Liège, Belgium, 314-317.

Wang, X.C., Zhu, Y.Y., Cescotto S. (1994b) Analytical solutions and finite element modelling of rotary tube forging, Proc. of *Metal Forming Process Simulation in Industry*, Baden-Baden, Germany, 249-269.

Wang, X.C., Habraken, A.M., Cescotto, S. (1995) Two- and three-dimensional finite element modelling of the industrial tube forging process, *Simulation of materials processing : theory, methods and applications*, SF. Shen&P.R. Dawson Eds, Balkema, Rotterdam/Brookfield, 899-905.

Wang, X.C. (1996) Le modèle de Bodner avec endommagement pour Alu-TAC. Une nouvelle calibration et la validation. Rapport partiel 2-9 du projet "Procédés intelligents de mise en œuvre par forgeage dynamique (2ème phase)". Programme Mobilisateur de la Région Wallonne, Convention 2394.

Wang, X.C., Habraken, A.M. (1996) An elastic-visco-plastic damage model : from theory to application, *supplément au Journal de Physique*, **6**, 549-558.

Zhu, Y.Y., Cescotto (1991) Modèles viscoplastiques unifiés pour le comportement dynamique des matériaux soumis à de grandes vitesses de déformation. Etude bibliographique. Programme mobilisateur multimatériaux de la Région Wallonne, Procédés intelligents de mise en œuvre par forgeage dynamique (forgeage rotatif), phase 1.

Zhu, Y.Y. (1992) Contribution to the local approach of fracture in solid dynamics, Ph. D. Thesis, University of Liège, Department MSM.

Zhu, Y.Y., Cescotto, S. and Habraken, A.M. (1992) A fully coupled elastoplastic damage modeling and fracture criteria in metalforming processes, *J. of Mater. Processing Technology* **32**, 197-204.

Zhu, Y.Y., Cescotto, S. (1994) A unified elasto-visco plastic theory of the Bodner model and an effective integration procedure, *J. DYMAT* **1**, 63-99.

Zhu, Y.Y., Cescotto, S. and Habraken, A.M. (1995a) Modelling of fracture initiation in metalforming processes, *Materials Processing Defects*, S.K. Gosh, M. Predeleanu Eds., 155-170, Elsevier Science B.V.

7. STUDY OF STEEL SHEETS

7.1. Introduction

This chapter presents in a unified way, compatible with the notations introduced in Chapter 3, the work performed by numerous co-workers. Its goal is to give an overview of the present state of the model as its theory, finite element implementation and experimental identifications have been built by a lot of different researchers: Zhu Yongyi, Raphaël Estevez, Jean-François Charles, Serge Munhoven, Anne-France Cambron, Michaël Wauters, with Anne-Marie Habraken acting as "memory", stimulator and coordinator. Zhu Yongyi has developed the first theoretical model (Zhu 1992), which is described in section 7.2. The approach used to follow the local axes is due to Munhoven 1995 and is described in section 7.3. Raphaël Estevez has proposed a first approach of the identification method (Estevez & Habraken 1996). Anne-France Cambron has tried to apply this approach on a Zinc sheet (Cambron 1997). Jean-François Charles has performed and analyzed a first set of experiments on RDCS steels (IF ULC Ti steel and SPXI steel) related to the model identification (Charles & Habraken 1996). Finally, Michaël Wauters (Wauters1997, 1998, 1999, 2000) has improved the model, the identification method (summarized in section 7.4) and the experimental device. His experimental results are presented in section 7.5. He has also made some steps towards a validation (Wauters 2000 and Wauters *et al* 2000) that are presented in sections 7.6 and 7.7. The final simulation on Nakazyma biaxial test is due to Charles *et al.* 1997.

In industry, simulations of sheet metal forming operations with FEM codes are becoming a necessity during product and process development. However, researches are still required to increase accuracy and correctly predict location and moment of failure events.

The anisotropic behavior of steel sheets is well known. For instance a circular cup drawn from a circular piece of metal sheet using axisymmetric tools often presents an undulating rim called earring. The origin of such a behavior is the crystallographic nature of the plastic metal deformation. The use of anisotropic elasto-plastic models allows the description of such phenomena. Current cases of 4 ears can be predicted by a classical Hill's model (Hill 1948), but more singular cases of 6 ears request an accurate yield locus shape based for instance, on texture measurements and polycrystal plasticity (see Part B of this thesis).

An initial accurate yield locus is not sufficient to model difficult sheet metal forming processes as complex strain paths induce size and shape modifications of the yield locus. So, the work-hardening rate requires a particular attention, if one wants to model Bauschinger's effect and the cross effect. For instance, the physics based work-hardening model proposed by Teodosiu & Hu 1995 is an interesting alternative to conventional phenomenological models, as this model complexity is still

reasonable to implement in a FEM code. Nevertheless, a macroscopic energetic approach is considered hereafter.

As recalled in Chapter 2, damage models such as Gurson's (Gurson 1977) or its recent improvement proposed by Gologanu *et al.* 1994 require precise data to describe accurately nucleation, growth and coalescence of voids. Such information is difficult to get from macroscopic tests and must rely on microscopic measurements of voids which consists in a very long investigation. The models proposed by Lemaître & Chaboche 1985 are perhaps less anchored in microscopic physics but offer the advantage of being calibrated by macroscopic tests; this is the major reason of MSM choice of such a type of models. Zhu's anisotropic elasto-plastic model is an attempt to extend such a model to anisotropic cases.

7.2. Zhu's anisotropic elasto-plastic damage model

7.2.1. Model characteristics

A short literature review of anisotropic elasto-plastic damage models based on thermodynamic approach can be found in Zhu 1992. The goals of the research conducted after Zhu's departure were the development of a calibration method for his model, a better understanding of the effect of the model assumptions and finally a validation step. In fact, Zhu's model is a modified version from previous constitutive laws proposed by Cordebois & Sidoroff 1979 or Cordebois 1983. Its main features are the following ones :

- three major anisotropies are taken into account: anisotropic elasticity, anisotropic plasticity and anisotropic damage;
- the generalized damage effect tensor $\underline{\underline{M}}$ proposed by Chow and Wang 1987 is used;
- a new damage characteristic tensor $\underline{\underline{J}}$ based on the hypothesis of damage energy equivalence is proposed;
- an effective computational integration algorithm with two steps split operators is proposed;
- as large displacements and strains happen, the definition of local axes fitted on material principal axes is necessary, the local reference system proposed by Munhoven *et al.* 1996 is used;
- Hill's yield locus is adapted to describe plastic behavior; however the plastic tensor $\underline{\underline{H}}$ is not assumed to be constant during hardening; a plastic energy equivalence rule is adopted;
- a very simple function is chosen to describe damage potential, the goal is to describe damage evolution with a limited number of material parameters.

As already presented in Chapter 3 concerning general thermodynamic approach, the concept of effective stress is used. This basic assumption is translated by means of a "damage effect tensor" $\underline{\underline{M}}(\underline{D})$ applied to the stress tensor $\underline{\sigma}$, which defines the effective stress tensor $\underline{\bar{\sigma}}$:

$$\underline{\bar{\sigma}} = \underline{\underline{M}}(\underline{D}) : \underline{\sigma} \quad \text{or} \quad \underline{\bar{\sigma}} = \underline{\underline{M}}(\underline{D}) : \underline{\sigma} \tag{7-1}$$

where the damage effect tensor is a second-order $\underline{M}(\underline{D})$ or a fourth-order tensor $\underline{\underline{M}}(\underline{D})$ tensor, depending on the damage tensor order $\underline{D}$. Note that four fundamental variables of continuum damage mechanics have been introduced in these assumptions, i.e. the damage tensor $\underline{D}$, the damage effect tensor $\underline{\underline{M}}(\underline{D})$, the effective stress tensor $\underline{\bar{\sigma}}$ and effective strain tensor $\underline{\bar{\varepsilon}}$.

By simplicity, anisotropic damage is characterized by a symmetric second-order tensor $\underline{D}$. There is no uniquely defined mathematical formulation of $\underline{\underline{M}}(\underline{D})$; Zhu's choice is the one proposed by Chow & Wang 1987, which offers the advantages of a possible reduction to a scalar variable for isotropic damage and of having a simple expression outside the stress tensor principle directions.

In the principal co-ordinate system of damage, which in the present formulation is the material principal system where Hill yield locus is expressed, the effective stress tensor is computed by:

$$[\bar{\sigma}_{11}\bar{\sigma}_{22}\bar{\sigma}_{33}\bar{\sigma}_{23}\bar{\sigma}_{31}\bar{\sigma}_{12}]^T = \underline{\underline{M}}[\sigma_{11}\sigma_{22}\sigma_{33}\sigma_{23}\sigma_{31}\sigma_{12}]^T \tag{7-2}$$

with the fourth rank symmetric tensor :

$$\underline{\underline{M}} = diag$$

$$\left[\frac{1}{1-D_1}, \frac{1}{1-D_2}, \frac{1}{1-D_3}, \frac{1}{\sqrt{(1-D_2)(1-D_3)}}, \frac{1}{\sqrt{(1-D_3)(1-D_1)}}, \frac{1}{\sqrt{(1-D_1)(1-D_2)}}\right] \tag{7-3}$$

So no special computation is required to follow damage principal directions; damage is simply defined by 3 scalars. This simple choice is of course poorer than Fichant's 1996 model (see section 3.2.7) or Gallerneau's 1995, where damage principal directions can rotate. The approaches of Hayakawa & Murakami 1998 (see section 3.2.4) or Gelin & Danescu, 1992 also use a second rank symmetric damage tensor that takes into account rotation of damage principal directions with stress or strain evolution. However as verified by sections 7.5 and 7.6, this chosen simple damage characterization is able to model anisotropic damage effect with a limited number of experiments to define the damage parameters.

Instead of the conventional postulate of strain or stress equivalence, an hypothesis of energy equivalence is used. It states that the complementary elastic energy for a damaged material has the same form as a fictitious undamaged material except that the stress is replaced by the effective stress in the energy formulation. Mathematically, this yields:

$$\psi^e(\underline{\sigma},\underline{D}) = \psi^e(\underline{\bar{\sigma}},\underline{D}) \quad \text{or} \quad \frac{1}{2}\underline{\bar{\sigma}}^T : \underline{\underline{C}}^{e-1} : \underline{\bar{\sigma}} = \frac{1}{2}\underline{\sigma}^T : \underline{\underline{\bar{C}}}^{e-1} : \underline{\sigma} \tag{7-4}$$

where $\underline{\underline{C}}^e$ and $\underline{\underline{\bar{C}}}^e$ are the stiffness tensors for the virgin and damaged elastic material respectively. By recalling (7-1), it can be easily proved that :

$$\underline{\underline{\bar{C}}}^{e-1} = \underline{\underline{M}}(\underline{D}) : \underline{\underline{C}}^{e-1} : \underline{\underline{M}}(\underline{D}) \tag{7-5}$$

and, according to the hypothesis of energy equivalence, the effective elastic strain vector is :

$$\underline{\bar{\varepsilon}}^e = \underline{\underline{M}}^{-1} : \underline{\varepsilon}^e \tag{7-6}$$

where :

$$\underline{\underline{M}}^{-1} = diag$$

$$\left[1-D_1, 1-D_2, 1-D_3, \sqrt{(1-D_2)(1-D_3)}, \sqrt{(1-D_3)(1-D_1)}, \sqrt{(1-D_1)(1-D_2)}\right] \tag{7-7}$$

7.2.2. General thermodynamic analysis

The internal variables used in the thermodynamic analysis are listed in Table 7-1 together with their associated thermodynamic forces. The general structure of the constitutive equations is furnished by the well-established thermodynamic theory of irreversible processes described in Chapter 3. Hereafter, isothermal condition is assumed.

State variables	Associated thermodynamic forces
Elastic strain $\underline{\varepsilon}^e$ Accumulated plastic strain p Damage variable $\underline{D} = (D_1\ D_2\ D_3)$ Overall damage β	Cauchy stress $\underline{\sigma}$ Plastic hardening threshold R Damage energy release rate $\underline{Y} = (Y_1\ Y_2\ Y_3)$ Damage strengthening threshold B

Table 7-1 State variables and associated thermodynamic forces (from Zhu 1992).

As it has been indicated in Lemaître 1985, uncoupled plasticity and elasticity are assumed so that the elastic properties depend only on damage variables and not on the dislocation density represented by p. For practical purposes, another hypothesis is introduced: energies involved in plastic flow and damage processes, dissipated by heat or stored in the material, are independent. Consequently, in the present model,

the Helmholtz free energy takes the following form, as proposed by Valliappan *et al.* 1976 or Hayakawa & Murakami 1998:

$$\rho\psi(\underline{\varepsilon}^e,\underline{D},p,\beta)=\psi^e(\underline{\varepsilon}^e,\underline{D})+\psi^p(p)+\psi^d(\beta) \tag{7-8}$$

where $\psi^e(\varepsilon^e,D)$ is the elastic strain energy, $\psi^p(p)$ the free energy due to plastic hardening and $\psi^d(\beta)$ the free energy due to damage hardening. The complementary energy is obtained from the Legendre transformation of the free energy with respect to strain, i.e.

$$\rho\Pi(\underline{\sigma},\underline{D},p,\beta)=\underline{\sigma}:\underline{\varepsilon}^e-\rho\psi(\underline{\varepsilon}^e,\underline{D},p,\beta)=\psi^e(\underline{\sigma},\underline{D})-\psi^p(p)-\psi^d(\beta) \tag{7-9}$$

According to the energy equivalence hypothesis, the elastic strain energy $\psi^e(\underline{\varepsilon}^e,\underline{D})$ and the complementary elastic energy $\psi^e(\underline{\sigma},\underline{D})$ can be evaluated. Following the rules of thermodynamics of irreversible processes, the associated thermodynamic forces are given by :

$$\begin{aligned}
\underline{\sigma} &= \frac{\rho\partial\psi}{\partial\underline{\varepsilon}^e}=\underline{\underline{M}}^{-1}:\underline{\underline{C}}^e:\underline{\underline{M}}^{-1}\underline{\varepsilon}^e \\
R &= \rho\frac{\partial\psi}{\partial p}=\frac{\partial\psi^p(p)}{\partial p} \\
B &= \rho\frac{\partial\psi}{\partial\beta}=\frac{\partial\psi^d(\beta)}{\partial\beta} \\
\underline{Y} &= \rho\frac{\partial\psi}{\partial\underline{D}}=-\rho\frac{\partial\Pi}{\partial\underline{D}}=-\frac{\partial\psi^e(\underline{\sigma},\underline{D})}{\partial\underline{D}}=-\underline{\sigma}^T:\underline{\underline{M}}:\underline{\underline{C}}^{e-1}:\frac{\partial\underline{\underline{M}}}{\partial\underline{D}}:\underline{\sigma}
\end{aligned} \tag{7-10.a,b,c,d}$$

The negative of $\underline{Y}$ can be considered as the elastic strain energy rate associated with a unit damage increment, as it is easy to show that :

$$-\underline{Y}=\frac{1}{2}\frac{d\psi^e}{d\underline{D}}\Bigg]_{\text{at constant }\underline{\sigma}} \tag{7-11}$$

$\underline{Y}$ is often given the name of "damage energy release rate". For this model, the Clausius-Duhem inequality recalled in Chapter 3 is written:

$$\Phi=\underline{\sigma}:\dot{\underline{\varepsilon}}_p-R\dot{p}-\underline{Y}:\dot{\underline{D}}-B\,\dot{\beta}\geq 0 \tag{7-12}$$

Within the hypothesis of independence of energy dissipations between plastic flow and damage process, equation (7-12) can be separated into two parts such that :

$$\underline{\sigma}:\dot{\underline{\varepsilon}}_p-R\,\dot{p}\geq 0 \quad\text{and}\quad -\underline{Y}:\dot{\underline{D}}-B\,\dot{\beta}\geq 0 \tag{7-13a, b}$$

Equations (7-13a, b) show the existence of a plastic dissipative potential and a damage dissipative potential, i.e.:

$$F_p(\underline{\sigma},\underline{D},R)=0 \quad\text{and}\quad F_d(\underline{Y},\underline{B})=0 \tag{7-14a, b}$$

in which the former represents the plastic yield criterion; the latter is the damage evolution criterion. In the case where the criteria $F_p = 0$ and $F_d = 0$ are satisfied, the actual values of $\underline{\sigma}, R, \underline{Y}, B$ will make the dissipation power of equation (7-12) a stationary value. If Lagrange multipliers $\dot{\lambda}_p$ and $\dot{\lambda}_d$ are introduced, equation (7-12) can be written:

$$\Phi = \underline{\sigma} : \underline{\dot{\varepsilon}}^p - R\dot{p} - \underline{Y} : \underline{\dot{D}} - B\dot{\beta} - \dot{\lambda}_p F_p - \dot{\lambda}_d F_d \tag{7-15}$$

The final evolution rules are:

$$\frac{\partial \Phi}{\partial \underline{\sigma}} = 0 \Rightarrow \underline{\dot{\varepsilon}}^p = \dot{\lambda}_p \frac{\partial F_p}{\partial \underline{\sigma}} \qquad \frac{\partial \Phi}{\partial \underline{Y}} = 0 \Rightarrow \underline{\dot{D}} = -\dot{\lambda}_d \frac{\partial F_d}{\partial \underline{Y}}$$
$$\frac{\partial \Phi}{\partial R} = 0 \Rightarrow \dot{p} = \dot{\lambda}_p \frac{\partial F_p}{\partial R} \qquad \frac{\partial \Phi}{\partial B} = 0 \Rightarrow \dot{\beta} = -\dot{\lambda}_d \frac{\partial F_d}{\partial B} \tag{7-16a, b, c, d}$$

This approach finally recovers Hayakawa & Murakami's 1998 proposals, as their experiments certify the assumption of damage potential identical to the damage surface and the corresponding normality rule for damage evolution equation.

7.2.3. Fully coupled anisotropic elasto-plastic damage model

A. Anisotropic elasticity and damage

When a material is damaged, its constitutive relation is:

$$\underline{\sigma} = \underline{\underline{\bar{C}}}^e : \underline{\varepsilon}^e \quad \text{or} \quad \underline{\varepsilon}_e = \underline{\underline{C}}^{e-1} : \underline{\sigma} \tag{7-17}$$

The classical Hooke's elastic tensor for orthotropic materials combined with equation (7-5) yields the following expression :

$$\begin{Bmatrix} \varepsilon_{11} \\ \varepsilon_{22} \\ \varepsilon_{33} \\ \varepsilon_{23} \\ \varepsilon_{31} \\ \varepsilon_{21} \end{Bmatrix} = \begin{bmatrix} \frac{1}{E_1(1-D_1)^2} & \frac{-\nu_{12}}{(1-D_1)(1-D_2)E_1} & \frac{-\nu_{13}}{(1-D_1)(1-D_3)E_1} & 0 & 0 & 0 \\ \frac{-\nu_{21}}{(1-D_1)(1-D_2)E_2} & \frac{1}{E_2(1-D_2)^2} & \frac{-\nu_{23}}{(1-D_3)(1-D_2)E_2} & 0 & 0 & 0 \\ \frac{-\nu_{31}}{(1-D_1)(1-D_3)E_3} & \frac{-\nu_{32}}{(1-D_2)(1-D_3)E_3} & \frac{1}{E_3(1-D_3)^2} & 0 & 0 & 0 \\ 0 & 0 & 0 & \frac{1}{2G_{23}(1-D_2)(1-D_3)} & 0 & 0 \\ 0 & 0 & 0 & 0 & \frac{1}{2G_{32}(1-D_1)(1-D_3)} & 0 \\ 0 & 0 & 0 & 0 & 0 & \frac{1}{2G_{12}(1-D_1)(1-D_2)} \end{bmatrix} \begin{Bmatrix} \sigma_{11} \\ \sigma_{22} \\ \sigma_{33} \\ \sigma_{23} \\ \sigma_{31} \\ \sigma_{12} \end{Bmatrix}$$

(7-18)

In order to guarantee the positive definiteness of $\underline{\underline{\overline{C}}}^e$, the following conditions should be satisfied :

$$0 < \Delta_c \leq 1 \text{ with } \Delta_c = 1 - \nu_{21}\nu_{12} - \nu_{31}\nu_{13} - \nu_{32}\nu_{23} - \nu_{12}\nu_{23}\nu_{31} - \nu_{21}\nu_{13}\nu_{32} \qquad (7\text{-}19)$$

$$0 < 1 - \nu_{ij}\nu_{ji} \leq 1 \text{ (no sum on i, j)}, \quad 0 \leq D_i < 1$$

$$G_{23} > 0, \quad G_{31} > 0, \quad G_{12} > 0, \quad E_1 > 0, \quad E_2 > 0, \quad E_3 > 0$$

Orthotropic symmetry assumes also the following equalities expressed in the initial state ($D_1 = D_2 = D_3 = 0$) :

$$\frac{\nu_{12}}{E_1} = \frac{\nu_{21}}{E_2}, \quad \frac{\nu_{31}}{E_3} = \frac{\nu_{13}}{E_1}, \quad \frac{\nu_{32}}{E_3} = \frac{\nu_{23}}{E_2} \qquad (7\text{-}20)$$

B. Anisotropic plastic yield surface

In the damage characterization of materials undergoing large plastic strains, Hill's yield criterion in stress space is expressed in the following form :

$$F_p(\underline{\sigma}, \underline{D}, R) = F_p(\underline{\overline{\sigma}}, R) = \overline{\sigma}_F - \sigma_y - R(p) = 0 \qquad (7\text{-}21)$$

where σ_y is the initial plastic stress.

The effective equivalent stress $\overline{\sigma}_F$ is:

$$\overline{\sigma}_F = \left\{ \frac{1}{2} \underline{\overline{\sigma}}^T : \underline{\underline{H}} : \underline{\overline{\sigma}} \right\}^{1/2} = \left\{ \frac{1}{2} \underline{\sigma}^T : \underline{\underline{\overline{H}}} : \underline{\sigma} \right\}^{1/2} \qquad (7\text{-}22)$$

The effective plastic characteristic tensor $\underline{\underline{\overline{H}}}$ is given by :

$$\underline{\underline{\overline{H}}} = \underline{\underline{M}}(\underline{D}) : \underline{\underline{H}} : \underline{\underline{M}}(\underline{D}) \qquad (7\text{-}23)$$

The positive definite tensor $\underline{\underline{H}}$ for orthotropic materials is represented by a 6x6 matrix in the material principal system (Hill 1948):

$$\underline{\underline{H}} = \begin{bmatrix} G+H & -H & -G & 0 & 0 & 0 \\ -H & H+F & -F & 0 & 0 & 0 \\ -G & -F & F+G & 0 & 0 & 0 \\ 0 & 0 & 0 & N & 0 & 0 \\ 0 & 0 & 0 & 0 & L & 0 \\ 0 & 0 & 0 & 0 & 0 & M \end{bmatrix} \qquad (7\text{-}24)$$

where F, G, H, L, M, N are parameters characterizing the current state of plastic anisotropy. For a strain-hardening material, the uniaxial yield stress varies with increasing plastic strain and, therefore, the anisotropic parameters should also vary, since they are functions of the current yield stress (see Valliappan *et al.* 1976). For

sheet metal forming, this can be easily verified experimentally by measuring the well-known Lankford coefficient r, ratio of transversal and thickness strain rate during a tensile test. This ratio depends on the angle between the tensile and the rolling direction, its value is directly connected to $F\ G\ H\ L\ M\ N$ parameters, expression of the anisotropic property of the sheet. However, the Lankford coefficient is not constant during every tensile test : it depends on plastic strain; this leads to the conclusion that $\underline{H}$ tensor must vary. As this increases the model complexity, a lot of implementations of Hill's model neglect this fact and use a constant $\underline{H}$ tensor.

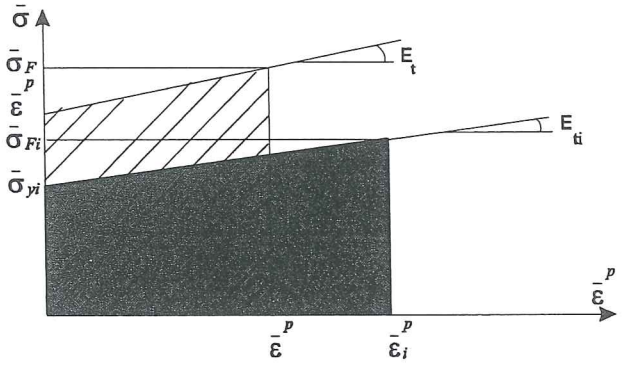

Figure 7-1 Equating plastic work for simple linear plastic behavior (from Zhu 1992).

$\bar{\sigma}_y$ = initial effective equivalent plastic stress,

$\bar{\sigma}_{yi}$ = initial effective plastic stress in direction i,

$\bar{\sigma}_F$ = effective equivalent stress corresponding to p,

$\bar{\sigma}_{Fi}$ = effective stress in direction i leading to the same plastic work as $\bar{\sigma}_F$,

E_t = slope of effective equivalent stress plastic strain curve,

E_{ti} = slope of effective stress plastic strain curve in direction i.

In Zhu's model, the evolution of the $\underline{H}$ tensor is based on the plastic work equivalence in each direction (Figure 7-1). Practically, one direction is chosen as the reference one (generally the rolling direction) and a uniaxial tensile test in this direction gives *the stress-plastic strain equivalent curve* ($\bar{\sigma}\ \bar{\varepsilon}^p$) where for shortness no *equivalence* or *reference* indice is noted. For any material state, the knowledge of the internal variable p and equation (7-21) yield to the associate effective equivalent stress $\bar{\sigma}_F$; then, with the help of ($\bar{\sigma}\ \bar{\varepsilon}^p$) curve, the equivalent plastic work is estimated. Knowing ($\bar{\sigma}\ \bar{\varepsilon}^p$)$_i$ curves in each direction i, the stress level $\bar{\sigma}_{Fi}$ giving the same plastic work in each direction can be found. The ratios between $\bar{\sigma}_F$ and $\bar{\sigma}_{F_i}$ are directly connected to the anisotropic parameters of the sheet (7-27).

The simple case of a linear work hardening material described by Figure 7-1 gives:

$$W^p = \frac{1}{2E_{ti}}(\bar{\sigma}_{Fi}^2 - \bar{\sigma}_{yi}^2) = \frac{1}{2E_t}(\bar{\sigma}_F^2 - \bar{\sigma}_Y^2) = \text{plastic work} \qquad (7\text{-}25)$$

In this simple case, equating plastic work leads to following ratios :

$$a_i = \left(\frac{\bar{\sigma}_F}{\bar{\sigma}_{Fi}} \right)^2 = \frac{\bar{\sigma}_F^2}{(E_{ti}/E_t)(\bar{\sigma}_F^2 - \bar{\sigma}_y^2) + \bar{\sigma}_{yi}^2} \qquad (7\text{-}26)$$

with $i = 1, 2, 3, 23, 31, 12$.

The relations between a_i and classical anisotropic parameters are listed hereafter:

$$\begin{cases} G+H=2a_1 & -H=-a_1-a_2+a_3 & N=2a_{23} \\ H+F=2a_2 & -G=-a_1+a_2-a_3 & L=2a_{31} \\ F+G=2a_3 & -F=a_1-a_2-a_3 & M=2a_{12} \end{cases} \qquad (7\text{-}27)$$

Obviously, if direction 1 is taken as reference direction, $a_1 = 1$. This hardening approach induces changes in yield shape and size.

As Zhu's proposal of linear hardening was too limited to fit with any material behavior, a multi-linear curve has been implemented by Wauters 1998. This choice of multi-linear description was preferred to a classical analytical curve description in order to retain generality. Note that the maximum number of linear segments is very high so very smooth curves can be introduced and they can accurately reproduce a large number of material behaviors.

The plastic constitutive equations incorporating material damage may be derived by taking the yield criterion (7-21) as a potential function. By assuming an associated flow rule, the plastic strain is characterized as follows :

$$\begin{cases} \underline{\dot{\varepsilon}}^p = \dot{\lambda}_p \dfrac{\partial F_p}{\partial \underline{\sigma}} = \dfrac{\underline{\underline{M}} : \underline{\underline{H}} : \underline{\underline{M}} : \underline{\sigma}}{2\bar{\sigma}_F} \dot{\lambda}_p \\ (\text{plastic flow rule}) \end{cases} \qquad (7\text{-}28)$$

$$\begin{cases} \dot{R} = \dot{\lambda}_p \dfrac{dR}{dp} \\ (\text{isotropic hardening rule}) \end{cases} \qquad (7\text{-}29)$$

$$\begin{cases} F_p \le 0, \dot{\lambda}_p \ge 0, \dot{\lambda}_p F_p = 0 \\ (\text{plastic loading/unloading rule}) \end{cases} \qquad (7\text{-}30)$$

C. Damage evolution law and damage surface

In a similar way to the arguments leading to plastic dissipative potential, one can assume that there exists a surface F_d=0, which separates the damaging domain from

the undamaging domain. A damage criterion in the form of a quadratic homogeneous function of the damage energy release rate $\underline{Y}$ was proposed by Cordebois & Sidoroff 1979 and Cordebois 1983:

$$F_d = Y_{eq} - B_o - B(\beta) = 0 \tag{7-31}$$

where the equivalent damage energy release rate Y_{eq} is defined by :

$$Y_{eq} = \left[\frac{1}{2}\underline{Y}^T : \underline{\underline{J}} : \underline{Y}\right]^{1/2} \tag{7-32}$$

in which $\underline{\underline{J}}$ is the damage characteristic tensor.

The determination of a suitable damage characteristic tensor $\underline{\underline{J}}$, which is simple enough to be applied and still accurately describes the non-linear nature of damage growth, is perhaps the most important aspect in the present formulation of anisotropic damage evolution law. $\underline{\underline{J}}$ should be a fourth order tensor as $\underline{\underline{H}}$. This has been adopted by Hayakawa & Murakami 1998 (see tensor $\underline{\underline{L}}$ equations (3-38) and (3-39)). However, since Zhu's model works in the principal co-ordinate system of damage, $\underline{\underline{J}}$ can be treated like a second order tensor $\underline{J}$. The purpose of introducing a damage characteristic tensor $\underline{\underline{J}}$ (like the introduction of plastic characteristic tensor $\underline{\underline{H}}$ in the theory of plasticity) is to take into account the anisotropic nature of damage growth. The damage characteristic tensor $\underline{J}$ proposed by Zhu is an extension of the formulation due to Lu & Chow 1990; it is based on the damage energy equivalence assumption.

$$\underline{J} = 2\begin{bmatrix} J_1 & \sqrt{J_1 J_2} & \sqrt{J_1 J_3} \\ \sqrt{J_1 J_2} & J_2 & \sqrt{J_2 J_3} \\ \sqrt{J_1 J_3} & \sqrt{J_2 J_3} & J_3 \end{bmatrix} \tag{7-33}$$

In the case of damage hardening materials, the equivalent damage energy release rate Y_{eq} increases with the total damage growth and, hence, the anisotropic parameters (J_1, J_2, J_3) in the above equation should also vary. Their evolution follows the same principle as $\underline{\underline{H}}$ tensor components except that plastic work is here replaced by damage work. For the case of linear damage hardening and the choice of component Y_1 as reference direction, J_2 and J_3 are computed by relation (7-34) and $J_1 = 1$.

$$J_i = \frac{Y_1^2}{(D_{ti}/D_{t1})(Y_1^2 - Y_{01}^2) + Y_{oi}^2} \tag{7-34}$$

with $i = 2$ or 3. Figure 7-2 recalls Y_1, Y_i, Y_{o1}, Y_{oi}, D_{t1}, D_{ti} significances.

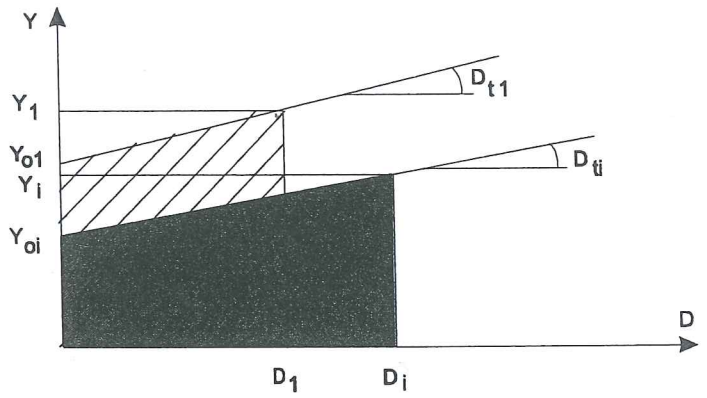

Figure 7-2 Equating damage work (from Zhu 1992).

As explained in section 7.4.4, the linear assumption of *Y-D* curves has strong effects on the model properties. However, for simplicity in the numerical model implementation and in the calibration method, this hypothesis is presently retained.

In the same way as the definition of plastic flow, the evolution law of anisotropic damage is characterized below:

$$\begin{cases} \underline{\dot{D}} = -\dot{\lambda}_d \dfrac{\partial F_d}{\partial \underline{Y}} = -\dfrac{\underline{J}.\underline{Y}}{2Y_{eq}}\dot{\lambda}_d = \underline{Y}^*\dot{\lambda}_d \\ \text{with } \underline{Y}^* = -\dfrac{\underline{J}.\underline{Y}}{2Y_{eq}} \\ \text{(damage evolution rule)} \end{cases} \tag{7-35}$$

$$\begin{cases} \dot{\beta} = -\dot{\lambda}_d \dfrac{\partial F_d}{\partial B} = \dot{\lambda}_d \\ \dot{B} = \dfrac{dB}{d\beta}\dot{\beta} = \dfrac{dB}{d\beta}\dot{\lambda}_d \\ \text{(damage hardening rule)} \end{cases} \tag{7-36}$$

$$\begin{cases} F_d \le 0, \dot{\lambda}_d \ge 0, \dot{\lambda}_d F_d = 0 \\ \text{(damage loading/unloading rule)} \end{cases} \tag{7-37}$$

D. Final constitutive relations

The complete set of equations is available in Zhu 1992, Zhu & Cescotto 1995; here the algebraic way to reach it and the final form of the result are presented. According to the elastic constitutive relations and effective strain tensor definition (7-6):

$$\overline{\underline{\sigma}} = \underline{\underline{C}}^{e} : \underline{\underline{M}}^{-1} : \underline{\varepsilon}^{e} \tag{7-38}$$

Using the additive decomposition of strain rate into an elastic and plastic part as well as the time derivative of the inverse of the damage effect tensor and the damage rate equation (7-35), the objective rate form of equation (7-38) is obtained :

$$\overset{\nabla}{\underline{\sigma}} = \underline{\underline{C}}^{e} : \underline{\underline{M}}^{-1} : \underline{\dot{\varepsilon}} - \underline{C}^{*}\dot{\lambda}_{p} - \underline{D}^{*}\dot{\lambda}_{d} \tag{7-39}$$

where $\underline{C}^{*}$ and $\underline{D}^{*}$ are explicitly defined in Zhu & Cescotto 1995 and, $\overset{\nabla}{}$ subscript means objective rate. So, the objective rate of the stress tensor is easily computed as :

$$\overset{\nabla}{\underline{\hat{\sigma}}} = \underline{\underline{M}}^{-1} : \overset{\nabla}{\underline{\sigma}} - \underline{\underline{M}}^{-1} : \dot{\underline{\underline{M}}} : \underline{\sigma} \tag{7-40}$$

Concerning damage evolution, starting from the damage energy released rate $\underline{Y}$ in (7-10d), its time derivative is computed :

$$\dot{\underline{Y}} = \underline{J}^{*}\,\underline{\dot{\varepsilon}} + \underline{H}^{*}\dot{\lambda}_{p} + \underline{T}^{*}\dot{\lambda}_{d} \tag{7-41}$$

where $\underline{J}^{*}$, $\underline{H}^{*}$ and $\underline{T}^{*}$ are second order tensors explicitly defined in Zhu & Cescotto 1995. The final set of equations is composed by equations (7-28, 7-29, 7-30, 7-35, 7-36, 7-37, 7-40, 7-41).

7.3. Computational algorithms for anisotropic damage model

7.3.1. Local axis computation

As the anisotropic yield locus and the damage locus are defined according to material principal axes, some local reference system must follow these material axes during the large strains and rotations of the sheet. Real material axes attached to a deforming body are subjected to distortion, while local axes remain cartesian. So, there is no unique definition of a local frame, however the various possible choices differ only through a spurious rigid body rotation. In Lagamine code, the method implemented to follow material axes is due to Munhoven and details can be found in Munhoven 1995 or Munhoven *et al.* 1995. As it is an important point for the present anisotropic damage law, but also for the anisotropic laws related to texture analysis described in Part B of this thesis, this approach is summarized here. Working in hypo-elastic formulation, constitutive equations are not required for a plastic spin. This choice of hypo-elastic formulation has different advantages and remains physically sound as long as the elastic strains are small. A discussion on this choice can be found in Hoferlin 2001. In Hoferlin 1999, this scientist also links the method proposed by Munhoven to the one presented by Ponthot 1995.

Let $\underline{x}=\underline{x}(\underline{x}_0,t)$ be the mapping at time t of the solid initial configuration $\gamma_0=\gamma(t_0)$ onto the current one $\gamma(t)$ in the global frame. The Jacobian matrix also called the global *deformation gradient* is:

$$\underline{F}=\frac{\partial \underline{x}}{\partial \underline{x}_0} \tag{7-42}$$

while the global *velocity gradient* with respect to the current configuration γ is defined as:

$$\underline{L}=\frac{\partial \dot{\underline{x}}}{\partial \underline{x}}=\dot{\underline{F}}\,\underline{F}^{-1} \tag{7-43}$$

The symmetric and skew-symmetric parts of $\underline{L}$ are $\underline{D}^c$, the *rate of deformation* tensor, and $\underline{\Omega}$, the *spin* tensor. The index c (for cinematic) aims to differentiate the $\underline{D}^c$ tensor from the second order damage tensor $\underline{D}$:

$$\underline{D}^c=\frac{1}{2}(\underline{L}+\underline{L}^T) \qquad \underline{\Omega}=\frac{1}{2}(\underline{L}-\underline{L}^T) \tag{7-44}$$

$$\underline{D}^c=\underline{D}^{cT} \qquad \underline{\Omega}=-\underline{\Omega}^T \qquad \underline{L}=\underline{D}^c+\underline{\Omega} \tag{7-45}$$

In the step by step procedure adopted in the nonlinear finite element LAGAMINE code, a strain path has to be chosen between 2 consecutive configurations, $\gamma(t_A)$ and $\gamma(t_B)$ with $t_B=t_A+\Delta t$, in order to integrate the constitutive equations. Different assumptions are possible in this context:

- velocity gradient based on *constant velocities* and with respect to the *initial* configuration $\gamma(t_A)$;
- velocity gradient based on *constant velocities* and with respect to the *final* configuration $\gamma(t_B)$;
- velocity gradient based on *constant velocities* and with respect to *substepped* configuration;
- constant velocity gradients.

This last possibility seems to be the most interesting assumption. As demonstrated by Cescotto 1992, this path is incrementally objective which explains its accuracy for steps including large rotations. First developed in two dimensions by Godinas & Cescotto 1984, this approach has been extended to three dimensions by Charles & Habraken 1998. Without computational details, this constant velocity gradient is reached by the following approach. The matrix system of differential equations is:

$$\underline{L}=\dot{\underline{F}}\,\underline{F}^{-1}=C^{te} \qquad (t_A<t<t_B) \tag{7-46}$$

which yields the following solution, with $(t_A<t<t_B)$:

$$\underline{F}(t) = exp(\underline{L}(t - t_A))\underline{F}_A \tag{7-47}$$

$$\underline{L} = \frac{1}{\Delta t} ln(\underline{F}_{AB}) \tag{7-48}$$

Knowing that:

$$\underline{F}_A = F(t_A) = \frac{\partial \underline{x}_A}{\partial \underline{x}_0} \qquad \underline{F}_B = F(t_B) = \frac{\partial \underline{x}_B}{\partial \underline{x}_0}$$

$$\underline{F}_{AB} = \underline{F}_B \underline{F}_A^{-1} \tag{7-49a, b, c}$$

The global incremental deformation gradient tensor F_{AB} is in general non-symmetric. In fact, Munhoven's idea is to require that the velocity gradient expressed in the local frame and called $\underline{L}'$ is *symmetric,* thus spin free and *constant*. This implicitly fixes the rotations of the local frame relative to the global axes. In what follows, quantities with reference to the local frame are identified by a $'$. The constraints are:

$$\underline{L}' = \underline{L}'^T = \underline{D}' \qquad \underline{L}' = C^{te} \qquad t_A < t < t_B \tag{7-50}$$

As $\underline{L}'$ is symmetric, $\underline{F}'_{AB}$ is also symmetric and easily computed:

$$\underline{F}'_{AB} = exp(\underline{L}'(t_B - t_A)) = \underline{F}'^T_{AB} \tag{7-51}$$

In general, the following relation holds between the global and local deformation gradient tensors:

$$\underline{F} = \frac{\partial \underline{x}}{\partial \underline{x}_0} = \frac{\partial \underline{x}}{\partial \underline{x}'} \frac{\partial \underline{x}'}{\partial \underline{x}'_0} \frac{\partial \underline{x}'_0}{\partial \underline{x}_0} = \underline{R}\underline{F}'\underline{R}_0^T \qquad or \qquad \underline{F}' = \underline{R}^T \underline{F}\, \underline{R}_O \tag{7-52a, b}$$

If, initially, global and local axes coincide, $\underline{R}_0 = \underline{I}$ and the above equations simplify to:

$$\underline{F} = \underline{R}\,\underline{F}' \quad and \quad \underline{F}' = \underline{R}^T \underline{F} \tag{7-53a, b}$$

So the local incremental deformation gradient tensor $\underline{F}'_{AB}$ is related to the global one $\underline{F}_{AB}$ by:

$$\underline{F}'_{AB} = \underline{F}'_B \underline{F}'^{-1}_A = \underline{R}_B^T \underline{F}_B \underline{F}_A^{-1} \underline{R}_A = \underline{R}_B^T \underline{F}_{AB} \underline{R}_A \tag{7-54}$$

The tensor $\underline{F}^*_{AB}$ is defined by:

$$\underline{F}^*_{AB} = \underline{F}_{AB} \underline{R}_A \tag{7-55}$$

According to equation (7-54), it appears that $\underline{R}_B$ and $\underline{F}'_{AB}$ form the right polar decomposition of $\underline{F}^*_{AB}$:

$$\underline{F}^*_{AB} = \underline{R}_B \underline{F}'_{AB} \tag{7-56}$$

As relation (7-55) is known from global frame definition and incremental step from t_A to t_B, relation (7-56) allows to reach $\underline{R}_B$ defining the position of local axis at time t_B. In practice, this local frame choice implies the following procedure during the stress integration scheme:

- Rotate the initial stress tensor from global to local axis:

$$\underline{\sigma}'_A = \underline{R}^T_A \underline{\sigma}_A \underline{R}_A \tag{7-57}$$

- Compute the constant symmetric velocity gradient $\underline{L}'$ and the final rotation $\underline{R}_B$:

$$\underline{L}' = \frac{1}{2\Delta t} ln((\underline{F}_{AB}\underline{R}_A)^T(\underline{F}_{AB}\underline{R}_A)) \tag{7-58}$$

$$\underline{R}_B = (\underline{F}_{AB}\underline{R}_A) exp(-\underline{L}'\Delta t) \tag{7-59}$$

- Integrate the local constitutive equations:

$$\begin{Bmatrix} \underline{\sigma}'_B \\ q_B \end{Bmatrix} = \begin{Bmatrix} \underline{\sigma}'_A \\ q_A \end{Bmatrix} + \int_{t_A}^{t_B} \begin{Bmatrix} \underline{f}_{\sigma'} \\ f_{q'} \end{Bmatrix} dt \tag{7-60}$$

where q are state variables (scalars, vectors or tensors), $\underline{f}_{\sigma'}$ and $f_{q'}$ represent the set of constitutive relations defining $\underline{\dot{\sigma}}$ and $\dot{q}$.

- Rotate back the final stress tensor from local to global axes:

$$\underline{\sigma}_B = \underline{R}_B \underline{\sigma}'_B \underline{R}^T_B \tag{7-61}$$

This approach has the advantage of requiring only limited additional storage for the rotation $\underline{R}$. In moderate tension and shear tests with superimposed large rigid-body rotations, this procedure performs quite well. Even if no explicit link with objective Jaumann stress rate is done, $\underline{\Omega}' = 0$ involves $\underline{\Omega} = \dot{\underline{R}}\underline{R}^T$. In consequence, under very large shear deformations, meaningless oscillating results are found (Szabo & Balla 1989).

7.3.2 Time integration procedure

The return mapping algorithms with the operator splitting methodology proposed by Simo and Ortiz (1985) is applied to Zhu's anisotropic elasto-plastic damage model. This results in a fully coupled integration scheme with a two-step procedure: elastic predictor and coupled plastic-damage corrector. There exists two coupled surfaces, and, for every iteration, the plastic surface and damage surface are both corrected. The details can be found in Zhu & Cescotto 1995.

7.4. Identification method of Zhu's anisotropic elastoplastic damage model

7.4.1. Description of the tests

As implemented in LAGAMINE code, Zhu's model requires the following data:

- the effective stress strain curves $\overline{\sigma}\ \overline{\varepsilon}$ in each tensile and shear direction (11, 22, 33, 23, 31, 12) in the material reference frame;
- the initial damage energy release rate Y_i versus associated damage component D_i in each material principal direction 1, 2, 3;
- the initial material reference frame position (1,2,3) expressed according to global axis *(x,y,z)* used for finite element mesh as shown on Figure 7-3.

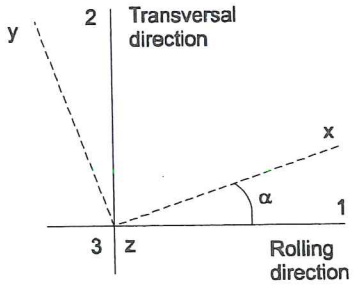

Figure 7-3 Definition of reference axes.

Considering a sheet, where rolling direction is assumed to be direction 1, three different sets of experiments are performed:

- Normalized tensile tests in directions 11, 22 and in direction x with $\alpha = 45°$ (Figure 7-3 defines α angle) with accurate measurements in the field of small strains allow to reach anisotropic *elastic* parameters.

- Normalized tensile tests in direction x with different values of angle α and accurate measurements in the field of large strains provide anisotropic *plastic* parameters. As explained by section 7.4.4 the *damage* parameters can also be deduced from these experiments and no specific damage tests are necessary if a linear assumption of $(Y_i\ D_i)$ curves is chosen.

- In order to validate damage evolution law, non classical tensile tests with numerous loading and unloading cycles in directions 11 and 22 have been performed with sample shape adapted to localize necking position.

The sample geometry used for elastic and plastic measurements is deduced from European standard and adapted to the limits of available extensometers. It is presented on Figure 7-4.

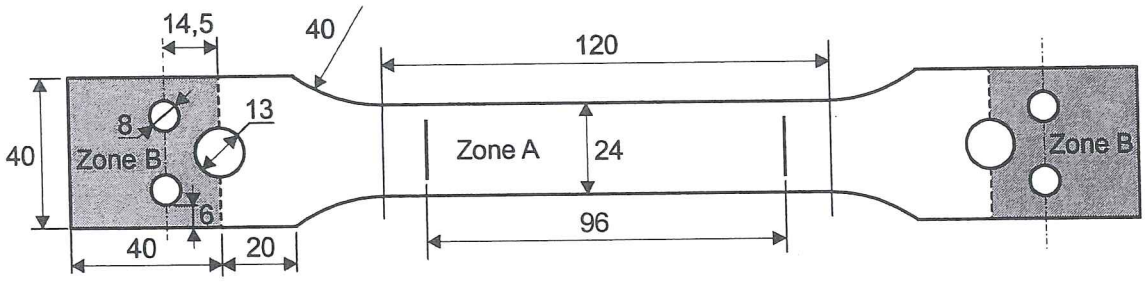

Figure 7-4 Description of the sample shape used for elastic and plastic measurements (from Wauters 2000).

Tensile tests out of orthotropic material directions require some care as principal stress and strain directions do not coincide (Boehler *et al.* 1987). If classical clamped boundary conditions are imposed, the sample tends to take a "S shape", characteristic of anisotropic solids and the homogeneity of stress and strain fields is lost. Figure 7-5 describes the grip developed by Ph. D. student Wauters to prevent this "S-shape". At one extremity, it allows the grip to rotate relative to the press by means of a kneecap piece, so the load will be well centered and applied longitudinally. At the other extremity, the grip presents 2 ball bearings, which allow a cylinder bar connected to the sample to rotate freely. Figure 7-6 defines *A* and *B* zones used in the FEM simulations and identifies points *D, C, E* required to define boundary conditions.

Figures 7-7a and b show the transversal displacement distribution produced by simulations of tensile test for an angle α of 45°. The material is the SPXI steel sheet studied in section 7.5. The boundary conditions are either imposed axial displacement of point *C* (see Figure 7-6), to model the grip described by Figure 7-5, or fixed transversal displacement and imposed axial displacement of segment *DCE*, to model a clamped test. Zone *A* is simulated by an elasto-plastic law and zone *B* by an elastic material to take into account the effect of the plate screwed tight on the sample. One can observe the "S shape" on Figure 7-7a computed with a clamped model, while the kneecap model leads to a more symmetric distribution (see Figure 7-7b).

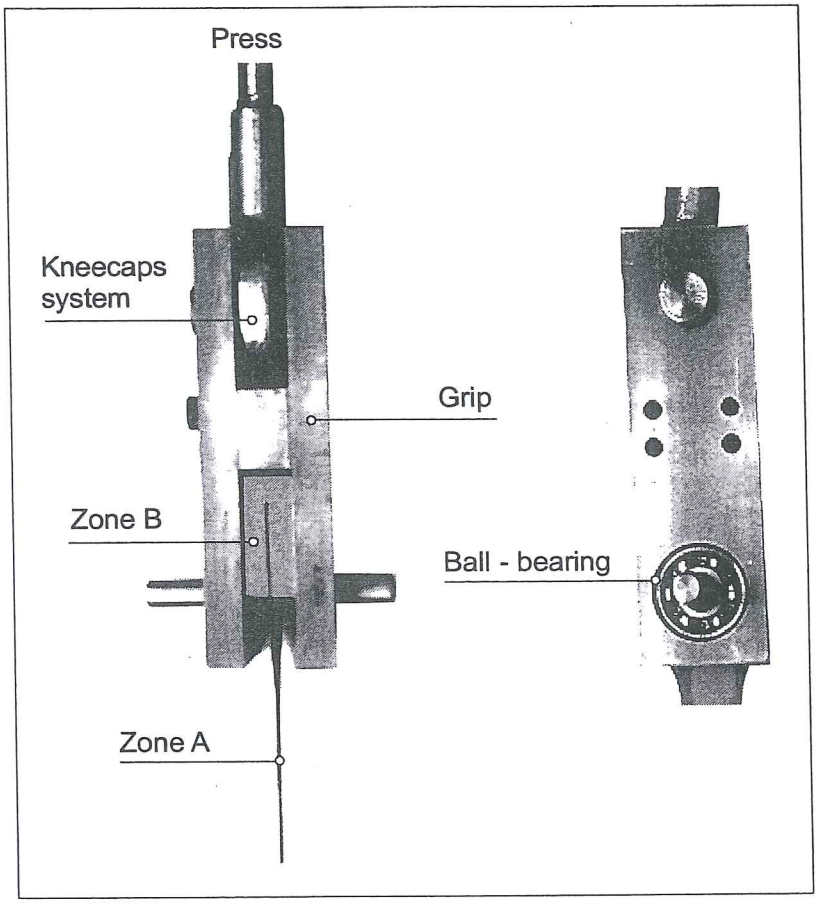

Figure 7-5 Description of the grip adapted to perform tensile tests out of material axes, (from Wauters 2000).

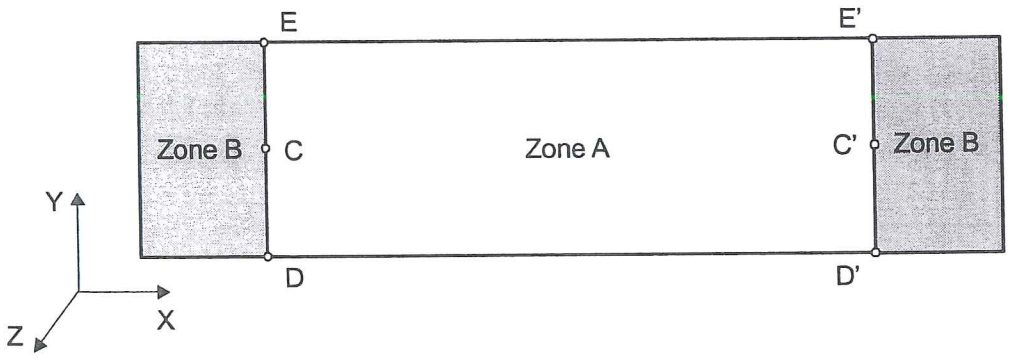

Figure 7-6. FEM model of the sample (from Wauters 2000).

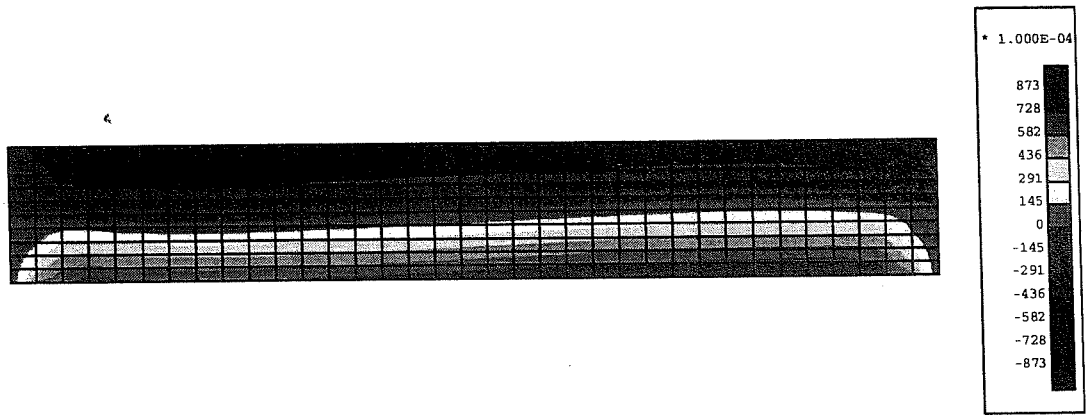

a) clamped model,

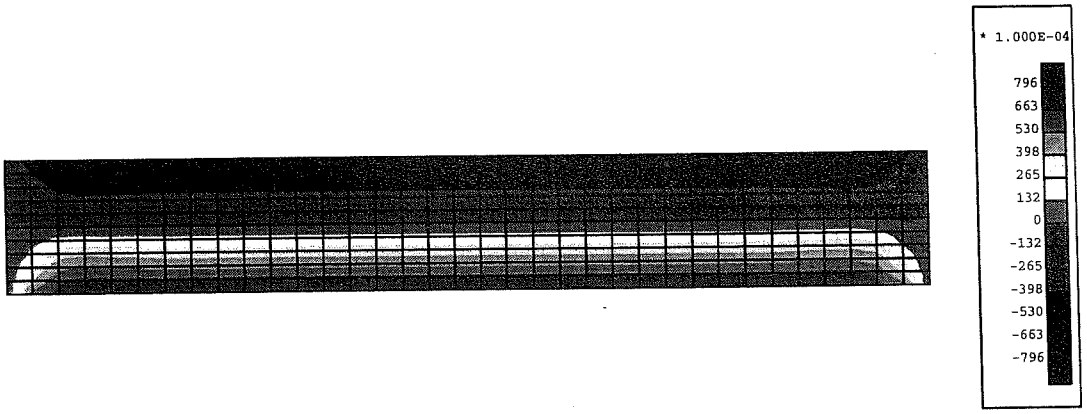

b) kneecap grip model

Figure 7-7 Simulations of tensile test with $\alpha = 45°$, transversal displacement distribution for an imposed axial displacement of 2mm,SPXI steel sheet (from Wauters 2000).

To determine the elastic parameters, the measurement device is a bi-directional MTS extensometer leading to longitudinal and lateral displacement measurements. The reference bases are respectively 25 and 24 mm. The thickness variation is measured by a thickness extensometer (Sadner).

For plastic parameters, the large strains domain prevents the use of the above bi-directional extensometer. The longitudinal extensometer of the press, with a reference basis of 50 mm, is used as well as a transversal extensometer, with a 24 mm reference basis. The same thickness extensometer as for elastic parameters is applied. The results are more accurate since the displacements are larger.

For the damage tests, cyclic loading-unloading tests are performed in order to measure the evolution of elastic moduli. Two sample geometries were deduced using an optimization shape process based on FEM simulations (Wauters 1999). A reduced section leads to localize the damage event, where measurements are performed. Computed with the damage-elasto-plastic model, the FEM simulations verify the homogeneity of stress, strain, and damage fields, which depends on the sample

geometry. As large strains are targeted, the same extensometer could not accurately cover all the tests. So sample 1 (Figure 7-8) is fitted for strain from 0 to 20 % with an extensometer of reference basis of 25 mm. Sample 2 (Figure 7-9) covers the near rupture zone; small extensometers with reference bases of 10 mm are used until 20% strain, then strain gages are pasted on the sample and used until rupture. These samples will also provide the material required for texture measurements after 5, 10, 20 and 30% of deformation

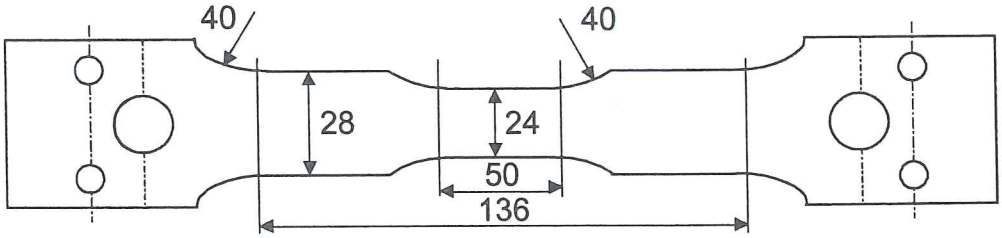

Figure 7-8 Sample geometry used for damage measures for strains less than 20% (from Wauters 2000).

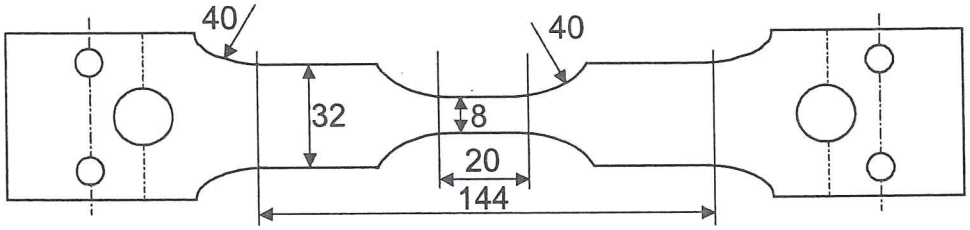

Figure 7-9 Sample geometry used for damage measure for strains greater than 20% (from Wauters 2000).

All the tensile tests have been performed on a 60 T Schenk press piloted by displacement and, for statistical reasons, repeated 5 times. The detailed procedure to deduce model parameters from these tests is described hereafter.

7.4.2. Identification of the initial anisotropic elastic properties

Tensile tests in direction x with α = 0, 45 and 90° are performed with accurate measurements of longitudinal ε_x, transversal ε_y and thickness ε_z strains. Figure 7-3 defines local axes during tensile experiment (x,y,z) and material reference frame (1, 2, 3). Recalling classical rotation equations, local stress and strain components (σ_x, σ_y, σ_{xy}, ε_x, ε_y, ε_{xy}) are directly related to stress and strain components in material axes (σ_{11}, σ_{22}, σ_{12}, ε_{11}, ε_{22}, ε_{23}).

$$\begin{Bmatrix} \xi_{11} \\ \xi_{22} \\ \xi_{12} \end{Bmatrix} = \begin{bmatrix} \cos^2\alpha & \sin^2\alpha & -2\cos\alpha\sin\alpha \\ \sin^2\alpha & \cos^2\alpha & 2\cos\alpha\sin\alpha \\ \cos\alpha\sin\alpha & -\cos\alpha\sin\alpha & \cos^2\alpha - \sin^2\alpha \end{bmatrix} \begin{Bmatrix} \xi_X \\ \xi_Y \\ \xi_{XY} \end{Bmatrix} \quad (7\text{-}62)$$

where ξ can be replaced by σ or ε.

Equation (7-18), written in material reference axes, describes the stress-strain relation in the elastic field. When damage has not yet occurred (D_1, D_2, $D_3 = 0$), one finds:

-for tensile test $\alpha = 0°$:

$$E_1 = \frac{\sigma_x}{\varepsilon_x} \qquad \nu_{12} = \frac{-E_1\varepsilon_{yy}}{\sigma_x} \qquad \nu_{13} = \frac{-E_1\varepsilon_{zz}}{\sigma_x} \quad (7\text{-}63)$$

-for tensile test $\alpha = 90°$:

$$E_2 = \frac{\sigma_x}{\varepsilon_{xx}} \qquad \nu_{21} = \frac{-E_2\varepsilon_{yy}}{\sigma_x} \qquad \nu_{23} = \frac{-E_2\varepsilon_{zz}}{\sigma_x} \quad (7\text{-}64)$$

-for tensile test $\alpha = 45°$:

$$\begin{aligned} \varepsilon_{11} &= \frac{\sigma_{11}}{E_1} - \nu_{12}\frac{\sigma_{22}}{E_1} = \frac{\varepsilon_{xx} + \varepsilon_{yy}}{2} \\ \varepsilon_{22} &= \frac{\sigma_{22}}{E_2} - \nu_{21}\frac{\sigma_{11}}{E_2} = \frac{\varepsilon_{xx} + \varepsilon_{yy}}{2} \\ \varepsilon_{12} &= \frac{\sigma_{12}}{2G_{12}} = \frac{\varepsilon_{xx}}{2} - \frac{\varepsilon_{yy}}{2} \\ \sigma_{11} &= \sigma_{22} = \sigma_{12} = \frac{\sigma_{xx}}{2} \end{aligned} \quad (7\text{-}65)$$

which yields to:

$$\frac{1}{G_{12}} = \frac{4\varepsilon_{xx}}{\sigma_x} - \frac{1-\nu_{12}}{E_1} - \frac{1-\nu_{21}}{E_2} \quad (7\text{-}66)$$

With such an identification procedure E_3, G_{23} and G_{31} are still missing and the following assumptions have been done:

$$\begin{aligned} G_{12} &= G_{31} = G_{23} \\ E_3 &= \frac{E_1 + E_2}{2} \end{aligned} \quad (7\text{-}67)$$

In the present research, a collaboration with professor van Houtte from Katholieke Universiteit Leuven provides elastic parameters deduced from texture measurements and physical crystal metallurgy for the two studied steel sheets. These values (see Table 7-3) help to choose the final elastic moduli. The nine independent coefficients

defining the elasticity of an orthotropic material are reduced to three (Gallerneau 95) in case of cubic anisotropy (additional symmetry of order 3 along the diagonal of the cube). For such a material, relation (7-67a) has a physical meaning. So, the assumption of a unique shear modulus is an extension of a cubic crystal property to textured polycrystal cubic material.

7.4.3. Identification of a classical Hill's matrix for plastic behavior

As described in section 7.4.5, this intermediate step is necessary in order to reach the required effective $(\bar{\sigma}\,\bar{\varepsilon})_i$ curves. So forgetting the frame of damage approach, the classical Hill's parameters must be adjusted from tensile experiments. The method proposed by Noat *et al.* 1995 has been chosen. The computed plastic parameters take into account both stress and strain measurements in a nice weighted way. However, this method was modified according to the plastic work equivalence assumption in each direction.

The classical Hill's model can be retrieved from (7-22, 7-23, 7-24) equations where no damage is assumed. This leads to the following expression:

$$F(\sigma_{22}-\sigma_{33})^2+G(\sigma_{11}-\sigma_{33})^2+H(\sigma_{11}-\sigma_{22})^2+2N\sigma_{12}^2+2L\sigma_{23}^2+2M\sigma_{31}^2=2\sigma_F^2 \tag{7-68}$$

Using axes transformation relation (7-62) and Hill's formula (7-68), the plastic stress for a tensile test in the α direction can be expressed by:

$$\sigma_H^2(\alpha)=\frac{2\sigma_F}{(H+G)+(F-G)\sin^4(\alpha)+(2N-2H-G)\sin^2(\alpha)\cos^2(\alpha)} \tag{7-69}$$

Lankford's coefficient can be expressed by means of the normality rule applied to Hill's criterion. This gives the final result:

$$r_H(\alpha)=\frac{H-(F+G+4H-2N)\sin^2(\alpha)\cos^2(\alpha)}{F\sin^2(\alpha)+G\cos^2(\alpha)} \tag{7-70}$$

In relations (7-69) and (7-70), H index means: value deduced from Hill's plasticity, and in the following functional ϕ, *exp* index identifies values deduced from experiments:

$$\phi=\sum_{i=1,j}(1-\eta)\left[\frac{\sigma_H(\alpha_i)-\sigma_{exp}(\alpha_i)}{\sigma_{F_{exp}}}\right]^2+\eta\left[r_H(\alpha_i)-r_{exp}(\alpha_i)\right]^2 \tag{7-71}$$

where j gives the total number of different directions α_i explored by experiments, η is a weighting factor defining the weight of stress and strain measurements and $\sigma_{F\,exp}$ is the stress measurement average.

The set of parameters F, G, H, N is determined by minimizing the functional ϕ by a classical least square method for k different material states. Each material state k is characterized by its internal variable $(p)_k$ and by its plastic work $(W^p)_k$ estimated from the reference stress-strain curve. The experimental stress $\sigma_{exp\,k}(\alpha_i)$ in each direction α_i giving the same plastic work $(W^p)_k$ is selected and introduced in relation (7-71). Such a procedure leads to one set of $(F\,G\,H\,N)_k$ parameters for each studied plastic work $(W^p)_k$. From the general Hill's formula (7-68) and the knowledge of plastic work level, the required multi-linear stress-strain curves $(\sigma_{11}\ \varepsilon_{11})$, $(\sigma_{22}\ \varepsilon_{22})$, $(\sigma_{33}\ \varepsilon_{33})$, $(\sigma_{12}\ \varepsilon_{12})$ can be produced. As no information on $(\sigma_{13}\ \varepsilon_{13})$ and $(\sigma_{23},\ \varepsilon_{23})$ curves are available, they are assumed to be equal to $(\sigma_{12}\ \varepsilon_{12})$ curve or, equivalently, $N=L=M$ can be used. As the physical reality of the material concerns stress and strain, η is chosen equal to 0,5, which means an equal weight for stress and strain prediction.

7.4.4. Identification of the damage model

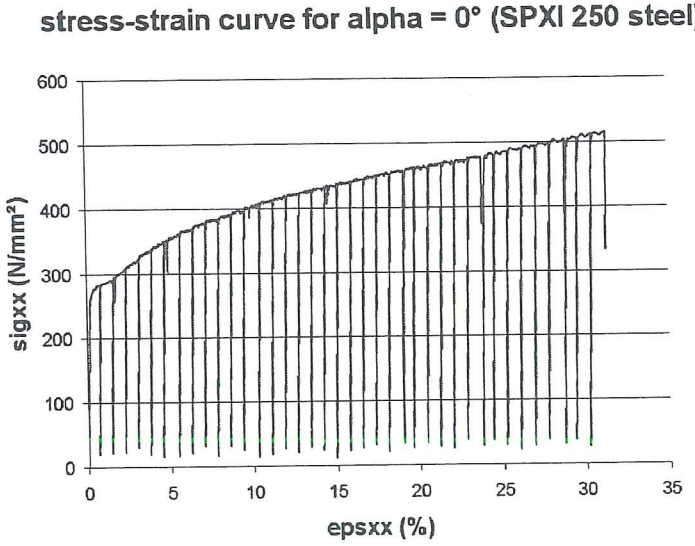

Figure 7-10 Loading-unloading cycles, tensile test in Rolling Direction, SPXI steel sheet (from Wauters 2000).

The required curves are the "damage energy release rate-damage" ones : $Y_i\ D_i$. From equation (7-10d) applied on a tensile test in direction i, one gets:

$$Y_i = \frac{\sigma_{ii}^2}{E_{0i}(1-D_i)^3} \qquad (7\text{-}72)$$

By means of loading-unloading cycles (Figure 7-10), the evolution of the effective Young's modulus $\overline{E}_i(\varepsilon_{ii})$ is measured. This curve, associated with equation (7-18), gives the damage component evolution $D_i(\varepsilon_{ii})$:

$$D_i(\varepsilon_{ii}) = 1 - \sqrt{\frac{\overline{E}_i(\varepsilon_{ii})}{E_{0i}}} \tag{7-73}$$

where E_{0i} is the initial value of the Young's modulus. This evolution is clear in Figure 7-11.

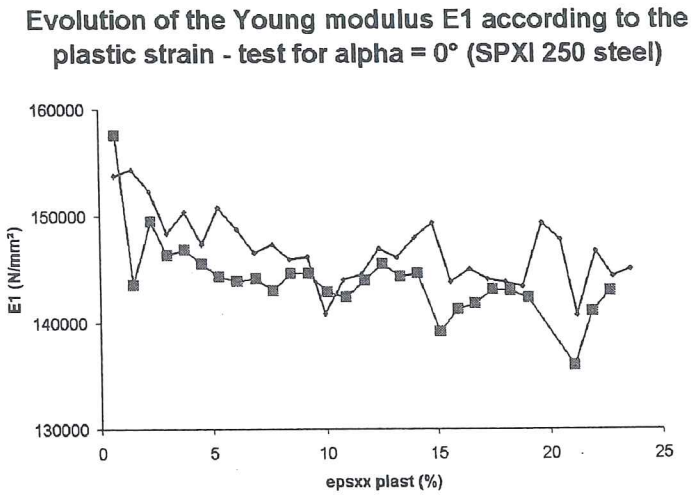

Figure 7-11 Decrease of Young's modulus measured by 2 sets of experiments, SPXI steel sheet (from Wauters 2000).

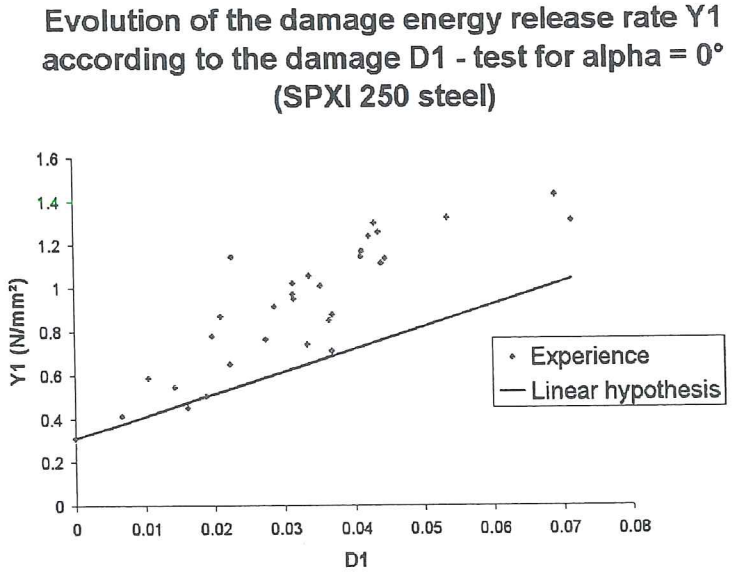

Figure 7-12 Linear description of the "damage energy release rate curve-damage" $Y(N/mm^2)-D$ for SPXI steel (from Wauters 2000).

As $\sigma_{ii}(\varepsilon_{ii})$ is known by measurement and $D_i(\varepsilon_{ii})$ is defined by equation (7-73), using equation (7-72), it is easily possible to produce points of Y_i D_i curves for i equal 1 and 2. The experimental results shown in Figure 7-12 allow adjusting a simple linear model as proposed by Zhu 1992.

Concerning the thickness direction, such a direct approach cannot be applied because it is not possible to perform cyclic tensile test in this direction. However, the Y_{O3} value can be directly deduced from equation (7-72), where D_3 is assumed to be equal 0 until plasticity entrance. For D_{t3} value, a direct algebraic transformation of equation (7-18) and the thickness measurement during the performed tensile tests give:

$$D_3(\varepsilon_{ii}) = 1 + \frac{\nu_{3i}\sigma_{ii}}{(1-D_i(\varepsilon_{ii}))E_3\varepsilon_{33}} \tag{7-74}$$

Knowing the damage work associated to ε_{ii} and assuming damage work equivalence in each direction, D_{t3} can be obtained. As accuracy of thickness measurements is poor, D_{t3} is really difficult to reach by this way.

In fact, the final approach to define Y_i D_i curves is not the one described here above. The simplicity of the assumption of linear behavior reduces the free parameters to two per curve: Y_{0i} and D_{ti}. The first one is imposed by the hypothesis that damage begins at plasticity entrance. In consequence, Y_{0i} is directly given in uniaxial state by relation (7-72) with $D_i=0$ and $\sigma_{ii} = \sigma_{yi}$. The second parameter D_{ti} is fixed by the knowledge of σ_{maxi} maximal stress in direction i in case of uniaxial state. Replacing Y_i by its linear expression (D_{ti} D_i + Y_{0i}) in relation (7-72) yields a non linear equation $\sigma_i(D_i)$. For instance in direction *1*:

$$\frac{\sigma_{11}^2}{E_{01}(1-D_1)^3} = D_{t1}D_1 + Y_{01} \tag{7-75}$$

The maximum of this non linear relation must coincide with σ_{max1}, so D_{t1} is computed by the following relation:

$$\sigma_{1max} = \sqrt{\frac{27E_{01}}{256D_{t1}^3}}(D_{t1} + Y_{10})^2 \tag{7-76}$$

As the 3 values σ_{maxi} can be deduced from Hill's yield locus determined on section 7.4.3, the damage parameters do not require any additional specific tests. This is of course very convenient but strongly limits the damage evolution that this model can reproduce. Consequently, the above described damage test provides the first validation of the model. Figure 7-12 compares experimental points to the linear behavior of (*Y-D*) curve.

7.4.5 Computation of effective stress-strain curves

The previous experiments, analytical analysis and hypothesis give:

-$(\sigma_{ii}\varepsilon_{ii})$ multi-linear curves for i = 11, 22, 33, 13, 32, 12 (see sections 7.4.2 and 7.4.3) ;

-Y_i D_i linear curves for i = 11, 22, 33 (see section 7.4.4).

Using relation (7-75) describing a uniaxial test in one direction allows computing damage evolution. Then$(\bar{\sigma}_{ii}\bar{\varepsilon}_{ii})$ curves are easily obtained for directions 11, 22, 33 by means of relations (7-2) and (7-3). For shear curves 23, 31, 12, analytical work provides damage evolution. Relation (7-10d) gives, in case of pure shear in 12 direction:

$$-Y_1 = \frac{\sigma_{12}^2}{2G_{12}^0(1-D_1)^2(1-D_2)} \qquad -Y_2 = \frac{\sigma_{12}^2}{2G_{12}^0(1-D_1)(1-D_2)^2} \tag{7-77}$$

Then, the equivalent damage energy release rate Y_{eq} is computed by relation (7-32):

$$Y_{eq} = Y_1 + \sqrt{J_2 Y_2} \tag{7-78}$$

where J_2 is defined by (7-34).

The damage surface (7-31) imposes a first constraint:

$$Y_{eq} - (D_{t1}D_1 + Y_{10}) = 0 \tag{7-79}$$

and the second relation required to solve D_1 D_2 is the equivalence of damage work (Figure 7-2):

$$\frac{D_1(Y_1 + Y_{10})}{2} = \frac{D_2(Y_2 + Y_{20})}{2} \tag{7-80}$$

$$Y_1 = D_{t1}D_1 + Y_{01} \quad and \quad Y_2 = D_{t2}D_2 + Y_{02} \tag{7-81}$$

The resolution of the system (7-79; 7-80), with the additional assumption of increasing damage, provides the damage evolution D_1 D_2 in pure shear state. This approach is repeated for each shear direction and the effective shear curves $(\bar{\sigma}_{ij}\bar{\varepsilon}_{ij})$ are easily obtained for directions 23, 31, 12 using relations (7-2) and (7-3).

7.5 Model identification for two different steel sheets

The above procedure has been applied on a classical deep drawing steel sheet (IF ULC Ti) and a "high-tensile" steel sheet (SPXI), both 0,8 mm thick. Microscopic investigations about these two materials are not discussed here. They are part of Wauters' Ph. D. thesis, which is still in progress. Table 7-3 gives the final set of elastic

parameters (called "experiment") issued from the various experiments described in section 7.4. A comparison is proposed with the values (called "texture") computed by professor van Houtte's team from texture measurements of non deformed samples. Repeating the computation of elastic parameters from texture measurements performed on deformed samples, it has been verified that, for these two steels and for tensile tests performed in rolling and transversal direction, texture evolution does not modify these computed "texture" elastic values (see Figure 7-13). One can conclude that damage is responsible for Young's modulus decrease observed for instance on Figure 7-11.

SPXI steel						
	E_1	E_2	E_3	G_{12}	G_{13}	G_{23}
Texture	205834	204256	196748	80385	85220	86231
Experiment	203407	209274	206341	77268	77268	77268
Gap (%)	1.19	2.4	4.65	4.03	10.29	11.6
	ν_{12}	ν_{21}	ν_{13}	ν_{31}	ν_{23}	ν_{32}
Texture	0.2748	0.2727	0.3135	0.2995	0.3188	0.3070
Experiment	0.2884	0.2967	0.3135	0.3180	0.3188	0.3143
Gap(%)	4.7	8.09	0.00	5.81	0.00	2.33
IF ULC Ti steel						
	E_1	E_2	E_3	G_{12}	G_{13}	G_{23}
Texture	207954	206048	201789	80796	80796	80796
Experiment	204129	185016	194573	82993	82993	82993
Gap (%)	1.87	11.37	3.71	2.65	0.57	2.01
	ν_{12}	ν_{21}	ν_{13}	ν_{31}	ν_{23}	ν_{32}
Texture	0.2813	0.2787	0.3028	0.2937	0.3092	0.3027
Experiment	0.3371	0.3055	0.3028	0.2884	0.3092	0.3251
Gap(%)	16.55	8.78	0.00	1.77	0.00	6.90

Table 7.3 Elastic material parameters, Young's moduli in N/mm^2 (from Wauters 2000).

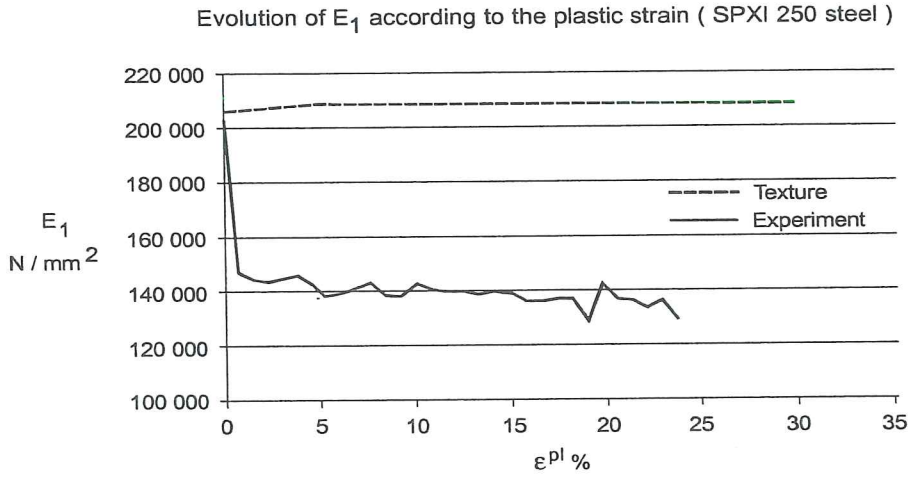

Figure 7-13 Young's modulus of SPXI steel from loading-unloading cyclic tensile tests or deduced from texture measurements (from Wauters 2000).

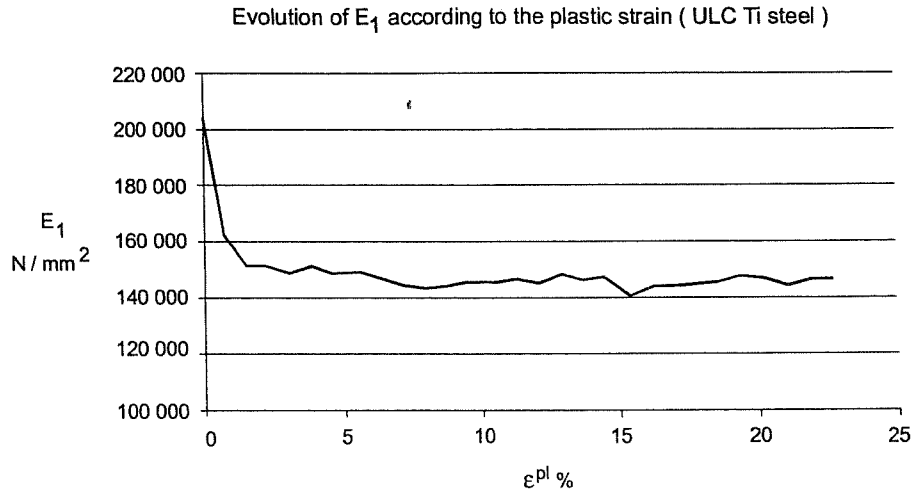

Figure 7-14 Young's modulus evolution during tensile test in Rolling Direction, IF ULC Ti steel (from Wauters 2000).

The decrease of Young's modulus at plasticity entrance and with damage has already been discussed in Chapter 3, section 3.2.1. Such results have also been presented in Chapter 6, section 6.2.7 for an aluminum alloy.

The identification of Hill's parameters has been performed by means of tensile tests in large strains in seven directions (α = 0, 15, 30, 45, 60, 75, 90) and with the weighting coefficient η equal to 0,5. The four resulting stress strain-curves in 1, 2, 3 directions and in 12 shear state are given in Wauters' 2000 DEA thesis for both steel sheets. The shear behaviors in 23, 13 directions are assumed identical to 12 direction.

SPXI steel					
Y_{10}	Y_{20}	Y_{30}	DT_1	DT_2	DT_3
0.3055	0.2989	0.2914	10.802	10.885	12.265

IF ULC Ti steel					
Y_{10}	Y_{20}	Y_{30}	DT_1	DT_2	DT_3
0.0623	0.0649	0.0647	7.96	8.33	15.769

Table 7.4 Linear data describing "damage energy release rate-damage" curves (from Wauters 2000).

The results of damage identification are summarized in Table 7.4. Figure 7-14 shows Young's modulus evolution for the IF ULC TI steel. The decrease of Young's modulus for this IF steel is not as clear as the one of SPXI steel but still exists. Figure 7-15 presents the result of damage computation during a simulated tensile test

and the value computed using relation (7-18) and experimental observations. The latter value is directly computed with the initial Young's modulus and not with Young's modulus after plasticity. The possible choices have already been discussed in section 6.2.7.

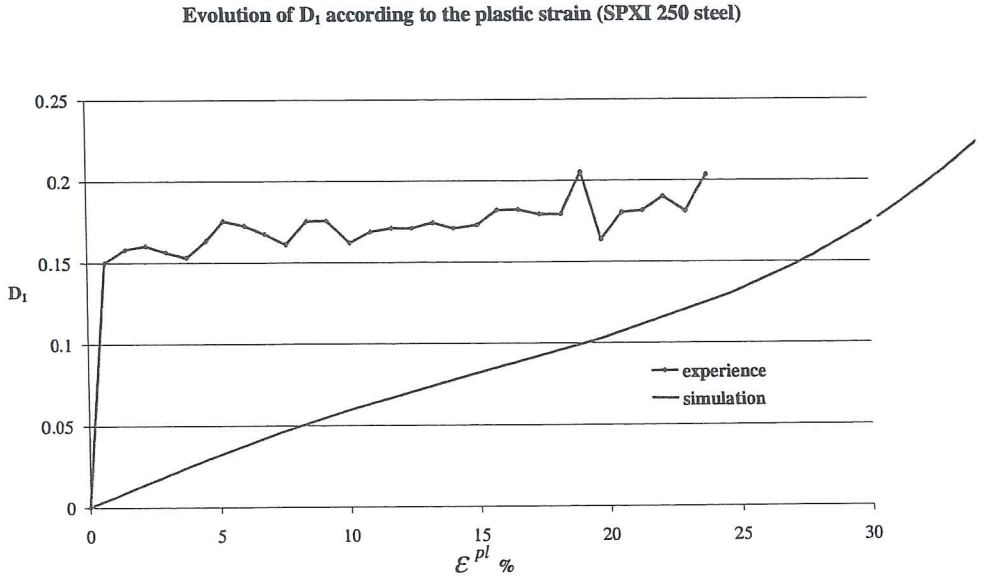

Figure 7-15 Simulated and measured damage component 1, during a tensile test, SPXI steel (from Wauters 2000).

With these final sets of parameters, a uniaxial tensile test in Rolling direction is simulated for each studied steel. Figure 7-16 and 7-17 compare experimental and simulated true stress-strain curves and present effective stress-strain curves.

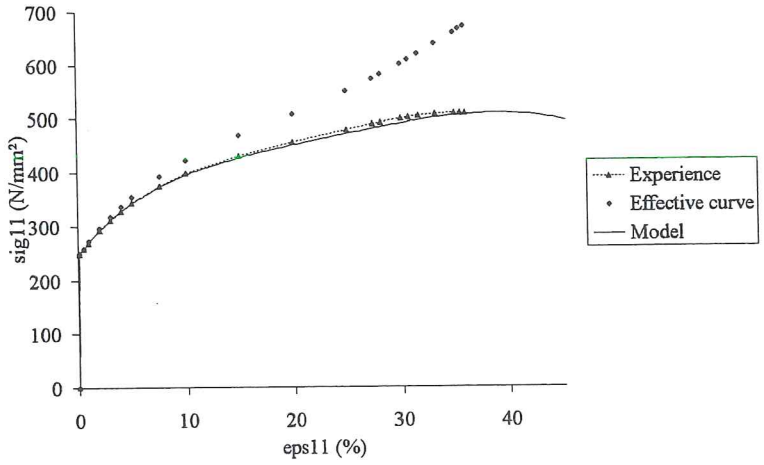

Figure 7-16 Stress-strain curves for a uniaxial tensile test, SPXI steel (from Wauters *et al.* 2000).

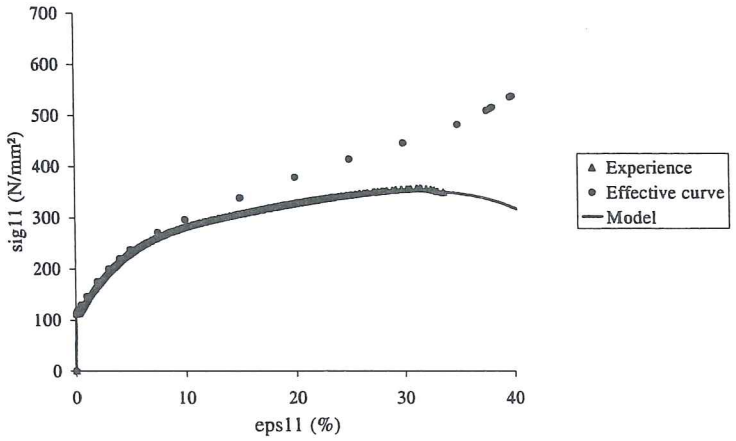

Figure 7-17 Stress-strain curves for a uniaxial tensile test, IF ULC TI steel (figure provided by Wauters, not yet published).

The model accurately reproduces the experimental tests.

7.6. Yield locus

Figure 7-18 shows the evolution of the global yield locus shape and size due to the damage and plastic processes during a tensile test in Rolling Direction. The assumption of energy equivalence in each direction to define hardening behavior induces a slight shape modification superposed with a strong increase of the yield locus size. If one looks at the "yield locus without damage", the perfect symmetry around the diagonal line present in the "initial yield locus" has been lost. When the coupled elasto-plastic-damage model is used, one can observe an additional change of shape as well as a decrease of the yield locus due to damage.

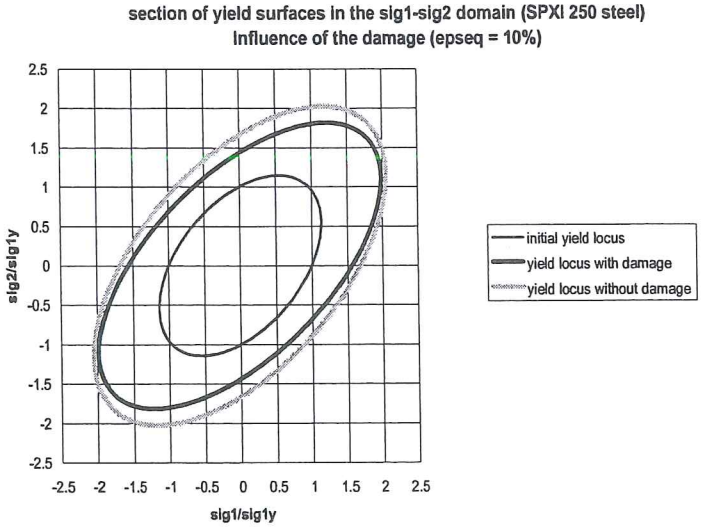

Figure 7-18 Initial and predicted yield loci of SPXI steel (from Wauters *et al.* 2000).

7.7 Validation

7.7.1 FLD prediction

The Forming Limit Diagram and Marciniak-Kuczynski's approach have already been presented in Chapter 4. The first validation is the prediction of FLD diagram with the developed model.

As shown on Figure 7-19, the application of the model with the parameters defined on section 7.5 is quite far from the reality. A modification (Figure 7-20) of the slope of $Y_1 - D_1$ curve provides a better correlation. This fact demonstrates how difficult it is to define this slope. The best solution should result from the inverse analysis of a set of experiments. The linear choice for $Y_i - D_i$ curve is perhaps very simple but too poor to give accurate predictions.

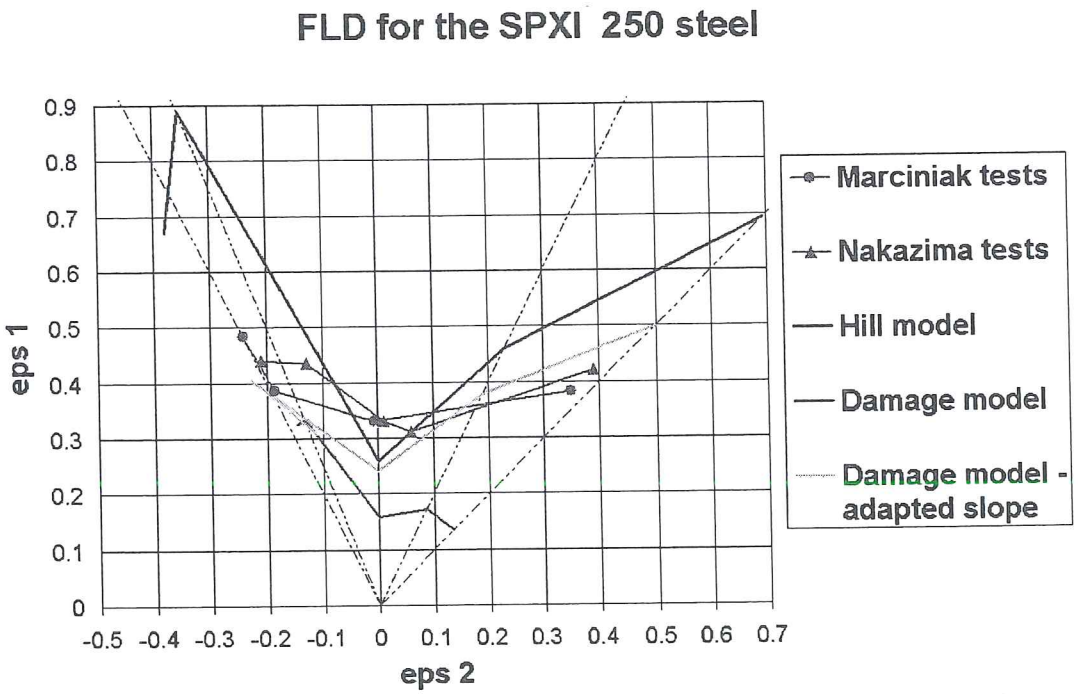

Figure 7-19 FLD predictions and measurements for SPXI steel (from Wauters *et al.* 2000).

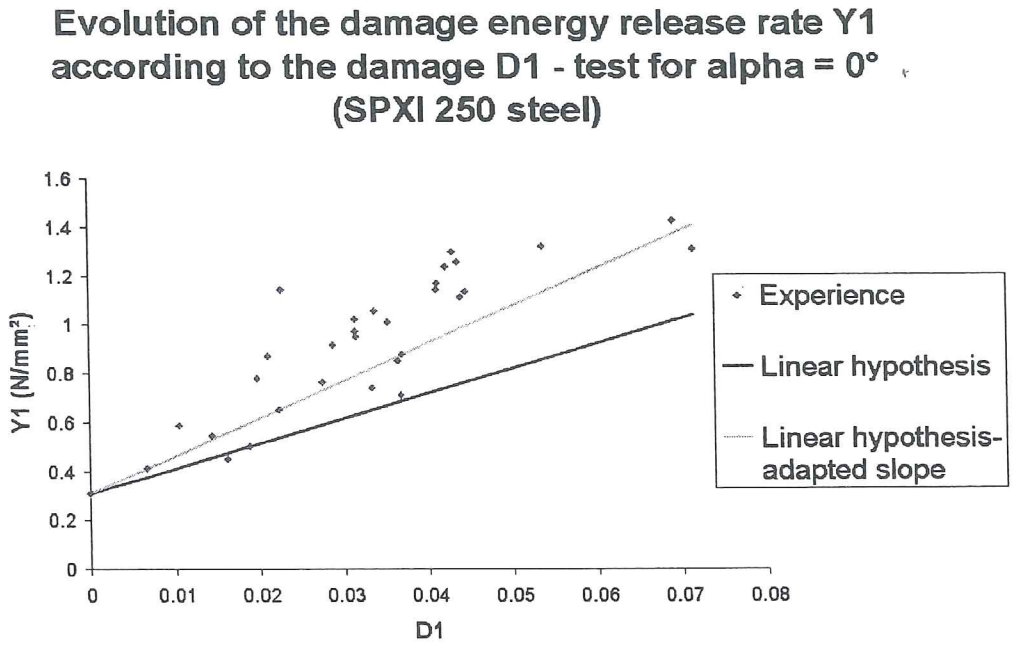

Figure 7-20 Damage energy release curves (Wauters *et al.* 2000).

7.7.2 Finite element simulations

Zhu's thesis 1992 already presented experiments and simulations such as hemispherical punch stretching or deep drawing by cylindrical and square punches, where data were adjusted on literature. Biaxial Nakazyma's tests performed on the studied steel sheets have been simulated. These tests can be described by the following features:

initial rectangular blank 0.8 mm thick;
spherical punch with a radius of 80 mm;
Coulomb's friction coefficient of 0,05;
blankholder shape and die shape are defined on Figure 7-21.

The simulations are computed with the LAGAMINE code. The volume finite element discretization consists in one layer of 705 8-nodes mixed elements. The tools are modeled by a spherical segment for the punch and two sets of 20 and 140 triangles respectively for the blankholder and die. The contact problem is treated by 1410 surface contact elements based on a penalty approach with a penalty coefficient of 500 Mpa/mm^3. The simulation is driven by the vertical punch displacement and is stopped for a punch depth of 32 mm. By symmetry only one quarter of the experiment is simulated. Figure 7-22 presents the equivalent strain at the punch depth of 30 mm; the material dependence is clearly illustrated. The IF ULC Ti steel shows a large distribution of the strain while the SPXI steel has a more localised strained zone with higher strain level. The equivalent damage component is very

interesting; again a different behavior can be verified for each steel (Figure 7-23). The rupture localization predicted by the higher value of damage is in good concordance with the experimental crack (Figure 7-24).

As underlined by experimenters, Marciniak's tests are very sensitive to friction. Some scientists doubt that the different material behaviors induce the crack localization. As great care has been given to the material surface state and lubrication, some confidence is given to this validation. However, it is clear that additional validations would be welcome.

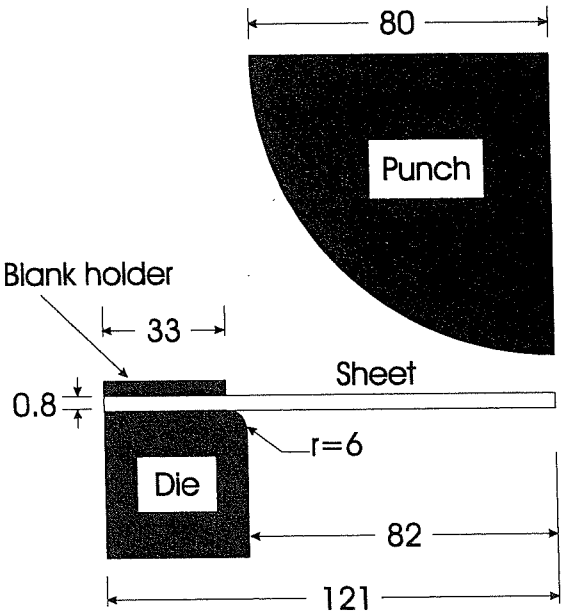

Figure 7-21 Description of Nakazyma biaxial test (from Habraken 1999).

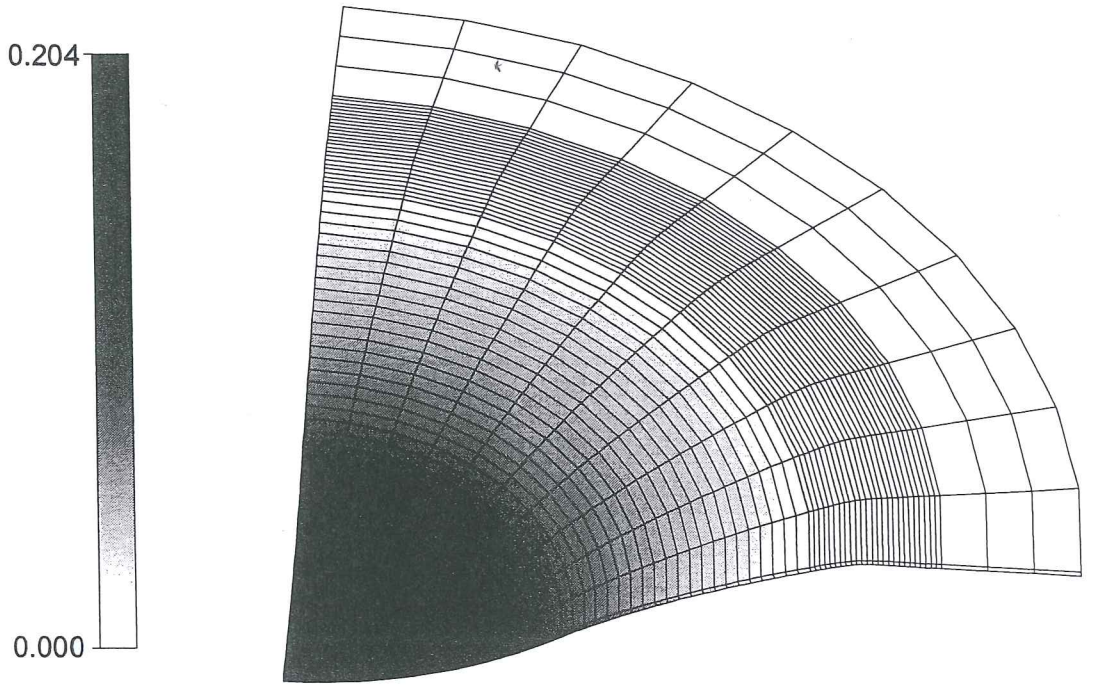

SPXI steel

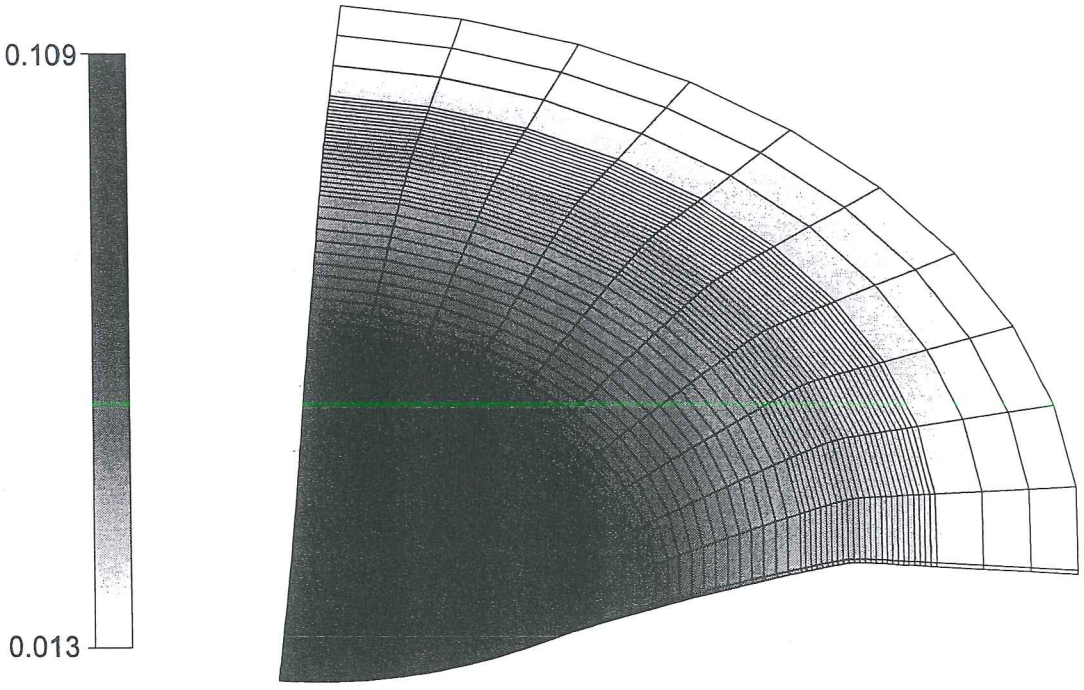

IF ULC Ti steel

Figure 7-22. Equivalent strain distribution for a punch depth of 30 mm (from Charles *et al.* 1997).

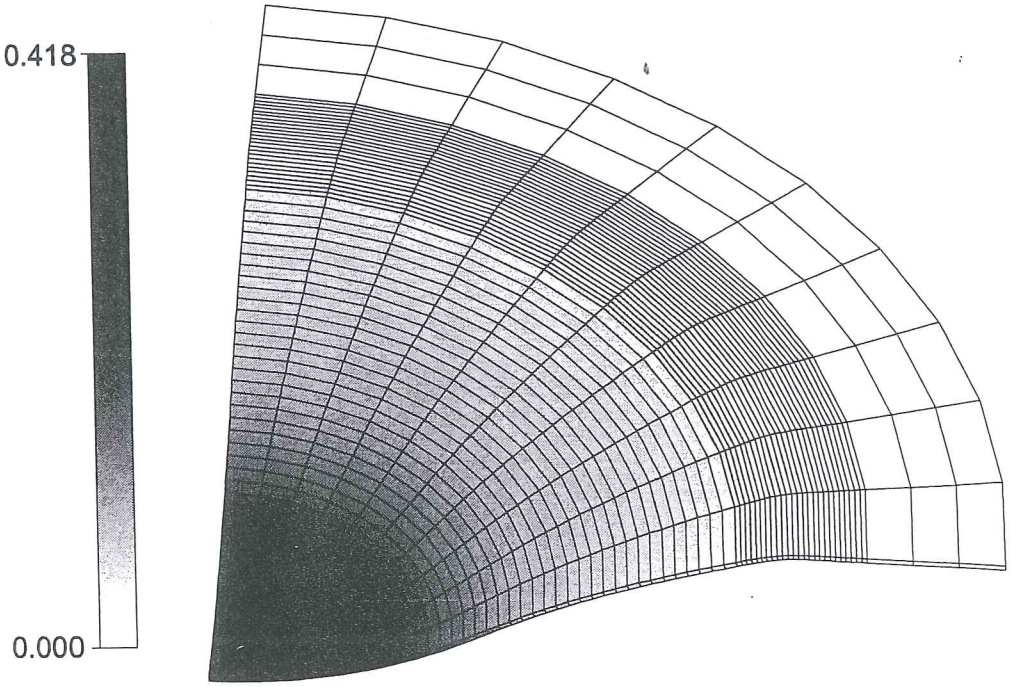

SPXI steel

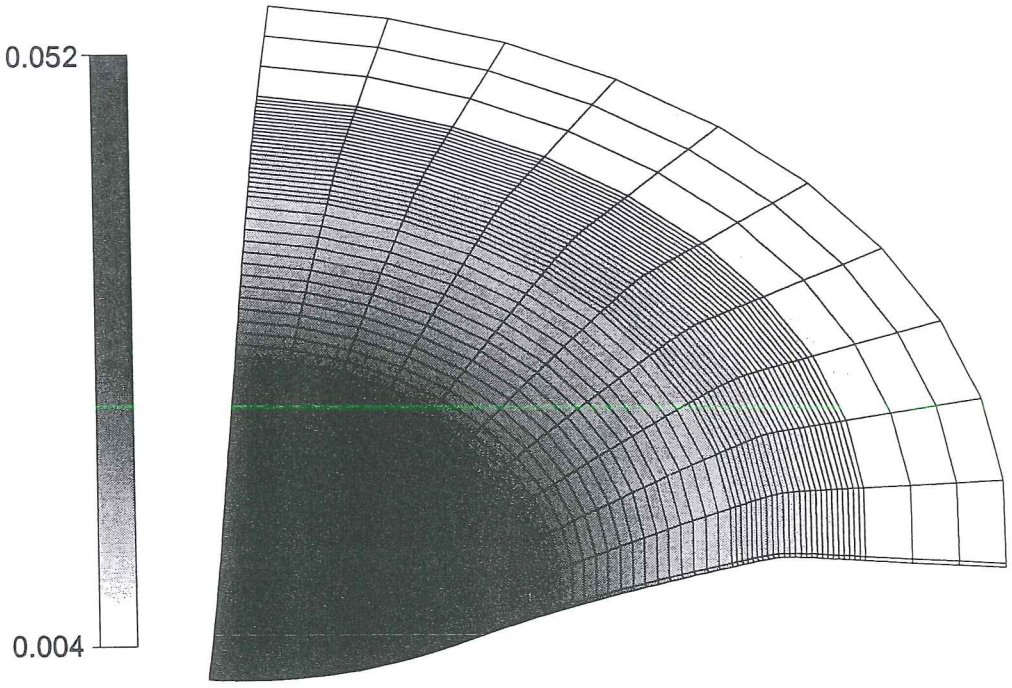

IF ULC Ti steel

Figure 7-23 Equivalent damage distribution for a punch depth of 30 mm (from Charles *et al.* 1997)

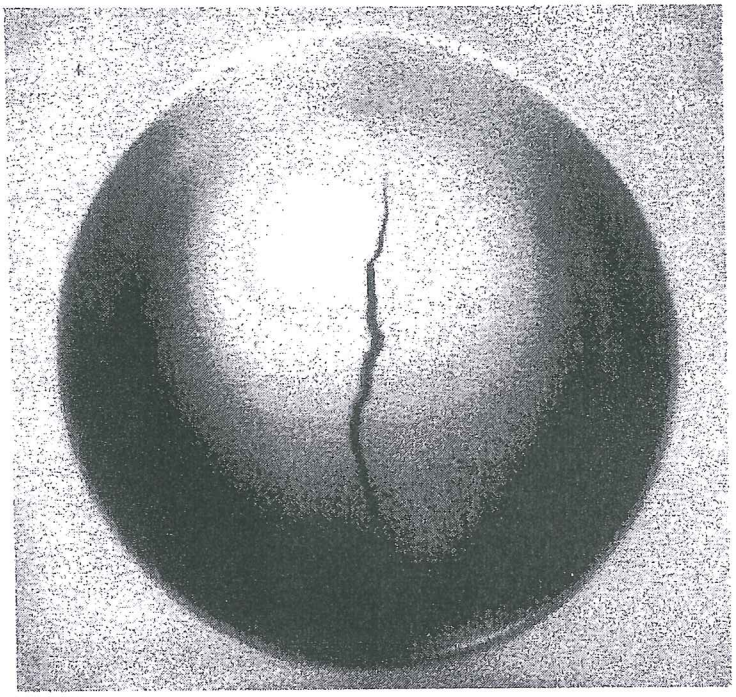

SPXI steel

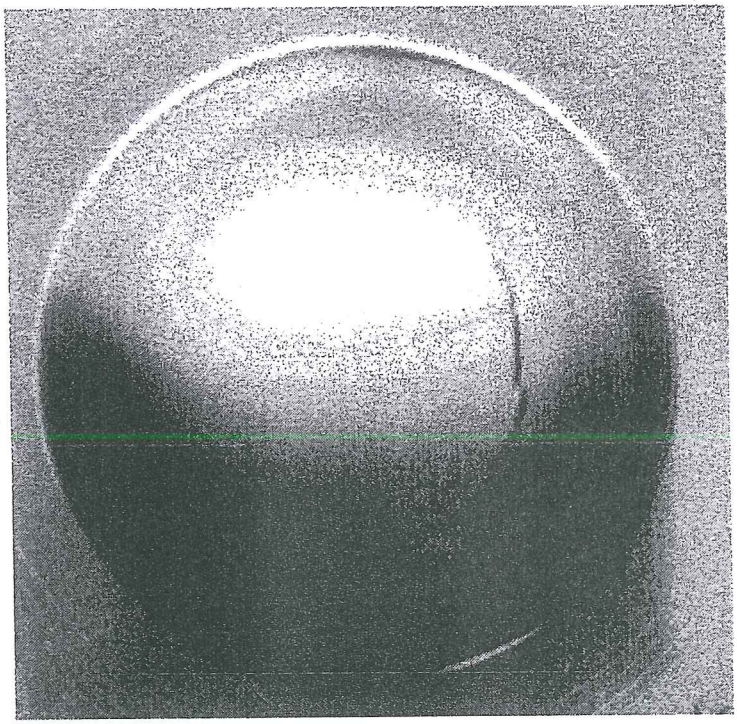

IF ULC Ti steel

Figure 7-24 Nakazyma's tests, punch displacement 69 mm
(from Habraken 1999).

7.8 Conclusion

To conclude, one can tell that the anisotropic model developed by Zhu 1992 has been improved. Now, this constitutive law proposes multiple linear segments to describe the hardening plastic curve. An experimental approach has been defined to determine the material parameters. The simple choice of a linear description of the damage energy release rate–damage curve has been proposed. It allows a quick identification process of the anisotropic elasto-plastic-damage model, without damage experiment. However, the performed damage experiments and the validation simulations (section 7.7.1) show that this choice has a limited range of applications. The slope curve is not easy to determine (section 7.4.4) and should result from a compromise between tensile stress-strain curves and FLD prediction. To increase the flexibility and accuracy of the model, one possibility is to use multi linear curves for damage energy release rate–damage curve.

An interesting result of this study consists in the fact that both studied steel sheets present Young's modulus decrease, which cannot be attributed to texture evolution. This damage effect, that is not well known, was interesting to verify.

Further experimental validations of the assumption of energy equivalence in each direction are required. Simulation of deep drawing processes, where cracks occur, should also be done to go on with the damage validation step. This work is still in progress.

References

Bockler, J.P., El Aoufi, L., Raclin, S. (1987) On experimental testing method for anisotropic materials, *Res Mechanica*, **21**, 73-95.

Cambron, A-F. (1997), La prédiction de fissures, Travail de fin d'études, Ingénieur physicien, Université de Liège.

Charles, J.F., Habraken, A.M. (1996) Dépouillement des essais de traction nécessaires à la calibration de la loi anisotrope élastoplastique avec endommegement de Y.Y. Zhu, Convention Région Wallonne n°2748, rapport intermédiaire n° 9.

Charles, J.F., Zhu, Y.Y., Habraken, A.M., Cescotto, S., Traversin, M. (1997) A fully elasto-plastic damage theory for anisotropic materials, in *Advanced Methods in Materials Processing Defects,* Predeleanu, M., Gilormini, P. editors, Elsevier Science.

Charles, J.F., Habraken, A.M. (1998) Amélioration de la version 3D de la loi Norton-Hoff, Convention Région Wallonne n°2748, rapport intermédiaire n° 24.

Chow, C.L., Wang, J. (1987) An anisotropic theory of elasticity for continuum damage mechanics, *Int. J. Fracture*, **33**, 3-16.

Cordebois, J.P., Sidoroff, F. (1979) Damage induced elastic anisotropy, F. *Euromech*, **115**.

Cordebois, J.P. (1983) Critères d'instabilité plastique et endommagement ductile en grandes déformations, applications à l'emboutissage, Doctoral Thesis, Paris.

Estevez, R., Habraken, A.M. (1996) Calibration method of an anisotropic elastoplastic model coupled with damage, *Nuphymat'96*, Workshop on numerical and physical study of material forming processes, final meeting, CEMEF, Sophia-Antipolis, Final Report.

Gallerneau, F. (1995) Etude et modélisation de l'endommagement d'un superalliage monocristallin revêtu pour aube de turbine, Thèse Docteur en sciences et génie des matériaux, Ecole Nationale Supérieure des Mines de Paris.

Golin, J.C., Danescu, A. (1992) Constitutive model and computational strategies for finite-strain elasto-plasticity with isotropic or anisotropic ductile damage, *3 rd COMPLAS int. conf.*, D.R.S. Owen et al. editors, *Pineridge Press*, 1413-1424.

Godinas, A., Cescotto, S. (1984) Calcul des gradients de vitesses constants au cours d'un pas, rapport interne MSM n° 159, Université de Liège.

Gologanu, M., Leblond, J.B., Devaux, J. (1994) Numerical and theoretical study of coalescence of cavities in periodically voided solids, *Computational Material Modeling, ASME*, AD- **42**/PVP- **294**.

Gurson, A.L. (1977) Continuum theory of ductile rupture by void nucleation and growth. *J. Engng. Materials Technology*, **99**, 2-15.

Habraken, A.M. (1999) Prise en compte des interactions micro-macro dans la modélisation par éléments finis de la mise à forme des métaux, Convention Région Wallonne n° 2748, Rapport final.

Hayakawa, K., Murakami, S. (1998) Space of damage conjugate force and damage potential of elastic-plastic-damage materials, *Damage Mechanics in Engineering Materials*, Voyiadjis, G.S., Ju, J.W., Chaboche, J.L. Eds, 27-44.

Hoferlin, E., van Bael, A., van Houtte, P., Teododiu, C. (1999) An accurate model of texture and strain-path induced anisotropy, *Proc. 4th Int. Conf.: Numerical Simulation of 3-D Sheet Metal Forming Processes. NUMISHEET'99*, Ed. J.C. Gélin and P. Picart, University of Franche Comté

Hoferlin, E. (2001), Incorporation of an accurate model of texture and strain-path induced anisotropy in simulations of sheet metal forming, Ph. D thesis , Hatholieke Universiteit Leuven

Hill, R. (1948) A theory of the yielding and plastic flow of anisotropic materials. Proc. Royal Soc. London, **A193**, 281-297

Lemaître, J., Chaboche, J.L. (1985) *Mécanique des matériaux solides*, Dunod, Paris.

Lemaître, J. (1986), Local approach of fracture, *Eng. Fracture Mech.*, **25**, 523-537.

Lu, T.J., Chow, C.L. (1990) On constitutive equations of inelastic solids with anisotropic damage, *J. Theory Appl. Fract. Mech.*, **14**, 187-218.

Munhoven, S., Habraken, A.M., Van Bael A., Winters J. (1996b) Anisotropic finite element analysis based on texture. *Proc. 3rd Int. Conf.: Numerical Simulation of 3-D Sheet Metal Forming Processes. NUMISHEET'96*, Ed. L.K. Lee, G.L. Kinzel, R.H. Wagoner, The Ohio State University, Columbus, 112-119.

Noat, P., Montmitonnet, P., Chastel, Y., Shahani, R. (1995) Anisotropic 3-D modelling of hot rolling and plane strain compression of Al alloys, *Simulation of Materials Processing*, 959-964.

Ponthot, J.P. (1995) Mécanique des milieux continues solides en grandes transformations et traitement unifié par la méthode des éléments finis, Ph. D thesis, University of Liège

Szabo, L. & Balla, M. (1989) Comparison of some stress rates, *Int. J. Solids&Structures*, **25**, 279-297.

Szabo, L. (1985) Evaluation of elasto-viscoplastic tangent matrices without numerical inversion, *Comp. & Struct.* **21**, 1235-1236.

Teodosiu, C., Hu, Z. (1998) Microstructure in the continuum modelling of plastic anisotropy, Proceedings of the 19th Riso Int. Symp. on Materials Science : Modelling of Structure and Mechanics of Materials from Microscale to Products, Carstensen, J.V., Leffers, T. Eds.

Valliappan, S., Boonlaulohr, P., Lee, I.K., (1976) Non-linear analysis for anisotropic materials, *Int. J. Num. Meth. in Eng.*, **10**, 597-606.

Wauters, M. (1997) Etude de la rupture des matériaux métalliques : approche expérimentale et simulations numériques par éléments finis couplés à la théorie de l'endommagement, FRIA, rapport annuel.

Wauters, M. (1998), Etude de la rupture des matériaux métalliques : approche expérimentale et simulations numériques par éléments finis couplés à la théorie de l'endommagement, FRIA, rapport annuel.

Wauters, M. (1999) Etude de la rupture des matériaux métalliques : approche expérimentale et simulations numériques par éléments finis couplés à la théorie de l'endommagement, FRIA, rapport annuel.

Wauters, M. (2000) Calibration of an anisotropic elasto-plastic damage model for sheet metal forming, Diplôme d'Etudes approfondies en Sciences Appliquées, Université de Liège.

Wauters, M., Habraken, A.M., Duchêne, L. (2000) A fully elasto-plastic damage model applied to anisotropic materials, Proceedings of 14th Engineering Mechanics Conference, Austin Texas, USA.

Zhu, Y.Y. (1992) Contribution to the local approach of fracture in solid dynamics, Ph. D. Thesis, University of Liège, Department MSM.

Zhu, Y.Y., Cescotto, S. (1995) A fully coupled elasto-visco-plastic damage theory for anisotropic materials. *Int. J. Solids & Structures*, **32-11**, 1607-1641.

8. CONCLUSIONS

An overview of damage models applied to ductile rupture has been proposed to the reader, providing background for the macroscopic models developed in MSM and described in Chapters 6 and 7.

Concerning rupture during sheet metal processes, Chapter 4 enhances the interest of criteria, such as those developed by Hora-Brunet or Boudeau-Gelin. The advantage of Thomason's criterion, based on microscopic roots and coupled with macroscopic results, has also been demonstrated. However, this latter criterion requires microscopic data. So it can only be applied if mechanical and metallurgical teams work together to study a material. The last investigated direction is rupture criteria based on energy consideration, as in fracture mechanics. Damage models developed by MSM have not yet been coupled with these criteria. This could be included in a possible extension of this work.

The thesis is limited to rupture detection, and the implemented models do not apply to the study of crack propagation as explained in chapter 5. Even for rupture detection, some mesh dependency problems appear when damage elasto-plastic models are used (see section 6.3). This problem also provides a development direction for further study.

This research on macroscopic models will go on. For instance, the validation of the anisotropic damage-elasto-plastic model is clearly not achieved.

The purely macroscopic mechanical experimental approach has prevented the use of interesting parameters such as the material characteristic length to define finite element sizes or apply Thomason's criterion. So for future research, collaborations with the metallurgy service are foreseen to provide such information.

Microscopic aspects are very important and a micro-macro approach such as that of Chaboche & Feyel 2001 seems very interesting from a scientific point of view. These authors use, at each integration point of the FE macroscopic mesh, another finite element mesh to study the material behavior on a microscopic scale with an elastoviscoplastic and damage constitutive law. Such research provides basic understanding of rupture and this will probably give new components to include in macroscopic models. However, even if parallel computation opens new dreams, macroscopic approaches (Gurson's model or Lemaître's law) retain their interest. They cover different types of loading and can provide a reliable prediction of rupture. They are easily included into a forming process optimization where free parameters are tool shape, sheet thickness and low value of damage parameters. To conclude, even if the micro–macro link is important to investigate and can provide new trends to develop new materials, the classical macroscopic approach still has a role to play in practical industrial problems.

Reference

Chaboche, J.L., Feyel, F. (2000) On the multiscale analysis of composite structures by using FE^2 technique and fibre-matrix damage mechanics, *Continuous Damage and Fracture* , Benallal, A. editor, Elsevier.

PART D

CONCLUSIONS AND PERSPECTIVES

Thèse présentée en vue de l'obtention du grade d'Agrégé de l'Enseignement Supérieur
par Anne-Marie HABRAKEN

Année académique 2000-2001

CONCLUSIONS AND PERSPECTIVES

Two types of material constitutive laws for finite element models have been investigated: micro-macro approaches based on texture analysis and damage models. In each case, the proposed literature review helps to understand the context of the models developed by the MSM team.

In the texture field, this thesis summarizes in a first step the results of the MSM collaboration with Professor van Houtte: the implementation of a 6^{th} order yield locus in the stress space and the use of his Taylor's software. In a second step, original proposals are described. The hyperplane method was developed; however its stability and convergence were not sufficient. Consequently, a second idea, in which more attention is given to continuity requirements, has been proposed. It consists in a new interpolation method, rather than an additional yield locus function. This interpolation approach can be considered as an extension to the five dimensional deviatoric stress space of the concept of isoparametric finite elements. The interest of this yield locus local description is linked to the goal of following texture evolution during FE computation. It is clear that if this evolution can be neglected, an accurate global yield locus function requires less CPU time. Validation of this method as well as optimization of its parameters to provide low CPU time is currently in progress with Laurent Duchêne's Ph. D. thesis.

In the damage field, the summarized research is characterized by the fact that new models are not only proposed but also applied to a large set of different loading states. Their numerical implementation, the identification of their parameters as well as their validation have been conducted. The damage extension of Bodner's elasto-visco-plastic law is able to localize a rupture event with simple damage criteria such as the threshold value of the damage parameter in a limited range of triaxiality value. The limits of an isotropic damage elasto-plastic model applied to the same experimental set as above Bodner's model have been demonstrated. Improvements of the anisotropic elasto-plastic model proposed by Zhu have been implemented. A method to identify these model parameters has been proposed; a simple choice can even ignore damage measurements. New skills have been developed in the MSM laboratory to provide accurate Young's modulus measurements and to perform tensile tests away from material anisotropy axes. An optimization of the sample shape according to the measurement devices has been performed. These results are available for next experiments to identify the parameters of the anisotropic damage model applied to sheet. For a classical deep drawing steel and a high tensile steel, the decrease of Young's modulus with plastic strain has been verified. The advantages and limitations of macroscopic damage models are defined.

The important state-of-the-art study performed for this thesis allows using it as material for third cycle courses and provides perspectives for further work. Some possible extensions or new fields connected to this research are as follows:

- Development of parallel computation adapted to the MSM micro-macro model based on texture analysis;
- Further investigation to find criteria telling when a texture updating is required;
- Implementation of a more sophisticated hardening rule in the MSM micro-macro model based on texture analysis;
- Development of experiments to identify this sophisticated hardening rule;
- Investigation of the variational multi-scale approach;
- Implementation of new criteria to detect damage;
- Development of non-local or gradient formulation of damage elasto-plastic laws;
- Mesh adaptation: the idea is to study an industrial process with a macroscopic damage model, then where possible rupture is detected, to remesh and provide a finer analysis of microscopic event;
- Specific development of finite elements able to model crack propagation;
- Robust inverse models to identify model parameters thanks to finite element simulations of experiment.

At the beginning of the thesis, applications of both anisotropic models developed for metal sheets (texture-based model described in Chapter 6, part B, and damage model described in Chapter 7, part C) were planned on both studied steel sheets (high tensile steel sheet or classical deep drawing steel sheet):

- FLD prediction;
- complete finite element simulations of biaxial Marciniak test.

However, as such results are not yet ready, they should be included in Duchêne's thesis (2001, 2002?). Note that, for a very large set of steel grades, Cayssials's approach provides an efficient way to predict FLD. Thus, FLD prediction is no longer such an important goal to save time and money, but rather becomes a validation step of a constitutive law. If Marciniak's approach is used, the result also depends on the size of the imposed defect; thus the constitutive law is not the only factor defining the reliability of the prediction.

A set of cup drawing experiments are available for the two steel grades studied; the prediction of their accurate final shape and final texture will therefore provide an additional validation of the developed constitutive laws.

To summarize, parts B and C of this thesis describe Habraken's scientific involvement in two fields: micro-macro models and damage models. Appendices 1 and 2 give an idea of the thermo-metallurgical-mechanical laws developed to simulate hot forming processes and to study recrystallization phenomena. One model of contact between two deformable bodies is proposed in the third appendix.

Reference

Cayssials, F. (1998) A new method for predicting FLC, IDDRG, Conference Geneval, Brussels 6/98.